4-26-2022

Building a Turbulent Jet: Measuring/Modeling Lagrangian Dispersion, Particle Trajectory Dynamics and Intermittency

Bianca Fontanin Viggiano
Portland State University

Building a Turbulent Jet: Measuring/Modeling Lagrangian Dispersion, Particle Trajectory Dynamics and Intermittency

by

Bianca Fontanin Viggiano

A dissertation submitted in partial fulfillment of the
requirements for the degree of

Doctor of Philosophy
in
Mechanical Engineering

Dissertation Committee:
Raúl Bayoán Cal, Chair
Mickaël Bourgoin
Dacian Daescu
Elliott Gall
Charles Meneveau
Gerald Recktenwald

Portland State University
2022

Abstract

The mechanics of how particles diffuse, interact, eject, etc. within a fluid is applicable to numerous industrial and environmental applications. Unwanted products of combustion, dust contamination of solar panels, pathogen transport during a cough and ejections of particles during volcanic eruptions, are a few examples of flows in which increased knowledge of particle dynamics could result in substantial reduction of negative environmental and economic impacts. To better understand the tendencies of particles within shearing flows (such as jets), an extensive experimental campaign was conducted. Measurements of a turbulent round water jet were performed within an icosahedral tank. Particle tracking velocimetry was employed to create three-component, three-dimensional trajectories. Particles of varying size and weight were used to seed the flow in order to provide a range of inertial effects based on the particle interaction with the fluid. Numerous Eulerian and Lagrangian parameters were characterized and most notable, a trajectory stationarization technique was successfully implemented to address the inhomogeneity of the flow field. This approach could be extended to provide systematic methods to analyze complicated flow fields, enhancing knowledge of their dynamics.

Alternatively, theoretical models of particle mechanics have been constructed, contributing to the baseline understanding of Lagrangian dynamics. Stochastic processes and phenomenological approaches are presented to accurately predict the low-order statistics of tracers, point particles which follow the motion of the fluid, for the idealized flow of homogeneous, isotropic and stationary turbulence (i.e. without

the inclusions of external forces).

In comparison to previous models, the proposed process is infinitely differentiable for finite Reynolds number and includes intermittent scaling properties. Furthermore, particle accelerations and velocities can be modeled based on the stochastic processes, providing full temporal information of the flow dynamics.

The advancements made to homogeneous, isotropic and stationary turbulence are then exploited and used as an input to generate an inhomogeneous flow field based on self-similar relations within a jet to include, in a simple way, the intermittent behavior of the turbulence. Specifically, a model is proposed to compensate a stationary signal by the evolution of the Eulerian background properties of a jet to transform Lagrangian velocities in order to build up an ensemble of turbulent jet trajectories. The modeled jet, based on inputted signals from a stochastic process and direct numerical simulation are compared against the experimental data. Statistics show remarkable agreement for statistics of velocity increments and for higher-order moments, accurately capturing dissipative behavior within the non-homogeneous flow. With some additional study, the proposed model could be applied to modeling of particle velocity statistics during volcanic eruptions, pathogen transport during a cough and pollutant contamination from smokestacks.

Acknowledgements

I cannot express enough gratitude to my advisor, Raúl Bayoán Cal. I would not be here without his unconditional support and encouragement. His enthusiasm for research is unparalleled and contagious. I have enjoyed my many years working in the turbulence lab at PSU in no small part because of Raúl and the environment he has cultivated. This is also noticed in the many students in our group that I have been lucky enough to work with and learn from. Thanks to Naseem Ali, for helping me get started in research and for patiently helping me on my first project in the lab as an undergraduate. Also, I want to thank Betsy Camp and Nicholas Hamilton, both of whom welcomed me into the lab, along with Naseem, and provided guidance and resources when needed. In addition, many thanks are extended to Karl Cardin and Facundo Cabrera, I always appreciate our discussions, both scientific and not.

Throughout my studies, I have been fortunate enough to collaborate with many tremendous researchers. The additional guidance of Mickaël Bourgoin and Laurent Chevillard throughout my time at École Normale Supérieure (ENS) de Lyon and continually since, is of great importance to the quality and quantity of the work presented. Furthermore, their welcoming of me into the lab and to the city of Lyon made my time in France even more memorable. At ENS I was also fortunate to work on projects with Thomas Basset and Jan Friedrich, both of whom are integral parts of the projects presented. Along with Raúl, the hours of discussion we have all had together led to the culmination of the work presented.

Over the years, I have also been able to collaborate on numerous projects, some

of which are part of the work presented in the thesis and some are part of larger collaborative projects. I especially want to thank Romain Volk, Murat Tutkun and Stephen Solovitz for guidance and support on the many projects we have performed over the years. Many thanks also to Larry Mastin, Alexa Van Eaton, John Eaton and Davis Hoffman for the valuable and enthusiastic discussions.

Thank you to Dacian Daescu, Elliot Gall and Gerald Recktenwald, the members of my committee, for their improvements to the thesis, with extended gratitude to Charles Meneveau for the always constructive discussions which have led to improvements of the work presented here and extensions of this work for the future.

Finally, I want to thank my family for the many years of support. I would not be here without the love and encouragement of my partner, Alex.

Table of Contents

List of Tables

List of Figures

Preface

Turbulence exists constantly around us, with endless examples of flows to visualize, interpret and quantify. However the subject is vast and therefore we must be thoughtful with our methods in order to make a targeted impact to progress our understanding. The jet is essential to research of turbulent inhomogeneous flow due to its well characterized behaviors and its relevance to many industrial and natural flow phenomena. For these reasons, we decided to take this fundamental flow, the turbulent round jet, and study it from an alternative perspective.

Despite being inhomogeneous in space, jets are well studied because, similar to boundary layers and wakes, they present Eulerian self-similar behavior. Specifically, as the flow develops, many pertinent quantities of the flow can be described by a single spatial parameter, encompassing effects in the relevant spatial directions. For a jet, this means that the averaged velocity, variance, covariance, etc. can be quantified by $\eta = f(r, z)$ which is a function of the radial, r, and axial, z, positions. The self-similarity relations further imply that much is known about how jets behave spatially as they develop downstream of the nozzle. With all this information, a novel approach can be built to study the Lagrangian characteristics of a jet.

In implementation, this is the study of fluid tracer dynamics by tracking their position in space and time. This Lagrangian approach gives an alternative perspec-

tive to study the dynamics of a jet, providing additional methods and quantities for characterization of the entrainment and mixing that jets induce. There has been a delay in the study of such a flow from a Lagrangian perspective which is primarily due to the slow development of measurement equipment capable of performing particle tracking velocimetry, the tracking of tracer particles at sufficient resolution in space and time. Furthermore, the inhomogeneous field translates to a non-stationary Lagrangian flow which disallows the use of many necessary relations which help to characterize important quantities such as the dissipation scales, time and length scales of the flow, diffusion properties, etc.

This last point was remedied by Batchelor [1957] through manipulation of the velocity along the trajectory to compensate for the turbulent decay and time step compensation for the Eulerian background field as the jet develops downstream. Using an extension of these methods allows us to characterize the trajectory dynamics within the jet. In turn, we can learn about entrainment, time scales and we can identify the Lagrangian "universal" constant C_0 (á la Kolmogorov), which is essential to accurate stochastic modeling and has yet to be well understood as a function of its location within an inhomogeneous field.

The lack of Lagrangian analysis of inhomogeneous flow fields provides an opening, not only to the characterization of free shear flow phenomena (such as is the case of a round jet), but also other non-homogeneous fields. Improved understanding of quantities such as time scales and C_0 can improve the modeling of inhomogeneous flows, yet there remains a dependence on the boundary conditions and much more experimental work is needed to fully characterize these variables.

Given a systematic approach to accurately analyze highly inhomogeneous flow

through some form of homogenizing the field (stationarizing the trajectories), we then aim to invert these relationships and build up a non-homogeneous flow based on stationary turbulence. Specifically, a jet could be produced by applying non-stationarity, based on well-known Eulerian relations of the jet, to a set of inputted trajectories obtained *a priori* as homogeneous, isotropic and stationary turbulence (HIST) velocity signals. This is appealing in that most classical perspectives have considered these idealized (HIST) flows, with critical advancements made to turbulent research. This allow us to make use of the major advancements that have been made to HIST modeling and simulations to accurately include intermittent behaviors of the signal as they are perceived by fluid parcels within the non-stationary flow.

If we can model a turbulent jet that exhibits intermittent behavior accurately, the implications are far-reaching. First, with the ability to provide quick, low cost and accurate representations of the fluid mechanisms within a turbulent jet, the model can benefit the geophysical community through improved predictions of ash distributions during an episode. Ash clouds formed as a result of eruptions can severely damage aircraft engines, causing safety concerns as well as the disruptions to air traffic and re-routing of flights. Furthermore, forecasting particle fallout is essential to the prevention of water supply and sewerage system contamination.

Another highly benefited field could be epidemiology. The ability to model small particle diffusion from a cough is advantageous to the reduction of disease spread. This could be implemented through parametrization by only a few known inputs of typical cough dynamics (i.e., velocity, angles of the expulsion). Directly applicable to the effective reproduction number, R, used to quantify contagion levels of a

virus, models could be built to quickly indicate safe distances and relative exposure. Identifying distance and dispersal of minute pathogens during a cough can help improve our knowledge of how to best mitigate long term spread of a disease.

Implications can reach beyond point diffusion problems and can be used to more appropriately analyze a broader range of inhomogeneous flow fields seen in nature and industry. One could use what we have built for generating a Lagrangian jet to more accurately represent how the fluid elements behave within numerous flows, such as atmospheric boundary layers and wind turbine wakes.

Outline of the thesis

The thesis is broken into three parts: Theoretical modeling of homogeneous and isotropic turbulence, experimental findings from Lagrangian measurements in a round jet and finally, we propose methods, using the homogeneous, isotropic velocity signals generated in part one, to build up a turbulent jet. The statistics of the model are compared to the experimental results of the jet from part two. Prior to these sections, Chapter 1 is devoted to a general introduction to turbulence; the equations of motion, statistical representations and particle dynamics.

Part one follows in Chapter 2, where an introduction to stochastic modeling is presented in Section 2.1, followed by a highly detailed description of the procedures, including an extension to inertial particle modeling, in Section 2.2. The results of these numerical investigations are provided in Section 2.3 and concluding remarks of the theoretic developments follow in Section 2.4.

Chapter 3 then discusses the jet experiments, first providing an introduction to inhomogeneous flows in Section 3.1. Next, precise descriptions of pertinent turbulent

quantities are presented systematically in Section 3.2. A detailed account of the experiments follows in Section 3.3. Section 3.4 presents the initial findings of the experimental analysis of the particle velocity and acceleration, including the applied stationarization procedure, inspired by the Lagrangian self-similarity hypothesis of Batchelor. Inertial particle dynamics in the jet are included in Section 3.5 and conclusions of the experimental findings are included in Section 3.6.

The concluding part of the thesis combines the efforts of Chapters 2 and 3. A model is proposed which is based on self-similarity relations to build up a jet from homogeneous, isotropic and stationary turbulence. Motivations for the model are presented in Section 4.1. A description of the model based on the self-similarity profiles follows in Section 4.2. Resulting statistics of the model are included and compared to those obtained from the experimental jet data in Section 4.3 and concluding remarks are provided in Section 4.4.

The major conclusions from each part of the thesis are reiterated in Section 5.1 and finally the thesis closes with a brief explanation of the future/ongoing work in Section 5.2.

Chapter 1

General introduction

1.1 Equations of motion

The governing equations of fluid dynamics are highly complex as the internal motion of individual fluid elements must be taken into account when studying bulk fluid mechanics. Therefore, the laws of governing fluid motion must include the effect that the fluid has on a surface or volume as well as what affects the fluid as it moves through said space. The Reynolds transport theorem,

$$\frac{\mathrm{d}}{\mathrm{d}t}\int_{cv}\psi \mathrm{d}V = \int_{cv}\left[\frac{\partial \psi}{\partial t} + \nabla\cdot(\boldsymbol{u}\psi)\right]\mathrm{d}V, \tag{1.1}$$

captures the fact that the control volume is deformable and transportable. The control volume cv is time dependent and $\boldsymbol{u}$ and ψ are respectively the velocity vector and an arbitrary scalar or vector. This theorem provides the derivation of the conservation of mass as well as the equation of motion of the velocity field by inputting either the density ρ or momentum $\rho\boldsymbol{u}$ as the input variable ψ. Notice also that the theorem presents two ways to describe the dynamics. As previously mentioned, this enables the fixed frame coordinates of a Eulerian approach as well as the moving frame of reference, allowing the coordinates to be local to the fluid

element in motion.

First, concerning the continuity equation, if mass is conserved than the rate of change must be zero and therefore,

$$\frac{\partial \rho}{\partial t} + u_j \frac{\partial \rho}{\partial x_j} + \rho \frac{\partial u_k}{\partial x_k} = 0. \tag{1.2}$$

The continuity equation is simplified further for a incompressible fluid to

$$\frac{\partial u_k}{\partial x_k} = 0, \tag{1.3}$$

due to the fact that the density is temporally and spatially uniform. Here index notation has been introduced and will be used for clarity when presenting the governing equations of motion.

Application of Newton's second law of motion yields the equation of motion,

$$\frac{\mathrm{d}}{\mathrm{d}t} \int_{cv} \rho u_i \mathrm{d}V + \int_{cv} \rho \frac{\mathrm{D}u_i}{\mathrm{D}t} \mathrm{d}V = \sum F_{\text{ext}}, \tag{1.4}$$

where F_{ext} are the applied external forces and the material derivative, $\mathrm{D}/\mathrm{D}t$, is introduced which measures the rate of change of a variable. It is defined mathematically as

$$\frac{\mathrm{D}(\ )}{\mathrm{D}t} = \frac{\partial(\ )}{\partial t} + u_j \frac{\partial(\ )}{\partial x_j}. \tag{1.5}$$

Neglecting external forces and considering an incompressible Newtonian fluid, the equation of motion (equation (1.4)) can be expressed as it is more commonly presented

$$\left(\frac{\partial u_i}{\partial t} + u_j \frac{\partial u_i}{\partial x_j}\right) = -\frac{1}{\rho}\frac{\partial p}{\partial x_i} + \nu \frac{\partial^2 u_i}{\partial x_j \partial x_j}, \tag{1.6}$$

where p is the instantaneous pressure and ν is the kinematic viscosity. The Navier-Stokes equations (equations (1.3) & (1.6)) are nonlinear and therefore can only be solved analytically for a few known scenarios of very simplified flows.

It has long been noted that flows can be laminar (uniform) or turbulent (chaotic) and the transition is dictated by the Reynolds number $Re = UL/\nu$, the ratio of inertial to viscous terms, where the characteristic velocity U and length scale L are chosen based on the type of flow. Most applications involve turbulent flow, the dynamics of which are complex, resulting in complicated equations of motion when compared to simpler laminar flow fields.

A statistical approach

This leads many to consider a statistical description of turbulence, formed on the basis that although the details of a turbulent signal are unpredictable, their statistics are reproducible. But turbulent descriptions can become even more complicated through manipulation of the equations of motion. For example, by taking average quantities into equations (1.3) & (1.6) one can obtain the Reynolds Averaged Navier-Stokes (RANS) equations:

$$\frac{\partial \overline{u}_k}{\partial x_k} = 0, \tag{1.7}$$

and

$$\left(\frac{\partial \overline{u}_i}{\partial t} + \overline{u}_j \frac{\partial \overline{u}_i}{\partial x_j}\right) = -\frac{1}{\rho}\frac{\partial \overline{p}}{\partial x_i} + \nu \frac{\partial^2 \overline{u}_i}{\partial x_j \partial x_j} - \frac{\partial}{\partial x_j}(\overline{u_i' u_j'}), \tag{1.8}$$

where the overbar denotes a time average and prime indicates the fluctuation from the mean. Reynolds decomposition, $u_i = \overline{u}_i + u'_i$, is implemented to convert the nonlinear term to the Reynolds stress, $\overline{u'_i u'_j}$. This equation is the basis for simple implementations of computational fluid dynamics and introduces the dilemma of these models, the six unknowns that are produced by the Reynolds stress. This underdetermined set of equations has commonly been referred to as the closure problem.

1.2 Kolmogorov's Hypothesis

A common approach to study turbulence is through probabilistic investigations into the velocity signal. For an idealized flow field (i.e., homogeneous and isotropic turbulence), a set of physically motivated hypotheses were put forth in the foundational work of Kolmogorov [1941], referred to as K41 theory. Applying to homogeneous, isotropic and stationary turbulence, the phenomenological model proposed that, given a high Reynolds number flow, universality exists within the small scales of turbulence. More specifically, indicating that the dissipation length scale, $\eta = (\nu^3/\varepsilon)^{1/4}$, dissipation time scale, $\tau_\eta = (\nu/\varepsilon)^{1/2}$, and dissipation velocity, $u_\eta = (\nu\varepsilon)^{1/4}$, are independent of large scale effects, where the mean dissipation rate is ε and ν is the kinematic viscosity. The dynamics of the fluid at larger scales are dictated by input/geometric parameters. Small scale flow was modeled by Richardson [1922] as a cascade process in which eddies break up into smaller eddies which break up further until a finite size is reached and the turbulent energy is converted into heat through dissipation. This process is schematically represented in figure 1.1.

The inertial range, introduced in figure 1.1, also exists within the range of scales

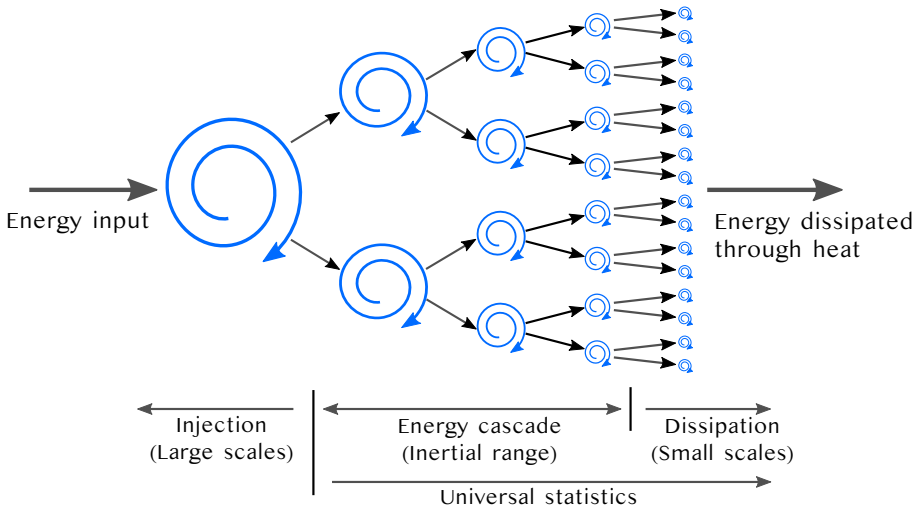

Figure 1.1: Richardson cascade schematic of energy mechanics within turbulent flow.

which are independent of input conditions (i.e., they only depend on the length scale r and mean rate of change of turbulent kinetic energy, ε). But this range of scales are too large to be dissipated and therefore fall between the large length scale L_E (injection) and small length scales η (dissipation), given as $\eta \ll r \ll L_E$. The subscript $_E$ denotes the Eulerian framework.

A description of the statistical behavior of turbulence within this framework is obtained via the Eulerian velocity structure functions defined at a given time, t, as the statistical moments of order, p, with r the spatial separations,

$$S_p^E(\boldsymbol{r}) = \langle [(\boldsymbol{u}(\boldsymbol{x}+\boldsymbol{r},t) - \boldsymbol{u}(\boldsymbol{x},t)) \cdot \boldsymbol{r}/r]^p \rangle, \tag{1.9}$$

where a bold symbol denotes a vector, i.e., $\boldsymbol{u} = (u_x, u_y, u_z)$. According to the second similarity hypothesis by Kolmogorov [1941] for homogeneous isotropic turbulence, within the inertial range the structure functions become solely dependent on the

energy dissipation rate ε and involve dimensionless universal constants C_p which depend on the structure function order p, such that

$$S_p^E(r) = C_p(\epsilon r)^{p/3}, \qquad \text{for } \eta \ll r \ll L_E. \tag{1.10}$$

For second-order statistics, which describe the energy distribution across the spatial scales of turbulence, the constant C_2 is empirically known (its value is of the order of $C_2^{\parallel} = 2.1$, where the $\parallel$-superscript indicates that longitudinal velocity increments and longitudinal spatial increments are considered [Pope, 2000]). In the Eulerian framework, third order statistics are particularly important, as they can be analytically calculated from the Navier-Stokes equation in connection with the Karman-Howarth relation for the energy flux across scales, leading in the limit of high Reynolds numbers to the celebrated constant $C_3^{\parallel} = -4/5$, the minus sign indicating a direct energy cascade [Batchelor, 1947]. At high orders (typically $p > 4$) deviations are expected due to the intermittency phenomenon [Frisch, 1995].

1.3 Lagrangian framework

Previously touched on, turbulent flow properties can be described either in a fixed frame of reference, the so-called Eulerian description, or alternatively by the Lagrangian description, where evolution of the flow is observed temporally through the trajectories of the point particles. The trajectory of an ideal tracer, the so-called Lagrangian path, can be determined from the first-order ordinary differential equation (ODE):

$$\frac{d\boldsymbol{X}}{dt}(\boldsymbol{x}, t) = \boldsymbol{u}(\boldsymbol{X}(\boldsymbol{x}, t), t), \tag{1.11}$$

where $\boldsymbol{u}(\boldsymbol{x},t)$ is the fluid velocity field, $\boldsymbol{X}$ is the particle trajectory position with the initial condition $\boldsymbol{X}(\boldsymbol{x},0)=\boldsymbol{x}$ and $\boldsymbol{x}=(x,y,z)$ in Cartesian coordinates. Furthermore, the Lagrangian velocity along a particle trajectory $\boldsymbol{X}(\boldsymbol{x},t)$ is defined as

$$\boldsymbol{v}(\boldsymbol{x},t)=\boldsymbol{u}(\boldsymbol{X}(\boldsymbol{x},t),t). \tag{1.12}$$

Lagrangian and Eulerian velocity are respectively denoted by v and u, unless otherwise noted, for the remainder of the thesis. The investigation of the behavior of ideal tracer particles in turbulent flows, which is governed by equation (1.11), is one of the main concerns of turbulence theory.

Taylor's theory of turbulent diffusion

The Lagrangian description in turbulence provides a complete view of particle transport and dispersion which can be traced back to the seminal work by Taylor who set the diffusion problem in the context of fluid element trajectories [Taylor, 1922]. Taylor's theory connects the mean square displacement (MSD) $D_x^2(\tau)$ of particles spreading from a point source in stationary homogeneous isotropic turbulence to the Lagrangian two-point correlation function $\mathcal{C}_v(\tau)=\langle v(t+\tau)v(t)\rangle$, where the average $\langle\cdot\rangle$ is taken over an ensemble of particle trajectories. Here, $v(t)$ represents the velocity of individual tracer elements along their trajectory (note that for simplicity only one velocity component is considered) and τ is the time lag. This is often called the Taylor theorem and is explicitly expressed as:

$$\frac{\mathrm{d}^2 D_x^2}{\mathrm{d}\tau^2}(\tau)=2\mathcal{C}_v(\tau). \tag{1.13}$$

Taylor's theory is of utmost practical importance, as it reduces the prediction of the spreading of tracer particles (and therefore of any passive substance spread by turbulence with negligible molecular diffusivity) to the knowledge of the Lagrangian two-point correlation function $\mathcal{C}_v(\tau)$ at all times. The correlation at $\tau = 0$, $\mathcal{C}_v(0)$, is the mean square of the velocity fluctuations σ_v^2.

The asymptotic regimes of the short and long time scales of turbulent diffusion do not depend on the details of the dynamics of turbulence. In the limit of very short times, the spreading follows trends of the trivial (purely kinematic) ballistic regime where $D_x^2(\tau) \simeq \sigma_v^2 \tau^2$. This can be retrieved from a simple one term Taylor expansion of the particle displacement itself, or equivalently by applying equation (1.13) and considering the limit at vanishing times for the Lagrangian correlation function, $\mathcal{C}_v(\tau) \simeq \sigma_v^2$ for small times. In the limit of very long time scales, equation (1.13) from Taylor's theory predicts that due to the finite Lagrangian correlation time of turbulence ($T_L = \sigma_v^{-2} \int_0^\infty \mathcal{C}_v(\tau) \mathrm{d}\tau$) the long term turbulent diffusion process behaves as simple diffusion (where the MSD grows linearly with time, $D_x^2 \propto 2K_T\tau$, for long times) with a turbulent diffusivity $K_T = \sigma_v^2 T_L$. Note that the Lagrangian integral time scale, T_L, has been introduced.

Detail of the diffusion process at intermediate time scales requires a deeper knowledge of the specific time dependence of $\mathcal{C}_v(\tau)$ at all times, particularly in the inertial range of scales of turbulence.

Kolmogorov extension to Lagrangian dynamics

In the Lagrangian framework, the multi-scale dynamics of turbulence is described by the Lagrangian structure functions, defined as the statistical moments of the

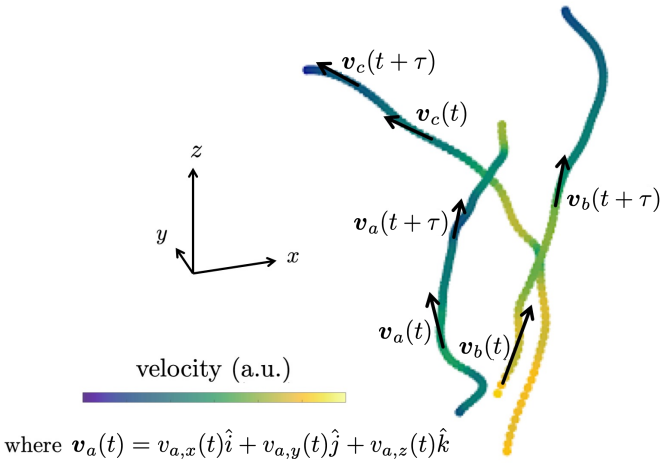

Figure 1.2: Schematic of the Lagrangian velocity increment in a Cartesian coordinate system for a given time lag τ.

temporal velocity increments along particle trajectories, $S_p^L(\tau)$, defined as

$$S_p^L(\tau) = \langle |\boldsymbol{v}(t+\tau) - \boldsymbol{v}(t)|^p \rangle. \tag{1.14}$$

Figure 1.2 provides a schematic of this approach, where for example, a particle tagged a is traveling along its trajectory and the velocity difference would be $\boldsymbol{v}_a(t+\tau) - \boldsymbol{v}_a(t)$ for a given time lag, τ. Note that for inhomogeneous flows, this formula relies on the initial location but, for sake of keeping formulas compact, explicit reference to initial position will be omitted when exploring inhomogeneous Lagrangian statistics.

Within the second similarity hypothesis by Kolmogorov [1941] for homogeneous, isotropic turbulence these increments are expected to follow the scaling

$$S_p^L(\tau) = C_p^L(\varepsilon\tau)^{p/2}, \qquad \text{for } \tau_\eta \ll \tau \ll T_L. \tag{1.15}$$

The second-order structure function is of great importance as it relates to the correlation function as $S_2^L(\tau) = \langle [v(t+\tau) - v(t)]^2 \rangle = 2(\mathcal{C}_v(0) - \mathcal{C}_v(\tau))$. Directly tied back into the full description of the diffusion process, such dependency can be inferred empirically from a Lagrangian second-order structure function with the now provided relationship $S_2^L(\tau) = C_0 \varepsilon \tau$. The universal constant C_0 (the proportionality constant used for C_p^L when $p = 2$) plays a similar role in the Lagrangian framework to the Kolmogorov constant in the Eulerian framework. As a consequence, a detailed description of the turbulent diffusion process, including the inertial scale behavior, relies on the knowledge of $S_2^L(\tau)$ (or equivalently of $\mathcal{C}_v(\tau)$) at all time scales and specifically on the knowledge of C_0 at inertial scales. Thereafter, stochastic models can be built giving reasonable Lagrangian dynamics descriptions at all time scales [Sawford, 1991].

As stated above, the similarity of velocity increments in the inertial range are supposed to scale as $\tau^{p/2}$. But this is known to fail, as it does within the Eulerian framework. This is evidenced by experimental and numerical which suggest that moments exhibit multifractal scaling $S_p^L(\tau) \sim \tau^{\zeta_p}$ which manifests itself in form of a nonlinear dependence of the scaling exponents ζ_p on order p [Mordant et al., 2001a].

1.4 Finite inertia effects

Depending on the particle characteristics (size, density with respect to the carrier fluid, volume fraction, etc.), its dynamics will follow that of the fluid (particles will then be considered as tracers) or it may be affected by inertial effects, finite size effects and couplings between the phases in highly seeded particle-laden flows [Berk and Coletti, 2020].

Once a particle gains inertia, either from its size or its density in comparison to the surrounding fluid, the dynamics of the particle become increasingly complicated. For example, there are now effects due to the Stokes drag force based on the relative velocities of the fluid and the particles and an added mass force which is caused by the displacement of the fluid from the motion of the particle, to name a few. Assuming that the initial particle velocity at $t = 0$ matches the fluid velocity $\boldsymbol{v}_p(\boldsymbol{x}, 0) = \boldsymbol{u}(\boldsymbol{x}, 0)$, this leads to an equation of motion defined as:

$$\frac{d\boldsymbol{v}_p(\boldsymbol{x},t)}{dt} = \beta \frac{\mathrm{D}\boldsymbol{u}(\boldsymbol{X}_p(\boldsymbol{x},t),t)}{\mathrm{D}t} + \frac{1}{\tau_p}\left[\boldsymbol{u}(\boldsymbol{X}_p(\boldsymbol{x},t),t) - \boldsymbol{v}_p(\boldsymbol{x},t)\right] \tag{1.16}$$

where $\boldsymbol{v}_p(\boldsymbol{x}, t)$ is the particle velocity, $\boldsymbol{X}_p(\boldsymbol{x}, t)$ is the particle position, β is the density ratio of the fluid ρ_f to the particle ρ_p where $\beta = 3\rho_f/(\rho_f + 2\rho_p)$ and recall, $\boldsymbol{u}(\boldsymbol{x}, t)$ is the fluid velocity field and $\mathrm{D}/\mathrm{D}t$ is the material derivative, previously defined. The particle response time, τ_p, is defined as $\tau_p = m_p/3\pi\mu_f d_p$ where m_p and d_p denote the mass and the diameter of the particle, respectively and μ_f is the viscosity of the fluid. The value of β ranges from 3, very light particles, to 0, infinitely heavy particles where the material derivative is neglected from equation (1.16).

Assuming heavy particles, inertial particle motion is governed by the following system of first order ODEs

$$\frac{d\boldsymbol{X}_p(\boldsymbol{x},t)}{dt} = \boldsymbol{v}_p(\boldsymbol{x},t)\ , \tag{1.17}$$

$$\frac{d\boldsymbol{v}_p(\boldsymbol{x},t)}{dt} = \frac{1}{\tau_p}\left[\boldsymbol{u}(\boldsymbol{X}_p(\boldsymbol{x},t),t) - \boldsymbol{v}_p(\boldsymbol{x},t)\right]. \tag{1.18}$$

In this simplified model, the Stokes number is the relevant parameter defined as St $= \tau_p/\tau_\eta$. This quantity describes the ratio of the response time of the particle to

the Kolmogorov time scale, the smallest temporal scales present in turbulent flow. In particular, for $\mathrm{St} = 0$ an adiabatic approximation yields equation (1.11) and the particle behaves as an ideal Lagrangian tracer.

Chapter 2

Modeling of particle dynamics in homogeneous isotropic and stationary turbulence[1,2]

2.1 Introduction

Stochastic models are built to describe the known phenomena of turbulence and have a long history in the literature of turbulent flows (see Pope [1990], Pope and Chen [1990], Sawford [1991], Borgas and Sawford [1994a], Wilson and Sawford [1996], Pope [2002], Mordant et al. [2003], Sawford et al. [2003], Beck [2003], Friedrich [2003], Reynolds [2003], Reynolds et al. [2005], Lamorgese et al. [2005], Minier et al. [2014a], and references therein). Typical modeling approaches consist of proposing a random process in time for the velocity $v(t)$ of a tracer particle advected by a turbulent flow to reproduce the expected behavior given by the standard phenomenology of turbulence. At very large Reynolds numbers, in a sustained, statistically stationary turbulent flow of characteristic large integral length scale L, (i) Lagrangian velocity itself is a statistically stationary process of finite variance $\langle v^2 \rangle = \sigma^2$ and is correlated over a large time scale $T \propto L/\sigma$ where σ is the standard deviation of

[1]Viggiano et al., 2020, Modelling Lagrangian velocity and acceleration in turbulent flows as infinitely differentiable stochastic processes. *J. Fluid Mech*, 900:A27

[2]Friedrich et al., 2022, Single inertial particle statistics in turbulent flows from Lagrangian velocity models. *Physical Review Fluids*, 7(1): 014303

the velocity, (ii) it is non-differentiable (i.e. rough) such that the velocity increment variance $\langle(\delta_\tau v)^2\rangle$, where $\delta_\tau v(t) = v(t+\tau) - v(t)$, is proportional to τ as the scale τ becomes smaller. This is the standard dimensional picture of Lagrangian turbulence at infinite Reynolds numbers [Monin and Yaglom, 1975, Tennekes and Lumley, 1972]. At finite Reynolds numbers, v is regularized at small scales by viscosity, and an appropriate modeling must produce differentiable kinematic quantities.

This leads to an interest in building up a random process $v(t)$ with $t \in \mathbb{R}$, and its respective dynamics ensuring causality, with the capability of reproducing these aforementioned statistical properties. More precisely, it is desirable to define such a process $v(t)$ as the solution of an evolution equation forced by a random force. The simplest linear and Markovian stochastic evolution is given by the so-called Ornstein-Uhlenbeck (OU) process that reads

$$dv(t) = -\frac{1}{T}v(t)dt + \sqrt{\frac{2\sigma^2}{T}}W(dt), \tag{2.1}$$

where $W(dt)$ is an instance of the increment over dt of a Gaussian Wiener process (i.e., a white noise). It is noted that since v is defined as a linear operation on a Gaussian random force, it is itself Gaussian. Furthermore, it is consistent with a finite variance process such that $\langle v^2\rangle = \sigma^2$ and the linear behavior of its respective second-order structure function.

The stochastic evolution of $v(t)$ using an OU process (Eq. 2.1) is typical of a non-differentiable process and therefore does not reproduce proper statistical behaviors for the acceleration a. To avoid this problem, the white noise term $W(dt)$ entering in Eq. 2.1 is replaced by a finite-variance random force, correlated over the dissipative

Kolmogorov time scale, τ_η. Furthermore, assuming that this random force is itself defined as the solution of an OU process of characteristic time scale τ_η, it recovers the two-layered embedded stochastic model of Sawford [1991]. This model is appealing since it incorporates the additional necessary time scale τ_η, and in turn, a finite Reynolds number. Both velocity and acceleration are statistically stationary and of finite variance in this framework, and the predicted acceleration correlation function reproduces a zero-crossing in the vicinity of τ_η, before decaying towards 0 over T. Nonetheless, although the model gives an appropriate description of the velocity correlation function in both the inertial and dissipative ranges, further comparisons to numerical data present its limitations, specifically the behavior of the acceleration correlation function in the dissipative range, i.e. for time lags smaller than this zero-crossing time scale [Sawford, 1991, Lamorgese et al., 2005].

In the model of Sawford [1991], velocity is once differentiable, leading to a finite variance acceleration process which is not twice differentiable (i.e., the obtained acceleration process is not a differentiable random function). This observation has strong implications on the shape of the acceleration correlation function which is important for small scale phenomena of turbulence, in particular in the dissipative range. This is observed in numerical data for both velocity and acceleration, and expected from the physical point of view when viscosity is finite, in that correlation functions of differentiable random functions are parabolic (or smoother) in the vicinity of the origin. In contrast, the predicted acceleration correlation function of Sawford [1991] behaves linearly, and therefore modeling Lagrangian velocity by a two-layered embedded OU process appears to be too simplistic to reproduce the correlation structure of acceleration in the dissipative range.

For this reason, the model of Sawford [1991] is generalized in order to construct a causal stochastic process which is infinitely differentiable at a given finite Reynolds number, consistent with the standard aforementioned phenomenology of turbulence in the inertial range (i.e., for scales $\tau_\eta \ll \tau \ll T$), and that converges towards an OU process at infinite Reynolds numbers (or equivalently as $\tau_\eta \to 0$).

2.2 Theoretical methods

2.2.1 Ordinary and embedded Ornstein-Uhlenbeck processes as statistically stationary models for Lagrangian velocity and acceleration

Standard arguments developed in turbulence phenomenology [Tennekes and Lumley, 1972] lead to the consideration of, as a stochastic model for velocity of Lagrangian tracers, the Ornstein-Uhlenbeck process. In particular, such a process reaches a statistically stationary regime in which variance is finite and exponentially correlated. Single and two-layer models are first presented to provide terminology and context for the subsequent introduction of the infinite layer process.

Ordinary single-layered Ornstein-Uhlenbeck process

Denoted as $v_1(t)$, the process is defined as the unique stationary solution of the following stochastic differential equation, also called Langevin equation,

$$dv_1(t) = -\frac{1}{T}v_1(t)dt + \sqrt{q}W(dt), \tag{2.2}$$

recall here T is the turbulence (large) turnover time, $W(t)$ is a Wiener process, and $W(dt)$ its infinitesimal increment over dt (i.e., independent instances of a Gaussian

random variable, zero-average and of variance dt). The variable q is the white noise weight, defined to ensure v_1 is a finite variance process. It obeys the following rule of calculation (cf. Nualart [2006]), for any appropriate deterministic functions f and g, which follow in particular integrability conditions such that; $\left\langle \int_{\mathcal{A}} f(t)W(dt) \right\rangle = 0$ and $\left\langle \int_{\mathcal{A}} f(t)W(dt) \int_{\mathcal{B}} g(t)W(dt) \right\rangle = \int_{\mathcal{A}\cap\mathcal{B}} f(t)g(t)dt$. Here $\langle\cdot\rangle$ stands for ensemble average, and $\mathcal{A}\cap\mathcal{B}$ is the intersection of the two ensembles $\mathcal{A}$ and $\mathcal{B}$.

The unique statistically stationary solution of the stochastic differential equation (SDE) provided in equation 2.2 can be written conveniently as

$$v_1(t) = \sqrt{q} \int_{-\infty}^{t} e^{-(t-t')/T} W(dt') \; . \tag{2.3}$$

Since v_1 is defined as a linear operation on the Gaussian white noise $W(dt)$, it is Gaussian itself. Following the integrability conditions of f and g, it is thus fully characterized by its average and correlation function. In particular, v_1 is a zero-average process, i.e. $\langle v_1 \rangle = 0$, and is correlated as

$$\mathcal{C}_{v_1}(t_1 - t_2) \equiv \langle v_1(t_1)v_1(t_2) \rangle = q \int_{-\infty}^{\min(t_1,t_2)} e^{-(t_1+t_2-2t)/T} dt = \frac{qT}{2} e^{-|t_1-t_2|/T}. \tag{2.4}$$

Notice that at $t_1 = t_2$, v_1 is a finite variance process $\langle v_1^2 \rangle = qT/2$ and behaves at small scales as a Brownian motion, as it is required by dimensional arguments developed in the standard phenomenology of turbulence at infinite Reynolds number [Tennekes and Lumley, 1972]. Defining the velocity increment as $\delta_\tau v_1(t) \equiv v_1(t+\tau) - v_1(t)$, it can be noted that

$$\left\langle (\delta_\tau v_1(t))^2 \right\rangle = 2 \left[\left\langle v_1^2 \right\rangle - \mathcal{C}_{v_1}(\tau) \right] \underset{\tau\to 0}{\sim} q|\tau|. \tag{2.5}$$

The scaling behavior, given in equation 2.5, is typical of non-differentiable processes and therefore the respective acceleration process $a_1(t) \equiv dv_1/dt$ is ill-defined. This behavior was alleviated by Sawford [1991] by introducing the dissipative Kolmogorov time scale τ_η into the model.

Embedded Ornstein-Uhlenbeck processes

Two layers: the Sawford model

Following the approach developed by Sawford [1991], the embedded OU process $v_2(t)$ is considered as

$$\frac{dv_2}{dt} = -\frac{1}{T}v_2(t) + f_1(t), \tag{2.6}$$

where $f_1(t)$, which replaces $W(dt)$, is now an external random force that obeys itself an ordinary OU process exponentially correlated over the small time scale τ_η and is defined as the solution of:

$$df_1(t) = -\frac{1}{\tau_\eta}f_1(t)dt + \sqrt{q}W(dt). \tag{2.7}$$

It is a zero-average Gaussian process, and its correlation function is given by

$$\mathcal{C}_{f_1}(\tau) \equiv \langle f_1(t)f_1(t+\tau)\rangle = \frac{q\tau_\eta}{2}e^{-|\tau|/\tau_\eta}. \tag{2.8}$$

The unique statistically stationary solution of equation 2.6 is again given by

$$v_2(t) = \int_{-\infty}^{t} e^{-(t-t')/T} f_1(t')dt',$$

and correlated as

$$\mathcal{C}_{v_2}(\tau) \equiv \langle v_2(t)v_2(t+\tau)\rangle = \int_{-\infty}^{t}\int_{-\infty}^{t+\tau} e^{-(2t+\tau-t_1-t_2)/T}\mathcal{C}_{f_1}(t_1-t_2)dt_1dt_2. \qquad (2.9)$$

Assuming without loss of generality $\tau \geq 0$ (recall that the correlation function of a statistically stationary process is an even function of its argument), splitting the integral entering in equation 2.9 over the dummy variable t_2 into the two sets $[-\infty, t]$ and $[t, t+\tau]$, and performing the remaining explicit double integral, the following expression is obtained:

$$\mathcal{C}_{v_2}(\tau) = \frac{q\tau_\eta^2 T^2}{2(T^2-\tau_\eta^2)}\left[Te^{-|\tau|/T} - \tau_\eta e^{-|\tau|/\tau_\eta}\right], \qquad (2.10)$$

which is in agreement with the formula given by Sawford [1991].

The respective acceleration process $a_2(t) \equiv dv_2(t)/dt$, obtained from equation 2.6, is a zero-average Gaussian process, and its correlation function is given by

$$\begin{aligned}\mathcal{C}_{a_2}(\tau) \equiv \langle a_2(t)a_2(t+\tau)\rangle &= -\frac{\mathrm{d}^2}{\mathrm{d}\tau^2}\langle v_2(t)v_2(t+\tau)\rangle \\ &= \frac{q\tau_\eta^2 T^2}{2(T^2-\tau_\eta^2)}\left[-\frac{1}{T}e^{-|\tau|/T} + \frac{1}{\tau_\eta}e^{-|\tau|/\tau_\eta}\right]. \qquad (2.11)\end{aligned}$$

Notice that the function $\mathcal{C}_{v_2}$ is twice differentiable at the origin, contrary to the function $\mathcal{C}_{v_1}$ from the single-layer model, and therefore a_2 has finite variance given by $\mathcal{C}_{a_2}(0)$.

Generalization to n layers

By iterating the previously described procedure, n additional layers can be considered. Acceleration is now a well-defined random process and the velocity derivatives of order n. Once again, these additional layers will eventually be modeled as OU processes. A similar type of procedure has been adopted in Arratia et al. [2014] in a different context. The obtained embedded structure is defined using a set of n coupled stochastic ODEs, with $n \geq 2$, that reads

$$\frac{dv_n}{dt} = -\frac{1}{T}v_n(t) + f_{n-1}(t) \tag{2.12}$$

$$\frac{df_{n-1}}{dt} = -\frac{1}{\tau_\eta}f_{n-1}(t) + f_{n-2}(t) \tag{2.13}$$

$$\ldots \tag{2.14}$$

$$\frac{df_2}{dt} = -\frac{1}{\tau_\eta}f_2(t) + f_1(t) \tag{2.15}$$

$$df_1 = -\frac{1}{\tau_\eta}f_1(t)dt + \sqrt{q_{(n)}}W(dt)\ . \tag{2.16}$$

The remaining free parameter $q_{(n)}$ can be chosen such that

$$\langle v_n^2 \rangle = \sigma^2, \tag{2.17}$$

independent of τ_η and/or the number of layers n, as it is required by the standard phenomenology of Lagrangian turbulence [Tennekes and Lumley, 1972].

The explicit computation of the correlation functions of velocity v_n and the respective acceleration a_n in the statistically stationary regime (obtained from the set of equations 2.12 to 2.16 as $t \to \infty$) are presented in Appendix A.1 in Proposition

A.1.1. Their expressions are especially simple in the spectral domain, and read, considering $n \geq 2$ to ensure that acceleration is a well-defined process,

$$\mathcal{C}_{v_n}(\tau) = q_{(n)} \int_{\mathbb{R}} e^{2i\pi\omega\tau} \frac{T^2}{1 + 4\pi^2 T^2 \omega^2} \left[\frac{\tau_\eta^2}{1 + 4\pi^2 \tau_\eta^2 \omega^2} \right]^{n-1} d\omega, \tag{2.18}$$

and

$$\mathcal{C}_{a_n}(\tau) = q_{(n)} \int_{\mathbb{R}} 4\pi^2 \omega^2 e^{2i\pi\omega\tau} \frac{T^2}{1 + 4\pi^2 T^2 \omega^2} \left[\frac{\tau_\eta^2}{1 + 4\pi^2 \tau_\eta^2 \omega^2} \right]^{n-1} d\omega, \tag{2.19}$$

where the multiplicative factor $q_{(n)}$ (defined in equation A.6) enforces the prescribed value of velocity variance (equation 2.17). It is of note that taking $n = 2$ layers, the correlation of the process v_2 coincides with the one proposed in Sawford [1991].

It is interesting to consider the limiting process v or a when the number of layers n goes toward infinity from a physical point of view, which would give an example of a causal infinitely differentiable process, if such a process exists. It is possible to show that the correlation function of v_n loses its dependence on the time scale τ, resulting in $\mathcal{C}_{v_n}(\tau) \to \sigma^2$ for any $\tau \geq 0$ as $n \to \infty$. Therefore, asymptotically, the limiting process does not decorrelate, which is at odds with the expected behavior. By considering the re-scaled dissipative time scale $\tau_\eta / \sqrt{n-1}$ instead of τ_η, the system of equations will converge towards a proper process with an appropriate correlation function as $n \to \infty$.

With this in mind, the time scale must be compensated accordingly, resulting in

the following set of embedded differential equations,

$$\frac{dv_n}{dt} = -\frac{1}{T}v_n(t) + f_{n-1}(t) \tag{2.20}$$

$$\frac{df_{n-1}}{dt} = -\frac{\sqrt{n-1}}{\tau_\eta}f_{n-1}(t) + f_{n-2}(t) \tag{2.21}$$

$$... \tag{2.22}$$

$$\frac{df_2}{dt} = -\frac{\sqrt{n-1}}{\tau_\eta}f_2(t) + f_1(t) \tag{2.23}$$

$$df_1 = -\frac{\sqrt{n-1}}{\tau_\eta}f_1(t)dt + \sqrt{\alpha_n}W(dt)\ , \tag{2.24}$$

with

$$\alpha_n = \left(\frac{n-1}{\tau_\eta^2}\right)^{n-1} \frac{2\sigma^2 e^{-\tau_\eta^2/T^2}}{T\,\mathrm{erfc}\,(\tau_\eta/T)}, \tag{2.25}$$

where $\mathrm{erfc}(t) = 1 - \mathrm{erf}(t)$ is introduced and the error function $\mathrm{erf}(t) = (2/\sqrt{\pi})\int_0^t e^{-s^2}ds$. The chosen white noise weight α_n ensures that the variance of the limiting process v is finite with $\langle v^2\rangle = \sigma^2$.

A derivation and summary of the statistical properties of the unique statistically stationary solution of the set of embedded differential equations 2.20 to 2.24 are provided in Appendix A.1 (see Proposition A.1.2). In the spectral domain, the velocity correlation function now reads

$$\mathcal{C}_{v_n}(\tau) = \frac{2\sigma^2 e^{-\tau_\eta^2/T^2}}{T\,\mathrm{erfc}\,(\tau_\eta/T)} \int_{\mathbb{R}} e^{2i\pi\omega\tau} \frac{T^2}{1+4\pi^2T^2\omega^2} \left[\frac{1}{1+\frac{4\pi^2\tau_\eta^2\omega^2}{n-1}}\right]^{n-1} d\omega. \tag{2.26}$$

In contrast to the function provided in equation 2.18, this correlation function does converge a well-behaved stochastic process as the number of layers goes to infinity. In other words, through iteration of the set of embedded differential equations,

2.20 to 2.24, over an infinite number of layers $n \to \infty$, an infinitely differentiable and causal Gaussian process is obtained, in which the velocity correlation function reads, in the stationary regime,

$$\mathcal{C}_v(\tau) = \sigma^2 \frac{e^{-|\tau|/T}}{2\,\mathrm{erfc}(\tau_\eta/T)} \left[1 + \mathrm{erf}\left(\frac{|\tau|}{2\tau_\eta} - \frac{\tau_\eta}{T}\right) + e^{2|\tau|/T}\,\mathrm{erfc}\left(\frac{|\tau|}{2\tau_\eta} + \frac{\tau_\eta}{T}\right)\right]. \quad (2.27)$$

It is of note that $\mathcal{C}_v(0) = \langle v^2 \rangle = \sigma^2$ and taking the second derivatives of equation 2.27 and multiplying by the factor $-1/2$, the respective acceleration correlation function is obtained

$$\mathcal{C}_a(\tau) = \frac{\sigma^2}{2T^2\,\mathrm{erfc}(\tau_\eta/T)} \left[\frac{2T}{\tau_\eta\sqrt{\pi}} e^{-\left(\frac{\tau^2}{4\tau_\eta^2} + \frac{\tau_\eta^2}{T^2}\right)} - e^{-|\tau|/T}\left(1 + \mathrm{erf}\left(\frac{|\tau|}{2\tau_\eta} - \frac{\tau_\eta}{T}\right)\right) - e^{|\tau|/T}\,\mathrm{erfc}\left(\frac{|\tau|}{2\tau_\eta} + \frac{\tau_\eta}{T}\right)\right]. \quad (2.28)$$

2.2.2 An infinitely differentiable causal process, asymptotically multifractal in the infinite Reynolds number limit

Herein, expansion of the system proposed in equations 2.20 to 2.24, in order to include intermittent (i.e. multifractal) corrections, is suggested. This requires more elaborate probabilistic objects to do so in the spirit of the multifractal random walk [Bacry et al., 2001], and since applied in a Lagrangian context by Mordant et al. [2002, 2003]. To go beyond this Gaussian framework, equations 2.20 to 2.24, where linear operations on a Gaussian white noise $W(dt)$ are involved, a non-linear operation while exponentiating a Gaussian field $X(t)$ must now be considered. This logarithmic correlation structure guarantees multifractal behaviors and the obtained random field is "$e^{\gamma X}$", where γ is a free parameter of the theory that encodes the

level of intermittency. This can be seen as a continuous and stationary version of the discrete cascade models developed in turbulence theory (see Meneveau and Sreenivasan [1987], Benzi et al. [1993], Frisch [1995], Arneodo and Muzy [1998] and references therein) and is known in the mathematical literature as a multiplicative chaos [Rhodes and Vargas, 2009]. For recent applications of such a random distribution to the stochastic modeling of Eulerian velocity fields, see Pereira et al. [2016] and Chevillard et al. [2019]. The application to OU infinite layer modeling requires the generalization of a probabilistic approach to a causal context, and the inclusion of finite Reynolds number effects that guarantee differentiability below the Kolmogorov time scale τ_η.

A causal multifractal random walk

First, the stochastic modeling of the Lagrangian velocity proposed by Mordant et al. [2002, 2003], which is based on the multifractal process of Bacry et al. [2001], is reviewed. This process can be considered as an OU process forced by a non-Gaussian uncorrelated random noise, and is called the multifractal random walk (MRW). Its dynamics reads

$$du_{1,\epsilon}(t) = -\frac{1}{T}u_{1,\epsilon}(t)dt + \sqrt{q}e^{\gamma X_{1,\epsilon}(t)-\gamma^2\langle X_{1,\epsilon}^2\rangle}W(dt), \tag{2.29}$$

where a new random field $X_{1,\epsilon}$ is introduced and $u_{1,\epsilon}$ is the Lagrangian velocity. It is Gaussian, zero-average, and taken independent of the white noise instance $W(dt)$ and therefore fully characterized by its correlation function. To reproduce intermittent corrections, as they have been observed in Lagrangian turbulence (see

[Yeung and Pope, 1989, Voth et al., 1998, La Porta et al., 2001, Mordant et al., 2001b, 2002, 2003, Chevillard et al., 2003, Biferale et al., 2004, Toschi and Bodenschatz, 2009, Pinton and Sawford, 2012, Bentkamp et al., 2019], and references therein), one must demand the Gaussian field $X_{1,\epsilon}$ to be logarithmically correlated [Bacry et al., 2001]. Such a correlation structure implies, in particular, that the variance of $X_{1,\epsilon}$ diverges as $\epsilon \to 0$, making it difficult to give a proper mathematical meaning to such a field. This divergence is amplified further when considering its exponential, as it is proposed in equation 2.29. Instead, an approximation procedure is used, at a given (small) parameter ϵ, that will eventually play, loosely speaking, the role of the small time scale τ_η of turbulence. Such a logarithmic correlation structure has to be truncated over the large time scale T in order to ensure a finite variance. These truncations are well understood from a mathematical perspective [Rhodes and Vargas, 2009], and a proper limit as $\epsilon \to 0$ leads to a well-defined, canonical, random distribution.

Nonetheless, nothing is said in Bacry et al. [2001] about causality. In order to include this important physical constraint, the field $X_{1,\epsilon}$ is defined as the unique statistically stationary solution of a stochastic differential equation, that will eventually be consistent with both truncations over the time scales ϵ and T, with logarithmic behavior in between. Being Gaussian, and independent of the white noise $W(dt)$ entering in equation 2.29, dynamics has to be defined as a linear operation on an independent instance of the Gaussian white noise, call it $\widetilde{W}(dt)$, such that $\langle W(dt)\widetilde{W}(dt')\rangle = 0$ at any time t and t'. In this context, a linear stochastic evolution

has been proposed by Chevillard [2017] and Pereira et al. [2018], and reads

$$dX_{1,\epsilon}(t) = -\frac{1}{T}X_{1,\epsilon}(t)dt - \frac{1}{2}\int_{-\infty}^{t}[t-s+\epsilon]^{-3/2}\,\widetilde{W}(ds)dt + \epsilon^{-1/2}\widetilde{W}(dt), \qquad (2.30)$$

which can be perceived as a fractional Ornstein-Uhlenbeck process of vanishing Hurst exponent [Chevillard, 2017, Pereira et al., 2018]. Notice also that the underlying integration over the past with a rapidly decreasing kernel that enters in the dynamics of $X_{1,\epsilon}$ implies that these are non-Markovian processes. A precise and comprehensive characterization of the statistical properties of the fields $X_{1,\epsilon}$ and its asymptotical log-correlated version $X_1 \equiv \lim_{\epsilon\to 0} X_{1,\epsilon}$ can be found in Appendix A.1, Section A.1.3.

For the statistical properties of the MRW that include a causal definition for the field X_1, the process is built, as much as possible, in the asymptotic regime (i.e., $\epsilon \to 0$). Keep in mind that the pointwise limit of such a process $u_1(t) = \lim_{\epsilon\to 0} u_{1,\epsilon}(t)$, where $u_{1,\epsilon}(t)$ is the unique statistically stationary solution of the SDE given in equation 2.29, is not straightforward to acquire because the random field $e^{\gamma X_{1,\epsilon}(t)-\gamma^2\langle X_{1,\epsilon}^2\rangle}$ becomes distributional in this limit [Rhodes and Vargas, 2009]. Therefore, the main concern is the statistical quantities of the asymptotic random process u_1, but standard calculations will be performed using the classical field $u_{1,\epsilon}(t)$ if necessary and convenient. Because quantification of the intermittent corrections implied by the this random distribution is desired, computation of the structure functions of the aforementioned stochastic model is proposed. Therefore, in the notation presented, the velocity increment expressed as $\delta_\tau u_{1,\epsilon}(t) = u_{1,\epsilon}(t+\tau) - u_{1,\epsilon}(t)$, and the respective asymptotic structure functions as

$$\mathcal{S}_{u_1,m}(\tau) = \lim_{\epsilon\to 0}\left\langle (u_{1,\epsilon}(t+\tau) - u_{1,\epsilon}(t))^m \right\rangle . \qquad (2.31)$$

Focusing now on the scaling properties of the structure functions of the causal MRW u_1. Recall that the log-correlated field X_1 and the underlying white noise W entering in the dynamics of $u_{1,\epsilon}$ are taken independently. This implies that all odd order structure functions vanish, namely $\mathcal{S}_{u_1,2m+1} = 0$ with $m \in \mathbb{N}$. Regarding the second-order structure function, it is the same as the one obtained from the OU process v_1 (equation 2.2), and given by,

$$\mathcal{S}_{u_1,2}(\tau) = \mathcal{S}_{v_1,2}(\tau) = qT\left[1 - e^{-\frac{|\tau|}{T}}\right] \underset{\tau\to 0^+}{\sim} q\tau. \tag{2.32}$$

In contrast, the fourth-order structure function is impacted by intermittency, under the condition $4\gamma^2 < 1$,

$$\mathcal{S}_{u_1,4}(\tau) \underset{\tau\to 0}{\sim} \frac{3}{1 - 6\gamma^2 + 8\gamma^4} q^2\tau^2 \left(\frac{\tau}{T}\right)^{-4\gamma^2} e^{4\gamma^2 c(0)}, \tag{2.33}$$

where the constant $c(0)$ is given in equation A.18. More generally, it is then possible to obtain an estimation of the $(2m)^{\text{th}}$ order structure functions that reads, for $2m(m-1)\gamma^2 < 1$,

$$\mathcal{S}_{u_1,2m}(\tau) \underset{\tau\to 0}{\propto} q^m\tau^m \left(\frac{\tau}{T}\right)^{-2m(m-1)\gamma^2}, \tag{2.34}$$

indicating that the causal MRW exhibits a lognormal spectrum. Proofs of these propositions are gathered in Appendix A.2.

An infinitely differentiable causal multifractal random walk

Finally, a causal stochastic process representative of the statistical behavior of Lagrangian velocity in homogeneous and isotropic turbulent flows at a given finite

Reynolds number (equivalently for a finite ratio τ_η/T) is proposed. The process is statistically stationary, correlated over a large time scale T, infinitely differentiable, acquiring rough and intermittent behaviors as the small time scale τ_η goes to zero, i.e. in the infinite Reynolds number limit.

Assume $n \geq 2$ and consider the following system of embedded differential equations

$$\frac{du_{n,\epsilon}}{dt} = -\frac{1}{T}u_{n,\epsilon}(t) + e^{\gamma X_{n,\epsilon}(t) - \frac{\gamma^2}{2}\langle X_{n,\epsilon}^2\rangle} f_{n-1}(t) \tag{2.35}$$

$$\frac{df_{n-1}}{dt} = -\frac{\sqrt{n-1}}{\tau_\eta} f_{n-1}(t) + f_{n-2}(t) \tag{2.36}$$

$$... \tag{2.37}$$

$$\frac{df_2}{dt} = -\frac{\sqrt{n-1}}{\tau_\eta} f_2(t) + f_1(t) \tag{2.38}$$

$$df_1 = -\frac{\sqrt{n-1}}{\tau_\eta} f_1(t)dt + \sqrt{\beta_n} W(dt)\ , \tag{2.39}$$

with

$$\beta_n = \left(\frac{n-1}{\tau_\eta^2}\right)^{n-1} \frac{\sigma^2\sqrt{4\pi\tau_\eta^2}}{T\int_0^\infty e^{-\frac{h}{T}} e^{-h^2/(4\tau_\eta^2)} e^{\gamma^2 \mathcal{C}_X(h)} dh}. \tag{2.40}$$

In the system above, the causal process $X_{n,\epsilon}$ obeys the set of stochastic differential

equations

$$\frac{dX_{n,\epsilon}}{dt} = -\frac{1}{T}X_{n,\epsilon}(t) + \sqrt{\tilde{\beta}_n}\tilde{f}_{n-1,\epsilon}(t) \tag{2.41}$$

$$\frac{d\tilde{f}_{n-1,\epsilon}}{dt} = -\frac{\sqrt{n-1}}{\tau_\eta}\tilde{f}_{n-1,\epsilon}(t) + \tilde{f}_{n-2,\epsilon}(t) \tag{2.42}$$

$$... \tag{2.43}$$

$$\frac{d\tilde{f}_{2,\epsilon}}{dt} = -\frac{\sqrt{n-1}}{\tau_\eta}\tilde{f}_{2,\epsilon}(t) + \tilde{f}_{1,\epsilon}(t) \tag{2.44}$$

$$d\tilde{f}_{1,\epsilon} = -\frac{\sqrt{n-1}}{\tau_\eta}\tilde{f}_{1,\epsilon}(t)dt - \frac{1}{2}\int_{-\infty}^{t}[t-s+\epsilon]^{-3/2}\,\widetilde{W}(ds)dt + \epsilon^{-1/2}\widetilde{W}(dt), \tag{2.45}$$

with

$$\tilde{\beta}_n = \left(\frac{n-1}{\tau_\eta^2}\right)^{n-1}. \tag{2.46}$$

where W and $\widetilde{W}$ are two independent copies of the Wiener process.

Similar to the Gaussian infinitely differentiable process v established in the first part, the Proposition A.1.5, in Appendix A.1 shows that the process u, obtained once the set of embedded differential equations is iterated an infinite number of times $n \to \infty$, and when the small parameter ϵ goes to zero, converges to a well-defined limit. Again, the choice made for the white noise weight β_n ensures that the variance of the limiting process u is finite with $\langle u^2 \rangle = \sigma^2$. Its value is precised during computation of the correlation function $\mathcal{C}_f(\tau) = \langle f(t)f(t+\tau)\rangle$ of the force f when $n \to \infty$ (see equation A.29).

Similarly, the coefficient $\tilde{\beta}_n$ (equation 2.46) entering in the dynamics of $X_{n,\epsilon}$ (equation 2.41) is dictated by the necessity that when $\epsilon \to 0$ and $\tau_\eta \to 0$, for any number of layers n, X_n is logarithmically correlated in an appropriate manner. Note that as far as the process $X_{n,\epsilon}$ is concerned, these limits can be taken in an arbitrary

way since they commute. The small parameters ϵ and τ_η have a similar physical interpretation, they mimic finite Reynolds number effects. They are defined *a priori* as separate entities and independently seek limits for the sake of generality. More precisely ϵ is taken finite to make sense of the dynamics of $\tilde{f}_{1,\epsilon}$ as it is proposed in equation 2.45. Finally, note that the multiplicative chaos entering in the dynamics of $u_{n,\epsilon}$ (equation 2.35) is renormalized by a smaller constant $\exp\left(\frac{\gamma^2}{2}\langle X_{n,\epsilon}^2\rangle\right)$ than in its non-differentiable version $u_{1,\epsilon}$ (equation 2.29), where there typically exists a larger normalization constant $\exp\left(\gamma^2\langle X_{n,\epsilon}^2\rangle\right)$. This is related to the finite correlation of the term f_{n-1} entering in equation 2.35, contrary to the dynamics proposed in equation 2.29 where a white noise $W(dt)$ enters.

For clarity, Propositions are included in Appendix A.1, a few details of these concerning the MRW infinite layers approach are provided here. A focus on the statistical properties of $X_{n,\epsilon}$ is included in Proposition A.1.4. Keeping in mind that, whatever the ordering of the limits $n \to \infty$ and $\epsilon \to 0$, the correlation function of $X_{n,\epsilon}$ converges towards a well-defined function $\mathcal{C}_X(\tau)$ (equation A.21), of which its value at the origin diverges logarithmically with τ_η as $\tau_\eta \to 0$ (equation A.24). In this limit of infinite Reynolds numbers, $\mathcal{C}_X(\tau)$ does converge towards $\mathcal{C}_{X_1}(\tau)$ (equation A.25), as expected.

Proceeding with the covariance structure of the limiting process u. Proposition A.1.5 provides a summary of the main second-order statistical properties of velocity u and acceleration a. The exact velocity correlation function $\mathcal{C}_u(\tau)$ is first derived in the joint commuting limit $\epsilon \to 0$ and $n \to \infty$ (equation A.28). From this it is noted that although $\mathcal{C}_u(\tau)$ depends weakly on intermittent corrections in the dissipative range, it loses this property as $\tau_\eta/T \to 0$ and coincides with the correlation function

of the OU process $\mathcal{C}_{v_1}(\tau)$ (equation A.30). Similarly, the acceleration correlation function $\mathcal{C}_a(\tau)$ can be derived (equation A.32). From there, acceleration variance is shown to diverge as T/τ_η as the Reynolds number increases (equation A.34).

It is of note that the proposed stochastic model of velocity u, that is claimed to be intermittent in a precise way and defined in the following Proposition A.1.6, predicts that, as far as the covariance of u is concerned, it is similar to an Ornstein-Uhlenbeck process at infinite Reynolds number, independent of any intermittency corrections. This is consistent with the standard phenomenology of Lagrangian turbulence. The predicted acceleration variance (equation A.34) does not exhibit either intermittent corrections: This precise behavior of acceleration variance with respect to the Reynolds number is at odds with the extrapolations that can be made from numerical simulations (see Ishihara et al. [2007]).

The intermittent, i.e. multifractal, properties of the velocity process u are presented, as they can be seen on higher-order structure functions in Proposition A.1.6. As it was shown previously, the correlations of u and the OU process v_1 equate as $\tau_\eta \to 0$. Similarly, the second-order structure function (equation A.37) follows this as well. Showing that the fourth-order structure function of u coincides with the one of the causal MRW process u_1 as first $\epsilon \to 0$ and then $\tau_\eta \to 0$ is obvious (equation A.38), the reversed order of limits is more involved. Nonetheless, an approximation procedure is proposed that confirms that u and u_1 possess the same intermittent properties (equation A.39). All statements and proofs can be found in Proposition A.1.6 and Appendix A.3.

2.2.3 Predictions of the multifractal formalism regarding the acceleration correlation function

An alternative method of modeling the velocity and acceleration correlation functions is by directly proposing their functional forms. As a second approach, to compare with the infinite layer process, models of the statistical behaviors of velocity are constructed, that will take into account the various range of scales pointed out by the phenomenology of turbulence, namely the inertial and dissipative ranges (with additional intermittent corrections). This results in an explicit form of the velocity correlation function (equivalently the second-order structure function) without building up the underlying stochastic process. Specifically, this approach appears only partial from a probabilistic point of view: The velocity correlation function is modeled (from which the acceleration correlation function is formed) and higher-order moments of velocity increments, although the velocity process itself is not fully characterized. Therefore, the following probabilistic description is not complete, but allows a better understanding of the rapid increase of the velocity increment flatness across the dissipative range.

The Batchelor parametrization of the second-order structure function

Beginning with the proposition of a simple model for the velocity correlation function, or equivalently a model of the second moment of velocity increments. Concerning the Eulerian framework, Batchelor [1951] proposed a simple form for the second-order structure function that includes the inertial behavior $\langle(\delta_\ell u)^2\rangle \sim \ell^{2/3}$ and the dissipative one $\langle(\delta_\ell u)^2\rangle \sim \ell^2$, with an additional polynomial interpolation relating these two behaviors across the Kolmogorov dissipative length scale [Mene-

veau, 1996, Chevillard et al., 2006, 2012]. A similar procedure can be adapted to the Lagrangian framework, that would include the respective inertial $\langle(\delta_\tau v)^2\rangle \sim \tau$ and dissipative $\langle(\delta_\tau v)^2\rangle \sim \tau^2$, behavior as it was considered by Chevillard et al. [2003], Arneodo et al. [2008], Benzi et al. [2010], Chevillard et al. [2012]. Assuming $\tau \ll T$, it is explicitly given as

$$\mathcal{S}_2(\tau) = \langle(\delta_\tau v)^2\rangle = 2\sigma^2 \frac{\frac{\tau}{T}}{\left[1 + \left(\frac{\tau}{\tau_\eta}\right)^{-\delta}\right]^{\frac{1}{\delta}}}, \tag{2.47}$$

where again, τ_η is the typical dissipative (Kolmogorov) time scale, and $\sigma^2 = \langle v^2\rangle$. The additional free parameter δ governs the transition between the inertial and dissipative ranges of scales. For instance, as far as the Eulerian framework is concerned, the value $\delta = 2$ was chosen by Batchelor [1951]. In the Lagrangian framework, the value $\delta = 4$ reproduces, appropriately, the behavior of the statistical quantities, as it was chosen in Arneodo et al. [2008]. At large scales, τ of the order of T and larger, equation 2.48 could be multiplied by a cut-off function of characteristic time scale T, as it was proposed in Bos et al. [2012]. Such a procedure is necessary to ensure a smooth transition towards decorrelation at large times. It is required that $\mathcal{S}_2(\tau)$ goes to $2\sigma^2 = 2\langle v^2\rangle$ as $\tau \to \infty$, simultaneously causing the integral of the velocity correlation function $C_v(\tau) \equiv \sigma^2 - \mathcal{S}_2(\tau)/2$ to converge, as it is required when assuming stationary statistics. Recall furthermore that the second derivative of $\mathcal{S}_2$ is of interest, in order to describe the acceleration correlation, for which statistical stationarity implies that its integral over time lags τ vanishes. Therefore, multiplying by a cut-off function of characteristic time scale T turns out to be too

schematic and instead, the following ad-hoc form, for any time lags $\tau \geq 0$, is used

$$\mathcal{S}_2(\tau) = \langle (\delta_\tau v)^2 \rangle = 2\sigma^2 \frac{1 - e^{-\frac{\tau}{T}}}{\left[1 + \left(\frac{\tau}{\tau_\eta}\right)^{-\delta}\right]^{\frac{1}{\delta}}}, \tag{2.48}$$

where the acceleration correlation function is given as

$$\mathcal{C}_a(\tau) \equiv \frac{1}{2} \frac{d^2 \mathcal{S}_2(\tau)}{d\tau^2}. \tag{2.49}$$

Including intermittency corrections using the multifractal formalism

The multifractal formalism [Frisch, 1995] provides a convenient theoretical framework to generalize the approach of Batchelor to include intermittent corrections. Mostly developed in the Eulerian framework, it has since been adapted to the Lagrangian framework by several authors, showing great success when compared to experimental and numerical data [Borgas, 1993, Chevillard et al., 2003, Biferale et al., 2004]. Here, the approach reviewed in Chevillard et al. [2012] is followed, where the smooth behavior at large scales is also implemented.

Arguments developed in this context concern the probabilistic modeling of the Lagrangian velocity increment, recalling $\delta_\tau v(t) = v(t+\tau) - v(t)$. Taking into account expected behaviors in the inertial and dissipative ranges, similar to the Batchelor parametrization, the following explicit expression for $\tau \geq 0$ can be obtained

$$\mathcal{S}_2(\tau) = \langle (\delta_\tau v)^2 \rangle = 2\sigma^2 \int_{h_{\min}}^{h_{\max}} \frac{\left(1 - e^{-\frac{\tau}{T}}\right)^{2h}}{\left[1 + \left(\frac{\tau}{\tau_\eta(h)}\right)^{-\delta}\right]^{\frac{2(1-h)}{\delta}}} \mathcal{P}_h^{(\tau)}(h) dh, \tag{2.50}$$

which can be regarded as a generalization of the parametrization used in equation 2.48 to a non-unique exponent h, that fluctuates according to its probability density $\mathcal{P}_h^{(\tau)}$ at a given scale τ. Notice also that a dependence of the dissipative scale $\tau_\eta(h)$ on this fluctuating exponent h is now included.

Following the arguments developed for the Eulerian framework [Paladin and Vulpiani, 1987, Nelkin, 1990], and adapted to the Lagrangian one in Borgas [1993] (and reviewed in Chevillard et al. [2012] with corresponding notations), one can assume that

$$\tau_\eta(h) = T\left(\frac{\tau_\eta}{T}\right)^{\frac{2}{2h+1}}, \tag{2.51}$$

where, to simplify notations, $\tau_\eta \equiv \tau_\eta(1/2)$, the value of the fluctuating dissipative time scale $\tau_\eta(h)$ at the very particular value $h = 1/2$. This fluctuating exponent h is characterized by its probability density function at a given scale τ, namely

$$P_h^{(\tau)}(h) = \frac{1}{\mathcal{Z}(\tau)} \frac{\left(1-e^{-\frac{\tau}{T}}\right)^{1-\mathcal{D}^L(h)}}{[1+(\frac{\tau}{\tau_\eta(h)})^{-\delta}]^{(D^L(h)-1)/\delta}} \tag{2.52}$$

and normalized in an appropriate manner using

$$\mathcal{Z}(\tau) = \int_{h_{\min}}^{h_{\max}} \frac{\left(1-e^{-\frac{\tau}{T}}\right)^{1-\mathcal{D}^L(h)}}{[1+(\frac{\tau}{\tau_\eta(h)})^{-\delta}]^{(\mathcal{D}^L(h)-1)/\delta}} \mathrm{d}h. \tag{2.53}$$

Besides the two free parameters T and τ_η of this model, the multifractal formalism [Frisch, 1995] requires the introduction of a parameter function $\mathcal{D}^L(h)$. It acquires the status of a singularity spectrum at infinite Reynolds number (i.e. when τ_η goes to 0) and then at vanishing scales $\tau \to 0$. Less precisely stated, it dictates the level of fluctuations of the exponent h around its average value, which is ex-

pected to be $\langle h \rangle = 1/2$. Several forms have been proposed in the literature [Frisch, 1995]. A simple quadratic form of $\mathcal{D}^L(h)$ is chosen, which is known as a *log-normal* approximation, parametrized by the intermittency coefficient γ^2, that reads

$$\mathcal{D}^L(h) = 1 - \frac{(h - 1/2 - \gamma^2)^2}{2\gamma^2}, \tag{2.54}$$

such that a linear behavior of $\mathcal{S}_2(\tau)$ is enforced with τ in the inertial range (in the appropriate infinite Reynolds number limit).

Correspondingly, the correlation function of acceleration $\mathcal{C}_a(\tau)$ can be defined, using the following notations, as

$$\mathcal{S}_2(\tau) = \frac{1}{\mathcal{Z}(\tau)} \int_{h_{\min}}^{h_{\max}} \mathcal{Q}(h,\tau) dh, \quad \text{where} \quad \mathcal{Q}(\tau,h) = \frac{\left(1 - e^{-\frac{\tau}{T}}\right)^{2h+1-\mathcal{D}^L(h)}}{[1 + (\frac{\tau}{\tau_\eta(h)})^{-\delta}]^{(2(1-h)+\mathcal{D}^L(h)-1)/\delta}}, \tag{2.55}$$

and therefore

$$\begin{aligned} \mathcal{C}_a(\tau) = & \left(\frac{\mathcal{Z}'(\tau)^2}{\mathcal{Z}(\tau)^3} - \frac{1}{2} \frac{\mathcal{Z}''(\tau)}{\mathcal{Z}(\tau)^2} \right) \int_{h_{\min}}^{h_{\max}} \mathcal{Q}(h,\tau) dh - \frac{\mathcal{Z}'(\tau)}{\mathcal{Z}(\tau)^2} \int_{h_{\min}}^{h_{\max}} \frac{\partial \mathcal{Q}(h,\tau)}{\partial \tau} dh \\ & + \frac{1}{2\mathcal{Z}(\tau)} \int_{h_{\min}}^{h_{\max}} \frac{\partial^2 \mathcal{Q}(h,\tau)}{\partial \tau^2} dh. \end{aligned} \tag{2.56}$$

This form can be considered as a model for the correlation function of acceleration, at a given Reynolds number, which includes intermittent corrections (using a non vanishing value for γ^2). Remaining integrals entering in equation 2.56 are evaluated using standard numerical integration algorithms.

Higher-order structure functions and their scaling behavior

The corresponding prediction for the structure function $\mathcal{S}_{2m}(\tau)$ of order $2m$, that will eventually enter in the expression of the velocity increment flatness is herein provided. Note that the statistics of the increments are expected and observed to be symmetric, making odd-order moments vanish. Specifically,

$$\mathcal{S}_{2m}(\tau) = \langle (\delta_\tau v)^{2m} \rangle = (\sqrt{2}\sigma)^{2m} \frac{(2m)!}{m! 2^m} \int_{h_{\min}}^{h_{\max}} \frac{\left(1 - e^{-\frac{\tau}{T}}\right)^{2mh}}{\left[1 + \left(\frac{\tau}{\tau_\eta(h)}\right)^{-\delta}\right]^{\frac{2m(1-h)}{\delta}}} \mathcal{P}_h^{(\tau)}(h) dh, \tag{2.57}$$

where the additional combinatorial factor originates from the moment of order $2m$ of a zero-average unit-variance Gaussian random variable that enters in the more complete probabilistic description detailed in Chevillard et al. [2012].

In the dissipative range, when $\tau \ll \tau_\eta$, $\mathcal{S}_{2m}(\tau) = \langle a^{2m} \rangle \tau^{2m} + \mathcal{O}(\tau^{2m})$. In the inertial range, when $\tau_\eta \ll \tau \ll T$, the standard prediction of the multifractal formalism is recovered, which relates the power-law behavior of the structure functions to the functional shape of the parameter function $\mathcal{D}^L(h)$ through a Legendre transform [Frisch, 1995]. In the proper ordering of limits,

$$\lim_{\tau_\eta \to 0} \mathcal{S}_{2m}(\tau) \underset{\tau \to 0}{\sim} c_{\gamma,2m} (\sqrt{2}\sigma)^{2m} \frac{(2m)!}{m! 2^m} \left(\frac{\tau}{T}\right)^{\min_h \left[2mh + 1 - \mathcal{D}^L(h)\right]}, \tag{2.58}$$

where the remaining multiplicative constant could be computed while pushing forward the underlying steepest-descent calculation. Assuming a quadratic form for

the parameter function $\mathcal{D}^L(h)$, the following intermittent behavior is obtained

$$\lim_{\tau_\eta \to 0} \mathcal{S}_{2m}(\tau) \underset{\tau \to 0}{\sim} c_{\gamma,2m} (\sqrt{2}\sigma)^{2m} \frac{(2m)!}{m! 2^m} \left(\frac{\tau}{T}\right)^{\left(1+2\gamma^2\right)m - 2\gamma^2 m^2}, \tag{2.59}$$

which contains a power-law exponent $\zeta_{2m} \equiv (1 + 2\gamma^2)\, m - 2\gamma^2 m^2$ which corresponds exactly to the one obtained for the infinitely differentiable multifractal random walk of Section 2.2.2.

Derivations of Reynolds number dependence based on the acceleration variance is presented in Appendix A.4.

2.2.4 Extensions of Lagrangian velocity modeling to inertial particle statistics

Theoretical arguments discussed up to this point are applicable to fluid tracer dynamics in homogeneous, isotropic and stationary turbulence. Although major advancements have been presented to Lagrangian modeling, the applications of tracer flow only gives insight into the behavior of the fluid. When a flow contains particles (i.e., volcanic eruptions, particulate from a cough), the particles then present alternative dynamics than those of the fluid, often dampened by their weight or size. More applicable to real world circumstances, the model should attempt to include some ability to predict these particle mechanics and therefore, a simple method is presented herein.

Recall that particle dynamics is governed by additional forces [Gatignol, 1983, Maxey and Riley, 1983] and that by assuming small, heavy particles, only the Stokes' drag is retained and the velocity of the particle is determined by [Gatignol, 1983,

Maxey and Riley, 1983, Pumir and Wilkinson, 2016]:

$$\frac{d\boldsymbol{X}_p(\boldsymbol{x},t)}{dt} = \boldsymbol{v}_p(\boldsymbol{x},t)\ , \tag{2.60}$$

$$\frac{d\boldsymbol{v}_p(\boldsymbol{x},t)}{dt} = \frac{1}{\tau_p}\left[\boldsymbol{u}(\boldsymbol{X}_p(\boldsymbol{x},t),t) - \boldsymbol{v}_p(\boldsymbol{x},t)\right]. \tag{2.61}$$

Recall that $\boldsymbol{X}_p(\boldsymbol{x},t)$ is the particle position, $\boldsymbol{v}_p(\boldsymbol{x},t)$ is the particle velocity, and $\boldsymbol{u}(\boldsymbol{x},t)$ is the fluid velocity field and furthermore, that the Stokes number is the relevant parameter used to characterize particles inertia in this simplified model.

Particle response based on the linear filter approximation

Finally, it is noted again that for an ideal tracer, the trajectory path can be determined from the following ODE

$$\frac{d\boldsymbol{X}(\boldsymbol{x},t)}{dt} \equiv \boldsymbol{v}(\boldsymbol{x},t) = \boldsymbol{u}(\boldsymbol{X}(\boldsymbol{x},t),t). \tag{2.62}$$

The statistical description of ideal tracer particles in turbulent flows, which is governed by equation (2.62), is one of the main concerns of turbulence theory. Inertial particle motion at low Stokes numbers, is determined by the system of first order ODEs (2.60-2.61) and requires the knowledge of the full spatiotemporal (Eulerian) fluid velocity field in equation (2.61).

Linear filtering of Lagrangian velocity

In order to model inertial particle statistics on the basis of the Lagrangian velocity, an approximation of the coupled system of first-order ODEs is invoked which can be termed "linear filtering of the particle velocity" due to its analogy to methods

from signal processing [Cencini et al., 2006]. In this approximation, the particle position $\boldsymbol{X}_p(\boldsymbol{x},t)$ that enters the fluid velocity field in equation (2.61) is approximated as the position of the ideal tracer $\boldsymbol{X}(\boldsymbol{x},t)$ whose temporal evolution governed by equations (2.61) and (2.62), is approximated by

$$\frac{d\boldsymbol{v}_p(\boldsymbol{x},t)}{dt} = \frac{1}{\tau_p}\left[\boldsymbol{u}(\boldsymbol{X}(\boldsymbol{x},t),t) - \boldsymbol{v}_p(\boldsymbol{x},t)\right]. \tag{2.63}$$

In this linear filter approximation, the particle velocity is effectively decoupled from the particle position. Hence, the temporal evolution of the particle velocity is solely determined by the Lagrangian velocity $\boldsymbol{v}(\boldsymbol{x},t)$ along the tracer trajectory starting from the initial position of the inertial particle $\boldsymbol{X}_p(\boldsymbol{x},0) = \boldsymbol{x}$. To some extent, the linear filter neglects the spatiotemporal organization of the fluid velocity, and in turn the segregation of inertial particles in regions of low vorticity, as is suggested by the phenomenon of preferential concentration. Furthermore, under this approximation, the evolution equation for the particle velocity (2.63) can be solved according to

$$\boldsymbol{v}_p(\boldsymbol{x},t) = \boldsymbol{v}(\boldsymbol{x},0)e^{-t/\tau_p} + \frac{1}{\tau_p}\int_0^t e^{-(t-t')/\tau_p}\boldsymbol{v}(\boldsymbol{x},t')\mathrm{d}t', \tag{2.64}$$

and the particle position can then be determined as

$$\boldsymbol{X}_p(\boldsymbol{x},t) = \boldsymbol{x} + \tau_p\boldsymbol{v}(\boldsymbol{x},0)(1-e^{-t/\tau_p}) + \frac{1}{\tau_p}\int_0^t\int_0^{t'} e^{-(t'-t'')/\tau_p}\boldsymbol{v}(\boldsymbol{x},t'')\mathrm{d}t''\mathrm{d}t'. \tag{2.65}$$

Herein, only a single component of the particle velocity vector and acceleration are considered, denoted as v_p and a_p, respectively. The particle velocity is also assumed to have reached a statistically stationary state, such that the dependence

on its initial position can be neglected, resulting in:

$$v_p(t) = \frac{1}{\tau_p}\int_{-\infty}^{t} e^{-(t-t')/\tau_p} u(\boldsymbol{X}(t'),t')\mathrm{d}t' = \frac{1}{\tau_p}\int_{-\infty}^{t} e^{-(t-t')/\tau_p} v(t')\mathrm{d}t' = \frac{1}{\tau_p}\int_{-\infty}^{+\infty} g_{\tau_p}(t-t')v(t')\mathrm{d}t', \tag{2.66}$$

where $g_{\tau_p}(t) = e^{-t/\tau_p}H(t)$ and $H(t)$ denotes the Heaviside step function.

The linear filter approximation for inertial particle velocities based on the trajectory of individual tracer particles can also be applied to the correlation functions of velocity,

$$\begin{aligned}\mathcal{C}_{v_p}(\tau) &= \frac{1}{\tau_p^2}(G_{\tau_p} \star \mathcal{C}_v)(\tau) = \frac{1}{\tau_p^2}\int_{-\infty}^{+\infty} G_{\tau_p}(\tau+t)\mathcal{C}_v(t)\mathrm{d}t \\ &= \frac{1}{\tau_p^2}\int_{0}^{+\infty} \left[G_{\tau_p}(\tau+t) + G_{\tau_p}(\tau-t)\right]\mathcal{C}_v(t)\mathrm{d}t \\ &= \frac{1}{2\tau_p}\int_{0}^{+\infty} \left[e^{-|\tau+t|/\tau_p} + e^{-|\tau-t|/\tau_p}\right]\mathcal{C}_v(t)\mathrm{d}t,\end{aligned} \tag{2.67}$$

where the kernel $G_{\tau_p}(t) = (g_{\tau_p} \star g_{\tau_p})(t) = \frac{\tau_p}{2}e^{-|t|/\tau_p}$ is introduced and recall that the convolution product is defined as $(g_1 \star g_2)(\tau) = \int_{-\infty}^{\infty} g_1(t)g_2(t-\tau)\mathrm{d}t$. Note that the Fourier representation of this correlation has been proposed previously by Tchen [2013].

The determination for the inertial particle acceleration correlation function $\mathcal{C}_{a_p}(\tau)$ based on the filtering of the tracer acceleration $\mathcal{C}_a(\tau)$ is performed in a similar fashion, resulting in

$$\mathcal{C}_{a_p}(\tau) = \frac{1}{2\tau_p}\int_{0}^{+\infty} \left[e^{-|\tau+t|/\tau_p} + e^{-|\tau-t|/\tau_p}\right]\mathcal{C}_a(t)\mathrm{d}t. \tag{2.68}$$

The linear filter approximation allows for direct assessment of velocity and acceleration correlation functions via the corresponding tracer correlation functions $\mathcal{C}_v(t)$ and $\mathcal{C}_a(t)$.

Process for inertial particles subject to Gaussian infinitely differentiable fluid velocity

In making use of the linear filter approximation discussed in the previous section, the embedded OU process can readily be extended in order to allow for the effects of finite particle inertia. The infinite layers approach provides guidance and therefore the system of coupled stochastic differential equations can be described as

$$\dot{v}_p = \frac{1}{\tau_p^*}\left(v - v_p\right) \ , \tag{2.69}$$

$$\dot{v} = -\frac{1}{T}v + f_{\tau_\eta} \ , \tag{2.70}$$

where τ_p^* denotes the model particle response time, an input parameter, and τ_η is a small-scale turbulence time scale of the order of the Kolmogorov dissipative time scale. The forcing term f_{τ_η} is a zero-average Gaussian random force, which is fully determined by its covariance in the statistically stationary regime. The covariance in both, physical and spectral space, reads

$$\begin{aligned}\mathcal{C}_{f_{\tau_\eta}}(\tau) \equiv \langle f_{\tau_\eta}(t) f_{\tau_\eta}(t+\tau)\rangle &= \frac{\sigma^2 e^{-\tau_\eta^2/T^2}}{\sqrt{\pi} T \tau_\eta \operatorname{erfc}\left(\tau_\eta/T\right)} e^{-\frac{\tau^2}{4\tau_\eta^2}} \\ &= \frac{2\sigma^2 e^{-\tau_\eta^2/T^2}}{T \operatorname{erfc}\left(\tau_\eta/T\right)} \int \mathrm{d}\omega \ e^{2i\pi\omega\tau} e^{-4\pi^2\tau_\eta^2\omega^2},\end{aligned} \tag{2.71}$$

where, recall that $\mathrm{erfc}(x) = 1 - \mathrm{erf}(x)$, the complementary of the error function $\mathrm{erf}(x)$. Similar to the fluid tracer embedded OU process, each layer increases the degree of differentiability of the Lagrangian velocity and thus improves modeling proficiency at small time scales. Moreover, it is possible to perform the limit to an infinite number of layers (and thus an infinitely differentiable Lagrangian velocity v).

As observed in the structure of its covariance (2.71), the Gaussian forcing term f_{τ_η} is correlated over the dissipative time scale τ_η, the correlation function being itself a Gaussian function. Moreover, this covariance structure shows that the random process $f_{\tau_\eta}(t)$ is infinitely differentiable, which is a direct consequence of the smoothness of its Gaussian shape. As previously discussed, the remaining parameter σ^2 entering equation 2.71 corresponds to the variance of the Lagrangian velocity v, that is the variance of the solution of equation (2.70) in the statistically steady range $\sigma^2 = \langle v^2 \rangle$.

Finally, the covariance function of the particle velocity v_p, defined as successive linear operations (equations 2.69 and 2.70) on the forcing term f_{τ_η}, can be obtained as

$$\begin{aligned}\mathcal{C}_{v_p}(\tau) &\equiv \langle v_p(t) v_p(t+\tau) \rangle \\ &= \frac{2\sigma^2 e^{-\tau_\eta^2/T^2}}{T\,\mathrm{erfc}\,(\tau_\eta/T)} \int e^{2i\pi\omega\tau} \frac{1}{1+4\pi^2(\tau_p^*)^2\omega^2} \frac{T^2}{1+4\pi^2 T^2\omega^2} e^{-4\pi^2\tau_\eta^2\omega^2} \mathrm{d}\omega, \end{aligned} \quad (2.72)$$

which can be calculated explicitly in physical space according to

$$\mathcal{C}_{v_p}(\tau) = \frac{\sigma^2 T}{2(T^2-(\tau_p^*)^2)\,\mathrm{erfc}(\tau_\eta/T)}\Bigg\{ Te^{-|\tau|/T}\Bigg[\mathrm{erfc}\left(\frac{\tau_\eta}{T}-\frac{|\tau|}{2\tau_\eta}\right) + e^{2|\tau|/T}\,\mathrm{erfc}\left(\frac{|\tau|}{2\tau_\eta}+\frac{\tau_\eta}{T}\right)\Bigg] - \tau_p^* e^{-|\tau|/\tau_p^*} e^{\frac{\tau_\eta^2}{(\tau_p^*)^2}-\frac{\tau_\eta^2}{T^2}}\Bigg[\mathrm{erfc}\left(\frac{\tau_\eta}{\tau_p^*}-\frac{|\tau|}{2\tau_\eta}\right) + e^{2|\tau|/\tau_p^*}\,\mathrm{erfc}\left(\frac{|\tau|}{2\tau_\eta}+\frac{\tau_\eta}{\tau_p^*}\right)\Bigg]\Bigg\}. \tag{2.73}$$

Herein, the dependence of the variance of the particle velocity on τ_p^* can be determined. Setting $\tau = 0$ in equation (2.73) yields

$$\sigma_{v_p}^2 = \frac{\sigma^2 T^2}{T^2-(\tau_p^*)^2}\left[1-\frac{\tau_p^*}{T}e^{\frac{\tau_\eta^2}{(\tau_p^*)^2}-\frac{\tau_\eta^2}{T^2}}\frac{\mathrm{erfc}\left(\frac{\tau_\eta}{\tau_p^*}\right)}{\mathrm{erfc}\left(\frac{\tau_\eta}{T}\right)}\right]. \tag{2.74}$$

Therefore, in the limit $\tau_p^* \to 0$, the variance of the Lagrangian model, $\lim_{\tau_p^*\to 0}\sigma_{v_p}^2 = \sigma^2$, is recovered. The acceleration correlation function can be calculated from equation (2.73) yielding

$$\mathcal{C}_{a_p}(\tau) = \frac{\sigma^2 T}{2(T^2-(\tau_p^*)^2)\,\mathrm{erfc}(\tau_\eta/T)}\Bigg\{ \frac{1}{T}e^{-|\tau|/T}\Bigg[\frac{2T}{\sqrt{\pi}\tau_\eta}e^{-\left(\frac{\tau_\eta}{T}-\frac{|\tau|}{2\tau_\eta}\right)^2} - \mathrm{erfc}\left(\frac{\tau_\eta}{T}-\frac{|\tau|}{2\tau_\eta}\right) - e^{2|\tau|/T}\,\mathrm{erfc}\left(\frac{|\tau|}{2\tau_\eta}+\frac{\tau_\eta}{T}\right)\Bigg] - \frac{1}{\tau_p^*}e^{-|\tau|/\tau_p^*}e^{\frac{\tau_\eta^2}{(\tau_p^*)^2}-\frac{\tau_\eta^2}{T^2}}\Bigg[\frac{2\tau_p^*}{\sqrt{\pi}\tau_\eta}e^{-\left(\frac{\tau_\eta}{\tau_p^*}-\frac{|\tau|}{2\tau_\eta}\right)^2} - \mathrm{erfc}\left(\frac{\tau_\eta}{\tau_p^*}-\frac{|\tau|}{2\tau_\eta}\right) - e^{2|\tau|/\tau_p^*}\,\mathrm{erfc}\left(\frac{|\tau|}{2\tau_\eta}+\frac{\tau_\eta}{\tau_p^*}\right)\Bigg]\Bigg\}. \tag{2.75}$$

The variance of the acceleration can be determined according to

$$\sigma_{a_p}^2 = \frac{\sigma^2}{T^2 - (\tau_p^*)^2} \left[\frac{T}{\tau_p^*} \frac{e^{\frac{\tau_\eta^2}{(\tau_p^*)^2}} \operatorname{erfc}\left(\frac{\tau_\eta}{\tau_p^*}\right)}{e^{\frac{\tau_\eta^2}{T^2}} \operatorname{erfc}\left(\frac{\tau_\eta}{T}\right)} - 1 \right] . \tag{2.76}$$

In the limit of $\tau_p^* \to 0$, the reduced tracer model is recovered. The proposed model possesses Gaussian properties, i.e., the particle velocity statistics is fully determined by the correlation function (2.73). In the present model, the fluid properties enter through the turnover time T and the small time scale τ_η, which can be parameterized in order to match certain characteristics of Lagrangian tracers. This model includes an additional parameter, the particle response time τ_p^*, which is determined in order to match the zero-crossing of the acceleration correlation function for different Stokes numbers.

Inertial particle statistics from Batchelor's model for Lagrangian tracers

Additionally, the Batchelor parametrization can be used to model inertial particle statistics directly at the level of the second-order structure function $\mathcal{S}_2(\tau) = 2\sigma^2 - 2C_v(\tau)$ and differentiability of the Lagrangian velocity is ensured by introducing the correct dissipation range behavior at small τ. Recall, proper cutoff at large scales lead to an alternative form of the second-order structure function equation,

$$S_2(\tau) = 2\sigma^2 \frac{1 - e^{-\frac{\tau}{T}}}{\left[1 + \left(\frac{\tau}{\tau_\eta}\right)^{-\delta}\right]^{\frac{1}{\delta}}} , \tag{2.77}$$

which entails a finite Lagrangian integral time scale. For the case of $\delta = 2$ used here in contrast to $\delta = 4$ of the multifractal formalism, this time scale can be calculated

explicitly

$$T_L = \int_0^\infty \mathrm{d}\tau \frac{\mathcal{C}_v(\tau)}{\mathcal{C}_v(0)} = \tau_\eta \left[1 - \frac{\pi}{2} Y_1\left(\frac{\tau_\eta}{T}\right) - \frac{\pi}{2} H_{-1}\left(\frac{\tau_\eta}{T}\right)\right], \tag{2.78}$$

where the Bessel function of the second kind, $Y_n(z)$, is introduced and $H_n(z)$ the Struve function, as it is provided by a symbolic calculation software. In this framework, the acceleration correlation function for the tracer particle can be calculated from the second-order structure function by $\mathcal{C}_a(\tau) = \mathrm{d}^2\mathcal{S}_2(\tau)/2\mathrm{d}\tau^2$.

Finite particle inertia can again be included in using the linear filter approximation discussed in Section 2.2.4 where equation (2.67) has to be evaluated from the Lagrangian velocity correlation $\mathcal{C}_v(\tau) = \sigma^2 - S_2(\tau)/2$. A closed expression for the integral could not be obtained and therefore a numerical evaluation is used.

2.3 Results

2.3.1 Illustrations of the stochastic processes for tracer particles

A numerical illustration of the Gaussian process is presented in order to observe how the statistical characteristics for a given set of values of the parameters τ_η and T go towards the limiting process v (and given in Proposition A.1.2) as the number of layers n increases.

Numerical Illustration of a Gaussian stochastic process

Simulations are performed of the set of equations 2.20 to 2.24 using $n = 9$ layers, and for $\tau_\eta = T/10$. For instance, choosing $T = 1$, which is equivalent to dimensionalized time scales in units of T. Time integration is performed with a simple Euler discretization scheme. The choice for dt is dictated by the smallest time scale

of the system, here $\tau_\eta/\sqrt{n-1}$. For $n = 9$, the value $dt = \tau_\eta/100$ is found to be small enough to guarantee the appropriate behavior. Choosing $\sigma^2 = 1$, and the respective weight α_9 of the white noise is given in equation 2.25, trajectories are then integrated over $10^4 T$ and results are shown in figure 2.1. A simulation using more layers is possible, although the simulation gets heavier, and as will be observed, the statistical properties of the nine layer process are very close to the asymptotic ones (as $n \to \infty$). Also, recall that the white noise weight α_{n+1} increases as n^n, so from a numerical point of view, if n is chosen large, it may introduce additional rounding errors related to the double-precision floating-point format.

Figure 2.1(a) displays time instances of the obtained processes $v_9(t)$ and its derivatives $a_9(t)$, over $5T$ after numerically integrating the equations 2.20 to 2.24. The first derivative of $v_9(t)$, namely $a_9(t)$, is 7-times differentiable; resulting in a smooth profile correlated over τ_η. In figure 2.1(b), three curves are presented: (i) the estimated correlation function $\mathcal{C}_{v_9}$ (dots), (ii) its theoretical expression (solid line), obtained when performing the integral entering in equation (2.26) using a symbolic calculation software, and (iii) the asymptotic correlation function $\mathcal{C}_v$ given in equation (2.27) (dashed line). The profiles collapse making it difficult to distinguish between these three curves. The velocity correlation functions $\mathcal{C}_{v_n}$ depend weakly on n (not shown), this can due to the fact that the dependence on n is only really evident in the dissipative scales.

To observe the improvements obtained by including increased layers, figure 2.1(c) provides the corresponding estimated and theoretical curves $\mathcal{C}_{a_n}$ for n ranging from 2 to 9. quantifying the convergence of the acceleration correlation function towards its asymptotic regime. Recall that $\mathcal{C}_{a_2}$ corresponds to the prediction of Sawford [1991],

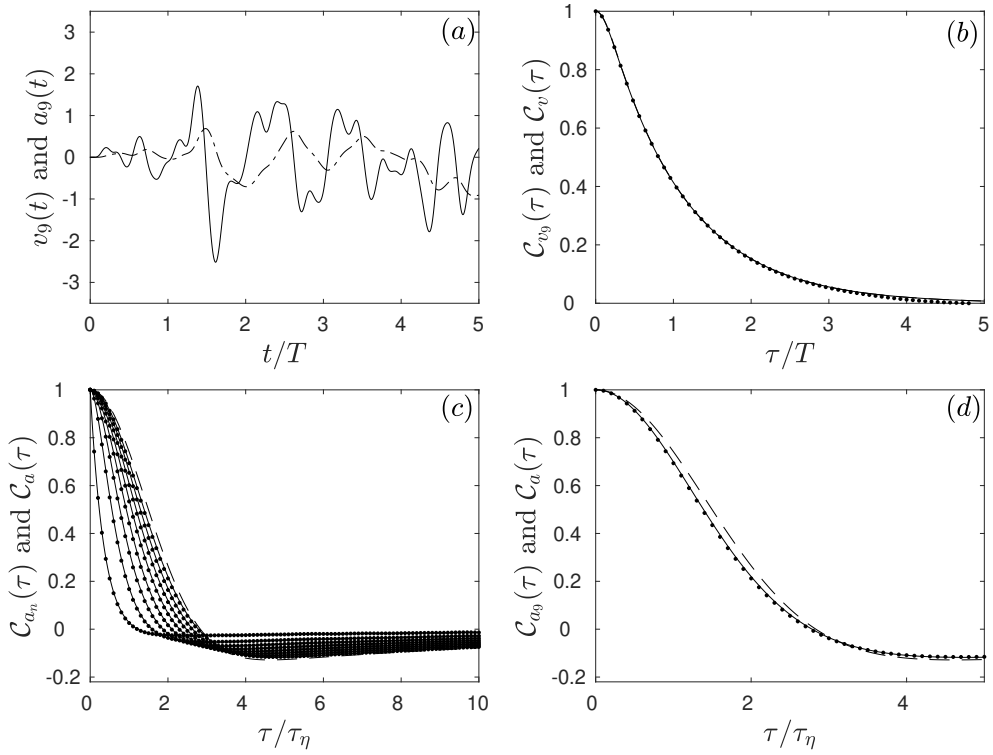

Figure 2.1: The numerical simulation of the Gaussian layered model, 2.20 to 2.24, for $\tau_\eta = T/10$ and $\sigma^2 = 1$. (a) Time series example of velocity $v_9(t)$ (dashed line) and acceleration $a_9(t)$ (solid line) with $n = 9$ layers. (b) Respective correlation function $\mathcal{C}_{v_9}$, estimated from numerical simulations (dots), theoretically derived from equation (2.26) (solid line), and the asymptotic process $\mathcal{C}_v$ (equation (2.27)) in dashed lines. (c) Acceleration correlation functions $\mathcal{C}_{a_n}$ using n layers, n ranging from 2 to 9 (from left to right), using $\sigma^2 = 1$ and $\alpha_n = \alpha_9$ (equation (2.25)). Numerical estimations are displayed with dots, respective theoretical expressions starting from equation (2.26) are represented with solid lines, and the asymptotic correlation function $\mathcal{C}_a$ (equation (2.28)) is a dashed line. For the sake of clarity, all curves are normalized by their values at the origin.

which is characteristic of the correlation function of a non-differentiable process ($\mathcal{C}_{a_2}$ is not twice differentiable at the origin). A perfect agreement between the numerical estimation based on random time series, and the theoretical expressions is observed and also derivable from equation (2.26). As the number of layers n increases, the acceleration correlation functions become more and more curved at the origin, guaranteeing finite variance of higher order derivatives. The associated asymptotic correlation function $\mathcal{C}_a$ is superimposed using a dashed line. $\mathcal{C}_{a_9}$ is very close to $\mathcal{C}_a$, as shown in figure 2.1(d), showing that considering $n = 9$ layers is enough to reproduce the statistical behaviors of the asymptotic process, at least for velocity and acceleration.

2.3.2 Numerical Illustration of the stochastic process with intermittency corrections

An efficient algorithm under the periodic approximation

A numerical algorithm able to reproduce in a realistic and efficient fashion the statistical behavior of the process u is proposed, the statistical properties of which are detailed in Propositions A.1.5 and A.1.6. Recall, the process u, contrary to the Gaussian process v, obeys non Markovian dynamics. More precisely, the process $X(t)$ at a given time t, the limiting solution, as the number of layers n goes to infinity and the small parameter ϵ goes to 0, of the system of embedded stochastic differential equations 2.41 to 2.45, requires the knowledge of its entire past. It is appealing to use the discrete Fourier transform to solve its dynamics. Therefore periodical solutions of the non Markovian dynamics are generated. Further, by considering very long trajectories, of order 10^5 times the largest time scale T of the

process, all aliasing effects will be negligible and thus, a periodic approximation is well justified.

Consider first an estimator for the process $\widehat{X}_{n,\epsilon}$ of the continuous solution $X_{n,\epsilon}$ of the coupled system equations (2.41) to (2.45). Call N the number of collocation points, T_{tot} the total length of the simulation, and Δt the timestep. As already mentioned, require $T_{\text{tot}} = N\Delta t \gg T$ to prevent aliasing errors. In the aforementioned periodic framework, the estimator becomes

$$\widehat{X}_{n,\epsilon}[t] = \sqrt{\widetilde{\beta}_n}\text{DFT}^{-1}\left(\text{DFT}\left(g_T\right)\text{DFT}^{n-1}\left(g_{\frac{\tau_\eta}{\sqrt{n-1}}}\right)\text{DFT}_c\left(h_\epsilon\right)\text{DFT}\left(\widetilde{W}\right)\right)[t]\times(\Delta t)^n, \tag{2.79}$$

where the discrete Fourier transform (DFT) is introduced as well as a multiplicative constant $\tilde{\beta}_n$ given in equation (2.46). Also entering into the expression above are properly discretized and periodized forms of the continuous function $g_\tau(t) = e^{-t/\tau}1_{t\geq 0}$ at the time scales T and $\frac{\tau_\eta}{\sqrt{n-1}}$. Similarly, a discretized and periodized form of the continuous function $h_\epsilon(t) = -\frac{1}{2}(t+\epsilon)^{-3/2}1_{t\geq 0}$, and $\text{DFT}_c(h_\epsilon)[\omega] = \text{DFT}(h_\epsilon)[\omega] - \text{DFT}(h_\epsilon)[0]$ are included. Finally, $\widetilde{W}[t]$ is an instance of the white noise field, composed of N independent Gaussian random variables of zero average and variance Δt. It is of note that subtracting from the DFT of h_ϵ its value at the origin is equivalent to adding the same white noise, as it is proposed in a continuous version (equation (2.45)), but reducing additional numerical error due to the finiteness of Δt. The $(\Delta t)^n$ factor originates from the convolution by the kernel $g_T(t)$ and $(n-1)$ convolutions by the kernel $g_{\frac{\tau_\eta}{\sqrt{n-1}}}$.

In a similar manner, the numerical, discretized and periodized, estimator $\widehat{u}_{n,\epsilon}$ of

the continuous solution $u_{n,\epsilon}$ of the coupled system equations (2.35) to (2.39) reads

$$\widehat{u}_{n,\epsilon}[t] = \sqrt{\beta_n}\mathrm{DFT}^{-1}\left(\mathrm{DFT}\left(g_T\right)\mathrm{DFT}^{n-1}\left(g_{\frac{\tau_\eta}{\sqrt{n-1}}}\right)\mathrm{DFT}\left(\frac{e^{\gamma\widehat{X}_{n,\epsilon}}}{e^{\frac{\gamma^2}{2}\langle\widehat{X}^2_{n,\epsilon}\rangle}}W\right)\right)[t]\times(\Delta t)^{n-1}, \tag{2.80}$$

where β_n is provided in equation (2.40), and recall that the white noise W is independent of $\widetilde{W}$ from equation (2.79). The fact that $(\Delta t)^{n-1}$ is used in 2.80, instead of $(\Delta t)^n$ (as in equation (2.79)), originates from the white (i.e. distributional) nature of W, whereas $\widetilde{W}$ is already smoothed out by the kernel h_ϵ.

The timestep Δt has to be chosen smaller than the smallest scale of motion, which is $\frac{\tau_\eta}{\sqrt{n-1}}$. Furthermore, a realistic simulation of the limiting process u is of interest, obtained in the limit $\epsilon \to 0$, at a given finite τ_η. A convenient choice for ϵ is therefore, to take it proportional to Δt, such that both of them go to 0 in the continuous limit. In subsequent simulations, this relates to:

$$\Delta t = \frac{\tau_\eta}{200\sqrt{n-1}} \text{ and } \epsilon = 5\Delta t. \tag{2.81}$$

This choice gives numerical stability and a proper illustration of the exact statistical quantities provided in Propositions A.1.5 and A.1.6 for the range of investigated values of τ_η. To prevent aliasing errors, a large number of collocation points $N = 2^{32}$ are used, such that $T_{\text{tot}} = N\Delta t$ is always much larger than T.

Numerical results and comparisons to theoretical predictions

Again, taking the large timescale to be $T = 1$, the (discrete) Fourier transforms, as they are detailed in equations (2.79) and 2.80, are numerically integrated using $T/\tau_\eta = 10,\ 20,\ 50,\ 100,\ 200$ and 500. Keeping in mind that τ_η is a fairly good

representation of the Kolmogorov time scale, these values correspond to a range of Reynolds numbers. Choosing for Δt and ϵ the values depicted in equation (2.81), and with $N = 2^{32}$ collocation points and $n = 9$ layers, the worst scenario corresponding to the smallest τ_η a total time of simulation $T_{\text{tot}} = N\Delta t \approx 10^4 T$ still prevents any aliasing effects. The particular value,

$$\gamma^2 = 0.085, \tag{2.82}$$

is found to be representative of the level of intermittency as it is seen in numerical simulations of the Navier-Stokes equations, consistent with previous estimations (see Mordant et al. [2002], Chevillard et al. [2003], Biferale et al. [2004], Chevillard et al. [2012] and references therein). The statistical quantities are averaged over three independent instances of these trajectories.

For clarity, the hat is herein omitted on the simulated discrete version of $u_{9,\epsilon}$ and figure 2.2(a) and (b) display two instances of this stochastic process for the largest $\tau_\eta = T/10$ (lowest Reynolds number) and the smallest $\tau_\eta = T/500$ (highest Reynolds number) ratios of the small over the large time scales. Velocity is represented using a dot-dashed line, and the acceleration with a solid line. All time series are divided by their respective standard deviation for the sake of comparison. In the low Reynolds number case (figure 2.2(a)), velocity is indeed correlated over t, while acceleration is correlated over a shorter time scale τ_η. In the highest Reynolds number case (figure 2.2(b)), the scale decoupling between the large T and the small τ_η time scales is observed. Also, the statistics of acceleration are observed to be non Gaussian. This is a manifestation of the intermittency phenomenon, which is modeled by

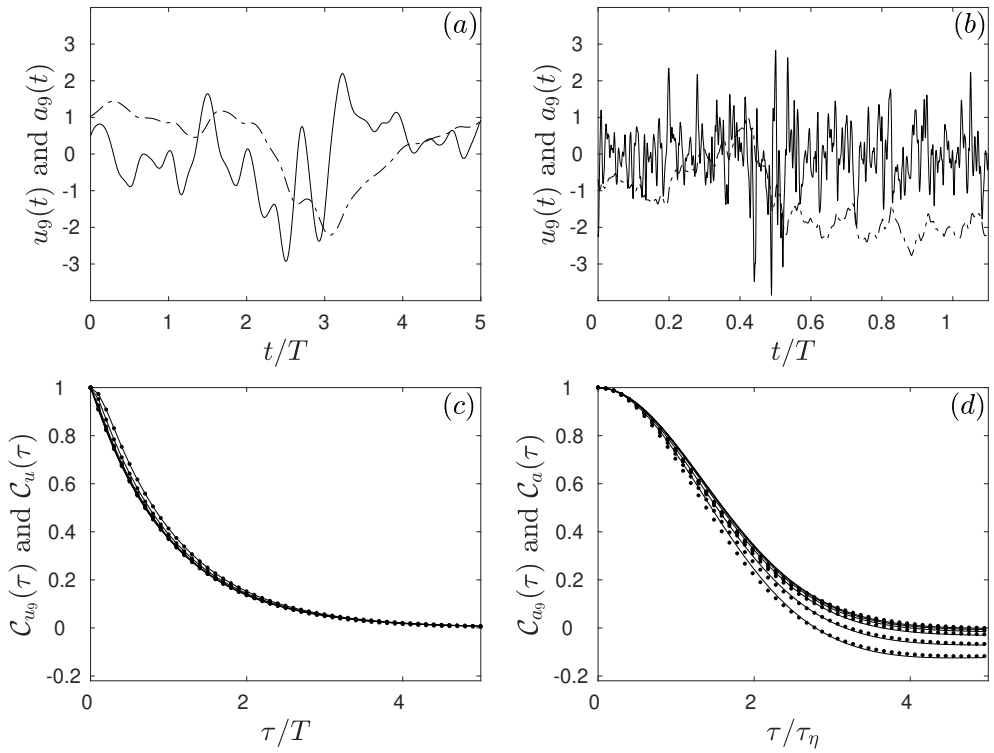

Figure 2.2: Numerical simulation, in a periodical fashion, of the set of equations 2.35 to 2.39 using $n = 9$ layers, for $T/\tau_\eta = 10$, 20, 50, 100, 200, 500, and $\sigma^2 = 1$. (a) Typical time series of the obtained processes $u_9(t)$ (dashed line) and $a_9(t)$ (solid line) for $T/\tau_\eta = 10$, normalized by their standard deviation. (b) Similar time series as in (a), but for $T/\tau_\eta = 500$. (c) Respective velocity correlation functions $\mathcal{C}_{u_9}$ for the six τ_η values, estimated from numerical simulations (dots), and asymptotic theoretical prediction $\mathcal{C}_u$ (equation (A.28)) (solid line). (d) Respective acceleration correlation functions $\mathcal{C}_{a_9}$ and compared to the asymptotic correlation function $\mathcal{C}_a$ (equation (A.32)). All curves are normalized by their values at the origin.

the multiplicative chaos that enters into the construction. These non Gaussian fluctuations would be enhanced by a higher value for γ (data not shown) than the one chosen presently (equation (2.82)).

Figure 2.2 also includes the velocity (c) and acceleration (d) correlation functions. Results from the numerical simulation of equations (2.79) and (2.80) for the

six values of τ_η are displayed using dots and the theoretical expressions provided in equations (A.28) and (A.32) are superimposed. The velocity correlations (figure 2.2(c)) show striking agreement between the numerical estimation based on time series of $u_{9,\epsilon}$ and the limiting theoretical expression (equation (A.28)) as was observed in the Gaussian case (figure 2.1). Furthermore, the dependence on τ_η is very weak due to the fact that velocity is a large scale quantity, mostly governed by the physics taking place at T. To this regard, acceleration correlation functions will highlight the physics ruling phenomena which occur at τ_η and are displayed in figure 2.2(d). All curves are normalized by the respective value at the origin (i.e. the acceleration variance). The low Reynolds number case (largest τ_η) is the curve going the most negative after the zero-crossing and as τ_η decreases, $\mathcal{C}_a(\tau)$ is closer to 0. This is consistent with the constraint that the integral of this curve has to vanish as a consequence of statistical stationarity. Once again, the collapse of the numerically estimated $\mathcal{C}_{a_9}(\tau)$ (dots) on the limiting theoretical expression given in equation (A.32) (solid line) is excellent.

Figure 2.3(a) presents the scaling behavior of the second-order structure function $\mathcal{S}_{u_{9,\epsilon},2}(\tau) = \langle(\delta_\tau u_{9,\epsilon})^2\rangle$ (solid lines) for the 6 values of τ_η. In this representation, $\mathcal{S}_{u_{9,\epsilon},2}(\tau)$ is normalized by $2\langle u_{9,\epsilon}^2\rangle$, such that it goes to unity at large arguments $\tau \gg T$. At small scales $\tau \ll \tau_\eta$ the dissipative behavior $\mathcal{S}_{u_{9,\epsilon},2}(\tau) \propto \tau^2$ is recovered, a consequence of the differentiable nature of the process. In the inertial range $\tau_\eta \ll \tau \ll T$, as expected by the theoretical prediction, a behavior similar to an OU process is obtained, that is $\mathcal{S}_{u_{9,\epsilon},2}(\tau) \propto \tau$. Using a dashed line, the expected behavior from an OU process, namely $S_{u_1,2}(\tau) = 2\langle u_1^2\rangle \left(1 - e^{-|\tau|/T}\right)$ is also included, which describes with great accuracy the scaling behavior of $\mathcal{S}_{u_{9,\epsilon},2}(\tau)$ in the inertial

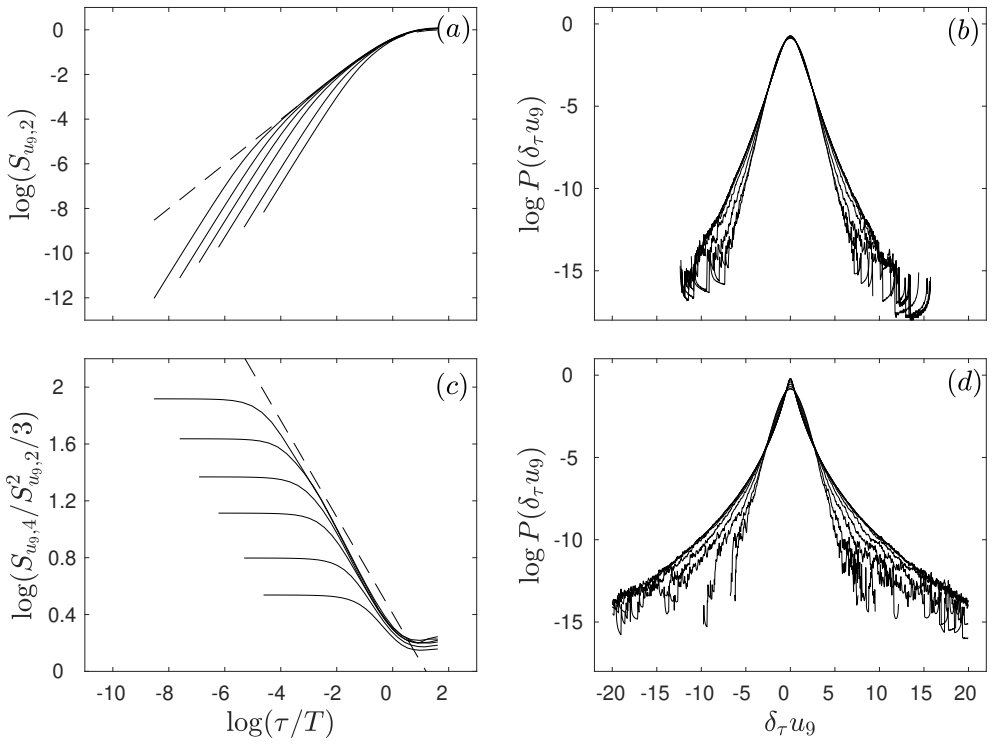

Figure 2.3: Illustration of higher order statistics of the processes studied in figure 2.2. (a) Logarithmic representation of the second-order structure function of the six different values of τ_η (solid lines), and the asymptotical prediction provided in equation (A.37) (dashed line). (b) Estimation of the Probability density Functions of velocity increment for $\tau_\eta/T = 1/10$. (c) Logarithmic process of the flatness of velocity increments with the theoretical prediction superimposed. (d) Similar plot as in (b), but for $\tau_\eta/T = 1/500$.

range and at larger scales. The second-order statistics of $u_{9,\epsilon}$ are well described by the asymptotic predictions in this range of scales. Similar conclusions were obtained while describing velocity correlation function in figure 2.2(c).

To investigate intermittent behaviors, figure 2.3(c) presents the scaling behavior of the flatness of velocity increments, that is $\mathcal{S}_{u_{9,\epsilon},4}/\mathcal{S}^2_{u_{9,\epsilon},2}$ (solid lines), and for the 6 different values of τ_η, in a logarithmic fashion. The flatnesses are normalized by 3, i.e. the value obtained for Gaussian processes. Flatnesses are observed close to 3

at large scales $\tau \geq T$, and then increase in the inertial range as a power-law, before saturating in the dissipative range $\tau \leq \tau_\eta$. This saturation is typical of differentiable processes: a Taylor series of increments makes the dependence on τ disappear. On this plot, using a dashed line, the theoretical prediction is included that was made for MRW (equation (2.33)) without the unjustified additional free parameter. The power-law exponent is given by $-4\gamma^2$, and the multiplicative constant is close to the one derived for the non-differentiable MRW (equation (2.33)). This theoretical prediction seems to be more and more representative of the intermittent properties of $u_{9,\epsilon}$ as τ_η gets smaller and smaller. This indicates that the constant $c_{\gamma,4}$ which is tedious to compute in an exact fashion for the infinitely differentiable MRW (equation (A.39)) is the same as in the non differentiable case (equation (2.33)). This shows that the limits $\epsilon \to 0$ and $\tau_\eta \to 0$ commute at the fourth-order too (equations (A.38) and (A.39)).

Finally, to illustrate the intermittent behavior of the process $u_{9,\epsilon}$, figures 2.3(b) and (d) display the probability density functions (PDFs) of velocity increments at various scales, from large to small: (b) $\tau_\eta/T = 1/10$ and (d) $\tau_\eta/T = 1/500$. The continuous shape deformation of these PDFS is observed as the scales τ decreases in length, from Gaussian at large scales $\tau \geq T$ to strongly non-Gaussian in the dissipative range. This is consistent with the behavior of flatnesses (figure 2.3(c)), becoming less and less Gaussian as τ_η diminishes in size.

2.3.3 Comparison to Direct Numerical Simulations for tracer particle modeling

To this point, only illustrations of the model based on input parameters have been presented. A comparison to simulations will show the capabilities of the model.

Description of the datasets

Two sets of data are considered which have been made freely accessible to the public. The data are statistically homogeneous and isotropic numerical flows obtained by solving the Navier-Stokes equations in a periodic box. Lagrangian trajectories are then extracted from the time evolution of the Eulerian fields while integrating the positions of tracer particles, initially distributed homogeneously in space. The first set is a direct numerical simulation (DNS) at a moderate Taylor based Reynolds number $\mathcal{R}_\lambda = 185$, referenced in Bec et al. [2006, 2011], which can be downloaded from HTTPS://TURBASE.CINECA.IT/. The second dataset has a higher Taylor based Reynolds number $\mathcal{R}_\lambda = 418$, hosted at JHTDB (see HTTP://TURBULENCE.PHA.JHU.EDU). Details on this DNS and how to extract Lagrangian trajectories can be found in Li et al. [2008], Yu et al. [2012]. Relevant parameters of these datasets and of the Lagrangian trajectories are given in Table 2.1. It is of note that the Kolmorogov time scale from the DNS is denoted as τ_K to differentiate from the modeling parameter of τ_η.

Definition and estimation of the Lagrangian integral time scale

A connection is required between the modeling approach and numerical investigations. This is achieved by considering quantities that can be extracted from DNS

Origin	Resolution	$\mathcal{R}_\lambda$	τ_K	T_L	Trajectories	dt	Duration
Turbase	512^3	185	0.0470	0.7736	126720	4.10^{-3}	$17.063\,T_L$
JHTDB	1024^3	418	0.0424	1.3003	32768	2.10^{-3}	$7.692\,T_L$

Table 2.1: Summary of relevant physical parameters of the two sets of DNS data.

data, and relating them to the free parameters entering in the definition of the stochastic process u, namely τ_η, T and γ.

Call T_L the Lagrangian integral time scale, defined as the integral of the velocity correlation function, i.e.

$$T_L = \int_0^\infty \frac{\mathcal{C}_u(\tau)}{\mathcal{C}_u(0)} d\tau, \tag{2.83}$$

where u stands for any Lagrangian velocity components extracted from DNS data, or the present stochastic model.

The definition of T_L (equation (2.83)) is appealing because it can be applied to and estimated from velocity time series coming indifferently from DNS or the model, but it requires proper statistical convergence of $\mathcal{C}_u(\tau)$ which is especially difficult to acquire from DNS. This becomes even more of an issue when considering experimental data (see a recent discussion on this by Huck et al. [2019]) in which the duration of trajectories are typically shorter. Moreover, on the entire accessible statistical sample, made of a minimum of tens of thousands of trajectories for each three velocity components, a non negligible level of anisotropy is observed for both sets of data, the standard deviation of the variance of the three velocity components is of order of 20% of the average variance. This level of anisotropy is surprising given the isotropic and periodic boundary conditions of the advecting flow, forcing the conclusion that in both DNSs, trajectories are not long enough to guarantee

statistical isotropy. This has consequences on the estimation of T_L. Nonetheless, and because ultimate expectation is that the flow, and incidentally its Lagrangian trajectories, is isotropic, the velocity correlation function is averaged over the three components, keeping in mind that the lack of statistical convergence can induce an error on the estimation of this large time scale. Findings are gathered in Table 2.1. Notice that this observed anisotropy on the velocity variance has weak impact on the acceleration correlation function once normalized by its value at the origin (data not shown). This can be understood by realizing that acceleration is governed by the small scales of the flow, whereas velocity by the large scales.

Statistical analysis of the DNS datasets

Figure 2.4(a) and (c) display the numerical estimation of velocity and acceleration correlation functions based on the Lagrangian trajectories extracted from DNS, at moderate Reynolds number $\mathcal{R}_\lambda = 185$ (○) and at high Reynolds number $\mathcal{R}_\lambda = 418$ (□). Time lags τ are normalized for $\mathcal{C}_u(\tau)$ by a large time scale T coming from the adopted calibration procedure of the model. At this level of discussion, keep in mind that T is very close to T_L (equation (2.83)). Concerning $\mathcal{C}_a(\tau)$ (figure 2.4(c)), the time lags τ are normalized by the Kolmogorov time scale τ_K that reads

$$\tau_K = \sqrt{\frac{\nu}{\langle \varepsilon \rangle}}, \tag{2.84}$$

where ν is the kinematic viscosity and $\langle \varepsilon \rangle$ the average viscous dissipation per unit of mass. It is observed that, in this representation where scales are normalized by τ_K, $\mathcal{C}_a(\tau)$ crosses zero at a Reynolds number independent time scale. Call such a scale τ_0,

thus defined by $\mathcal{C}_a(\tau_0) = 0$, as has been observed in numerical and laboratory flows [Yeung et al., 2007, Huck et al., 2019]: the zero-crossing time scale of acceleration has a universal (i.e. Reynolds number independent) behavior with respect to the Kolmogorov time scale τ_K (equation (2.84)), such that

$$\tau_0 \approx 2.2\,\tau_K, \tag{2.85}$$

in the range of investigated Kolmogorov time scales. For the DNS, a value of $\tau_0 = 2.11\,\tau_K$ at $\mathcal{R}_\lambda = 185$, and $\tau_0 = 2.14\,\tau_K$ at $\mathcal{R}_\lambda = 418$, similar to previous findings of Yeung et al. [2007] (equation (2.85)). This can be used to fully calibrate the model by relating the free parameter τ_η to the characteristics of the numerical flows.

Similarly, the scaling behavior of the second-order structure function $\mathcal{S}_{u,2}$ (figure 2.4(b)) and of the flatness of velocity increments (figure 2.4(d)) are displayed. The three expected ranges of scales: the dissipative one with $\mathcal{S}_{u,2}(\tau) \propto \tau^2$, the inertial one with $\mathcal{S}_{u,2}(\tau) \propto \tau$, and the saturation towards $2\langle u^2 \rangle$ at larger scales are observed. The flatness, again shows saturation at the Gaussian value 3 at large scales, and a power-law behavior in the inertial range, reminiscent of the intermittency phenomenon. There are differences observed between the processes and their respective DNS, for example, more rapid increase in the intermediate dissipative range is observed, and then a Reynolds number dependent saturation towards the flatness of acceleration. This is a known effect of the fine structure of turbulence, linked to subtle differential action of viscosity that depends on the local regularity of the velocity field [Chevillard et al., 2003, 2005, 2006, Arneodo et al., 2008, Benzi et al., 2010, Chevillard et al., 2012]. This phenomenon is well reproduced by the

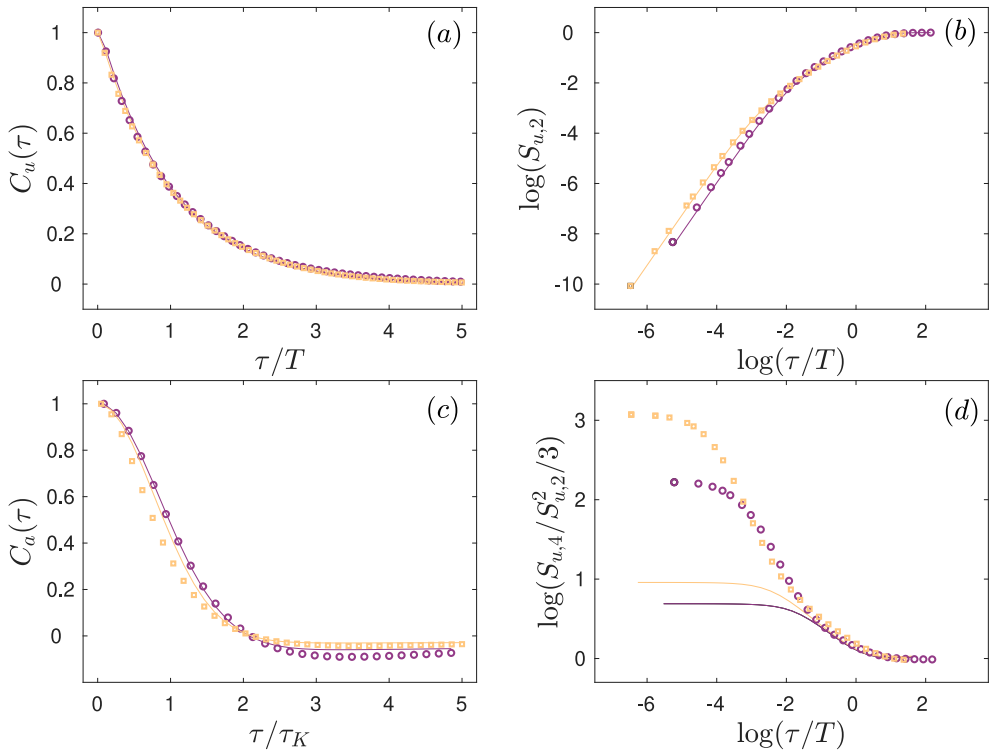

Figure 2.4: Comparison of DNS data $\mathcal{R}_\lambda = 185$ (○) and $\mathcal{R}_\lambda = 418$ (□) to model predictions. Estimation of the (a) velocity correlation function with theoretical predictions where time lags are normalized by the calibrated time scale T and (b) the second-order structure function. DNS comparison with the model for the acceleration correlation function, normalized by its value at the origin (c) and the flatness (d) are also included. Theoretical predictions are obtained via numerical estimation of velocity time series of the model (Section 2.3.2).

phenomenology of the intermittency phenomenon developed in the framework of the multifractal formalism [Paladin and Vulpiani, 1987, Frisch, 1995].

Reynolds number dependence of the zero-crossing time scale of the acceleration correlation function

Model predictions of the zero-crossing time scales

The present model, both for the Gaussian version v (Proposition A.1.2 and figure 2.1(d)) and for its intermittent generalization u (Proposition A.1.5 and figure 2.2(d)), predicts this aforementioned zero-crossing time scale τ_0 of the acceleration correlation function, as a function of its parameters τ_η and T. At this level of discussion, the influence of the intermittency parameter γ is neglected in this picture, it has a weak influence on its overall shape, even in the dissipative range (data not shown). Therefore, given the low value of $\gamma^2 = 0.085$, making the predicted intermittent acceleration correlation function indiscernible from its Gaussian approximation, further theoretical discussions are herein presented, which neglect these non-Gaussian effects. It is moreover convenient since in this case, $\mathcal{C}_a(\tau)$ has an explicit form (equation (2.28)), that makes its dependence present on τ_η and T.

Further inspection of the numerical results presented in figure 2.2(d) when τ_η is varying shows that this predicted zero-crossing time scale depends in a non trivial way on τ_η. Keeping only the leading terms entering in equation (2.28) as τ_η, asymptotically, this time scale behaves as

$$\tau_0 \underset{\tau_\eta \to 0}{\sim} 2\tau_\eta \sqrt{\log\left(\frac{T}{\sqrt{\pi}\tau_\eta}\right)}. \tag{2.86}$$

Taking into account the empirical fact that the zero-crossing time scale is proportional to the Kolmogorov time scale τ_K in a universal way (equation (2.85)), this shows that τ_η, up to logarithmic corrections, has the same Reynolds number depen-

dence as τ_K, and thus can be considered as a dissipative time scale. Interestingly, for the process proposed by Sawford (Section 2.2.1), named here v_2, such a zero-crossing time scale can be exactly derived from equation (2.11). This case results in $\tau_0 = \tau_\eta \frac{\log(T/\tau_\eta)}{1-\frac{\tau_\eta}{T}}$. The present prediction for τ_0 (equation (2.86)) made with an infinitely differentiable process can be seen as an improvement of the model by Sawford, since the parameter τ_η is closer to τ_K.

The proposed calibration procedure of models parameters

As suggested, neglecting all possible intermittent effects in this discussion, developments are executed with the explicit second-order statistical properties of the Gaussian process v (Proposition A.1.2). To determine the free parameters of the model τ_η, given the characteristic scales of the DNS τ_K and T_L, the nonlinear system of coupled equations

$$T_L = T \frac{e^{-\tau_\eta^2/T^2}}{\operatorname{erfc}(\tau_\eta/T)} \tag{2.87}$$

$$\mathcal{C}_a(\alpha\tau_K) = 0, \tag{2.88}$$

are solved, where the exact expression of T_L in equation (2.87) can be easily obtained from equation (A.8), the explicit expression of $\mathcal{C}_a$ is provided in equation (2.28), and α being equal to 2.11 at $\mathcal{R}_\lambda = 185$, and 2.14 at $\mathcal{R}_\lambda = 418$. This is the calibration procedure. Using a standard numerical solver of nonlinear equations and the values of (τ_K, T_L) provided in Table 2.1, the solution of the system of equations 2.87 and 2.88 provides $(\tau_\eta/\tau_K, T/T_L) = (0.6335, 0.9562)$ for $\mathcal{R}_\lambda = 185$, and $(0.5759, 0.9791)$ for $\mathcal{R}_\lambda = 418$.

2.3.4 Comparison of model predictions to DNS data

Having performed the calibration procedure depicted in Section 2.3.3, and obtained the respective values for the free parameters τ_η and T, a comparison of the present model predictions to data is performed. Theoretical second-order statistics are presented in figures 2.4(a) and (b) using solid lines where an almost perfect collapse with the statistical estimations based on DNS data is shown.

The acceleration correlation function is shown in figure 2.4(c). At the moderate Reynolds number, $\mathcal{R}_\lambda = 185$, the agreement is excellent in the dissipative range, i.e. for scales smaller that the zero-crossing time scale τ_0. A slight disagreement above τ_0 is observed which could be due to the lack of statistical convergence at large scales which overestimates the integral time scale T_L, as previously discussed in Section 2.3.3. At the current level of precision, overall agreement with second-order statistics is satisfactory at this Reynolds number. At a higher Reynolds number $\mathcal{R}_\lambda = 418$, discrepancies can be seen in the dissipative range. This is very probably due to intermittency effects, that are negligible in the model, but not in DNS. To see this more clearly, the flatness of velocity increments is considered.

In figure 2.4(d) the theoretical predictions of the model for flatnesses using the prescribed value γ^2 are superimposed using solid lines. To get these theoretical predictions, additional numerical simulations of time series of the model are performed, as it is done in Section 2.3.2, for the calibrated values of the parameters τ_η and T obtained in Section 2.3.3. Good agreement is seen in the inertial range, showing that the chosen value for the intermittency coefficient γ is realistic of DNS. Unfortunately, the model is unable to reproduce the rapid increase of intermittency in the dissipative range. To go further in this direction, the predictions of the multifractal

formalism are presented to accurately depict the behavior of the flatnesses in this range of scales.

2.3.5 Multifractal formalism calibration of the free parameters and comparisons to DNS data

The same calibration of the free parameters τ_η and T is adopted for the multifractal formalism. The nonlinear problem is solved numerically, obtaining τ_η and T from the empirical value of T_L and the appropriate zero-crossing of acceleration time scale given in unit of τ_K. It is very similar to solving the system of equations (2.87) and (2.88), with the exception that the integral time scale T_L predicted from the model has to be computed numerically using a standard integration scheme of the expression provided in equation (2.50). To give an initial estimate to the numerical algorithm that looks for zeros of functions, as it is required to solve this nonlinear problem, a initial prediction for the zero-crossing of acceleration time scale τ_0 can be made. Using the parametrization per Batchelor of the second-order structure function (equation (2.48)), and the corresponding prediction of the acceleration correlation function (equation (2.49)), a good approximation of τ_0 is expected to be

$$\tau_0 \underset{\tau_\eta \to 0}{\approx} \tau_\eta \left(\frac{\delta - 1}{2} \right)^{-\frac{1}{\delta}}, \tag{2.89}$$

showing that the free modeling parameter τ_η is expected to be proportional to the Kolmogorov dissipative time scale τ_K.

Using the physical parameters of the DNS data provided in Table 2.1, assuming furthermore $\gamma^2 = 0.085$ and $\delta = 4$, the solution of this aforementioned nonlinear

system of equations is pursued, resulting in $(\tau_\eta/\tau_K, T/T_L) = (2.7596, 0.9927)$ for $\mathcal{R}_\lambda = 185$, and $(2.6106, 0.9983)$ for $\mathcal{R}_\lambda = 418$.

With these calibrated inputs a comparison is made to DNS data. Figures 2.5(a), (b) and (c) present the predictions of the velocity correlation function $\mathcal{C}_v(\tau)$, the second-order structure function $\mathcal{S}_2(\tau)$ and the acceleration correlation function $\mathcal{C}_a(\tau)$, all based on the multifractal parametrization of the second-order structure function (equation (2.50)), and its second derivative (equation (2.56)). As far as velocity is concerned, a perfect agreement between predictions and DNS data is observed, for both correlation (figure 2.5(a)) and second-order structure function (figure 2.5(b)).

Concerning the acceleration correlation function $\mathcal{C}_a(\tau)$ (figure 2.5(c)), predictions slightly overestimate the negative values after the zero-crossing, opposite to the behavior seen by infinitely differentiable process (figure 2.4(c)). Below the zero-crossing time scale, predictions overestimate the decrease of correlation. Compared to the curves of the stochastic process, displayed in figure 2.4(c), the predictions based on the multifractal formalism do not perform as well.

Focusing on the intermittency corrections, as it is quantified by the flatness of velocity increments, figure 2.5(d) compares the flatness of increments, based on DNS and on the current multifractal model using the expression given in equation (2.57). The multifractal predictions accurately reproduce the overall shape of the flatness, including the rapid increase in the intermediate dissipative range, for both Reynolds numbers. Recall here that this dissipative behavior is not reproduced by the stochastic approach. Furthermore, a slight shift between numerical and theoretical curves is seen: this indicates that the large time scale associated with intermittent correc-

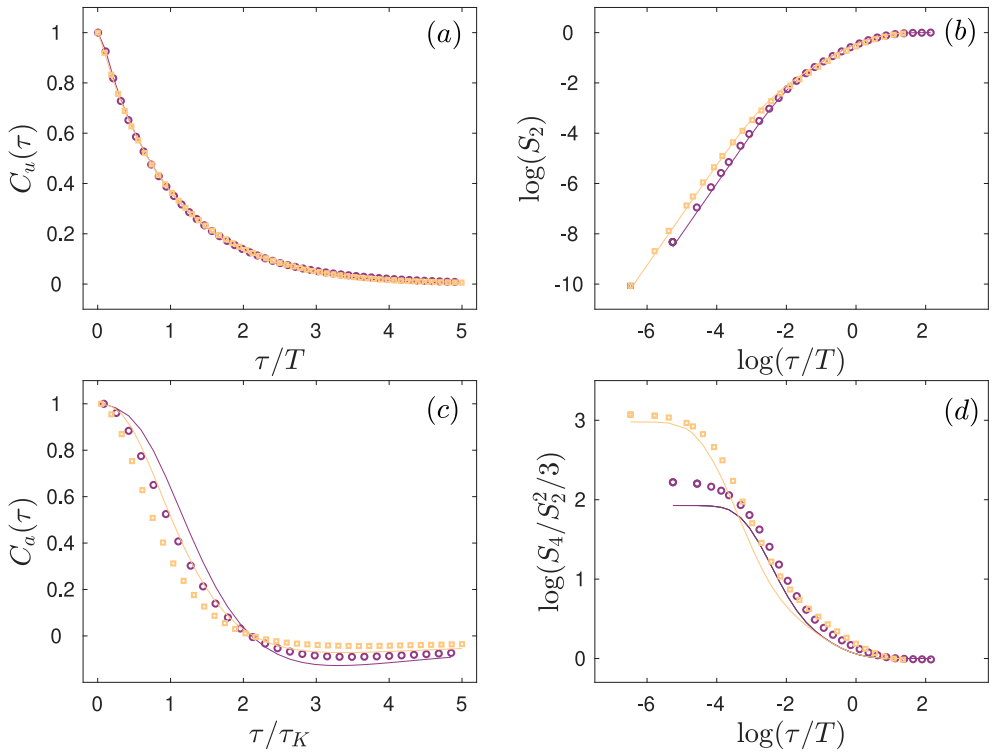

Figure 2.5: Comparison of DNS data $\mathcal{R}_\lambda = 185$ (○) and $\mathcal{R}_\lambda = 418$ (□) to model predictions for multifractal predictions. (a) Estimation of the velocity correlation function from DNS data and the theoretical predictions based on the multifractal parametrization. Time lags are normalized by the calibrated time scale T. (b) The second-order structure function. DNS comparison with the multifractal formalism output for the acceleration correlation function, normalized by its value at the origin (c) and the flatness (d). Theoretical predictions are obtained from the expression given in equation (2.57).

tions is slightly larger that the one associated to the velocity correlation time scale. This could be included in the expressions of structure functions (equations (2.50) and (2.57)) at the price of introducing another ad-hoc free parameter of order unity, without further justifications (data not shown). Nonetheless, overall, the present multifractal model reproduces, in good agreement, the curves of DNS data, both in the inertial and dissipative ranges.

2.3.6 Illustrations of the stochastic processes for inertial particles

Resulting processes and statistics of a model, which includes the effects of finite inertia, are herein presented.

Direct numerical simulations of Lagrangian trajectories of the inertial particles

Utilizing the abilities of the DNS from JHTDB (dataset information provided in Section 2.3.3, Table 2.1), in addition to the tracers, twenty datasets are created containing the particle trajectories of varying Stokes numbers [Yu et al., 2012]. The equation of motion of inertial particles equations (2.60-2.61) are solved by a second-order Runge-Kutta scheme and each DNS subset of data contains 32^3 trajectories. Here, in addition, the generated particles tracks contain a St = [0:0.2:2] to provide a range of low to high Stokes for validating the model.

For a first look at the dynamics associated with inertial particles in comparison to tracers, the temporal evolution of particle position $\boldsymbol{X}_p(t)$, a velocity component $v_p(t)$, and the corresponding acceleration $a_p(t)$ for St= 0.2 are presented in figure 2.6 for a time span of $\approx 110\tau_K$. For comparison, figure 2.6(b), shows the three-dimensional trajectory of an ideal tracer $\boldsymbol{X}(\boldsymbol{x}, t)$ starting from the same initial condition $\boldsymbol{X}_p(0) = \boldsymbol{x}$. While the tracer (yellow) velocity exhibits several strong oscillations, the inertial particle (purple) velocity seems much less affected. From figure 2.6(b), it is noted that, at already at such low Stokes numbers, the trajectory of the particle follows a substantially different path. In the context of preferential concentration [Cencini et al., 2006, Pumir and Wilkinson, 2016], one could interpret this in terms of the inertial particle evading strong vortical flow structures. This

might also be supported by the evolution of the acceleration whose amplitude (and statistically speaking its variance) is significantly decreased in comparison to the tracer particle.

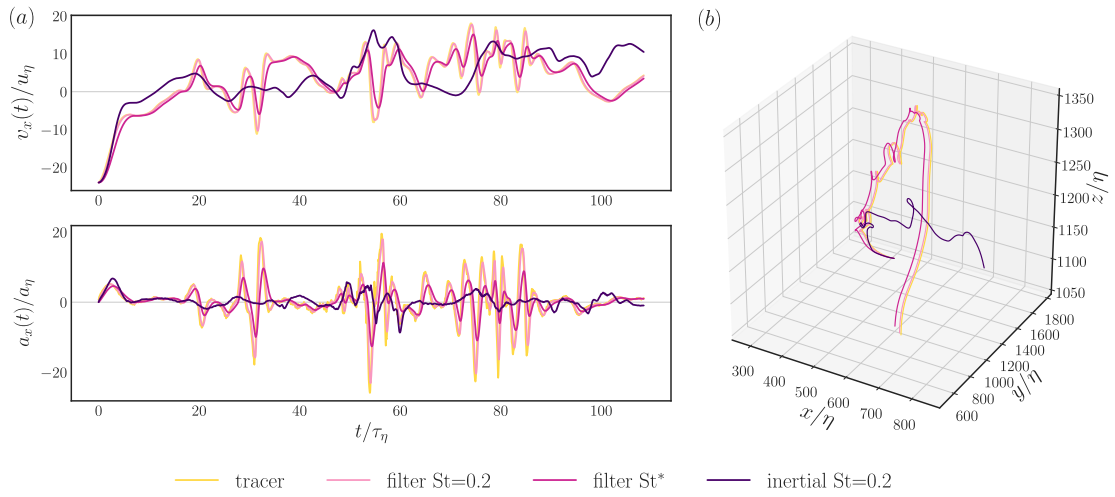

Figure 2.6: (a) Velocity $v_x(t)$ (upper panel) and acceleration $a_x(t)$ (lower panel) of tracers, filtered tracers with τ_p (St=0.2) and τ_P^* (St*) and true inertial particles for St = 0.2. (b) Trajectories of tracer, filtered tracers, and inertial particles.

Figure 2.6 also includes the trajectory modeled for St = 0.2 form the linear filter approximation from equation (2.63) which remains very close to its determining tracer trajectory. This is most visible by the temporal evolution of the acceleration, suggesting that the linear filter overestimates the acceleration variance in comparison to the ordinary inertial particle. Cencini et al. [2006] applied the same technique to compare root-mean-squared accelerations and observed large discrepancies between filtered and true a_{rms} at low St. Nonetheless, for larger Stokes numbers, true and filtered a_{rms}-values seemed to approach one another. This suggests that non-trivial effects of the preferential concentration, when inertia is introduced to the particles, creates the gap between true and filtered results for St <1. To better understand

these effects, the acceleration auto-correlation function which has been obtained by averaging over all $N_p = 32^3$ particle trajectories is depicted in figure 2.7(a). Here, the dash-dotted curves correspond to the linear filter approximation (2.68) for $\tau_p = \mathrm{St}\tau_K$ with St= $[0.1, 0.2, 0.5, 1, 2]$ from left to right. The fluid velocity correlation function $\mathcal{C}_a(\tau)$ was integrated over the entire time range of the simulation T (see also Table 2.1). In agreement with the findings by Cencini et al. [2006], the modeling breaks down initially, drastically underestimating the correlation of the particle for St $\leq$1, but recovers to generate meaningful statistics for St=2. It is noted that for low Stokes, the correlations are similar to the ideal tracer (not shown in the figure), therefore they decorrelate much faster.

These profound changes between inertial particle and tracers (or filtered tracers) acceleration properties at low Stokes also manifest themselves in the root mean square of acceleration. Figure 2.8 depicts the root mean square values of acceleration a_{rms} as a function of St for inertial particles and filtered tracer particles according to equation (2.66). The a_{rms}-values of inertial particles decreases much faster than their filtered counterparts. These strong discrepancies were interpreted by Cencini et al. [2006] in terms of inertial particles which preferentially sample regions of low turbulence intensity (or depleted vorticity regions) whereas the filtered tracer particles are still impacted by strong acceleration events of tracer trajectories trapped in vortical structures. In other words, by restricting itself to individual tracer trajectories $\boldsymbol{X}(\boldsymbol{x}, t)$, the filtering approach bears no information on the spatial organization of the surrounding fluid velocity field, which apparently is crucial for a better understanding of the dynamics of inertial particles.

Therefore, a modification of the linear filter is proposed, which is in better agree-

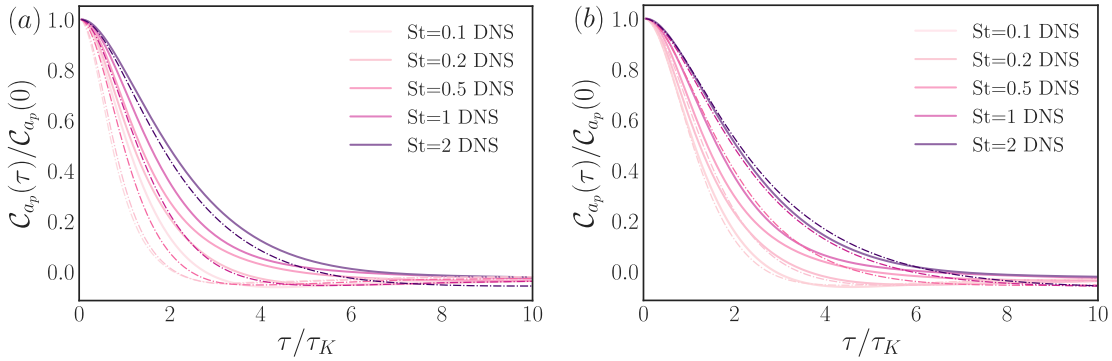

Figure 2.7: (a) Acceleration correlation from DNS for inertial particles with Stokes numbers $\mathrm{St} = 0.1, 0.2, 0.5, 1., 2$. The dash-dotted lines correspond to the linear filter approximation with $\tau_p = \mathrm{St}\tau_K$. (b) Acceleration correlation function for a filter with an effective Stokes number $\mathrm{St}^* = \tau_p^*/\tau_K$ which has been determined from the zero-crossing of the acceleration correlation from DNS (dash-dotted curves and DNS curves now possess the same zero-crossing).

ment with DNS but at the same time still is solely based on the Lagrangian velocity $\boldsymbol{v}(\boldsymbol{x}, t)$ of an individual tracer. This is accomplished by introducing an effective particle response time τ_p^* in the linear filter approximation (2.63) which does not necessarily obey the usual relation $\tau_p = \mathrm{St}\tau_K$, but henceforward is considered as a free model parameter. Similar to methods presented for tracer modeling, which identified the zero-crossing of the acceleration correlation as a crucial ingredient for model calibration, in a similar way. First, the zero-crossing $\tau_0(\mathrm{St})$ of the acceleration auto-correlation functions are determined from DNS curves. Subsequently, with the help of a suitable roots-finding algorithm, the effective particle response time $\tau_p^*(\mathrm{St})$ in equation (2.68) is determined in such a way that $\mathcal{C}_{a_p}(\tau_0(\mathrm{St})) = 0$.

Figure 2.7(b) depicts the acceleration auto-correlation functions (dash-dotted curves) after this calibration. By introducing an effective particle response time τ_p^* based on matching zero-crossing of the acceleration correlation functions, a better

agreement with DNS has been achieved, particularly for low Stokes numbers. The corresponding filtered trajectories with $\mathrm{St}^* = \tau_p^*/\tau_K$ are also included in figure 2.6. Due to the increased damping ($\tau_p^* > \tau_p$) in the filter, τ_p^*-filtered accelerations are closer to their DNS counterparts.

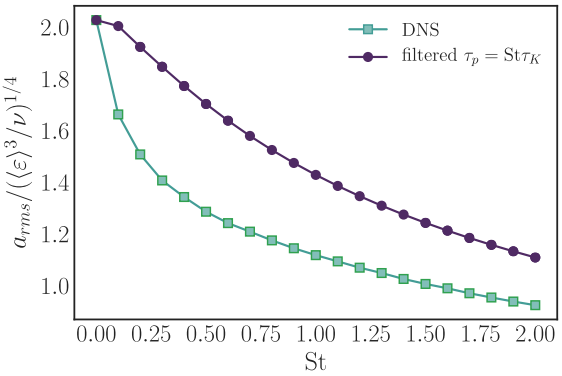

Figure 2.8: Root mean square values of acceleration a_{rms} as a function of the Stokes number for inertial particles in DNS and filtered tracer particles according to equation (2.63). The a_{rms}-values from DNS exhibit a rapid decrease for small but finite St whereas the linear filter approximation decays much slower.

2.3.7 Comparison to DNS

Presented modeling techniques are applied to the DNS. In order to connect these approaches to the simulated data, recall that the parameters of the DNS must be defined to properly calibrate the models, namely the integral length scale, T, the dissipative scale, τ_η, and now in addition, the effective particle response time τ_p^*. Recall that for the Lagrangian model ($\tau_p^* = 0$), calibration suggests the values $(\tau_\eta/\tau_K, T/T_L) = (0.5759, 0.9791)$. For the Batchelor model, the same calibration has to be carried out, where now the Lagrangian integral time scale is given by

equation (2.78) and $(\tau_\eta/\tau_K, T/T_L) = (1.7956, 0.9941)$ is obtained. It can be noted that τ_η from the Batchelor model is larger than τ_K whereas the stochastic model exhibits a τ_η smaller than τ_K after calibration.

With the inclusion of St, an additional free parameter of the models is available for calibration, the effective particle response time τ_p^*. As discussed, the acceleration correlation function for the stochastic Gaussian process is given by equation (2.75), from which τ_p^* can be extracted based on the zero-crossing of the DNS data for each Stokes number. In a similar fashion, the new model parameter τ_p^* is obtained from the linear filtering of the acceleration correlation function of the Batchelor model derived from equation (2.77).

Figures 2.9(a) and 2.9(b) depict the comparison of second-order structure function $S_2(\tau) = \langle(\delta_\tau v_p)^2\rangle$ obtained using the stochastic and Batchelor model, respectively (dash-dotted curves), to DNS for St=0-1 (solid curves). For the tracers, St=0, the stohcastic Gaussian model from Section 2.2.1 and Batchelor model are implemented.

For St >0, linear filtering of the velocity correlation function for tracer particles agrees well with $S_2(\tau)$ from DNS for both models. The stochastic approach, figure 2.9(a) shows agreement between the model and DNS at small scales and deviates slightly as the time lag τ increases. Notably, slight deviations appear in the inertial range and might be attributed to the Gaussianity of the stochastic model, which thus neglects intermittency corrections. The application of the filtering technique to the statistics of the Batchelor model, figure 2.9(b), shows similar tendencies. At small scales, the model coincides with the DNS profiles for the given St presented. At τ/τ_K >1, again a deviation occurs where the model begins to overestimate the struc-

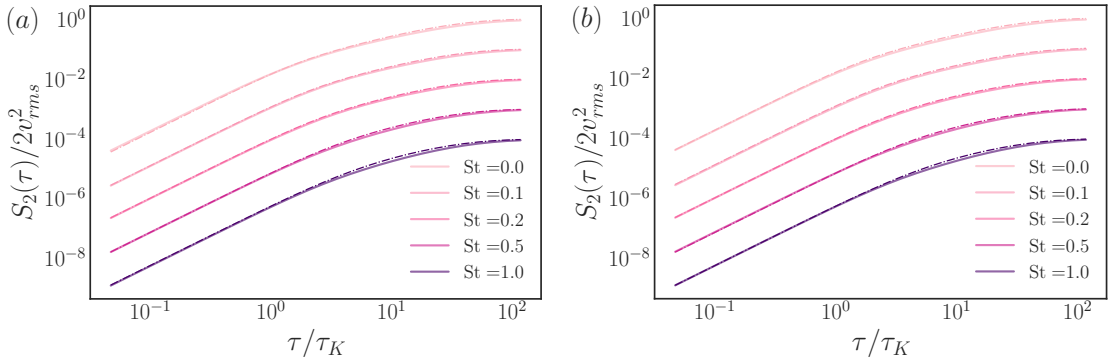

Figure 2.9: Comparison of the second-order structure function to DNS (solid lines) from (a) the stochastic model (dash-dotted lines) and (b) the Batchelor model (dash-dotted lines) for 5 St parameters in between 0 and 1. The structure functions have been shifted vertically arbitrarily for clarity.

ture function of its corresponding DNS curve, the near-dissipative range seems to extend further than the one present in the simulated data. These deviations slightly increase with St. The application of the models to the acceleration correlation function is presented in figure 2.10. Here, the discrepancy between modeled correlations and those obtained from the simulated data can be observed at all scales. The stochastic modeling of the inertial particle correlations is presented in figure 2.10(a) for the considered St range. The model over-predicts correlations in the dissipative range. For increasing Stokes number, linear filtering of the model improves the ability to accurately describe small scale correlations and still the large scale variations between the two curves are minimal, for example for St=0.2. As St increases further, quickly the filtered model and the DNS show increased discrepancies between the profiles, as the decorrelation of the acceleration occurs more rapidly than the model predicts. Filtering of the Batchelor model, figure 2.10(b), shows similar tendencies of the results of the stochastic approach, but with even greater variation. The correlation of tracer velocity at St=0 is slightly over-predicted at small scales and slightly

under-predicted at large scales. Comparable dissimilarity is observed between the DNS and model at St=0.1. As the Stokes number increases, the linear filter of the model breaks down and the predictions decorrelate slower when compared to the simulated data responses.

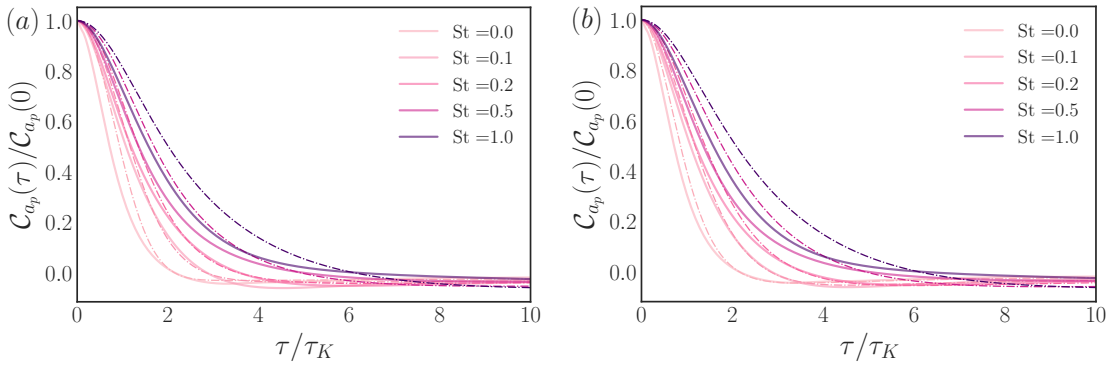

Figure 2.10: Comparison of acceleration auto-correlation function from (a) the stochastic model (dash-dotted lines) and (b) the Batchelor model (dash-dotted lines) to DNS for 5 different St parameters in between 0 and 1.

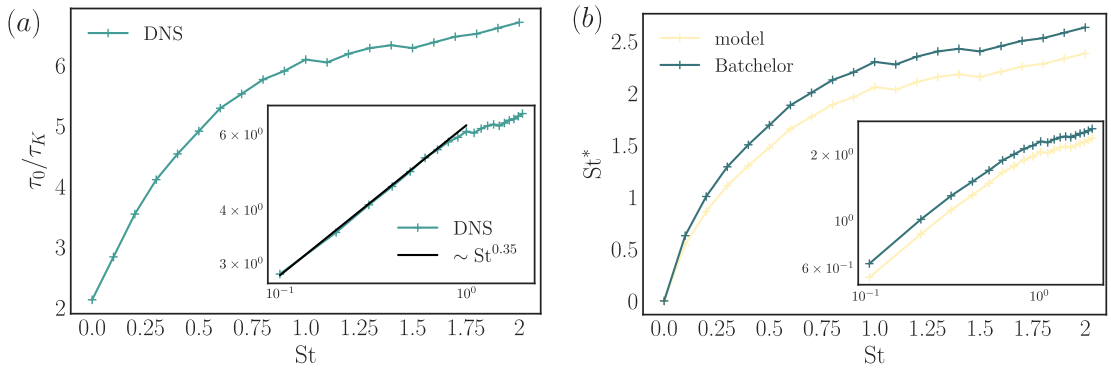

Figure 2.11: (a) zero-crossing τ_0 of the acceleration correlation functions from DNS (as partially shown in figure 2.7) as a function of St. The inset shows a double-logarithmic representation with the black line indicating $\tau_0 \sim \mathrm{St}^{0.35}$. (b) Recalibrated particle response time τ_p^* expressed as $\mathrm{St}^* = \tau_p^*/\tau_K$ based on the zero-crossing τ_0 as a function of St.

Due to the fact that the model calibration for finite St is based on the zero-

crossing of the acceleration correlation, it is worth studying the St-dependence of this quantity as well. Therefore, figure 2.11(a) depicts the zero-crossing τ_0 from DNS as a function of the Stokes number. For the case of Lagrangian tracers $\mathrm{St} = 0$, the zero-crossing is at around $2.2\tau_K$ and increases sharply for $\mathrm{St} > 0$. For $\mathrm{St} \approx 1$, a new quantitative behavior sets in, and the zero-crossing exhibits a slower increase. Furthermore, the zero-crossing becomes rather noisy, therefore, it is not entirely clear whether the zero-crossing would saturate at even higher St. The inset of figure 2.11(a) shows a double-logarithmic representation of τ_0. For $\mathrm{St} < 1$, the zero-crossing appears to be a power law, whereas deviations from this power law appear at $\mathrm{St} \approx 1$. For comparison, the black line shows a power law $\sim \mathrm{St}^{0.35}$. However, at this point, no clear phenomenological description could be provided that would allow for the explanation of such a power law of the zeros of acceleration for inertial particle motion.

Figure 2.11(b) depicts the calibrated effective Stokes number $\mathrm{St}^* = \tau_p^*/\tau_K$ as a function of the DNS Stokes number for both the stochastic and the Batchelor model (violet). Interestingly, the curves strongly resemble figure 2.11(a) which suggests a nearly linear relation between the zero-crossing τ_0 and the effective (calibrated) particle response time τ_p^*.

The a_{rms} values as a function of the Stokes number for all modeling techniques are included in figure 2.12 for direct comparison of the statistic. The filtered acceleration, found directly from equation (2.68), and the stochastic model, based on τ_p, quickly deviate from the DNS a_{rms} curve while the two models with the updated τ_p^* for the stochastic process and Batchelor representation show improved agreement at all St and good agreement between $0.2 \leq \mathrm{St} \leq 1.1$. Cencini et al. [2006] present

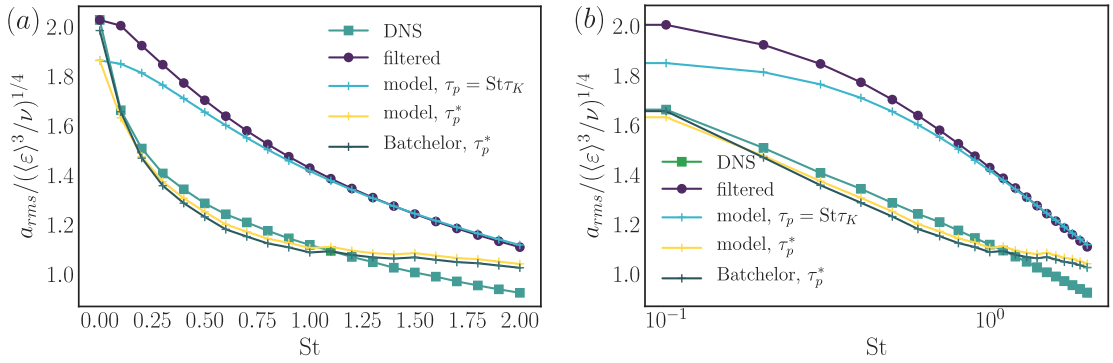

Figure 2.12: (a) Comparison of root mean square values of acceleration for DNS and the different models. (b) Semi-logarithmic representation of (a).

a similar comparison and suggest that the deviation between the profiles at small Stokes numbers is due to preferential concentration captured which is not captured by the linear filter approximation. The inclusion of the effective particle response time τ_p^* in our model counteracts this discrepancy, providing accurate representations of acceleration statistics for the presented Stokes numbers.

2.4 Concluding remarks

Finally, to summarize the findings in the context of the stochastic modeling of Lagrangian velocity and acceleration. First, a stochastic dynamics model has been proposed, which is causal, infinitely differentiable at a given Reynolds number, or equivalently in a good approximation, for a given finite ratio of a dissipative time scale τ_η over a large one T. The process, u, is defined as the limit $n \to \infty$ of the n-layered embedded process u_n. Furthermore, intermittent properties are included in a causal and exact way through an intermittent coefficient γ. At infinite Reynolds number, i.e., when $\tau_\eta \to 0$, both processes converge towards a statistically stationary and finite variance causal process, which is a (Gaussian) Ornstein-Uhlenbeck

process and a multifractal random walk. For the multifractal version, the intermittent behavior of the structure functions were computed in an exact fashion. Using an efficient algorithm such processes were modeled and compared with success to numerical simulations of the underlying dynamics.

Lagrangian trajectories extracted from a set of DNS of the Navier-Stokes equations were analyzed and their statistical properties were compared to those of the multifractal process. Following a calibration procedure, the statistical properties of the DNS trajectories were reproduced although some discrepancies below the zero-crossing time scale of the acceleration correlation function and the flatness of velocity increments at similar dissipative time scales were observed.

To better understand the observed rapid increase of the flatness in the intermediate dissipative range, and to explore some new types of prediction for the acceleration correlation function, a phenomenological procedure mostly based on the multifractal formalism is recalled and developed. This alternative approach differs from building up a stochastic process, as it was done for u. Instead, it models statistical properties directly such as structure functions. Nonetheless, it allows the derivation of new predictions for the acceleration correlation function and flatness of velocity increments, that reproduce in a very accurate way DNS data. In particular, the theoretically predicted flatness reproduces its rapid increase in the intermediate dissipative range, a phenomenon that is related to the differential action of viscosity depending on the local singular strength of velocity.

Additionally, a second modeling technique for inertial particle statistics based on a filtering approach for the Lagrangian fluid velocity has been proposed. The introduction of an effective particle response time τ_p^* in the linear filter is motivated

by the strong discrepancies in the dynamics of tracer and inertial particles at low Stokes numbers. Both the stochastic and the Batchelor parametrization are capable of reproducing this characteristic feature of inertial particles.

In these methods, using the effective particle response time, the "response of particles to fluid structures" is modified. This has the advantage that the calibration is rather simple in comparison to evaluating fluid quantities on the basis of individual inertial particle trajectories. In principle, in cases where zeroes of the acceleration correlation are inaccessible, a phenomenological parametrization could be implemented through a fit of the variances of acceleration. Therefore, the proposed modeling approach might offer additional diagnostic tools, e.g., for a more accurate determination of integral time scales whose estimation are usually limited by the length of particle trajectories. This benefits the general community of modeling particle dynamics with finite inertia, which facilitates modeling of a greater number of real world applications (i.e., droplets, ash, pathogens)

Chapter 3

Experimental findings of a turbulent round jet

3.1 Introduction

As mentioned in the motivations, the axisymmetric jet lends itself to research due to its known characteristics as the flow becomes fully developed. The interface that materializes between the turbulent and non-turbulent regions of the flow field is of particular interest as it relates to entrainment and ejection of particles. Although more experimentally taxing, these dynamics are innately Lagrangian due to the importance of particle transport processes in the formation of this turbulent/non-turbulent interface (TNTI), therefore the study of such flows from a Lagrangian perspective provides significant advantages to enhance our understanding.

Previous studies of jets have been performed to analyze the TNTI from a Lagrangian perspective. Holzner et al. [2008] analyzed a turbulent/non-turbulent interface realized by an oscillating planar grid, characterizing the enstrophy increase across the interface as a function of viscous diffusion effects. Taveira et al. [2013] used DNS to investigate the TNTI to study the enstrophy production and diffusion. The study found that particles spend more time crossing the region near the interface than traveling inside the turbulent region. An approach by Gervais et al.

[2007] was able to accomplish Eulerian and Lagrangian measurements of a turbulent jet of air at $Re_\lambda \simeq 320$ through acoustic Doppler scattering. This study presents a technique for performing simultaneous Eulerian and Lagrangian measurements in a jet and compares main statistical properties of the flow in each framework. In comparing scales in Eulerian and Lagrangian space, it becomes evident that these scales differ from each other [Gervais et al., 2007]. This could be due to how characteristics of the flow field affect the spatial shape of a coherent structure in a different manner than the temporal evolution of that feature. Additional analysis should be performed to compare these scales and quantify how these discrepancies affect underlying mechanics in a jet. Insight is relevant to fluid transport and dispersion as they relate to large scale dynamics.

Through the study of homogeneous turbulence it is known that the diffusion process of fluid elements can be related to simple Lagrangian statistical properties of the carrier flow. While this connection has been extensively investigated for this idealized flow, in the spirit of Taylor's turbulent diffusion theory [Taylor, 1922], the case of inhomogeneous flows remains largely unexplored, despite an extension of Taylor's theory proposed by Batchelor [1957]. Due its dependence on knowledge of the correlation function (or equivalently the second-order structure function) at all time scales, the empirical determination of the constant C_0 is critical in describing the turbulent diffusion process. Accurate characterization of this constant has implications in modeling of free shear flow, such as volcanic episodes, pollutant dispersion, COVID particle dynamics, etc., with greater accuracy. Such a determination requires accessing accurate inertial range Lagrangian statistics and has received attention in the past two decades in several experimental and numerical

studies [Sawford, 1991, Mordant et al., 2001a, Yeung, 2002, Ouellette et al., 2006c, Toschi and Bodenschatz, 2009] as well as some field measurements in the ocean [Lien et al., 1998]. This leads to a range of C_0 estimates ranging from 2 to 7 (c.f. Lien and D'Asaro [2002] and Toschi and Bodenschatz [2009] for a complete comparison of theoretical, simulated and experimental results). The variability of reported values in literature has been in part attributed to the relatively strong dependence of this constant on Reynolds number [Sawford, 1991, Ouellette et al., 2006c] and to the existence of large scale anisotropy and inhomogeneity [Ouellette et al., 2006c].

3.1.1 Batchelor's extension of theory of turbulent diffusion

Despite this variability of the tabulated values for C_0, the connection between turbulent diffusion and Lagrangian statistics in homogeneous isotropic and stationary turbulence is now well documented. The situation is more complex when it comes to inhomogeneous and anisotropic flows. One strong hypothesis of Taylor's turbulent diffusion theory relies on the statistical Lagrangian stationarity of the particle dynamics, which requires not only a global temporal stationarity of the flow, but also a statistical Eulerian homogeneity: a particle travelling across an inhomogeneous field will indeed experience non-stationary temporal dynamics along its trajectory.

As previously stated, one such inhomogeneous flow field is the turbulent round jet. Although limited Lagrangian experimental campaigns have been carried out [Holzner et al., 2008, Wolf et al., 2012, Kim et al., 2017, Gervais et al., 2007], this type of flow has received much attention in Eulerian studies, as mentioned, due to the fact that turbulence is self-preserving [Corrsin, 1943, Hinze and Zijnen, 1949, Hussein et al., 1994, Weisgraber and Liepmann, 1998]. More specifically, as the

jet develops downstream of the nozzle, the turbulence properties (length, time and velocity scales) evolve in such a way that the Reynolds number remains constant at all downstream positions. Note that such self-similarity generally applies only at sufficiently large downstream positions, typically $z \gtrsim 20D$, with D the nozzle diameter [Pope, 2000].

In 1957, Batchelor proposed an extension of Taylor's stationary diffusion theory to the case of turbulent jets in a Lagrangian framework, exploiting the Eulerian self-similarity property of these flows [Batchelor, 1957]. The approach by Batchelor uses the Eulerian self-similarity to define a *compensated* time step $\mathrm{d}\tilde{\tau}$ and a *compensated* Lagrangian velocity $\tilde{v}(\tilde{\tau})$ which exhibits statistically stationary Lagrangian dynamics.

The idea of this stationarization is to compensate the effect of Eulerian inhomogeneity on the Lagrangian variables to retrieve Lagrangian dynamics which becomes independent of the initial position and statistically stationary and in turn, to generalize results originally established for stationary situations (such as Taylor's theory of turbulent diffusion). Based on the Eulerian self-similarity properties, Batchelor considers the case of the dispersion of particles released at the origin of a turbulent jet, whose Lagrangian dynamics is stationarized by considering the just mentioned compensated variables. Explicitly, through consideration of the velocity at the position $\boldsymbol{x}(\tau)$ reached by the particle at a given time τ since it has been released (at $\tau = 0$ and $\boldsymbol{x} = 0$) as well as the time steps of the flow properties at this position $\boldsymbol{x}(\tau)$:

$$\tilde{v}(\tau) = \frac{v(\tau) - \overline{u}^e(\boldsymbol{x}(\tau))}{\sigma_u(\boldsymbol{x}(\tau))} \quad \text{and} \quad \mathrm{d}\tilde{\tau} = \frac{\mathrm{d}\tau}{T_E(\boldsymbol{x}(\tau))}, \tag{3.1}$$

where $\overline{u}^e(\boldsymbol{x}(\tau))$ represents the local (Eulerian) average velocity at the position $\boldsymbol{x}$ of

the particle at time τ and $T_E(\boldsymbol{x}(\tau))$ the local Eulerian time scale (only one velocity component is considered). Similarly, $\sigma_u(\boldsymbol{x}(\tau))$ is the local (Eulerian) standard deviation of the velocity at the position $\boldsymbol{x}$ of the particle at time τ. The temporal transformation simply rescales the time in order to account for the evolution of the Eulerian background properties as the particle moves downstream in the jet. The transformation of the velocity intends to stationarise the effective dynamics by: (i) subtracting the local average velocity, so that the average of $\tilde{v}$ is zero, and (ii) the denominator $\sigma_u(\boldsymbol{x}(\tau))$ is chosen as a general compensation for the decay of the turbulent fluctuations of the background Eulerian field as the particles moves downstream. Note that the transformations, as they were presented by Batchelor [1957], directly considered the Eulerian power-law dependencies (in space) of $\overline{u}^e$, σ_u and T_E in the self-similar region of the jet near its centerline. The transformations as written in equations (3.1) are therefore more general, although Batchelor's transformations are eventually equivalent if such power-law dependencies are assumed. The more general expression considered here allows one to explore the relevance of the stationarization procedure not only in the centerline of the jet (as done by Batchelor) but to also probe away from the centerline.

As a result of the stationarization procedure, compensated Lagrangian statistics are expected to exhibit similar properties (time scales, correlations, etc.) at any position in the jet and hence at any time along particle trajectories. Batchelor then demonstrates that Taylor's theory can be extended to the stationarized dynamics by connecting the mean square displacement of the particles to $\mathcal{C}_{\tilde{v}}(\tilde{\tau})$, the Lagrangian correlation function of $\tilde{v}(\tilde{\tau})$.

Three important aspects arise regarding Batchelor's diffusion theory: (i) it ex-

tends the Eulerian self-similarity to the Lagrangian framework, with this respect it is often referred to as Lagrangian self-similarity hypothesis [Cermak, 1963], (ii) it connects the turbulent diffusion process of particles in jets to the Lagrangian correlation function (or equivalently to the second-order structure function) of the stationarized velocity statistics and (iii) it proposes a systematic method of analyzing the non-stationary data of the jet.

Largely based on measurements of the mean square displacements of particles [Kennedy and Moody, 1998], only indirect evidence of the validity of Batchelor's hypothesis exists with respect to free jets. Direct Lagrangian measurements which show the stationarity of the compensated velocity correlations are still lacking, as well as the full characterization of the inertial scale Lagrangian dynamics in jets. As previously noted, Lagrangian correlation functions in turbulent round jets have been reported in experiments by Gervais et al. [2007], using acoustic Lagrangian velocimetry [Mordant et al., 2001a], although the question of the Lagrangian self-similarity has not been addressed, neither has the detailed characterization of the inertial range dynamics, the estimation of the related fundamental constants such as C_0, and the relevance of simple Lagrangian stochastic models derived for homogeneous isotropic conditions as considered in the part one of the thesis. It can be noted that the Lagrangian stationarization idea introduced by Batchelor is not limited to the case of the jet. Implications of this characterization could extend to provide a systematic analysis method of more complicated flow fields and in turn enhanced comprehension of the dynamics as they relate to other self-preserving flows [Batchelor, 1957, Cermak, 1963].

3.1.2 Multi-particle diffusion

Another method to study turbulent diffusion in the jet is conducted through analysis of multi-particle dynamics. Pair dispersion has been studied in turbulence for many years, with seminal works by Richardson [1926], Obukhov [1941] and Batchelor [1950]. These studies resulted in the Richardson-Obukhov regime and Batchelor regime for pair dispersion which depend on a relative time step. In this complementary approach to studying diffusion, the local concentration fluctuations are connected to the separation of pairs of fluid elements. The relevancy of the spreading of fluid elements and if they are dependent on initial conditions (i.e., the initial separation of the pairs), is consequential on the decay of concentration fluctuations with applications to biological and chemical systems [Bourgoin et al., 2006]. For example, this is directly related to the ozone destruction rate in our atmosphere [Edouard et al., 1996].

This method also provides an alternative, and sometimes simpler, method to obtain relevant parameters of the flow field, for example, from pair dispersion calculations one can obtain the Eulerian second-order structure functions, and in turn, the energy dissipation of a flow [Berk and Coletti, 2021, Ouellette et al., 2006b]. In addition, pair dispersion has been investigated in detail to better understand how pairs of inertial particles drift in a turbulent flow. Preferential concentrations of particles has long been an area of interest for turbulent flows, where particles are known to either expel from or concentrate towards the cores of vortical structures depending on their Stokes number [Eaton and Fessler, 1994, Bec et al., 2010].

3.2 Theoretical methods

Eulerian second-order structure functions

Recall that in homogeneous isotropic stationary turbulence, K41 theory [Kolmogorov, 1941] predicts for the second-order structure function in the *inertial range*, scales between the Kolmogorov scale, η, and the integral length scale, L, that:

$$S^E_{2-\parallel}(\Delta) = \langle[\delta\tilde{u}_\parallel(\boldsymbol{x},\Delta)]^2\rangle = C_2\frac{(\varepsilon\Delta)^{2/3}}{\sigma^2_{u_\parallel}}. \tag{3.2}$$

Here, the structure function for a given separation, Δ, is expressed with respect to the stationarized Eulerian velocity $\tilde{u}$, with ε the average energy dissipation rate per unit mass and $C_2 \simeq 2.0$ [Pope, 2000]. The $\sigma^2_{u_\parallel}$ denominator (the variance of longitudinal velocity component) has been added here in the right hand term to account for the fact that the stationarized velocity is considered.

Alternatively, the transverse structure function $S^E_{2-\perp}(\Delta)$ can be considered where increments are taken for the velocity components perpendicular to the separation vector. In HIST, within the inertial range, $S^E_{2-\perp}(\Delta)$ follows the same K41 scaling but with a constant $C_{2\perp} = \frac{4}{3}C_2$. Previous studies have found that these relations *a priori* established for HIST, apply reasonably well to the inertial scales of turbulent jets, despite the large scale inhomogeneity and anisotropy (see for instance Romano and Antonia [2001]). Relation (3.2) is used together with the relation $C_{2\perp} = \frac{4}{3}C_2$ to analyze longitudinal and transverse structure functions in the jet.

Within cylindrical coordinates, the longitudinal second-order structure function

is usually estimated based on the axial component of the velocity:

$$S^E_{2-z,\|}(z,\delta z) = \langle[\tilde{u}_z(z+\delta z, r) - \tilde{u}_z(z,r)]^2\rangle, \tag{3.3}$$

with $\tilde{u}_z$ the fluctuating axial velocity (recall that stationarization is applied) and δz the axial distance between the two considered points (the explicit z dependency is kept here to emphasize the streamwise inhomogeneity of the jet centerline statistics). This is, for instance, the quantity typically measured when using hot-wire anemometry (sensitive to the streamwise velocity component) combined with the Taylor frozen field hypothesis.

Lagrangian second-order structure functions

Recall that the application of the known K41 phenomenology for HIST, generally applied to Eulerian inertial scaling, can be extended to the Lagrangian framework [Toschi and Bodenschatz, 2009], where dynamics is investigated as a function of temporal increments along particle trajectories. Namely, for the second-order Lagrangian structure function, this reads (for the stationarized velocity):

$$S^L_{2,i}(\tau) = \langle[\tilde{v}_i(t+\tau) - \tilde{v}_i(t)]^2\rangle = C_{0_i}\frac{\varepsilon_i \tau}{\sigma^2_{u_i}}, \tag{3.4}$$

within the inertial range ($\tau_\eta \ll \tau \ll T_L$), where i denotes a single velocity component (i.e., no summation and i is simply x, y or z, by symmetry, statistics along x and y are identical and equivalent to statistics of the radial r-component of velocity), and T_L is the Lagrangian integral time scale, which is expected to be related to the Eulerian integral time. Note that while for the Eulerian structure functions, spatial

velocity increments were computed between pairs of particles and then averaged, now, for Lagrangian analysis, temporal velocity increments are computed on each individual trajectories before being averaged.

Multiparticle dispersion

Pair dispersion can be classified into three regimes according to the time dependence. Explicitly, there is the Batchelor (ballistic) regime, where the separation, $\boldsymbol{D}(t)$, is dependent on the initial separation and it scales as t^2, followed by the Richardson (super diffusive) regime, which is said to only dependent on the time step and the separation scales as t^3 and finally the diffusion becomes diffusive (i.e., proportional to t) at large time lags. Mathematically this is expressed as:

$$\langle [\boldsymbol{D}(t) - \boldsymbol{D}_0]^2 \rangle = \begin{cases} 11/3 C_2 (\varepsilon D_0)^{2/3} t^2 & t \ll t_0 \\ g\varepsilon t^3 & t_0 \ll t \ll T_L \\ t & T_L \ll t, \end{cases} \tag{3.5}$$

where the initial separation is denoted as $\boldsymbol{D}_0$, C_2 is again the scaling constant for the Eulerian velocity structure function of the second-order and g is a universal constant (Richardson constant). These expressions are time dependent as they pertain to t_0, a characteristic time scale of an eddy of size D_0, defined as $t_0 \propto \varepsilon^{-1/3} D_0^{2/3}$ in the framework of K41.

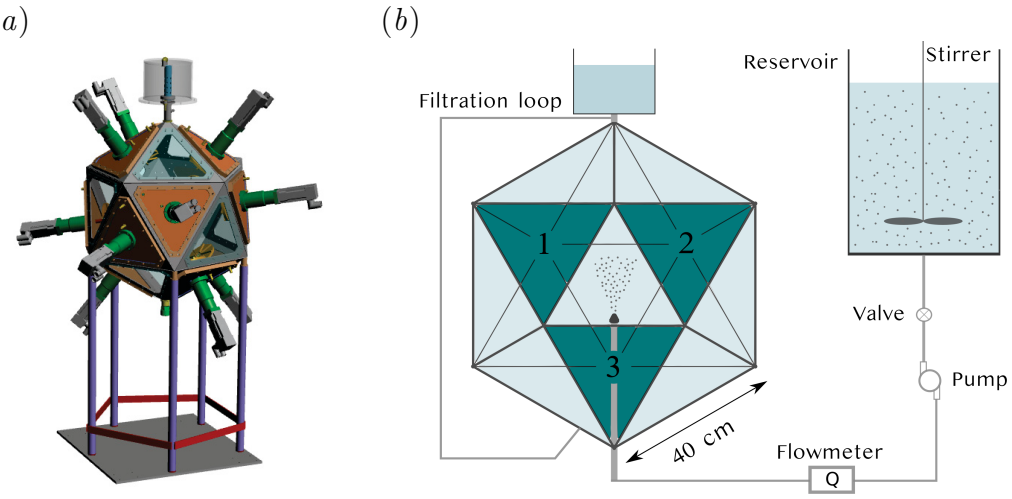

Figure 3.1: (a) Three-dimensional CAD rendering of the Lagrangian Exploration Module. (b) Schematic of the hydraulic setup. Cameras 1, 2 and 3 are oriented orthogonal to the green faces labelled accordingly as 1, 2 and 3.

3.3 Experimental Setup

3.3.1 Hydraulic system

All experiments were performed in the Lagrangian Exploration Module (LEM) [Zimmermann et al., 2010] at École Normale Supérieure de Lyon. A vertically-oriented jet of water is injected into the LEM, a convex regular icosahedral (twenty-faced polyhedron) tank full of water, as seen in figure 3.1(a). The LEM is originally designed to generate homogeneous isotropic turbulence when the twelve propellers on twelve of its faces are activated, however, for this experiment, the LEM is only used as a tank, its optical access makes it an ideal apparatus for three-dimensional particle tracking of a jet.

The hydraulic system setup of the experiments is shown in figure 3.1(b). The vertical jet is ejected from a round nozzle with a diameter $D = 4$ mm from an external reservoir. This allowed for a variety of seeding configurations for the tracer

particles. Specifically, seeding inside the tank only, seeding of both the tank and the jet as well as only seeding of the jet (from the external reservoir alone). For all cases when seeding from the external reservoir, the fluid was stirred to ensure homogeneous seeding of the jet. An overflow valve releases the excess water from the top of the tank at the same rate as injection from the nozzle. Experiments are performed at ambient temperature.

A range of downstream locations are considered by moving the vertical position of the nozzle. Namely, two locations are considered in order to study near-field (NF) and far-field (FF) dynamics, with interrogation volumes spanning from 0 mm $\leq z \leq$ 120 mm ($0 \leq z/D \leq 30$) and 80 mm $\leq z \leq$ 200 mm ($20 \leq z/D \leq 50$), respectively. For both regions, the jet is sufficiently far from the walls of the tank and a free-jet is observed [Hussein et al., 1994].

Particles can be classified into two categories; inertial particles and marked fluid tracers. If particles do not follow the flow, i.e. they have their own dynamics and can affect the flow dynamics, they are referred as inertial. It is the case for too big particles with a different density than the fluid. Both tracer and inertial particles are utilized in the experimental campaign. A comprehensive list of the experimental parameters is presented in Table 3.1. The tracers, made of polystyrene, and inertial particles, glass beads, have corresponding density ratios, ρ_p/ρ_f, of 1.06 and 2.3, where ρ_p is the particle density and ρ_f is the fluid density. As previously mentioned, for the tracers, the seeding was configured to only track fluid of the jet, the ambient water and both fluids (the entire interrogation volume). Only the jet was seeded for all experiments performed with glass beads. Adjustments to the particle diameter of the beads as well as mass loading provided a range of effects of the inertial particles

Tracers:	polystyrene, ρ_p/ρ_f=1.06		
mass loading	particle diameter d_p [μm]	pump speed	seeding configuration
0.1%	250	low	jet
0.1%	250	high	jet
0.05%	250	high	jet
0.1%	250	high	ambient
0.1%	250	high	jet + ambient
Inertial:	glass, ρ_p/ρ_f=2.3		
mass loading	particle diameter d_p [μm]	pump speed	seeding configuration
0.1%	160	high	jet
0.1%	250	low	jet
0.05%	250	high	jet
0.1%	250	high	jet
0.1%	425	high	jet

Table 3.1: Experimental parameters of the jet.

on the jet dynamics. Finally, for both tracers and glass beads, the jet speed was adjusted to probe Reynolds number effects. At the nozzle exit, two flow rates are considered, $Q \simeq 2$ L/min and $Q \simeq 4$ L/min, denoted in Table 3.1 as low and high, respectively.

3.3.2 Optical setup

Three high speed cameras (Phantom V12, Vision Research), mounted with 100 mm macro Zeiss Milvus lenses, are used to track the particles. The optical configuration is shown in figure 3.2. The top and side view present the locations of the three cameras in space and the angles are related to the geometry of an icosahedron. Each camera lens is parallel to its respective window. Also presented in the figure, the interrogation volume is illuminated in a backlight configuration with three 30 cm square LED panels oriented opposite the three cameras. The spatial resolution

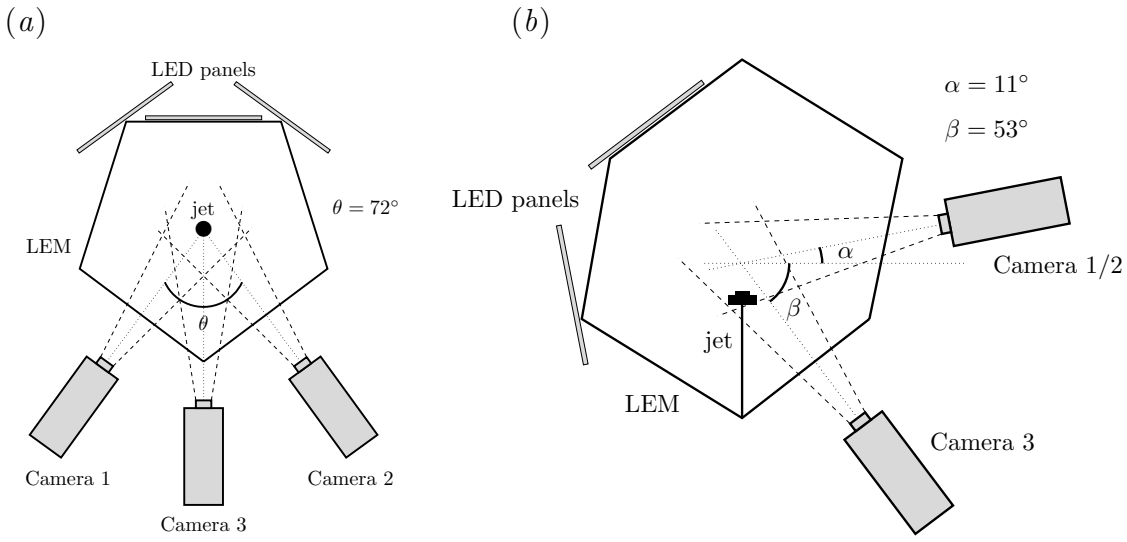

Figure 3.2: Schematic of the optical setup: (a) top view and (b) profile view.

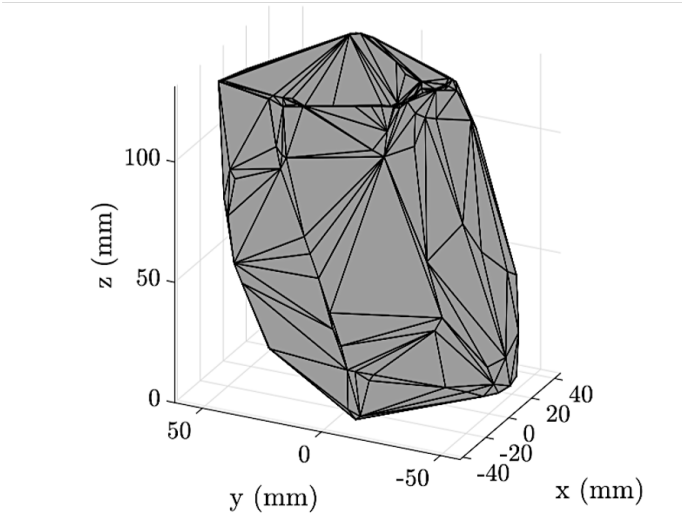

Figure 3.3: Measurement volume captured by the three camera setup for the near-field measurements.

of each camera is 1280×800 pixels, creating a measurement volume of around $80 \times 100 \times 130$ mm^3, hence one pixel corresponds to roughly 0.1 mm. By identifying the locations of all particles within the interrogation volume, the extent of the volume of interest can be visualized, as seen in figure 3.3. This represents the volume attainable for the near-field conditions (a similar convex hull is found for the far-field). The three cameras are synced via TTL triggering at a frequency of 6 kHz for 8000 snapshots, resulting in a total record of nearly 1.3 s. For each nozzle position (NF and FF), a minimum of 50 runs are performed to ensure statistical convergence of ensemble averaging.

3.3.3 Particle Tracking Velocimetry (PTV)

Particle detection

To create particle trajectories through PTV, two-dimensional images are first analyzed to measure the positions of the centers of the particles. The particle detection procedure used in this study is an *ad hoc* process which uses classical methods of image analysis. First a nonuniform illumination correction is applied to the images. This is followed by morphological operations (opening), then thresholding of the intensity permitted, binarization and finally the detection of the centroid. An example of the raw camera image with detected particles is presented in figure 3.4. The inset highlights the accuracy of the post-processed centerfinding scheme that was employed. Here, the particles are well captured within the effective focal range of the camera as seen by the red and blue (inset) tagged particles in the representation.

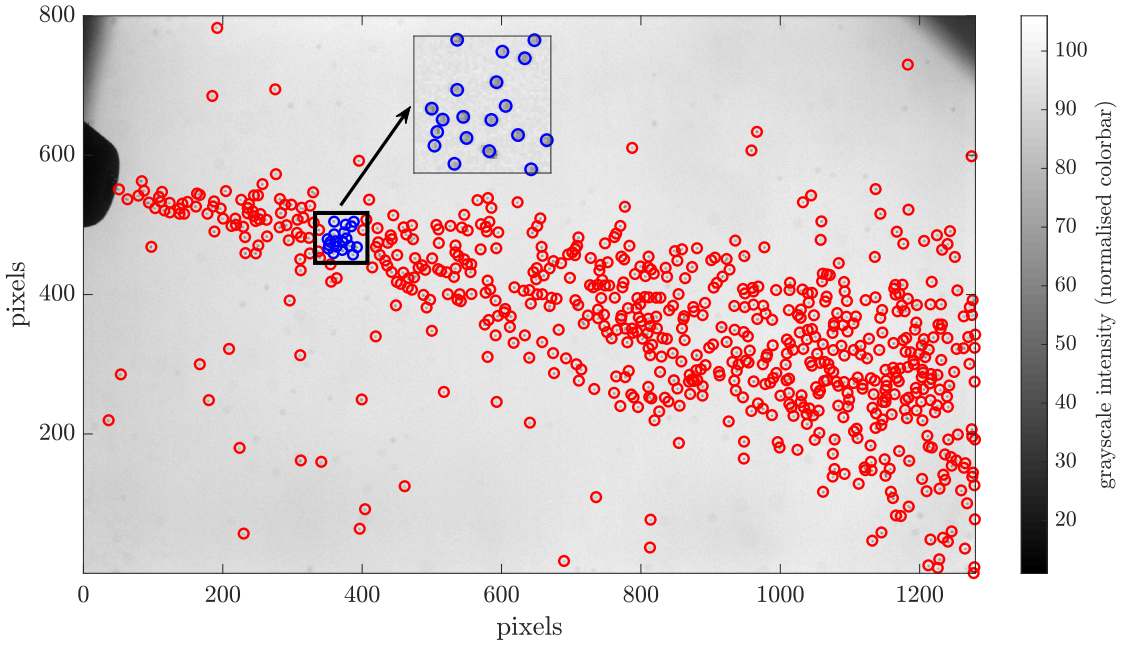

Figure 3.4: Detection of 705 particles on camera 2 in the near-field jet (nozzle in the top left-hand corner). Inset: zoom on the boxed zone.

Stereoscopic reconstruction

After the particle centers for all images and all cameras have been determined, the actual three-dimensional positions of the particles can be reconstructed, knowing that each camera image is a two-dimensional projection of the measurement volume. More typically, methods based on optical models are used to achieve real particle positions, but for this study a geometric method developed by Machicoane et al. [2019] is used due to its increased precision and ease of implementation. This method is based on an initial polynomial calibration, where each position on a camera image corresponds to a line in real space (a line of possible positions in three-dimensional space). The calibration has an accuracy of 1 μm.

The rays for each detected center in the two-dimensional images are computed

based on the calibration then those rays are matched in space for all three camera locations to create a volume of particles in real space. specifically, the intersections of the computed rays give the real particle coordinates. A simple diagram of matching is given in figure 3.5 where the point of intersection represents a perspective match. As a final result, the location of the particles in real space based on the calibration coordinate system (figure 3.6) is obtained. The matching algorithm employed was recently developed by Bourgoin and Huisman [2020].

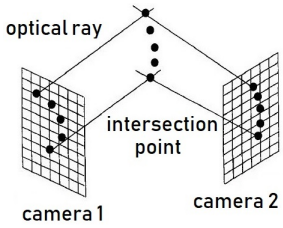

Figure 3.5: Diagram of three-dimensional matching with two cameras (adapted from Guezennec et al. [1994])

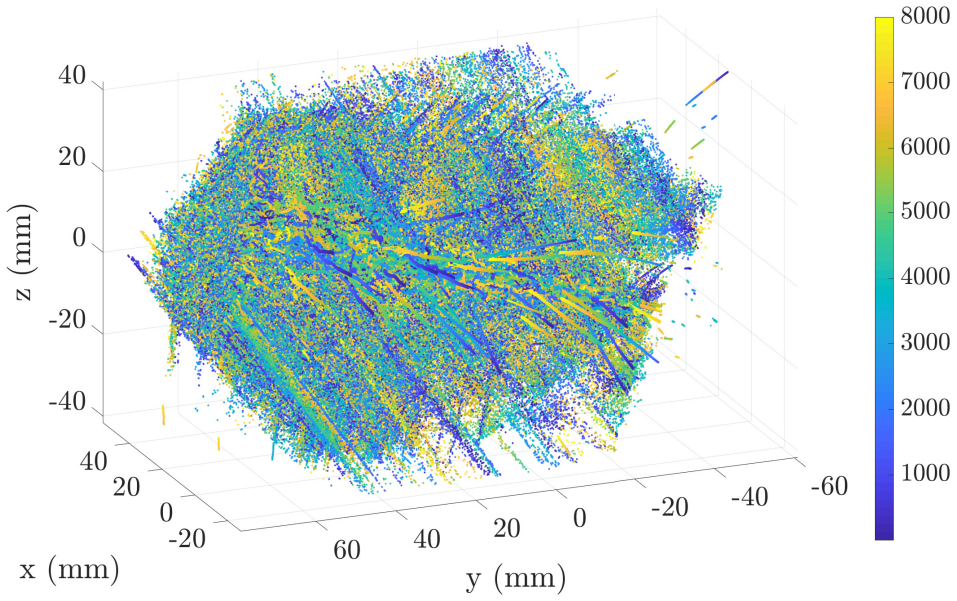

Figure 3.6: Matching of 3,229,762 particles (frame number in colorbar)

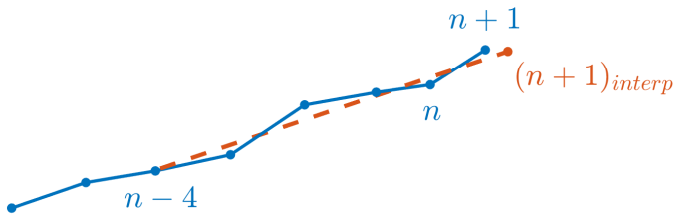

Figure 3.7: Predictive tracking schematic where the solid line signifies the real trajectory and the dotted line indicates the position extrapolation.

To create the largest convex hull possible, dictated by the orientation of the cameras, the particle positions in real space are matched based on the intercept of only two rays (i.e. two cameras) and, to take into account possible overlapping of particles in one dimension, two matches per ray are allowed. Intermediately this allows the inclusion of non-existent "ghost" particles as observed in figure 3.6, where clear rows of these particles are initially captured. Fortunately these "ghost" particles cannot form a trajectory and therefore they are removed when the trajectories are formed in the subsequent steps. The tolerance to allow a match is 50 μm (recall that calibration accuracy is around 1 μm).

Tracking

The stereoscopic reconstruction gives a cloud of points for every time step. The goal of the tracking is to transform this cloud into trajectories by following particles through time. To track the position of a considered particle as it moves among numerous other particles, the simplest algorithm is to consider the nearest neighbor: If one considers a particle in frame n, its position in frame $n+1$ is the nearest particle in frame $n+1$ (c.f. Ouellette et al. [2006a]). But, for increased mass loading of

particles, the trajectories are tangled, as observed in this study. Moreover, several points are "ghost" particles and should not be tracked. Thus an advanced method is employed, namely *predictive tracking*, presented in figure 3.7. The trajectories are assumed to be relatively smooth and self-consistent, i.e. there are no severe variations in velocity and therefore past positions give accurate indications of future positions [Guezennec et al., 1994]. If one considers a particle at frame n, its position in frame $n+1$ can be extrapolated and finally the nearest neighbor approach is employed based on the extrapolated position. For all data presented, the extrapolated position is determined by fitting the previous five positions from frame $n-4$ to n with a simple linear relation (i.e. velocity), as is shown in figure 3.7. If there are less than five positions, the available positions are used. A maximum distance of 1 mm between extrapolated position and real position to continue the trajectories is applied in order to avoid the tracking of absurd trajectories. If the same particle is the nearest neighbor for two different tracks, the nearest trajectory is chosen and the other trajectory is stopped.

3.3.4 Post processing of the trajectories

The tracking of particles results in a set of trajectories for each of the 50 experimental runs. A minimum trajectory length of 10 frames is required to remove presumably false trajectories. Some real trajectories are also removed, but their statistical value is negligible. Finally, the basis is adapted by coinciding the z-axis with the jet axis and centering it in x and y directions. Positions and velocities are computed in adapted cylindrical coordinates (z, r, θ) with z the axial coordinate, r the radial one and θ the circumferential one. A visualization of tracks is shown in figure 3.8. For

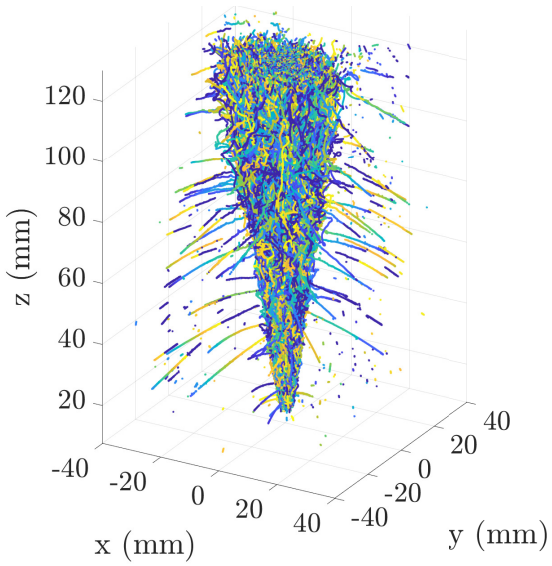

Figure 3.8: 41,032 trajectories longer than or equal to 10 frames (one color per trajectory)

cases when only the jet is seeded, it can be noted that most trajectories come from the nozzle (where they are injected) and very few come from the outside and are entrained in the jet (visible in figure 3.8 as radial trajectories towards the jet).

3.4 Fluid tracer results[1]

Prior to analysis, noise reduction must be considered. The trajectories reconstructed by the tracking algorithm always exhibit some level of noise due to errors eventually accumulated from particle detection, stereo-matching and tracking. It is important to properly handle noise, in particular when it comes to evaluating statistics associated with differentiated quantities (particle velocity and acceleration). Two techniques are implemented to do so. For all Eulerian statistical analysis requir-

[1]Viggiano et al., 2021, Lagrangian diffusion properties of a free shear turbulent jet. *J. Fluid Mech.*, 918:A25

ing the estimate of local velocity, the trajectories are convolved with a first-order derivative Gaussian kernel with a length of 6 time instances and a width of 2 (*ad hoc* smoothing parameters) [Mordant et al., 2004b]. For all two-time Lagrangian statistical analysis (correlation and structure functions), an alternative noise reduction method, presented by Machicoane et al. [2017a,b], is implemented to obtain unbiased statistics based on an estimation from discrete temporal increments of position, without requiring explicit calculation of individual trajectory derivatives. For example, to compute the noiseless Lagrangian two-point correlation of velocity, $\mathcal{C}_{\hat{v}}$, the first-order increments are considered as follows:

$$\mathcal{C}_{dxdx}(\tau, dt) = \mathcal{C}_{\hat{v}}(\tau)dt^2 + \langle (db)^2 \rangle + \mathcal{O}(dt^3), \tag{3.6}$$

where dx is the temporal increment of the signal x over a time dt with $dx = x(t + dt) - x(t) = d\hat{x} + db$. The circumflex signifies the real (noiseless) signal and the noise is denoted as b (assumed to be a white noise). From the presented relationship, the noiseless correlation function of velocity $R^L_{\hat{v}\hat{v}}(\tau)$ can be extracted from the correlation of measured position increments dx, exploring its polynomial dependency with dt at the lowest (quadratic) order and neglecting higher-order terms (i.e. $\mathcal{O}(dt^3)$), by applying a simple polynomial fit of $c_1 dt^2 + c_2$. This method, called "dt-method" in the following, allows the estimation, with increased accuracy and less sensitivity to noise, of statistics of differentiated quantities (and hence to explore small scale mechanisms), without actually requiring estimation of derivatives, but by simply considering position increments at various temporal lags. More information is provided in Machicoane et al. [2017a,b].

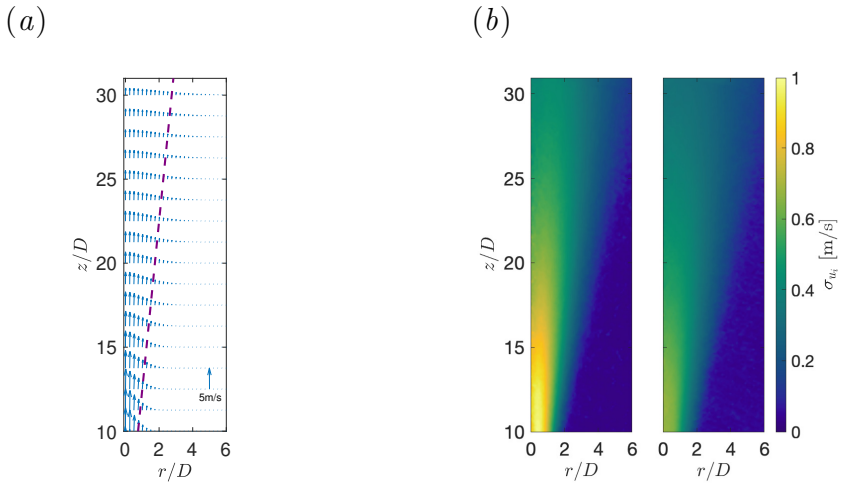

Figure 3.9: (a) Vector field of the $\overline{\boldsymbol{u}}^{\boldsymbol{e}}$ field for the normalized locations, including the half-width of the jet (−−), $r_{1/2}$, at all downstream locations for the near-field. (b) Contour representations of the local standard deviations σ_{u_z} (left) and σ_{u_r} (right) for the axial and radial velocity components for near-field locations.

As noted in the introduction, methods are taken to address the Lagrangian non-stationarity (related to the Eulerian inhomogeneity) of the flow, according to the proposed self-similarity of a turbulent jet by Batchelor [1957], i.e. based on the transformation of the Lagrangian velocity and time scales of a particle at a given time τ after it has been released from a point source. Equation (3.1) provides a relationship to achieve proper stationarization. For this study, the fluctuating stationarized velocity is obtained by subtracting the local Eulerian velocity (and assuming cylindrical symmetry of the jet, hence neglecting the θ dependence on spatially averaged quantities), $\overline{u}_i^e(z,r)$, and scaled by the local standard deviation, $\sigma_{u_i}(z,r)$. Explicitly,

$$\tilde{v}_i(\tau) = \frac{v_i(\tau) - \overline{u}_i^e(\boldsymbol{x}(\tau))}{\sigma_{u_i}(\boldsymbol{x}(\tau))} = \frac{v_i(\tau) - \overline{u}_i^e(z,r)}{\sigma_{u_i}(z,r)}. \tag{3.7}$$

The local standard deviation is an optimal choice for compensation as it generalizes the methods presented in Batchelor [1957], where a specific decay rate (Batchelor assumed a power-law) is required for stationarization. This velocity $\tilde{v}$ takes the mean drift and decay into account although the term becomes dimensionless as a result. For this reason, for all statistical calculations of dimensional quantities (such as the turbulent dissipation rate) inferred from this analysis, velocity is redimensionalized through multiplication with the average local standard deviation within the considered measurement region or location. For transparency, the Eulerian mean and standard deviation velocity fields used for the stationarization are presented in figure 3.9 (figure 3.9(a) the mean velocity as a vector field and figure 3.9(b) the standard deviation of the axial and radial velocity components). The half-width of the jet, $r_{1/2}(z)$, where $\overline{u}_z^e(z, r = r_{1/2}(z)) = \frac{1}{2}\overline{u}_z^e(z, r = 0)$, is included in the Eulerian mean velocity field as the dashed line to provide clarity to the sampling methods based on this quantity, as discussed in sections 3.4.1 and 3.4.2. Note that Lagrangian velocity components are used for the Eulerian statistical characterization therefore the stationarization technique described is required for all analyses presented in the study.

3.4.1 Eulerian velocity statistical analysis

This section aims to extract flow parameters such as length scales and energy dissipation rate from different Eulerian statistics: Second-order structure functions and two-point correlation functions. The jet flow is inhomogeneous, therefore these quantities depend on z and r. Focus is placed on centerline statistics for the Eulerian characterization of the jet, limited to radial distances up to $r_{1/2}$ and consideration

of only the z-axis evolution is used to characterize the main property of the base turbulence.

Eulerian second-order structure functions

To explore the streamwise evolution of Eulerian properties of the jet, a set of data (particle velocities) is considered for a given z position, which falls within a short cylinder (*disk*), $\mathcal{D}_z$, of limited height (0.5 mm in the z-direction) and a radius of $r_{1/2}(z)$ for statistical analysis, see figure 3.10. The disk radius is chosen to include sufficient particles for statistical convergence but, in being limited to the half-width, the volume does not encompass particles from the turbulent/non-turbulent interface. This gives a canonical description of turbulent properties representative of the centerline of the jet. Consideration of statistics in a thin disk allows the more detailed exploration of z dependence of statistical quantities, however this sampling technique forbids exploration of δz values over a range relevant to estimate $S^E_{2-z,\parallel}(z,\delta z)$ at inertial scales. To overcome this issue, two strategies are considered: (i) Still based on the axial z-component of the velocity, $S^E_{2-z,\perp}(z,\delta r)$, the transverse structure function of $\tilde{u}_z$ (with the separation vector $\boldsymbol{\delta r}$ taken within the plane of the disk) is estimated in lieu of $S^E_{2-z,\parallel}(z,\delta z)$; (ii) For radial velocities, the longitudinal structure function is considered through use of the velocity components perpendicular to the z-axis (i.e. within the sampling disk $\mathcal{D}_z$), projected onto the increment vector $\boldsymbol{\delta r}$ within the disk $\mathcal{D}_z$. This is denoted as $S^E_{2-r\theta,\parallel}(z,\delta r)$ (where the subscript $r\theta$ recalls that only velocity components perpendicular to z are considered). For any redimensionalization of a Eulerian quantity, the averaged standard deviation within a respective disk, $\langle\sigma_{u_i}\rangle_{\mathcal{D}_z}$, is employed. For brevity this is herein denoted as σ_{u_i} for

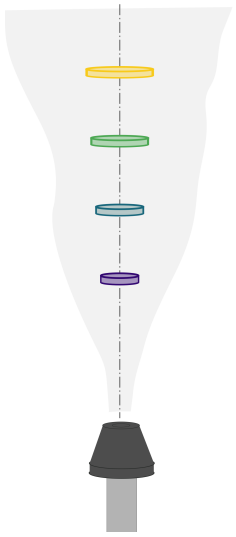

Figure 3.10: Schematic of the downstream locations of the disks, $\mathcal{D}_z$, for Eulerian analysis (not to scale).

all Eulerian calculations.

The discussions of this subsection (and in the two following) illustrate the extraction of the main Eulerian turbulent properties (and of their streamwise evolution) based on $S^E_{2-z,\perp}(z,\delta r)$. The same analysis was also repeated based on $S^E_{2-r\theta,\parallel}(z,\delta r)$. Analysis follows the same recipe as is described for $S^E_{2-z,\perp}(\delta r)$.

The transverse structure function based on the Eulerian stationarized axial velocity, $\tilde{u}_z$, at a given z position is estimated as

$$S^E_{2-z,\perp}(z,\delta r) = \langle [\tilde{u}_z(\boldsymbol{r}+\boldsymbol{\delta r}) - \tilde{u}_z(\boldsymbol{r})]^2 \rangle_{\mathcal{D}_z}, \tag{3.8}$$

where the average is taken over pairs of particles within the disk $\mathcal{D}_z$ separated by a vector $\boldsymbol{\delta r}$. Note that, given the reduced height of the disk (not exceeding two particle diameters), $\boldsymbol{\delta r}$ is within an acceptable approximation perpendicular to the z axis,

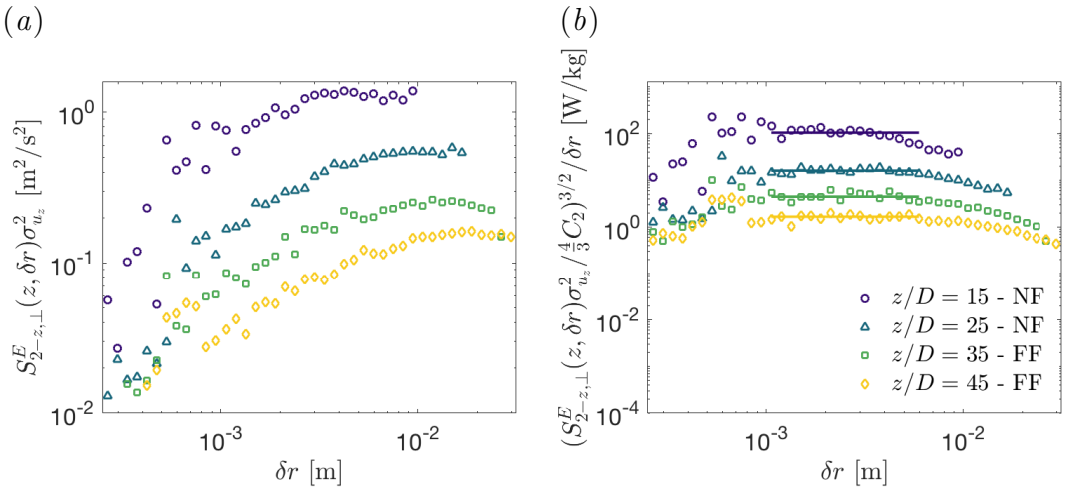

Figure 3.11: Eulerian second-order structure functions of the axial velocity on the axis, (a) uncompensated $S^E_{2-z,\perp}(z,\delta r)\sigma^2_{u_z}$ and (b) compensated $(S^E_{2-z,\perp}(z,\delta r)\sigma^2_{u_z}/\frac{4}{3}C_2)^{3/2}/\delta r$ (the solid lines are the plateaus to extract ε_z), for the four denoted downstream locations.

ensuring that equation (3.8) indeed corresponds to a transverse structure function (except maybe for the smallest separations, comparable to the disk height).

$S^E_{2-z,\perp}(z,\delta r)$ is computed for different z positions (in the near and far-fields of the jet) and shown in figure 3.11(a). While the stationarized (hence dimensionless) velocity is used for all estimates, $S^E_{2-z,\perp}$ is made dimensional by multiplying it by the square of σ_{u_z}, the standard deviation of u_z within $\mathcal{D}_z$ (see Table 3.2). This redimensionalization is required in order to extract the dimensional value of ε, and the associated derived parameters (in particular the dissipation scales and Taylor micro-scale). To this end, figure 3.11(b) includes the compensated structure function $(S^E_{2-z,\perp}(z,\delta r)\sigma^2_{u_z}/\frac{4}{3}C_2)^{3/2}/\delta r$ (measurements by Romano and Antonia [2001] suggest that at despite the large scale anisotropy, the isotropic relation $C_{2\perp} = \frac{4}{3}C_2$ applies reasonably well for the inertial scale dynamics of the jet). Well defined plateaus, corresponding to inertial range dynamics, are observed from which the dissipation

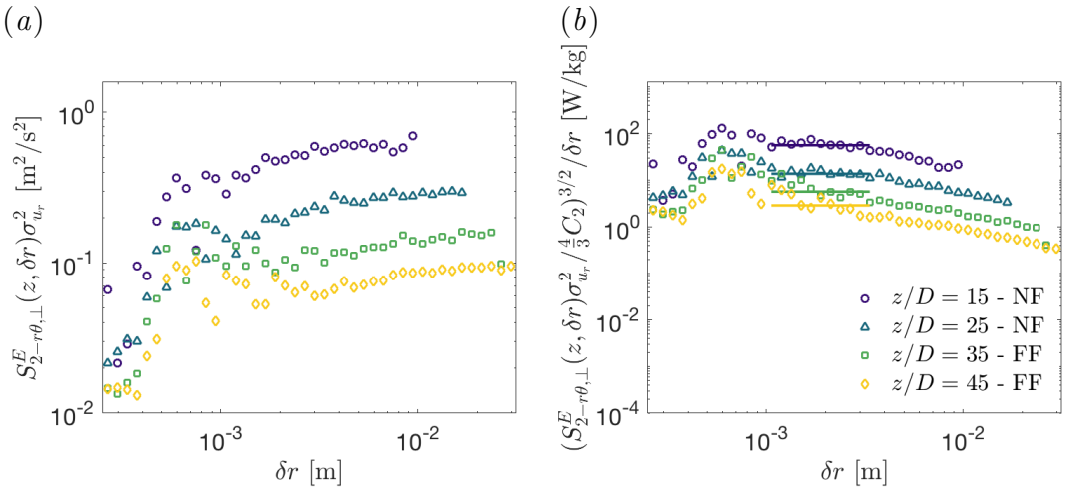

Figure 3.12: Eulerian second-order structure functions of the radial velocity on the axis, (a) uncompensated $S^E_{2-r\theta,\perp}(z,\delta r)\sigma^2_{u_r}$ and (b) compensated $(S^E_{2-r\theta,\perp}(z,\delta r)\sigma^2_{u_r}/\frac{4}{3}C_2)^{3/2}/\delta r$ (the solid lines are the plateaus to extract $\varepsilon_{r\theta}$), for the four denoted downstream locations.

rate ε_z can be extracted according to equation (3.2). The subscript z in ε_z simply refers to the fact that this estimate is based on the axial component of the velocity. It can be seen that, as the location downstream increases, the plateau of the second-order structure function (and hence ε_z) decreases, due to the streamwise decay of turbulence along the jet.

Figure 3.12 presents the uncompensated (a) and uncompensated (b) Eulerian structure functions of the radial component of velocity. Larger scales are observed and noise is present within the small scales. From the plateaus of $(S^E_{2-r\theta,\perp}(z,\delta r)\sigma^2_{u_r}/\frac{4}{3}C_2)^{3/2}/\delta r$, the radial-based dissipation rate is found. Here the plateaus from figure 3.12(b) show a similar trend to those observed in the axial structure functions although the first plateau corresponds to a lower initial dissipation rate.

It is noted that small scales (typically for $\delta r < 1 \times 10^{-3}$ m) are not statistically

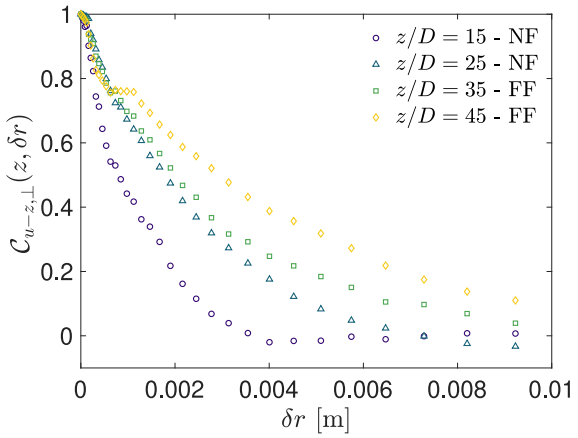

Figure 3.13: Normalized two-point spatial correlation of the Eulerian axial velocity on the axis, $\mathcal{C}_{u-z,\perp}(z,\delta r) = 1 - S^E_{2-z,\perp}(z,\delta r)/2$.

well converged. This is due to the lack of statistics for pairs of particles with very small separation due to the moderate seeding of particles used for the Lagrangian tracking.

Eulerian two-point correlation functions

The second-order Eulerian statistics shown in the previous section from the structure functions can be equivalently investigated in terms of the two-point correlation function. The correlation of axial velocity is obtained via the non-dimensional second-order structure function, $\mathcal{C}_{u-z,\perp}(z,\delta r) = 1 - S^E_{2-z,\perp}(z,\delta r)/2$, to depict the evolution of the velocity interactions through space. The results from the near-field and far-field are presented in figure 3.13. The curves are ordered depending on their downstream location z. The location nearest the jet exit, $z/D = 15$, exhibits a rapid decorrelation. As the flow advances downstream, the turbulent length scales grow, resulting in a dynamics which remains correlated over longer distances, as seen by the $z/D = 45$ profile. This trend can be investigated

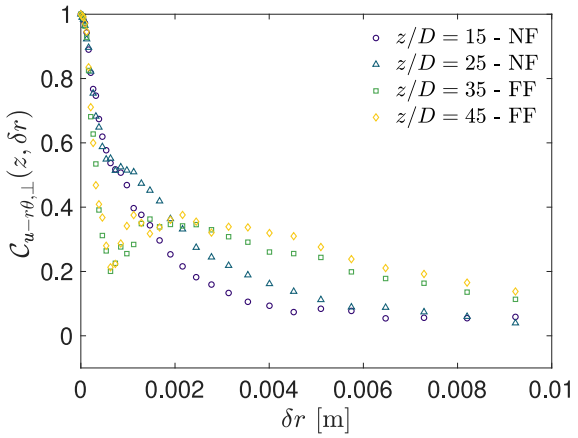

Figure 3.14: Normalized two-point spatial correlation of the Eulerian radial velocity on the axis, $\mathcal{C}_{u-r\theta,\perp}(z,\delta r) = 1 - S^E_{2-r\theta,\perp}(z,\delta r)/2$.

quantitatively using the Eulerian correlation length (or Eulerian integral scale) $L_{E_{z,\perp}}(z) = \int_0^\infty \mathcal{C}_{u-z,\perp}(z,\delta r)\,\mathrm{d}\delta r$. Recall that transverse and longitudinal correlation lengths are kinematically related in HIST by $L_{E_{z,\parallel}} = 2L_{E_{z,\perp}}$ [Pope, 2000]. Since most studies in the literature refer to the longitudinal length, the present study will then consider $L_{E_z}(z) = 2\int_0^\infty \mathcal{C}_{u-z,\perp}(z,\delta r)\,\mathrm{d}\delta r$, avoiding the $\perp$ or $\parallel$ subscripts. However, it is noted that measurements by Burattini et al. [2005] suggest that the ratio may actually be slightly lower than 2, and closer to 1.8 in free shearing jets due to large scale anisotropy.

Similar to the axial component, the radial correlation functions are obtained for the stationarized velocity and results are provided in figure 3.14. Here, noise is observed at the very small scales but the curves exhibit trends similar to those observed in the axial velocity two-time correlations with respect to downstream dependency.

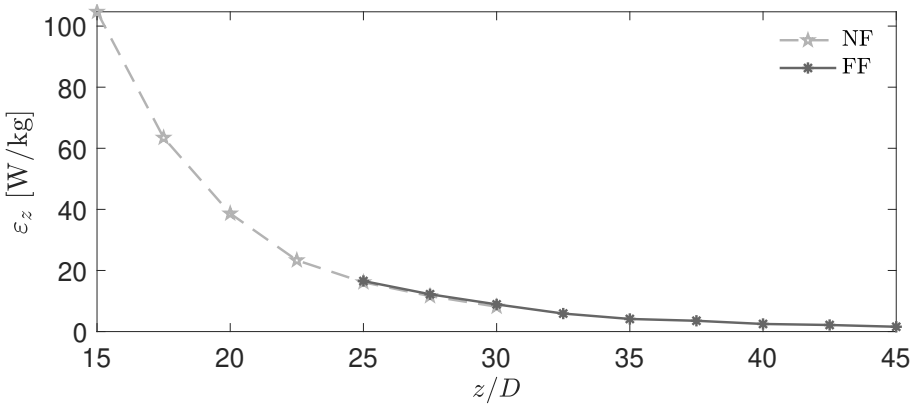

Figure 3.15: Evolution of ε_z along the jet axis.

Evolution of Eulerian parameters

The evolution of ε_z, estimated from the plateaus of the compensated second-order structure functions (figure 3.11(b)), is represented in figure 3.15. There exists a tendency of $1/z^4$ (more clearly visible in figure 3.16(c)), as expected for canonical self-similar jets. The observed consistency in the values and shape of the profiles between the near and far-field experimental locations, validates the presented ε_z values from the independent measurements carried over the overlapping region.

From the dissipation rate ε_z, other relevant parameters of the flow field can be extracted, namely the Kolmogorov time scale, $\tau_{\eta_z} = (\nu/\varepsilon_z)^{1/2}$, and length scale, $\eta_z = (\nu^3/\varepsilon_z)^{1/4}$, as well as the Taylor microscale, $\lambda_z = (15\nu\sigma_{u_z}^2/\varepsilon_z)^{1/2}$, and the Taylor-based Reynolds number $Re_\lambda = \sigma_{u_z}\lambda_z/\nu$, both of which assume HIST. Further, large length and time scales are obtain from the two-point correlation profiles in figure 3.13. For a more accurate estimate of the correlation length, $L_{E_z}(z)$, the integral of the correlation functions is based on a fit of the curves shown in figure 3.13 using a Batchelor type parametrization [Lohse and Müller-Groeling, 1995]. Recall that the factor 2 is the HIST correction that relates the transverse correlation (given

z/D	σ_{u_z} [m/s]	ε_z [W/kg]	η_z [µm]	τ_{η_z} [ms]	λ_z [µm]	Re_λ	L_{E_z} [mm]	T_{E_z} [ms]
15	0.80	104.7	9.9	0.098	304	245	2.2	2.8
25	0.51	16.1	15.8	0.249	491	250	4.4	8.6
35	0.35	4.5	21.7	0.472	643	226	5.6	16.0
45	0.28	1.7	27.8	0.774	825	227	7.8	28.2

z/D	σ_{u_r} [m/s]	$\varepsilon_{r\theta}$ [W/kg]	$L_{E_{r\theta}}$ [mm]	$T_{E_{r\theta}}$ [ms]
15	0.57	63.9	1.7	2.9
25	0.38	14.6	2.0	5.3
35	0.28	5.7	3.6	13.0
45	0.22	2.4	5.1	23.2

Table 3.2: Eulerian parameters of the jet on the axis for different z/D positions.

by the integral of $\mathcal{C}_{u-z,\perp}$) to the longitudinal one. The calculated L_{E_z} shall therefore be interpreted as the longitudinal integral scale associated with the z component of velocity. The integral time scale is then computed as $T_{E_z} = L_{E_z}/\sigma_{u_z}$. All relevant quantities of the jet have been accumulated for the considered streamwise locations in Table 3.2. The streamwise evolution for the velocity standard deviation, dissipation rate and integral scale are also shown in figure 3.16, where the well known self-similar power-law profiles can be seen.

The characterization of basic Eulerian properties from the radial components of velocity are also included in Table 3.2 to quantify anisotropy. The dissipation rate for the radial velocity is lower than the axial component near the exit of the jet, but declines more slowly as the jet develops, resulting in similar values for $\varepsilon_{r\theta}$ and ε_z at $z/D > 25$. As a result, in this region dissipation scales are found almost identical with both estimates. This supports the idea that small and inertial scales are nearly isotropic. The large scales show however a certain degree of anisotropy,

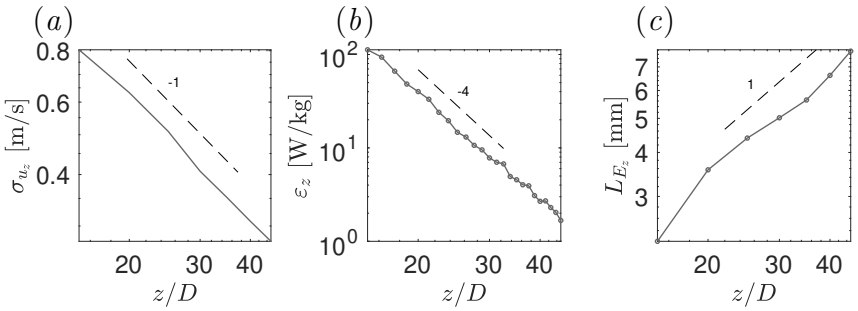

Figure 3.16: (a) The standard deviation averaged within the disk $\mathcal{D}_z$, (b) the dissipation rate and (c) the integral length scale for the axial component of velocity for all downstream locations. Power-law relation is given as a dashed line.

in particular regarding the integral length scale and in a lesser degree the integral time scale which are found larger for the z-component than for the $r\theta$-components.

3.4.2 Lagrangian velocity statistical analysis

In this section the Lagrangian statistics of the jet tracer dynamics are investigated with a particular focus on second-order statistics (namely velocity second-order structure function and two-point correlation function), which are key ingredients to model turbulent diffusion, as discussed in the introduction. In particular, the relevance of Batchelor's Lagrangian self-similar stationarization idea is further assessed.

Lagrangian second-order structure functions

Recall that in lieu of Gaussian filtering previously applied to the Eulerian structure functions, the dt-method presented in section 3.3.4 is implemented, which has been shown to better handle noise for Lagrangian velocity statistics estimates [Machicoane et al., 2017a].

The trajectory length now becomes important and therefore, for all Lagrangian statistics presented in this section, methods are implemented to acquire sufficient convergence of statistics. Explicitly, for each location z, the ensemble selected for the Lagrangian statistics consists of all trajectories passing through a small sphere, $\mathcal{S}_z$, centered at downstream position z along the jet centerline, with a radius of $r_{1/2}(z)/3$, see figure 3.17. This volume allows sufficient particles for convergence of statistics yet does not overlap in the axial direction as the half-width increases. Similar to methods presented in the Eulerian framework, the averaged standard deviation from within each respective sphere, $\langle \sigma_{u_i} \rangle_{\mathcal{S}_z}$, is used for redimensionalization of Lagrangian quantities when necessary (for calculation of C_0) and denoted simply as σ_{u_i}. Figure 3.18(a) presents the corresponding curves for $S^L_{2-z}(\tau)$ at the four different downstream locations. All curves exhibit a transition from a dissipative behavior at small time lags (where $S^L_{2-z} \propto \tau^2$) to the inertial range (where $S^L_{2-z} \propto \tau$). The main figure shows the structure function in stationarized variables, while the inset provides the same data but non-stationarized. Several interesting points emerge:

(i) **Effect of stationarization at inertial scales:** The non-stationarized statistics (inset of figure 3.18(a) are widely spread while the stationarized statistics (main figure) collapse reasonably well, in particular in the far-field ($z/D > 25$). Similarity between the curves is improved for the inertial range dynamics (which presents similar trends even at distances $z/D \gtrsim 20$), but less adequate for the small scale dissipative dynamics, for which the collapse becomes reasonable only at far downstream locations ($z/D > 35$). This suggests that the stationarization procedure is efficient to retrieve self-similar inertial range Lagrangian statistics in the far-field

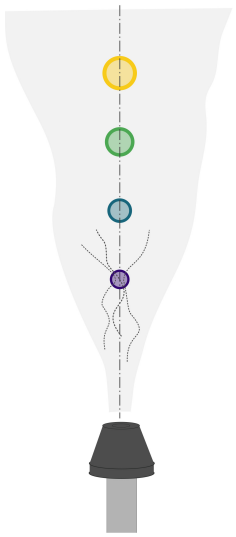

Figure 3.17: Schematic of the downstream locations of the spheres, $\mathcal{S}_z$, for Lagrangian analysis (not to scale).

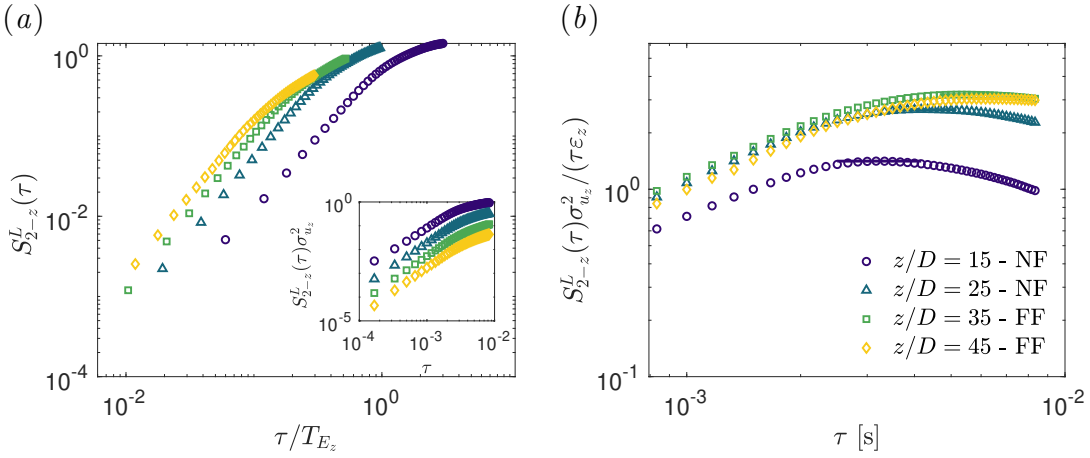

Figure 3.18: Lagrangian second-order structure functions of the axial velocity on the axis, estimated at four downstream locations ($z/D = 15$, 25, 35, and 45). (a) Non-dimensional $S^L_{2-z}(\tau)$ as a function of the non-dimensional time τ/T_{E_z} (dimensional $S^L_{2-z}(\tau)\sigma^2_{u_z}$ as a function of time τ in inset) and (b) compensated $S^L_{2-z}(\tau)\sigma^2_{u_z}/(\tau\varepsilon_z)$, for the denoted downstream locations. The universal scaling constant, C_{0_z}, can be extracted from the plateau of the compensated structure functions.

(in Batchelor's sense, meaning that Lagrangian statistics become independent of the downstream position as particles travel along the jet), while discrepancies remain in the small scales until the very far-field.

(ii) **Small scale dynamics discrepancies:** In the Lagrangian framework, the small scale dynamics of structure functions is associated with particle acceleration statistics. Figure 3.18(a) therefore suggests that stationarized acceleration statistics eventually fall in line, but only in the very far-field (curves at $z/D = 40$ and 45 almost perfectly collapse). As will be observed in section 3.4.3, acceleration statistics are strongly affected by the finite size of the particles, which in our study remains much larger than the dissipation scale of the flow ($d_p/\eta = 25$ at $z/D = 15$ and 9 at $z/D = 45$). Although further investigation focusing specifically on the small scale dynamics would be required, it is probable that the observed discrepancy at small scales reflects these finite size effects. This is supported by the fact that as considered positions are farther downstream (where d_p/η gets smaller and hence finite particle size effects disappear), the stationarized acceleration dynamics seems to better converge to a single curve.

(iii) **Large scale dynamics:** By construction, the second-order structure function of the stationarized velocity should reach, in the large scales, an asymptotic constant value of 2 as the Lagrangian dynamics becomes fully decorrelated. This asymptotic regime is not reached in our data, where S_2^L reaches at best values of order 1, without exhibiting an asymptotic decorrelated plateau. This is due to the lack of statistics for long trajectories. One of the well-known difficulties of Lagrangian diagnosis is indeed the capacity to obtain sufficiently long trajectories allowing to explore the large scale dynamics. In the present study, most trajectories are efficiently tracked

over a few tens of frames at most (very few are over hundreds of frames). At the operating repetition rate of 6000 frames per second, this corresponds to trajectories at most 10 ms long, what represents (according to Table 3.2) a few Eulerian integral times scales in the near-field, and only a fraction of this integral scale in the far-field, where only a part of the inertial range dynamics is accessible. In subsection 3.4.2, it is demonstrated that large scale behavior (and the effect of stationarization on it), can still be addressed by estimating the Lagrangian correlation time scales.

(iv) **Estimate of C_0 constant:** Figure 3.18(b) shows the compensated structure functions, $S^L_{2-z}(\tau)\sigma^2_{u_z}/(\tau\varepsilon_z)$, built with ε_z values found in the Eulerian analysis (for consistency regarding possible anisotropy effects, the estimate of dissipation rate based on Eulerian statistics of corresponding components is used). Based on relation (3.4), within the inertial range the value of C_{0_z} can be extracted from the plateau of the curves. The value of the plateau is observed to saturate, as considered positions reach farther towards the far-field, at a value of $C_{0_z} \simeq 3.2$. The downstream evolution of C_{0_z} will be further discussed in the coming sections.

All observations also apply to estimates of S^L_{2-r}, based on the radial component of velocity with the curves of the Lagrangian structure functions presented in figure 3.19. Here the velocity and time lag are stationarized, figure 3.19(a) and the inset provides dimensional representations of $S^L_{2-z}(\tau)\sigma^2_{u_r}$. The compensated structure function, figure 3.19(b) is included to extract the constant C_{0_r} from the plateaus of the curves. This quantity is compared with the axial C_{0_z} for insight into anisotropy.

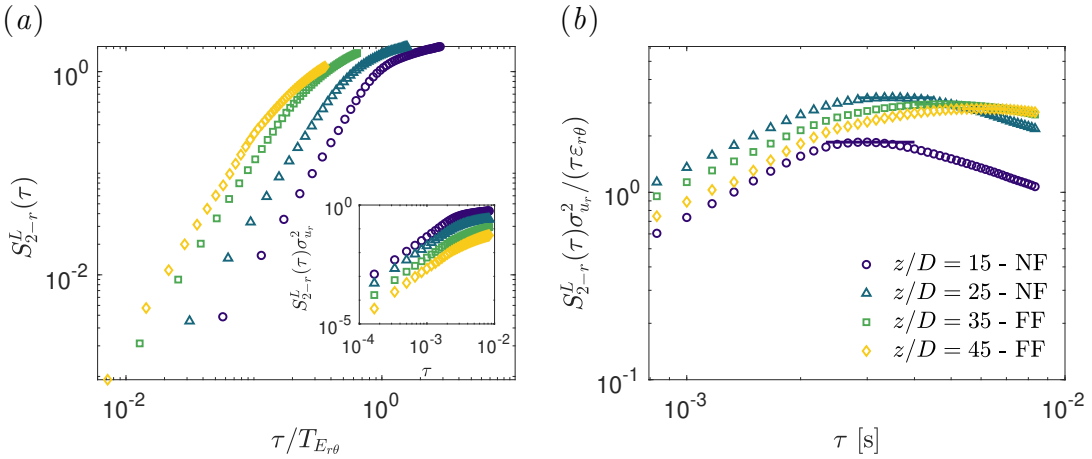

Figure 3.19: Lagrangian second-order structure functions of the radial velocity on the axis, estimated at four downstream locations ($z/D = 15$, 25, 35, and 45). (a) Non-dimensional $S^L_{2-z}(\tau)$ as a function of the non-dimensional time $\tau/T_{E_r\theta}$ (dimensional $S^L_{2-r}(\tau)\sigma^2_{u_r}$ as a function of time τ in inset) and (b) compensated $S^L_{2-r}(\tau)\sigma^2_{u_r}/(\tau\varepsilon_{r\theta})$, for the denoted downstream locations. The universal scaling constant, C_{0_z}, can be extracted from the plateau of the compensated structure functions.

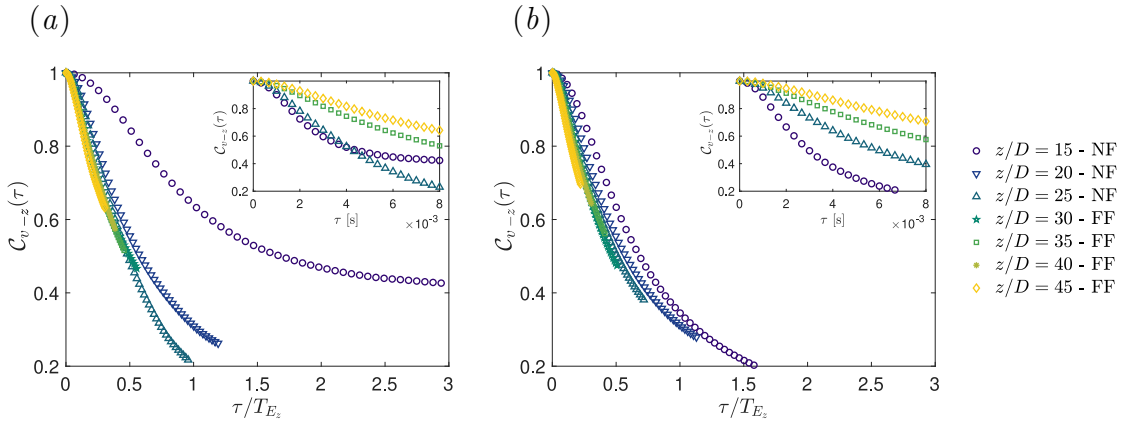

Figure 3.20: Normalized Lagrangian correlation of the axial velocity for the compensated time lag τ/T_{E_z}. Inset provides the Lagrangian correlation as a function of the dimensional time lag τ for the same seven downstream locations previously considered. Locations are (a) along the centerline ($r = 0$) and (b) at the jet half-width ($r = r_{1/2}$) for all downstream positions.

Lagrangian two-point correlation functions

The two-point correlation functions of the Lagrangian axial velocity as a function of the compensated time lag, τ/T_{E_z}, are presented in figure 3.20(a) where $\mathcal{C}_{v-z}(\tau) = \langle \tilde{v}_z(t+\tau)\tilde{v}_z(t)\rangle$. It can be seen that, as for the structure functions previously discussed, the stationarization results in a remarkable collapse of the correlation functions, in particular at $z/D > 20$. Note that the small scale discrepancy observed for S^L_{2-z} is also expected to be present for the correlation function, which carries essentially the same information; it is however less emphasized due to the linear (rather than logarithmic) scale used to represent the correlation function. The observed agreement between the two-point correlation functions confirms again the Lagrangian self-similarity hypothesis at inertial scales, resulting in two-point correlation functions of the stationarized variables which do not depend on the downstream position of the particles as they evolve along the jet (beyond $z/D \gtrsim 20$).

Although the shortness of the trajectories does not allow to directly explore the large scale, fully decorrelated, regime (where $\mathcal{C}_{v,i}$ vanishes), the observed collapse at intermediate scales allows speculation that the self-similarity hypothesis may also extend to the large scales. This would lead, in particular, to a univocal relation between the Lagrangian correlation time (defined as $T_{L_i} = \int_0^\infty \mathcal{C}_{v,i}(\tau)\,\mathrm{d}\tau$) and the Eulerian timescale at all positions along the jet (except in the very near-field, where Lagrangian two-point correlation clearly deviates). This point will be further tested in the subsequent section where we estimate T_L based on appropriate fits (exponential or double exponential [Sawford, 1991]) of the Lagrangian two-point correlation, supporting the validity of self-similarity in the large scales and the univocal link between T_L and T_E.

A test of the Lagrangian self-similarity hypothesis when off-axis dynamics is considered is provided in figure 3.20(b). The original stationarization proposed by Batchelor [1957] used centerline power-laws for a self-similar jet to compensate the Lagrangian velocity and time. As discussed, these formulas have been generalized (compatible with Batchelor's approach in the centerline), using actual local measurements of Eulerian properties rather than prescribed centerline power-laws. The stationarization transformations can therefore be applied at any arbitrary position along particle trajectories. Figure 3.20(b) explores the application of the proposed stationarization considering trajectories passing through a ball centered off-axis, at a radial location of $r = r_{1/2}(z)$, instead of $r = 0$. As for the centerline analysis, the correlation functions of the stationarized variables collapse for all locations $z/D > 20$. This substantiates the generalized stationarization technique, and its application to locations beyond the centerline. Although the present study focus on diffusion of particles near the jet centerline, this result motivates future dedicated studies to explore more deeply the generalized Lagrangian stationarization for off-axis statistics as well as for other inhomogeneous flows (such as von Kármán flows, which are widely used for Lagrangian studies of turbulence).

Finally, for completeness, the stationarized radial correlation of velocity is shown as a function of the stationarized time lag in figure 3.21. The collapse seen by all profiles (expect the nearest location) is indicative of the validity of the stationarization methods. The dimensionalized functions are provided in the inset.

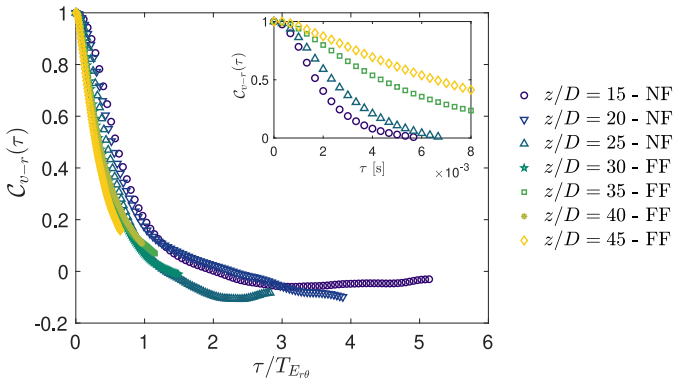

Figure 3.21: Normalized Lagrangian correlation of the radial velocity along the centerline for the compensated time lag $\tau/T_{E_r\theta}$. Inset provides the Lagrangian correlation as a function of the dimensional time lag τ. Downstream locations denoted in the legend.

z/D	C_{0_z}	T_{L_z} [ms]	T_{E_z}/T_{L_z}	C_{0_r}	T_{L_r} [ms]	$T_{E_{r\theta}}/T_{L_r}$
15	1.4	4.5	0.6	1.9	1.4	2.1
25	2.7	5.3	1.6	3.2	2.3	2.3
35	3.2	11.1	1.5	3.0	5.3	2.5
45	3.0	15.9	1.8	2.8	8.9	2.6

Table 3.3: Lagrangian parameters of the jet on the axis for different z/D positions.

Evolution of Lagrangian parameters

This subsection provides the estimates of C_0 and T_L, their streamwise evolution along the jet centerline, their connection to Eulerian properties of the jet and the reliability of Lagrangian stochastic models derived for HIST [Sawford, 1991] to address the stationarized Lagrangian dynamics of the jet. Investigations are made into these quantities for both axial and radial components of the velocity.

Table 3.3 presents these Lagrangian parameters of the jet for different z locations in the near and far-fields. The scaling constant C_{0_z} is observed in the compensated Lagrangian structure functions, figure 3.18(b). The Lagrangian integral time scale

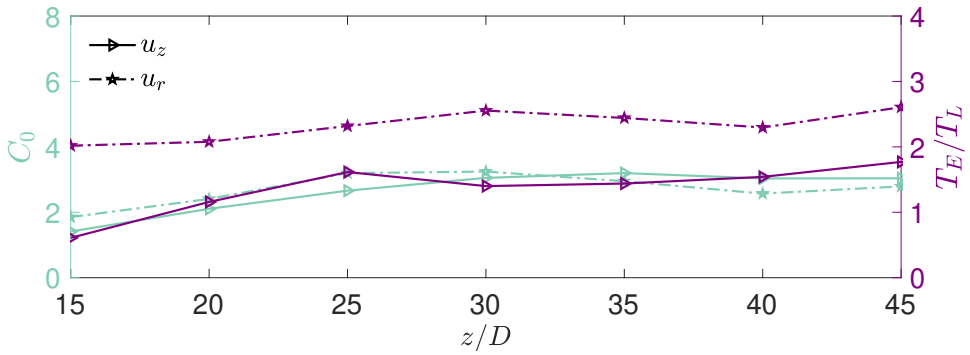

Figure 3.22: Evolution of the scaling constant C_0 (*left*) and the ratio of the integral time scales T_E/T_L (*right*) as a function of downstream location within the jet center. The axial (−) and radial (-··-) components are both presented.

T_{L_z} is estimated based on an exponential fit of the velocity correlation curves, due to the lack of experimental data for large time lags, figure 3.20(a). Lagrangian correlation functions are indeed known (at least in HIST) to be well fitted by double exponential functions, and even simple exponential functions at sufficiently large Reynolds number, if the focus is on the estimate of inertial and large scales behavior [Sawford, 1991]. In the present case, the fit by a simple exponential ($e^{-\tau/T_{L_z}}$) leads to very similar estimates of T_{L_z} compared to a more sophisticated double exponential fit. Corresponding radial quantities are extracted in the same way by considering $S^L_{2-r}(\tau)$ and $\mathcal{C}_{v-r}(\tau)$.

C_{0_z} is found to converge to a constant value $C_{0_z} \simeq 3.2$ at $z/D > 30$. This is more easily observed in figure 3.22 which provides the evolution of the Lagrangian parameters as a function of the downstream position z. The asymptotic far-field value of C_{0_z} can be compared to values reported in the literature for C_0. A relationship presented by Lien and D'Asaro [2002] accounting for finite Reynolds number effects on C_0 suggests an altered $C_0^*(Re_\lambda) = C_0^\infty[1 - (0.1Re_\lambda)^{-1/2}]$ where according to Sawford [1991], $C_0^\infty \simeq 7.0$. This gives an estimated C_0^* of 5.6 for the Reynolds

number corresponding to the present study as a benchmark value. As previously mentioned, discrepancies exist between numerous studies of this parameter, for example a C_0^* of 4.8 was extracted for direct numerical simulation data with $Re_\lambda = 240$ by Sawford and Yeung [2001], while experimental data taken between two counter-rotating disks at $Re_\lambda = 740$ produced a C_0^* of 2.9 [Mordant et al., 2001a]. Ouellette et al. [2006a] found in a similar flow at $Re_\lambda \simeq 200$ an anisotropic behavior, with $C_0^* \simeq 3.5$ for the velocity component aligned with the axis of rotation of the disks and $C_0^* \simeq 5.5$ for the transverse components. It is therefore difficult to be fully conclusive regarding the expected value of C_0 in our case, as it appears to be non-universal and not only dependent on the Reynolds number, but for a given Reynolds number to also depend on specific geometrical properties of the considered flow. It is observed however that the measured value of C_{0_z} in the jet is in the same range of magnitude as other studies in different flows at a similar Reynolds number. With regard to anisotropy, Table 3.3 and figure 3.22 suggest that C_{0_z} and C_{0_r} behaves almost identically along the jet, C_{0_z} converging to a value of 3.0 and C_{0_r} to a value of 2.8. This indicates, on one hand, that Lagrangian dynamics exhibit a level of isotropy, and on the other hand that at a specific location downstream, C_0 becomes independent of axial location and hence supports the idea that inertial Lagrangian statistics reaches self-similarity.

Regarding the Lagrangian correlation time scale both T_{L_z} and T_{L_r} increase with increasing axial distance, with T_{L_z} being however significantly larger (about double) than T_{L_r}, see Table 3.3. Large scale Lagrangian dynamics therefore exhibits a persistent anisotropy, somehow more pronounced than the anisotropy previously reported for the Eulerian integral time scales (see for instance T_{E_z} and $T_{E_{r\theta}}$ in Ta-

ble 3.2). To further compare Lagrangian and Eulerian large scales properties, the ratio of the Eulerian to Lagrangian integral time scales, for both the axial and the radial components of velocity is provided in Table 3.3 and figure 3.22. For all locations, the Eulerian to Lagrangian time scale ratio for the radial component is notably larger (about double) that of the axial component. The axial component trends are consistent with similar results reported by Gervais et al. [2007], wherein T_{E_z}/T_{L_z} was found to be less than one in the near-field, and to evolve towards a value greater than one (between 1.3 and 1.8) as the jet develops. Interestingly, in the well developed region, the Lagrangian dynamics decorrelates significantly faster compared to the Eulerian dynamics, as originally intuited by Kraichnan [1964]. This relation between Eulerian and Lagrangian time scales has been examined numerically by Yeung [2002] where a ratio of $T_E/T_L = 1.28$ was found for HIST. This value is slightly lower than the value found in the present experiments, but is still consistent with a Lagrangian dynamics decorrelating faster than the Eulerian.

Since the study by Kraichnan [1964] who suggested that $T_E/T_L > 1$, a similar prediction has been made by Sawford [1991] based on simple Lagrangian stochastic modeling. In this approach, Eulerian and Lagrangian time scales can be simply related to each other via the scaling constant C_0:

$$T_E/T_L = C_0/2. \tag{3.9}$$

As observed in figure 3.22, this relation is tested against the experimental results for the axial and radial velocity components. Note that the limits of the axis for T_E/T_L on the right of the figure are half the limit of the axis for C_0 on the left

of the figure, therefore if $T_E/T_L = C_0/2$ holds, the curves for T_E/T_L and for C_0 shall superimpose). For the axial component, the agreement is almost perfect at all locations, including in the near-field. This is not observed for the radial component, while the two curves exhibit proportionality, the ratio of time scales is nearly equal to the scaling constant C_0 at all presented locations.

3.4.3 Lagrangian tracer acceleration statistical analysis

This section explores the statistics of the Lagrangian acceleration, to further elucidate small scales dynamics and its evolution along the jet. Particularly, the role of finite particle size effects (which evolve along the jet, and therefore may be to blame for preventing self-similarity to be recovered until the very far-field and the associated dimensionless constant a_0 (appearing in the Heisenberg-Yaglom relation [Monin and Yaglom, 1975]) are addressed. At the same time, investigation into the connection between Eulerian and Lagrangian dissipative time scales can be carried out to further probe the applicability of stochastic models. All analysis is performed on trajectories that pass through a sphere of radius $r_{1/2}(z)/3$, as it was done for the Lagrangian velocity analysis. Only the axial component of velocity is considered for the acceleration discussion (radial component gives almost identical conclusions).

Acceleration variance

The variance of acceleration components is traditionally characterized by the scaling constant a_0 through the Heisenberg-Yaglom relation [Monin and Yaglom, 1975]:

$$\langle a_z^2 \rangle = a_0 \nu^{-1/2} \varepsilon^{3/2}, \tag{3.10}$$

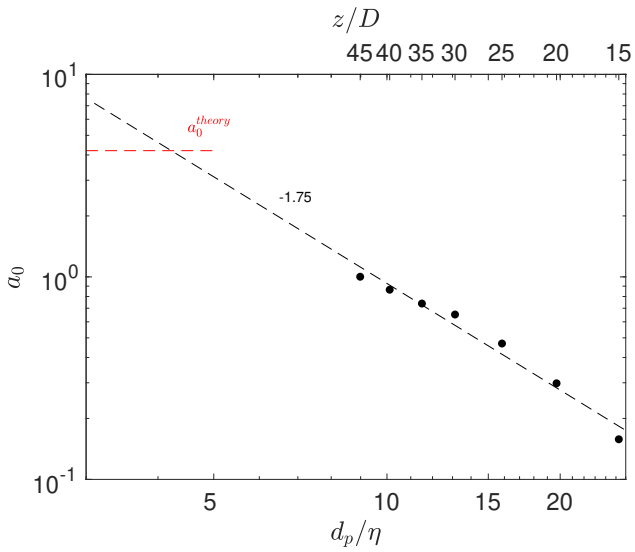

Figure 3.23: Evolution of the scaling constant of acceleration a_0 along the centerline as a function of the finite particle size d_p/η.

where ν is the fluid viscosity and ε is the dissipation rate. The acceleration variance is taken directly from the trajectories with the dt-method implemented to find the noiseless values of $\langle a_z^2 \rangle$ [Machicoane et al., 2017a]. This is done for different z positions along the jet. a_0 is then deduced at the different positions as $\langle a_z^2 \rangle \nu^{1/2} \varepsilon_z^{-3/2}$, where ε_z is the estimate of the dissipation rate at the considered position, based on the considered acceleration component.

Acceleration variance, and therefore the dimensionless constant a_0, is known to be highly sensitive to particle finite size effects and to converge to the value expected for actual tracers only when the normalized particle diameter $d_p/\eta \lesssim 5$ [Voth et al., 2002, Qureshi et al., 2007, Calzavarini et al., 2009, Volk et al., 2011], where η is the Kolmogorov length scale (see Table 3.2). In the present study the ratio d_p/η varies typically between 9 and 25 depending on the distance to the nozzle. Therefore, the constant a_0, as a function of the normalized particle size d_p/η (bottom axis) and

of the downstream normalized location z/D (top axis), is provided in figure 3.23. Included is a power-law fit of -1.75 and a red dashed line of the expected value (from numerical simulations of HIST), $a_0^{theory} \simeq 4.2$, calculated from Sawford [1991]. The power-law of -1.75 provides the expected a_0^{tracer} value of a true tracer through extrapolating the trend as $d_p/\eta \to 5$, from which a value of $a_0^{tracer} \simeq 3.0$ is found, in reasonable agreement with values reported in previous experimental studies in von Kármán flows [Voth et al., 2002] and numerical simulations in HIST [Sawford, 1991, Vedula and Yeung, 1999] for a similar Reynolds number. Furthermore, the power-law fit intersects with the theoretical value of a_0^{theory} at $d_p/\eta \lesssim 5$, what is generally considered as the diameter for which finite size effects become noticeable. These observations suggest that acceleration statistics in the jet should eventually behave for tracers as in HIST, without a major influence of large scale inhomogeneity of the jet. With the present considered particles (with $d_p \simeq 250\,\mu m$) the tracer behavior is expected to be reached at a downstream distance $z/D \simeq 65$, which is out of reach of the present data set. To deepen this question, it would be interesting to perform further experiments specifically dedicated to acceleration measurements, by considering either smaller particles or further downstream distances.

Regarding finite size effects, previous studies have reported in HIST a power-law dependency of a_0 on particle size, with $a_0 \propto (d_p/\eta)^{-2/3}$ [Qureshi et al., 2007, Brown et al., 2009], while a study by Volk et al. [2011] of von Kármán dynamics report a slightly steeper decay with an exponent -0.81. In the present study, an even steeper decrease of constant a_0 is observed with particle size, with an exponent -1.75, about double of the values reported previously. This stronger dependence of a_0 on particle size remains to be elucidated. It is likely due to a coupling between the finite size

effects and the streamwise dependence of turbulent properties in the jet, although further investigation would be necessary to further explore this point.

Acceleration two-point correlation

Beyond the value of a_0, acceleration statistics are also of great interest as they reflect the Lagrangian dissipative dynamics of the particles. In particular, they give access to the dissipative timescale of the Lagrangian dynamics, traditionally defined based on τ_0, the zero-crossing time of the acceleration two-point correlation function, $R_{aa,z}(\tau) = \langle a_z(t+\tau)a_z(t)\rangle$ with $R_{aa,z}(\tau_0) = 0$. Acceleration two-point correlation is estimated with a variant of the dt-method [Machicoane et al., 2017a]. Briefly, the acceleration two-point correlation is obtained from second-order position increments d^2x according to the relation

$$R_{d^2xd^2x}(\tau, dt) = R_{\hat{a}\hat{a}}(\tau)dt^4 + R_{d^2bd^2b}(\tau, dt) + \mathcal{O}(dt^6), \tag{3.11}$$

where $R_{d^2bd^2b}$ represents the contribution of noise. A polynomial fit of dt^4 is implemented to extract the true correlation values of $R_{\hat{a}\hat{a}}$, eliminating the noise contribution. This method is extended, herein, to more accurately describe the correlation of acceleration of the given data set.

The two-point correlation of acceleration is presented in figure 3.24 for four downstream locations along the centerline, where the time lag has been normalized by τ_η. It has been noted in previous studies that for tracers $\tau_0 \simeq 2.2\tau_\eta$ [Yeung and Pope, 1989, Calzavarini et al., 2009, Volk et al., 2008]. For the current study, the zero-crossing time is not unequivocally close to τ_η and therefore the ratio τ_0/τ_η depends

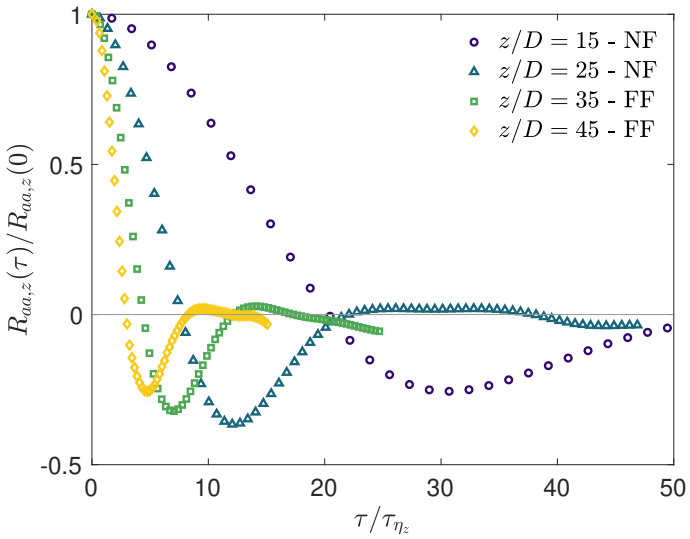

Figure 3.24: Normalized axial acceleration correlation on the axis as a function of time lag normalized by the Kolmogorov time scale.

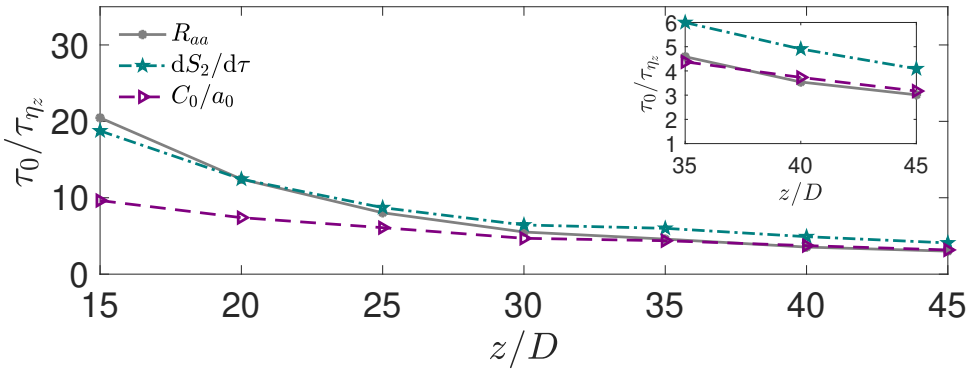

Figure 3.25: The zero-crossing of the acceleration correlation normalized by the Kolmogorov time scale as a function of the downstream location along the center of the jet. Three estimations are presented based on the acceleration correlation R_{aa}, the derived second-order structure function $\mathrm{d}S_2^L/\mathrm{d}\tau$, and the model driven values obtained from C_0/a_0.

on the location of the measurement. The expected value of 2 is only approached in the farthest downstream locations within the jet. The solid line in figure 3.25 shows the downstream evolution of the zero-crossing time τ_0. As for a_0 the observed streamwise dependency of τ_0/τ_η is likely due to finite size effects, which have been reported in HIST to be affected by finite size effects [Volk et al., 2008, Calzavarini et al., 2009]. It shall be noted though, that τ_0/τ_η seems to eventually approach the expected value of nearly 2 for the farthest positions (and hence for the smallest d_p/η ratios), presented in the inset of figure 3.25. Following the considerations previously discussed on the trends of a_0, it could then be expected that the actual tracer behavior (free of finite size effects) would be fully recovered for τ_0 near $z/D \simeq 65$, with a ratio τ_0/τ_η of the same order of what is usually reported for HIST.

Beyond the discussed finite size effects, acceleration correlation is also insightful to shed further light on the Lagrangian properties of the jet of relevance for the application to diffusion problems, as motivated in the introduction.

First, the stationarization of velocity *à la* Batchelor can be tested further tested by recalling that for any random stationary signal ξ, the two-point correlation of the derivative of ξ, $R_{\dot{\xi}\dot{\xi}}$, is simply related to the second derivative of the two-point correlation of ξ: $R_{\dot{\xi}\dot{\xi}} = -\ddot{R}_{\xi\xi}$ (derivatives are denoted in dot notation). In the present case, this relation gives that the zero-crossing of acceleration correlation corresponds to an inflection point of the velocity two-point correlation. If Lagrangian stationarity holds, τ_0 can therefore be simply extracted from the peak of the derivative of the second-order structure function, $\mathrm{d}S_2^L/\mathrm{d}\tau$ (figure not included). The corresponding values are presented in figure 3.25 (dot-dashed line) which exhibit a fair agreement with the direct estimate of τ_0 from R_{aa}. This observation supports the

validity of the proposed stationarization procedure at each explored location independently. Although, finite size effects influence the streamwise dependence of τ_0 therefore impeding the validation of the small scale Lagrangian self-similarity based on streamwise evolution of τ_0 (or a_0).

Second, the relevance of stochastic models to characterize the Lagrangian dynamics (and therefore to predict diffusion properties) can be further tested from the acceleration timescales. As presented in section 3.4.2, simple (Langevin) stochastic models accurately predict large scale properties, such as the connection between Lagrangian and Eulerian integral timescales and C_0. Two-time stochastic models [Sawford, 1991] also predict a similar relation for the small Eulerian and Lagrangian timescales, involving the constant C_0 and a_0 (see Huck et al. [2019]). Namely, the prediction from such models can be written as

$$\tau_a = \int_0^{\tau_0} R_{aa}(\tau)\,\mathrm{d}\tau = \frac{C_0}{2a_0}\tau_\eta. \tag{3.12}$$

Neglecting the curvature of R_{aa} at the origin, the integral $\int_0^{\tau_0} R_{aa}(\tau)\,\mathrm{d}\tau$ can be approximated as $\tau_a \simeq \frac{1}{2}\tau_0$ (because of the curvature, it is actually slightly larger than that). It is therefore expected from stochastic models that $\tau_0/\tau_\eta \simeq C_0/a_0$. The dashed line in figure 3.25 represents the downstream evolution of the ratio C_{0_z}/a_{0_z} extracted from the measurements. Neglecting the near-field locations of $z/D < 25$, it can be seen that the agreement is also adequate when compared to the two previously presented independent estimations of τ_0/τ_η.

3.5 Inertial particle results

3.5.1 Eulerian velocity statistical analysis

It has been noted that a jet shows a self-similar behavior as a function of downstream location. First, the centerline statistics provide power law representations as was evidenced in figure 3.16, where the axial velocity standard deviation, dissipation rate and integral length scale are presented as a function of z/D. The mean velocities, variance and covariance all exhibit self-similar relations within the fully-developed region of the jet and show collapsing curves when normalized by the centerline velocity. To assess how inertia affects these statistical quantities, the time-averaged axial and radial velocity, the covariance and the concentration of the particles are presented in figure 3.26 as a function self-similarity variable $\eta = r/(z - z_0)$. Here, all profiles are taken at $z/D = 25$ for comparison. The tracer particles are compared against the inertial particles with $d_p = 160\mu$m and $d_p = 250\mu$m. Note that the length and time scales are dependent on location and therefore the diameter of the particle is used for notating between the three cases. The four self-similar profiles are compared to understand if the particles are impeding or advancing the flow in this region, adding to stresses or subduing them.

First, for figure 3.26(a), typically, a Gaussian profile is observed for fluid tracer dynamics and this is captured well by the tracer experimental results. This signifies that the axial velocity decays as a function of its axial and radial position, leading to near zero values by $\eta = 0.3$, which agrees well with canonical results [Pope, 2000]. Although similar, the two inertial particles with St $\sim 10, \sim 30$ for I_{160} and I_{250}, respectively, show a slower decay as $\eta \to 0.3$. This is caused by the inertia,

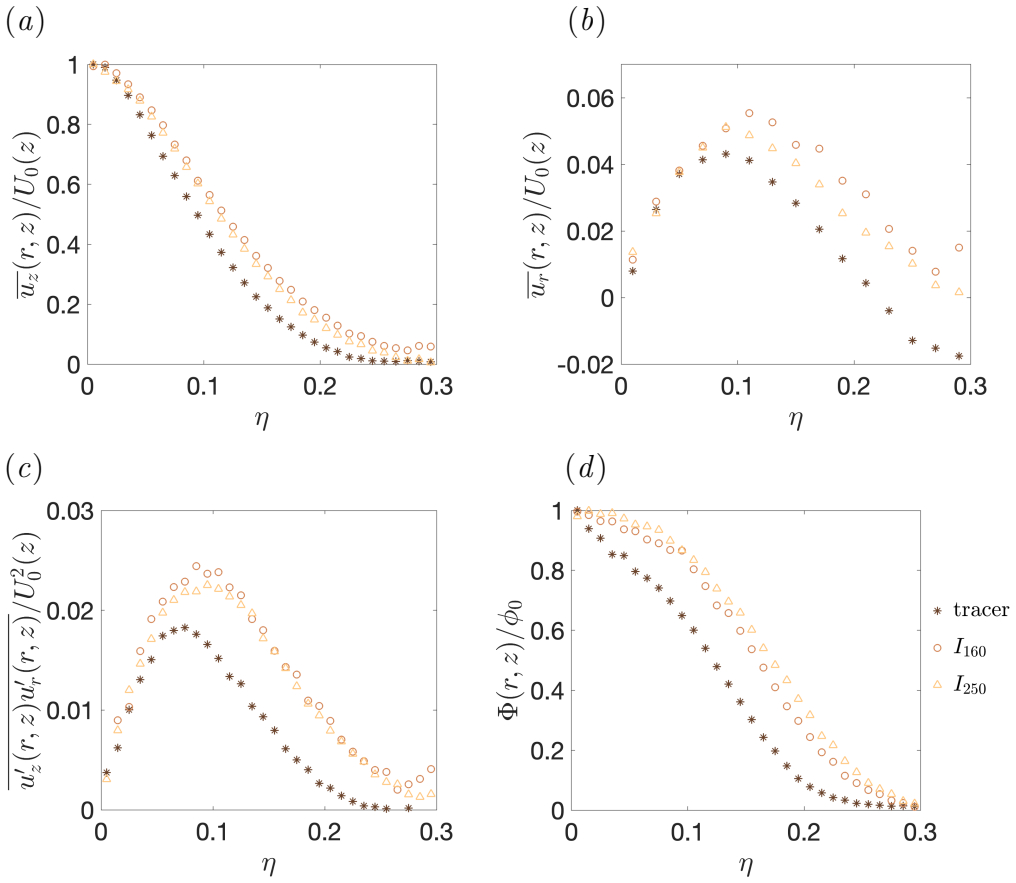

Figure 3.26: Self-Similarity profiles for the tracers, inertial particles with $d_p = 160\mu$m and $d_p = 250\mu$m at $x/D = 25$. Profiles include (a) the axial mean velocity, (b) the radial mean velocity, (c) the Reynolds stress and (d) the concentration profile, all as a function of the self-similarity variable $\eta = r/(z - z_0)$.

inducing greater speeds of the jet, relative to the centerline velocity, at slightly larger η values in comparison to the fluid tracer dynamics. The axial velocity has known characteristics of its velocity deficit $B \sim 5.8$ and spreading rate $S \sim 0.094$ [Pope, 2000, Lipari and Stansby, 2011]. These parameters are based on the streamwise velocity and are calculated as $B = U_0(z - z_0)/U_J D$ where U_J is the exit speed of the jet and $S = r_{1/2}/(z - z_0)$. Table 3.4 provides the B and S values obtained for the

three considered cases. This quantifies the fact that the centerline is decaying more slowly for the inertial particles and that the spreading rate is slightly increased. The larger glass (250μm) particles tend to decay more slowly although the difference is minimal when compared to the tracer results and the spreading rate is nearly identical between the two inertial particles.

The radial velocity profile is provided in figure 3.26(b) which again exhibits increased values for the two inertial cases in comparison to the tracer particles. Here it has been noted that the radial velocity is highly effected by the seeding of the particles only from the nozzle and the lack of seeding of entrained fluid [Basset et al., 2022]. A typical radial self similarity curve would show a more gradual increase of $\overline{u_r'}/U_0$ from $\eta = 0$, with peak values of ~ 0.02 and would become negative near $\eta \sim 0.1$. Very different trends have been noted by Basset et al. [2022] which is attributed to the lack of tagged particles from the outside (ambient) fluid. All three cases presented follow these newly quantified trends of the jet and are actually amplified by the I_{160} and I_{250} particles. This result is similar to the relations of the axial velocity where the glass particles have greater inertia and therefore slightly higher rates of velocity for both components.

The second-order statistics observed by the Reynolds shear stress in figure 3.26(c) present the now expected amplified turbulence of the glass beads in comparison to the tracer particles. Although time averaged statistics would be expected to increase, the fact that the fluctuations provide greater values for $0.08 < \eta < 0.3$, indicate that the variance of the signals for the inertial particles is also intensified. Recall that this is all relative to the centerline velocity. Not only is the magnitude of the stress larger for the glass particles but the location of the maximum is at a greater value

Particle type	B (centerline decay)	S (radial spreading)
tracer	5.9	0.103
inertial $d_p = 160\mu$m	4.93	0.126
inertial $d_p = 250\mu$m	4.78	0.121

Table 3.4: Axial velocity parameters of the jet.

of η, possibly due to the decreased B and increased spreading rate and in turn slower onset of the turbulent/non-turbulent interface of those cases. Here minimal differences are observed between the two types of inertial particles.

Finally, the concentration profile is also investigated because boundary-layer equations for a scalar field (i.e., the concentration of particles) are similar to those of the mean axial velocity and therefore the self-similar profile is similar but typically wider [Pope, 2000]. This is observed in the experimental tracer data as well as the inertial particle data which shows even wider concentration profiles. Again, this ties into the increased spreading of the particles and decreased B, leading to a wider jet.

From the Lagrangian perspective, the interaction of the particles within the centerline and at the shear layer can be quantified by multi-particle statistics. Recall, that when considering pair dispersion, three regimes are expected in turbulent flows depending on the time scale of dispersion relative to a characteristic scale. To quantify the effects of inertia on these regimes, the scaled mean-squared particle separation, $(\boldsymbol{D}(t) - \boldsymbol{D}_0)^2/(11/3)C_2(\varepsilon D_0)^{2/3}\tau_\eta^2$ is presented in figure 3.27 for the tracer particles and the two glass beads of diameter $d_p = 160\mu$m and 250μm. The data are probed at two locations, along the centerline, figure 3.27(a), and at $r = r_{1/2}$, figure 3.27(b). The dispersion is taken for particles that fall within a sphere of size $r_{1/2}/3$ at $z/D = 15$.

Along the centerline, the near-field of the jet shows a well described Batchelor

regime then then no super-diffusive Richardson scaling at t/τ_η increases. Instead, due to the magnitudes of the initial separation and the dissipation rate, the characteristic time scale, t_0 of pair dispersion is actually larger than the largest scale of the flow, T_L and therefore the dispersion appears to transition from a scaling of t^2 in the ballistic regime, directly to t, a diffusive regime. The onset of the diffusion regime is later for the most inertial particles in comparison to the smaller, $d_p = 160\mu$m particles and the tracers. For the off-axis dispersion, a longer Batchelor regime for all particle types is observed in comparison to the centerline possibly due to the increased turbulent activity and increased integral time scale at that location. Again, the I_{250} particles contain the longest ballistic regime. Previous studies of inhomogeneous flow have applied techniques of pair dispersion to characterize the diffusion processes [Pitton et al., 2012, Watanabe et al., 2016]. Both Pitton et al. [2012], Watanabe et al. [2016] use DNS and are able to extract larger and smaller time scales than those presented here, although tendencies of the inertial particles to surpass the scaling behaviors of the tracers was observed in the channel flow DNS of Pitton et al. [2012]. As the jet develops and the integral time scale increases, recall that $T \propto z^2$, pair dispersion is again applied to the centerline trajectories as well as those off-axis at $z/D = 35$, and resulting curves are provided in figure 3.28. Note that the particle time has decreased for figure 3.28(a) and 3.28(b) due to the slowed particle motions relative to the Kolmogorov time scale, τ_η. Similar behaviors are present as those from near the jet exit (figure 3.27) with the exception that the Batchelor scaling is extended in time t/τ_η for all considered cases at all radial locations for the far-field. Likely due to the larger structures developed and therefore smaller relative t values in comparison to T_L. It is of note that the largest and most

inertial particles show increased scaling for each considered location in comparison to the smaller glass beads, I_{160}, as well as the tracer particles.

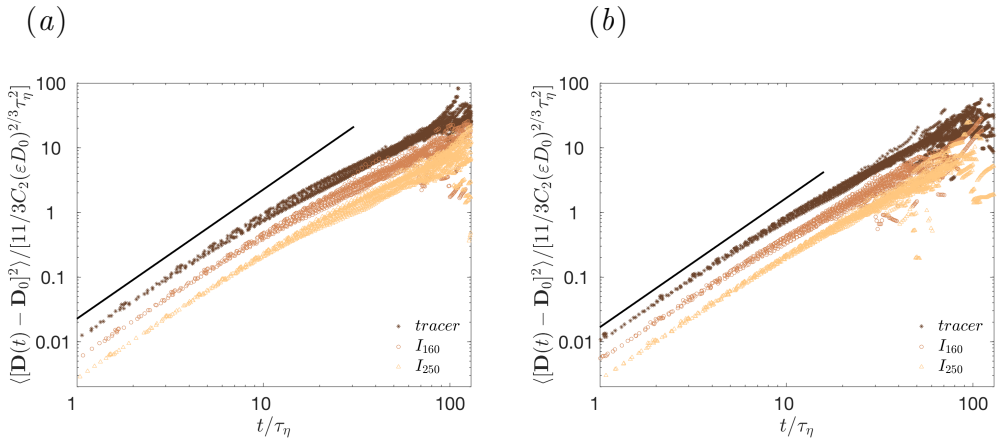

Figure 3.27: Mean-square particle separation, $(\boldsymbol{D}(t) - \boldsymbol{D}_0)^2$, scaled by $(11/3)C_2(\varepsilon D_0)^{2/3}\tau_\eta^2$ is plotted for 16 different initial separations, ranging from 0–1 mm to 39-40 mm. Two initial locations of the dispersion calculations are presented: (a) $z/D = 15$, $r = 0$ and (b) $z/D = 15$, $r = r_{1/2}$. A t^2 power law is also included as a solid line.

3.5.2 Acceleration

Acceleration statistics are highly sensitive to the size of the particle, providing an opportunity to understand how the Stokes number effects acceleration when the density of the particle is also a factor. Three data sets are compared for a variety of flow conditions in figure 3.29. Two sets of data from the jet experiment are included, the tracer particle data along the centerline of the jet as well as the inertial data for particles with $d_p = 160\mu m$. St evolves in the jet and therefore high values are reached very near the nozzle and lower values are obtained in the far-field. Other data included are the direct numerical simulations of Bec et al. [2006] using particle

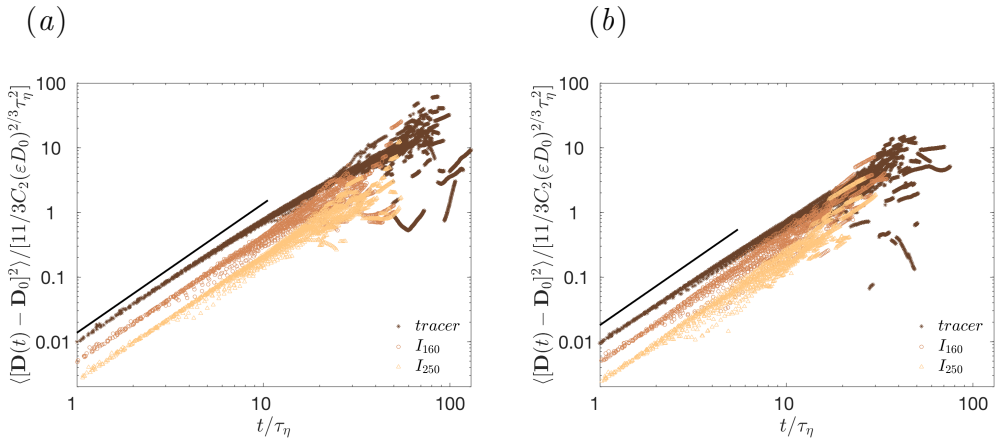

Figure 3.28: Mean-square particle separation, $(D(t) - D0)^2$, scaled by $(11/3)C_2(\varepsilon D_0)^{2/3}\tau_\eta^2$ is plotted for 16 different initial separations, ranging from 0–1 mm to 39-40 mm. Two initial locations of the dispersion dynamics are presented: (a) $z/D = 35$, $r = 0$ and (b) $z/D = 35$, $r = r_{1/2}$. Again, a t^2 power law is also included as a solid line.

trajectories experiencing homogeneous, isotropic and stationary turbulence. Re_λ for all cases are within 180-240.

General trends between all cases show nice agreement with minimal scattering observed between the various methods. Slight increases in the a_0 values are observed for experimental tracers in comparison to the DNS but a similar power law is observed between the two. This difference in magnitude could be due to the added mass of the two cases, while the DNS present data with an added mass, $\beta = 0$, the tracer particles in the jet are neutrally buoyant, i.e., $\beta \sim 1$, possibly causing the offset [Huck, 2017]. In contrast, the inertial particles show different trends, with a more gradual decay in acceleration variance in comparison. This could also be due to the added mass, which is closer to 0.5 for the glass beads. Furthermore, the dampened magnitudes could also be due to the convergence of the acceleration variance as it reaches zero, although lower St values would be required to observe if

the curve regains the power law observed in the $\text{LEM}_{\text{tracer}}$ and DNS data.

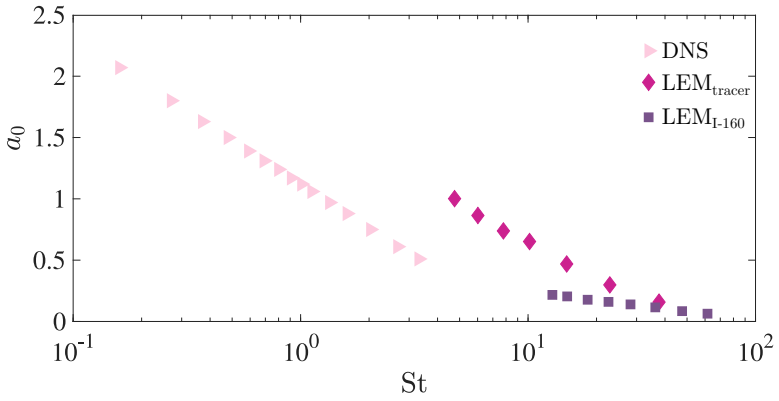

Figure 3.29: Heisenberg-Yaglom coefficient (a_0) of the tracer and inertial particle data from the LEM as well as DNS of isotropic homogeneous turbulence [Bec et al., 2006].

3.6 Concluding remarks

Particle tracking velocimetry was implemented to create three component jet trajectories in three-dimensional space. Generation of such a large scale database facilitates the study of how fundamental Lagrangian parameters behave when exposed to a highly anisotropic and inhomogeneous flow field. The Lagrangian self-similarity theory of turbulent diffusion by Batchelor [1957] has been applied to account for the Lagrangian non-stationarity of the flow field due to the spatial Eulerian inhomogeneity. The stationarization technique leading to Lagrangian self-similarity is validated in the far-field of the jet for Lagrangian inertial scales dynamics by the collapse of the Lagrangian velocity structure functions and correlation profiles (after a given location downstream) for the stationarized variables. Lagrangian self-similarity is also validated for the large scales, as the Lagrangian and Eulerian time

scales are found to be univocally tight in the far-field of the jet. For the small scale Lagrangian dynamics, self-similarity is only observed in the farthest downstream locations explored. This is attributed to the impact of particle finite size effects which evolve along the jet axis and therefore influence the small scale Lagrangian dynamics differently depending on the downstream position, as confirmed by the acceleration statistics. Further studies, with experiments specifically dedicated to small scale (acceleration) measurements of small tracers would be required to draw final conclusions concerning the small scale Lagrangian self-similarity. In turn, this confirmation of the validity of the Lagrangian self-similarity at inertial and large scales is an important element supporting Batchelor's extension of Taylor's stationary theory of turbulent diffusion to the case of self-similar jets and wakes where particles have a non-stationary Lagrangian dynamics.

Regarding the inertial scales of the Lagrangian dynamics, results indicate that the Lagrangian scaling constant, C_0, is a function of downstream location in the near-field and eventually converges (around $z/D = 30$) to a value of the order of 3, with a small ($\sim 10\%$) difference between axial and radial components, indicating a weak role of anisotropy on inertial scale Lagrangian dynamics in the jet. It is noted that this value may be Reynolds number dependent (its order of magnitude is consistent though with HIST simulations and experiments carried in other flows at similar Reynolds number), and further studies in a jet configuration at different Reynolds number will be required to explore this dependence.

The evolution of the Eulerian to Lagrangian integral time scale ratio shows convergence towards $T_E/T_L \simeq 1.8$ around $z/D = 25$ for the axial velocity timescales and $T_E/T_L \simeq 2.6$ by the same location downstream for the radial based timescale ratio.

This points towards three interesting observations: (i) In the well developed region of the jet, the Lagrangian dynamics decorrelates faster (about twice faster) than the Eulerian (as predicted for HIST by Kraichnan [1964]); (ii) The ratio between Lagrangian and Eulerian integral scales is about 40% larger for the radial component compared to the axial, what is to be related to the large scale anisotropy of the jet; (iii) In spite of this difference, sufficient agreement is found between the measured ratio for these time scales and the prediction from simple stochastic models for HIST, $T_E/T_L \simeq C_0/2$ (the agreement is favorable between the axial based parameters while the value predicted by the model underestimate the actual time scale ratio for in the radial direction).

Considering the small scale dynamics, the normalized acceleration variance shows a strong dependence on the downstream location from the nozzle, presumably associated to finite particle size effects, which are known to influence acceleration when $d_p/\eta > 5$ typically. This presumably explains why self-similarity is not fully recovered at small scales in the present study, as tracer-like behavior for acceleration would only be recovered around $z/D \simeq 65$. Besides, the power-law slope of a_0 as a function of d_p/η found in the current study is larger than in previous studies in HIST and von Kármán flows, suggesting that the jet dynamics interplay with finite size effects. The zero-crossing of the acceleration correlation also demonstrates a strong dependence on the downstream location from the nozzle, converging towards typical values ($\tau_0/\tau_\eta \simeq 2$) only at the farthest position explored ($z/D \gtrsim 40$). Although the actual value of τ_0 is likely also altered due to finite size effects, the agreement between several independent estimates of τ_0 supports on the one hand the validity of the proposed stationarization method and on the other hand the relevance of

simple stochastic approaches to link (in the far field) the Eulerian and Lagrangian dissipative time scales to the experimentally determined constants C_0 and a_0.

The ability of the implemented stationarization technique provides adequate methods for calculating the scaling constant, a non-trivial task within an inhomogeneous flow field. Overall, after a proper stationarization, the Lagrangian properties for the jet are interestingly found to match reasonably well the behaviors previously reported for HIST. From the perspective of building simple and practical diffusion models, the success of the method validates Batchelor's extension of Taylor's theory, providing estimates of turbulent diffusion properties based on the Lagrangian second-order structure function (or two-point correlation function) of velocity. Further, the relations presented between the Eulerian and Lagrangian time scales (both integral and dissipative) suggests that simple stochastic modeling is well suited to find reasonable estimates of such correlation functions. Actually, based on these models, the simple knowledge of the constants a_0 and C_0 may be sufficient to build reasonable proxies (with exponential or double exponential functions) of these correlations to be used for estimating turbulent diffusion properties.

Investigations into inertial particle dynamics in the jet revealed that the spread of the jet is faster for the glass beads in comparison to the neutrally buoyant tracer particles, as observed in Eulerian self-similarity profiles. Between the two finite inertia particles with varying diameters, minimal differences were observed for the spatial analysis. Pair dispersion displayed the ability of the particles to diffuse as a function of the separation time. A ballistic regime is present for all cases and locations explored. The span of the regime depended on the axial and radial location within the jet as well as the type of particle. Explicitly, as the jet developed

downstream, the ballistic regime, t^2 scaling, extended into larger scales. Similarly the ballistic behavior was also present for off-axis pairs at larger separations. Finally, it was noted that the particle inertia effected the onset of the diffusive regime as well, increasing the ballistic regime at a given location with increased St.

Acceleration was investigated for the tracer particles and the small sphere inertial particles, namely I_{160}. The scaling constant, a_0, demonstrated a power law as a function of St. The tracers, which contain finite size effects due to their diameter in comparison to the small scale dynamics of the flow, present inertial affects when considering small scale phenomena such as acceleration. Similar power law scaling is presented for the tracers and a set of homogeneous, isotropic and stationary simulated turbulence, although an offset is present. This is likely due to the added mass of the tracers, where a density ratio $\beta \sim 1$ is present in comparison to the DNS which evaluates heavy point particles and therefore $\beta = 0$. The inertial particle dynamics (glass beads with $\beta \sim 0.5$) extracted from the jet show a more gradual decay of a_0 as a function of Stokes, possibly due to the magnitude of the universal constant converging towards zero at St$\sim$ 70.

Chapter 4

Jet modeling based on homogeneous, isotropic and stationary turbulence

4.1 Introduction

In practice, for both Eulerian and Lagrangian approaches, the complicated dynamics of turbulence often require (or simplify greatly when considering) homogeneous, isotropic and stationary turbulence (HIST) and therefore, an overwhelming amount of research has been concentrated on this simplified flow. Although more accessible, HIST does not generally equate to real world applications in which inhomogeneity and anisotropy are commonly observed. This predicament leads us to question if the progress that has been made for homogeneous turbulence research could somehow be exploited to characterize inhomogeneous flow fields? Moreover, could it be used in modeling inhomogeneous flow with higher accuracy than current efforts, in particular regarding subtle properties such as intermittency?

Regarding HIST, advancements in experimental techniques have improved the phenomenological understanding and the accurate characterization of the full multi-scale dynamics of turbulence. Moreover, the increased computational power leads to a rise in the precision and detail feasible for simulations and numerical modeling.

The study of turbulence relies on statistical descriptions due to the non-repeatable nature of instantaneous descriptions. This is often achieved through the use of correlation functions and velocity increment analysis (through the so-called *structure functions* for instance, which correspond to the statistical moments of velocity increments in space for the Eulerian approach and in time for the Lagrangian). Along this line, crucial to the developments in HIST research, Taylor [1922] provided a connection between diffusion rate of a cloud of fluid parcels and two-time Lagrangian correlations of velocity, an important advancement to model turbulent diffusion. On the Eulerian side, Kolmogorov [1941] postulated that within inertial scales statistics of turbulence could be characterized by the mean energy dissipation rate ε, leading the well-known $K41$ self-similar scalings for the structure functions, which accurately predict for instance the energy spectrum and the asymmetry of velocity increment associated to the turbulent energy cascade.

Extensions to include deviations from scale invariance, such as intermittency have been since proposed [Kolmogorov, 1962, Vassilicos et al., 2001, She and Leveque, 1994] and although its physical origin has not yet been fully unveiled, accurate statistical descriptions such as the multi-fractal formalism [Chevillard et al., 2012] have been developed to account for such peculiar multi-scale dynamics. These statistical relations presented by Kolmogorov [1941] and others have since been developed for Lagrangian structure functions by Obukhov and Landau [Falkovich et al., 2012].

It therefore is appealing, regarding the ongoing efforts to study HIST, to understand fundamental aspects of this flow because theoretical relations are often well defined and therefore greater amounts of analysis can be executed. Experimentally, this manifests itself in the study of decaying turbulence in wind tunnels (experi-

ments with approximately HIST conditions) using spatial (Eulerian) measurements [Comte-Bellot and Corrsin, 1971, Gad-el Hak and Corrsin, 1974, Warhaft and Lumley, 1978, Kang et al., 2003, Krogstad and Davidson, 2010]. Similarly, substantial work has been done to strengthen our understanding of turbulence though Lagrangian approaches in experiments, theory and numerics using HIST. Experimentally, the Lagrangian exploration module provides near HIST conditions though the use of counter-positioned motors within an icosahedron tank [Zimmermann et al., 2010]. Otherwise, near HIST conditions are again often observed though decaying turbulence behind a grid and have been extensively explored through tracer particle dynamics [Snyder and Lumley, 1971, Sato and Yamamoto, 1987].

Computationally, HIST is also often employed to better understand turbulence. For example, in direction numerical simulations (DNS) [Orszag, 1969, Siggia, 1981, Jiménez et al., 1993, Gotoh and Fukayama, 2001], which have improved characterization of passive scalars, pressure and vorticity in HIST. Furthermore, homogeneous turbulence is often an assumption to decrease complexities to simulate flow fields via large-eddy simulations (LES) [Chollet, 1985, Fureby et al., 1997, Hughes et al., 2001] and by Reynolds-Averaged-Navier-Stokes (RANS) [Torrano et al., 2015]. Again, extensions to these Eulerian based approaches have been proposed to characterize Lagrangian HIST by tracking particles through the computed field and extracting the tracer velocities and velocity gradients for analysis [Yeung and Pope, 1989, Kimura and Herring, 1996, Anderson and Meneveau, 1999, Ishihara and Kaneda, 2002, Biferale et al., 2005, Ishihara et al., 2009]. It is noted that the use of LES and RANS provides faster, and therefore and lower cost computations but at the expense of resolving all scales. This has been noted and alleviated at times with

various methods to introduce small scale intermittency [Byggstøyl and Kollmann, 1981, Rogallo and Moin, 1984, Lesieur and Metais, 1996].

Touched on previously, despite the abundance of research, past and present, devoted to HIST, the majority of turbulent flows observed in industry and nature do not fall into this category. For example, urban boundary layers, plumes, jets and wakes are all non-homogeneous flow fields due to walls, blunt bodies or free-shearing with ambient fluid. Moreover, when a flow is inhomogeneous in a Eulerian (spatial) sense, it is therefore non-stationary in a Lagrangian (temporal) sense, and tracers of the flow become dependent on their location within the flow, constantly interacting with ever-changing large-scale development in the background flow.

Based on observations and relations of how particles behave within turbulence, additional advancements to turbulent research, for (temporally) stationary and non-stationary flows, have been made through the development of Lagrangian modeling, e.g. multifractal models, stochastic dispersion processes and random walk models [Sawford, 1991, Borgas, 1993, Borgas and Sawford, 1994b, Bacry et al., 2001, Chevillard et al., 2003, Mordant et al., 2003]. These models have been proposed to predict and explain fluid element behavior within turbulent flow. Multifractal formalism is used to predict the highly non-Gaussian statistical representations of the particle velocity and acceleration increments through phenomenological approaches [Borgas, 1993, Chevillard et al., 2003]. Fluid tracer trajectories can be obtained through stochastic approaches [Sawford, 1991, Borgas and Sawford, 1994b, Mordant et al., 2003] and the inclusion of intermittency effects can employed in these models as presented in Section 2.3 as well as according to Bacry et al. [2001], Mordant et al. [2003]. Again, HIST simplifies the modeling requirements, such as symmetries of the

flow field and stationarity of the signal, but stochastic processes have shown success in accounting for inhomogeneities or anisotropy through model modifications. Non-homogeneous modeling of plumes [Weil, 1994, Franzese, 2003] and boundary layer fluid dispersion [Aylor and Flesch, 2001, Shnapp et al., 2020] have found success although many criteria must be satisfied to provide accurate trajectory behaviors [Thomson, 1987]. Examples include, well-mixed condition, small scale behavior of particles from point sources and forward and reverse diffusion, to name a few [Thomson, 1987]. Another noted issue is the required knowledge of parameters for these flow, for example the Kolmogorov scaling constant ($\mathcal{C}_0$) which is critical to Lagrangian stochastic modeling. Although said to be constant, it has been observed that this parameter is dependent on Re [Du et al., 1995] as well as location within inhomogeneous flows as observed in Section 3.4.

The difficulties in analytical descriptions of inhomogeneous flow fields are most evident when trying to quantify times scales and calculate dissipation or diffusion rates. As previously mentioned, most known relations, for example statistical techniques such as those presented by Kolmogorov [1941] or kinematic relations, the diffusion theory of Taylor [1922], require the flow field to be HIST. As noted previously, Batchelor [1957] proposed methods to mitigate this dilemma by stationarizing flows which experience inhomogeneity but also exhibit self-similarity through a novel modification of the theory of diffusion presented by Taylor [1922]. The previous chapter shows successful application of this method to an experimental turbulent jet, and furthermore provides a simple and clear approach of the methods, which can be applied to any self-similar flows, e.g. wakes, jets, boundary layers [Ouellette, 2021].

The technique [Batchelor, 1957] requires only a few parameters of the flow field to create a HIST signal and associated time lag. If such a simple model can be built to mimic HIST, can these same relations be used to generate a non-stationary Lagrangian flow (e.g. a jet) based on a HIST signal alone? This leads one to wonder if all the advancements that have been made to DNS and Lagrangian modeling of particle trajectories can be exploited to accurately model self-similar flows, e.g., wakes, jets and boundary layers. More generally, can the modeled intermittency of the HIST signal continue to be captured by the pseudo jet velocity signal to produce true dynamics at small scales without high computational costs?

Implementations of this modeling technique have been attempted in numerous ways within the past [Minier et al., 2014b], specifically regarding the compensations suggested by Batchelor [1957]. In the three part article, Wilson et al. [1981a,b,c] presents methods to build up a turbulent boundary layer flow based on stochastic processes. This work provides a framework to apply these non-stationarity techniques to atmospheric flows, but some assumptions are required due to the complexity of the flow and furthermore, the implementation methods are not straightforward. A method to build up a jet has also been attempted by Lipari et al. [2007], presenting an adequate model for dilute suspensions, where they use two separate steps to work out solutions of the carrier and dispersed phase.

This lead us to propose an initial pathway using very simple equations to build a jet with a given Reynolds number. The methods are based on the known Eulerian self-similarity relations of a jet. In addition to simplifying application of the model based on previous attempts, it is able to take any set of HIST trajectory velocities an input to produce the jet, i.e., a HIST signal created by a stochastic process (models

presented in Chapter 2 and trajectories extracted from DNS). It is also relevant to the study to further investigate the capabilities of the OU process (presented in Chapter 2). The Batchelor transformation can be applied to any modeled HIST signal and therefore, the number of layers as well as the level of intermittency correction included can be varied to understand the benefits and drawbacks of a given HIST signal depending on its simplicity or complexity. Finally, it is noted that this method could be applied to any flow field as long as knowledge of the time-averaged velocity, standard deviation and integral time scale are known.

4.2 Theory

Inspired by the work of Batchelor [1957], a stationarization scheme was presented and tested in Chapter 3 wherein the tracer velocity and time increment are rescaled to account for Eulerian properties that evolve in the background.

Reversal of the stationarization process leads to methods of creating non-homogeneous flow fields through the transformation of the equations provided by Batchelor [1957]. Therefore given a HIST velocity signal, $\tilde{v}$, and a respective time step, $\mathrm{d}\tilde{\tau}$, a non-stationary velocity signal along a trajectory can be generated by,

$$v(\tau) = \overline{u}(\boldsymbol{x}(\tau)) + \tilde{v}(\tilde{\tau})\sigma_u(\boldsymbol{x}(\tau)) \quad \text{and} \quad \mathrm{d}\tau = T_E(\boldsymbol{x}(\tau))\mathrm{d}\tilde{\tau}. \tag{4.1a,b}$$

HIST trajectories of the tracer particles are created using two separate modeling techniques: i) stochastic processes of Chapter 2 or ii) extracted from direct numerical simulations, as discussed in Section 2.3. The inputs into the proposed non-stationarization methods need to be nondimensionalized to be used in equa-

tions (4.1a,b). This is accomplished by using parameters from the DNS and the OU model to normalize the velocity and time lag to obtain respectively, $\tilde{v} = v_{_{HIT}}/\sigma_{u_{HIT}}$ and $\mathrm{d}\tilde{\tau} = \mathrm{d}\tau_{_{HIT}}/T_{L_{HIT}}$.

Equations (4.1a,b) require knowledge of the spatial distribution of the velocity and integral timescale. Here, a set of self-similarity relations are proposed to generate a jet from a point source. Based on relations presented in Hussein et al. [1994] and So and Hwang [1986], the mean streamwise velocity can be described by a Gaussian approximation for first order analysis and through continuity of an incompressible fluid the radial velocity is defined as:

$$\frac{\overline{u}_z(r,z)}{U_0(z)} \propto e^{-A_1\eta^2} \quad and \quad \frac{\overline{u}_r(r,z)}{U_0(z)} \propto \eta e^{-A_1\eta^2} - \frac{1-e^{-A_1\eta^2}}{2A_1\eta}, \tag{4.2a,b}$$

where $U_0(z)$ is the centerline velocity and η is a self-similarity variable defined as $r/(z-z_0)$ and z_0 is the virtual origin of the jet. It has been noted that $U_0(z) \propto (z-z_0)^{-1}$. The circumferential velocity does not contain a mean velocity, but fluctuations are relevant and must be considered.

The velocity variance, and therefore standard deviation for each component, also follows self-similarity relations obtained experimentally and defined as:

$$\frac{\sigma^2_{u_z}(r,z)}{U_0^2(z)} \propto e^{-A_2(\eta-B_2)^2}, \quad \frac{\sigma^2_{u_r}(r,z)}{U_0^2(z)} \propto e^{-A_3\eta^2} \quad and \quad \frac{\sigma^2_{u_\theta}(r,z)}{U_0^2(z)} \propto e^{-A_4(\eta-B_4)^2}. \tag{4.3a,b,c}$$

where $\sigma^2_{u_i} = \overline{u_i'^2}$ and u_i' is introduced as the fluctuating Eulerian velocity of component i provided by the Reynolds decomposition, $u_i'(r,z,t) = u_i(r,z,t) - \overline{u}_i(r,z)$.

The relation of T_E can be directly linked to the linear relations found for length

scales within the developing jet, specifically $L \propto z$. Then, defining the integral length scale $L \approx \sigma_u T_E$ and $\sigma_u \propto 1/z$, the Eulerian integral time scale evolves in the jet as:

$$T_{E_z}(z) \propto z^2, \tag{4.4}$$

and is consistent with the experimental trends observed in Section 3.4. Constants are found empirically by fitting the experimental data, explicit values are provided in the Appendix B.1.

4.3 Results

For the presentation of the results, HIST data modeled from Ornstein–Uhlenbeck are referred to as OU, HIST data which is extracted from the simulation is denoted with DNS. If the data has then been converted (ie., from HIST to non-stationary turbulent jet flow) it is prefaced with as Bachelor transformation (BT) prior to the acronym which describes whether it is acquired from OU or DNS. All experimental data will be denoted with EXP.

A first look at the trajectories that are generated by the non-stationarization process is included in figure 4.1. A detailed algorithm of the modeling process is included in Appendix B.2. For reference, a subset of HIST trajectories is presented in figure 4.1(a) prior to the transformation. Figure 4.1(b) provides the modeled trajectories based on the stochastic process HIST signals, BT-OU, and 4.1(c) presents the experimentally measured trajectories for visual comparison. Note that the trajectories originate from a point source to form the jet for the model and the experiment.

Qualitatively there are noticeable similarities between the two jets shown, the general spread of the jet as well as the decay of streamwise velocity are both captured well by the model, but differences are observed. The length of the trajectories obtained from the experiment are much shorter, resulting in the ending of trajectories at the turbulent/non-turbulent boundary layer while the model continues to track those particles that fall into the ambient and are often recaptured into the fast moving jet.

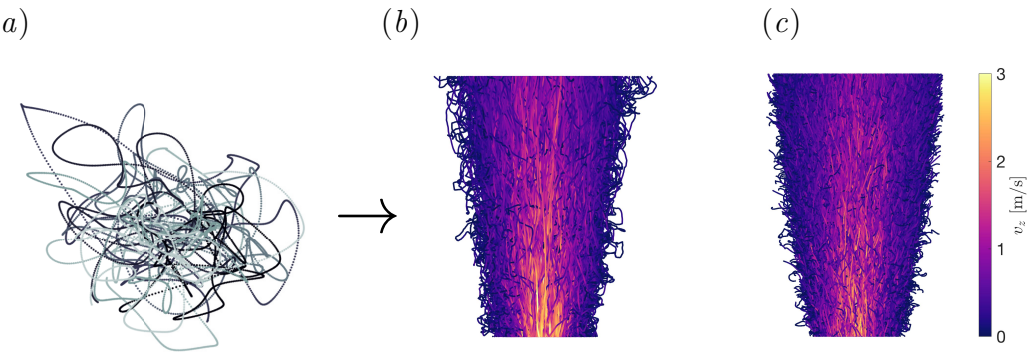

Figure 4.1: (a) HIST trajectories extracted prior to the Batchelor transformation, (b) the modeled trajectories from the Ornstein–Uhlenbeck process and (c) the experimental data. The colorbar denotes the axial velocity (same colorbar is used for both representations).

4.3.1 Eulerian statistics

A quantitative verification of the mean velocities and standard deviations can be obtained through Eulerian evaluations of the flow field. In this regard, the modeled Lagrangian trajectories, which are in cylindrical coordinates, are binned in z and $\eta = r/(z - z_0)$ every step of 0.5 mm and 0.01, respectively, to compute the time-averaged first and second-order statistics of particle velocities inside each bin. Figure 4.2

presents self-similarity profiles of streamwise, radial and concentration statistics for the outputs of the Batchelor transformed Ornstein–Uhlenbeck trajectories (BT-OU) at four locations downstream, $z/D = 15$, 25, 35 and 45. The statistics are normalized by a respective centerline axial velocity, U_0, or centerline concentration, ϕ_0. Additionally, the self-similarity profile for the experimental data is provided for comparison.

The time-averaged normalized streamwise velocity profiles, figure 4.2(a), collapse nearly perfectly, indicating that the modeled jet spreads and decays with similar behavior to the experimental data. For the radial velocity, there are small deviations observed in the mean velocity profiles, figure 4.2(b). There is good agreement with the experimental data in overall trends, although noise is observed at large η due to the minimal data available at the edges of the jet. It is important to note here that this agreement for the radial velocity is critical and indicates the ability of the model to capture the unique dynamics of the jet when seeded only within the jet. This is evidenced by the fact that the model matches the experimental data but inputs into the model are different than what is obtained from the trajectories. Specifically, for the incompressible jet, the known profile has an initial slope of 1/2 and the velocity becomes negative near $\eta \sim 0.12$, different than what is observed in figure 4.2(b) for the model and for the experiment. This is due to the entrained fluid which causes negative radial velocity at large η, which is not captured by the experiment because only the particles exiting the nozzle are tagged and equally not captured by the BT-model because particles are intentionally seeded only within the jet. This behavior was previously noted in Basset et al. [2022] and is validated here where the model is fed with the incompressible jet model but due to the input

to the model of particles from a point source, the true profiles observed by the data are recovered.

Figures 4.2(c) and 4.2(d) present the variance of the streamwise and radial velocity in self-similarity variables, where generally, a decay is observed in the variance as a function of η. Again, a collapse is observed for the two sets of profiles, signifying that the model is capturing the second-order trends present in the experimental data. This already demonstrates that the model can capture the variance of the jet and that it retains the self-similarity as the jet develops. Covariance is provided in figure 4.2(e), which, similar to the normal variances, shows a collapse. It is noted here that the HIST trajectories are not correlated (prescribed by the modeling techniques) and therefore a diagonalization of the covariance is imposed to correlate the two signals, see Appendix B.3 for details.

Finally the concentration profile is provided in figure 4.2(f) to see the diffusion of the jet into the quiescent surrounding fluid. No input into the model is associated with the jet concentration therefore all dynamics presented in the figure are purely from the particle motions indicated by the velocities of the model. Here, the resulting curves of the BT-model still present similar trends to those observed in the experimental data, although the parabolic behavior is not captured and the curves depict an almost linear relation for most values of η.

4.3.2 Lagrangian statistical model comparisons to experimental data

Due to the non-stationarity of the trajectories, conditions need to be applied to accurately characterize and compare statistics of the model output and the experimental results. As depicted in the schematics of figure 4.3, one method to accurately

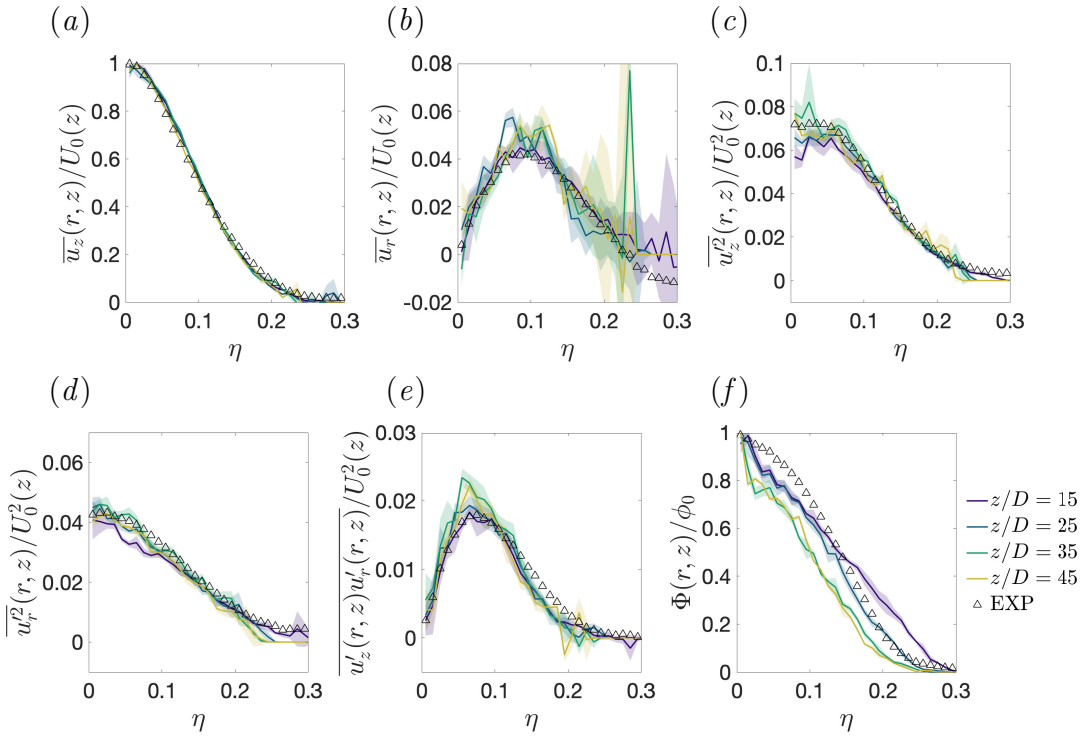

Figure 4.2: Self-Similarity profiles for the model vs. data. For each figure mean values are presented by the solid lines and the colored bands provide an additional standard deviation for a given η position.

compare the signals is to look at velocity differences of the trajectories conditioned on an initial location within a small sphere with a radius r_{max}. The given ensemble is created based on the trajectories that fall within the sphere, namely X_b and X_c from figure 4.3. The sphere radius, r_{max}, is set to the jet half-width divided by two, $\frac{1}{2}R_{1/2}$, to ensure convergence of the statistics while still sampling near the given axial location of interest. Next, statistics are calculated based on the t_0 (at the location close to the center of the interrogation sphere), i.e., the trajectories are now given a pseudo origin at t_{0b} and t_{0c}, for X_b and X_c, respectively. In an attempt to accurately average over the non-stationary trajectories, each time step is taken

from t_0, explicitly.

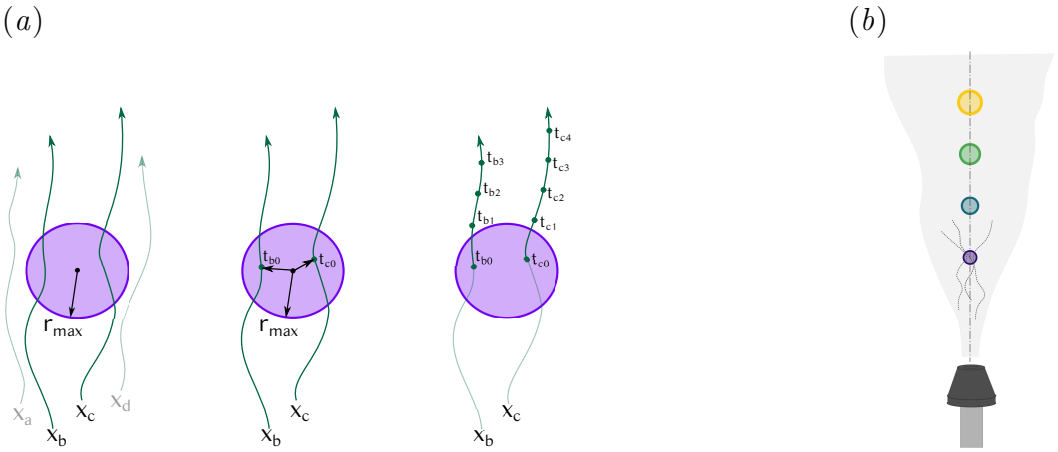

Figure 4.3: Schematic of the conditioning for statistical analysis of the non-stationary trajectories.

4.3.3 One-time statistics

Probability density functions (PDF) for the normalized axial and radial velocity (zero mean and unit variance) are given in figure 4.4. Four downstream positions $z/D = 15$, 25, 35 and 45 are included for comparison of the non-stationarity of the jet and the ability of the model to reproduce at a given location axial location. For each subsequent figure, all locations show the experimental data ($\triangle$), the outputs of the Batchelor transformation applied to the OU (-) and DNS (--). In figure 4.4, the PDFs are shifted for clarity of the fits and a Gaussian curve is also included in a dash-dotted line.

The axial velocity, figure 4.4(a), presents good agreement between the modeled data and the experimental PDF near the mean velocity. Both models and the experimental data show near Gaussian profiles, as is expected for this large scale

quantity. Small deviations start to occur around $v_z - \langle v_z \rangle \approx \pm 3.5\sigma_z$, when the experiment appears to be sub-Gaussian, possibly due to limitations in experimental interrogation volume and ability to obtain sufficient data with large velocities. The resulting curves also show very little dependence on the location, with the data following the Gaussian curve for all downstream locations. Trends observed here are similar to those in Gervais et al. [2007] for the longitudinal (v_z) component of velocity of the jet.

Similar to the streamwise velocity, the experimental radial component PDFs, figure 4.4(b), also demonstrate a Gaussian profile that is well captured by the modeling techniques until about $v_r - \langle v_r \rangle \approx \pm 3\sigma_r$. Here, the modeled data and the experimental data results still show fair agreement, both becoming over-Gaussian, presenting intermittent behaviors. Again, the curves fall nearly on top of each other, with minimal distinction between the z/D location. Furthermore, these profiles also agree with the PDFs of normalized traverse velocity from Gervais et al. [2007].

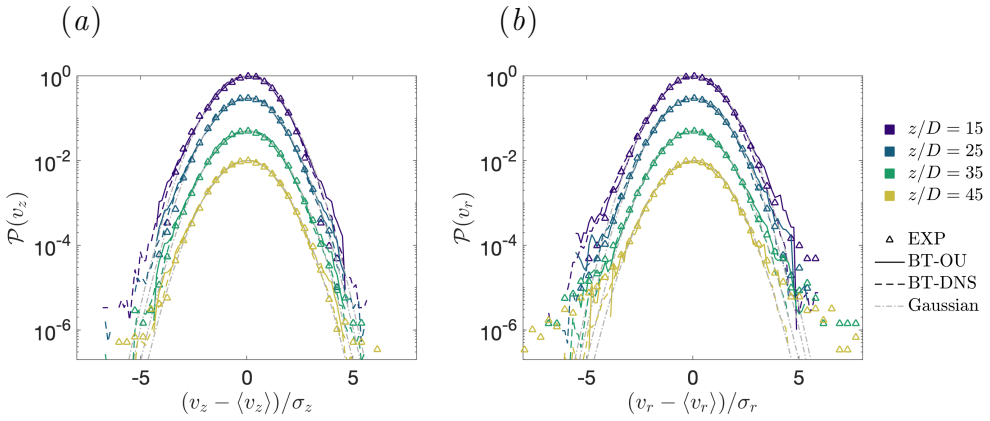

Figure 4.4: PDF of the axial and radial velocity from the model at 4 locations downstream.

4.3.4 Two-time statistics

Further information is gained from two-time statistics of the flow and therefore the correlation of velocity for the axial and radial component are presented in figure 4.5(a) and 4.5(b), respectively, where $\mathcal{C}_{v_i}(\tau) = \langle v_i(t_0 + \tau)v_i(t_0)\rangle$ and i is the component of velocity. The timescale is compensated by D/V_J, where D is the diameter of the nozzle and V_J is the exiting jet velocity. All of the following Lagrangian statistics are based on the conditioned trajectories as describe above. Finally, it is noted that the time-scale is adjusted at each location to collapse temporally with the experimental data, these adjustments could be due to the global differences of T_E and T_L, which has been previously shown to depend on location within the near-field of the jet (Section 3.4). Both axial and radial time shifts converge to a value of 0.8 and 1 within the considered locations.

The correlation of velocity gives information on accuracy of large scale modeling. For the axial velocity correlation function, figure 4.5(a), the model provides a very good agreement with the results from the experiment in shape at small and large time scales, $\tau D/V_J$, for each of the considered locations. The radial velocity, figure 4.5(b), also demonstrates remarkable agreement, with the model presenting small deviations from the experimental curves only at large time scales, likely when the experiment has low convergence due to track length deficiencies. Furthermore, the model shows an ability to obtain better statistics at great $\tau D/V_J$ values, and therefore large scale information can be extracted from the data with greater ease.

Velocity increment statistics of the modeling technique and the experiment are presented in figure 4.6 at four downstream positions $z/D = 15$, 25, 35 and 45. The structure functions used for the analysis are defined as $S_{n-i}(\tau) = \langle[v_i(t_0 + \tau) -$

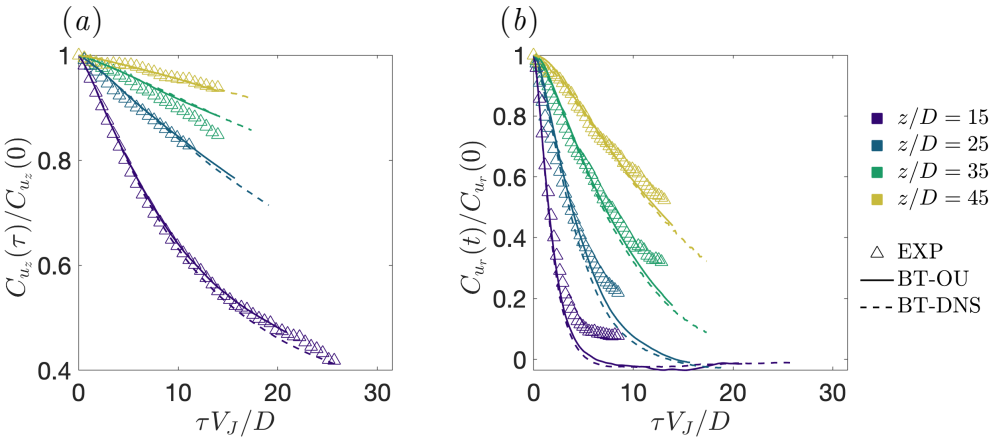

Figure 4.5: Two-time velocity correlations for the (a) axial and (b) radial components for the considered locations of $z/D = 15$, 25, 35 & 45.

$v_i(t_0)]^n\rangle$, where n is the moment and i is the velocity component. In addition to the modeling outputs, the second-order structure function of the HIST-OU data (dash-dotted) is included to better understand the transformation of the statistics. Again the timescale is non-dimensional, compensated by D/V_J. The axial component results, figure 4.6(a), show a collapse of the two models and the experimental data for all considered locations. There is a slight overestimation of the $z/D = 15$ profiles for the two models, likely due to the fact that the jet is not completely self-similar at the location. In general, the BT-OU trajectories provide both an extended dissipative range and large scale plateau in comparison to the trajectory statistics from the experiment. The BT-DNS also provides increased small scale information at the farthest downstream locations, but due to the time step of the DNS, as well as the length of the dataset, some small scale information and the large scale plateau are not recovered.

The radial velocity Lagrangian statistics can also be investigated and comparisons between the models and the experimental results are presented in figure 4.6(b).

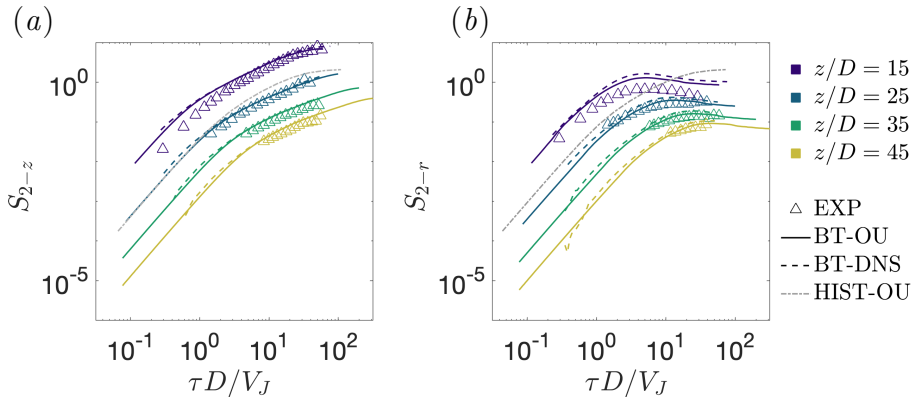

Figure 4.6: Second-order structure function for the (a) axial and (b) radial velocity component.

Similar to the axial velocity statistics, collapses are seen for the second-order structure function. Here the nearest-field location, $z = 15D$, shows a poor collapse for the structure functions although the behavior of the curves are similar in their tendency, which may be expected due to the overestimation of the velocity observed in the Eulerian statistics, figure 4.2(b). It is noted that large differences are observed between the outputs of the axial and radial components (most easily observed by comparing the jet curves to the HIST-OU curve) which is well captured globally by the models.

To better understand the ability of the model to include intermittent effects, small scale dynamics must be analyzed. It has been previously noted that Lagrangian velocity has Gaussian statistics but Lagrangian acceleration is strongly non-Gaussian in its behavior [Mordant et al., 2004a,b]. Therefore, expectations are that the velocity increments will present the intermittent behavior through non-Gaussian distributions as the time scale approaches the dissipative range. For this reason, the evolution of the Lagrangian velocity increments are presented as PDFs in figure 4.7 and figure 4.8 as a function of the time scale separation τ. The com-

pensated velocity difference (unit-variance), are presented for the time separation τ varying from τ_η to $20\tau_\eta$ for the four considered downstream locations, as denoted in their title. Note that the Kolmogorov time scale, τ_η, obtained from the experimental results, is dependent on location and velocity component. τ_η ranges from 0.098 ms to 0.774 ms for the axial time scale at the nearest to farthest downstream locations respectively and for the radial time scale, 0.125 ms at $z/D = 15$ and 0.646 ms at $z/D = 45$. As τ approaches $20\tau_\eta$, the integral time scale, T_L, is nearly reached at each axial location. Note that there is no experimental data available for the smallest time scale (and $5\tau_\eta$ at $z/D = 15$) due to temporal resolution. The DNS also presents challenges at these small time steps and are therefore only curves for $\tau \geq \tau_\eta$ are provided.

For the normalized axial velocity increments in figure 4.7, the profiles show expected results for Lagrangian turbulence, similar to those observed in homogeneous and isotropic turbulence [Mordant et al., 2004a] where the small scale separations show longer tails, indicating intermittency of the signal, which dissipates and the profiles become near Gaussian as $\tau \to 20\tau_\eta$. Minimal differences are visible between the sets of PDFs for the four presented locations. Comparing the ability of the two presented models, the model is incredibly accurate and near perfect agreement is observed across the four locations for the PDFs, at the largest time scale separations the modeled PDFs also show Gaussian behavior and as the time separations decrease, non-Gaussian behavior increases. The most prominent feature of these figures is the accuracy at which both the BT-OU and BT-DNS modeled PDFs collapse with those from the experiments. This highlights the ability of the model to pick up the highly specific behavior at small and large scales and at all locations within the

jet. There appears to be a minimal difference at the tails of the PDFs for the two models and the experiments. The BT-OU model under predicts the experimental data for rare events, for example, for $z/D = 25$, the model provides smaller values at $\delta_\tau \sim \pm 5\sigma_z$, not quite capturing the complete intermittent behavior of the rarest of events. The BT-DNS appears to provide better agreement with the data for these extreme events.

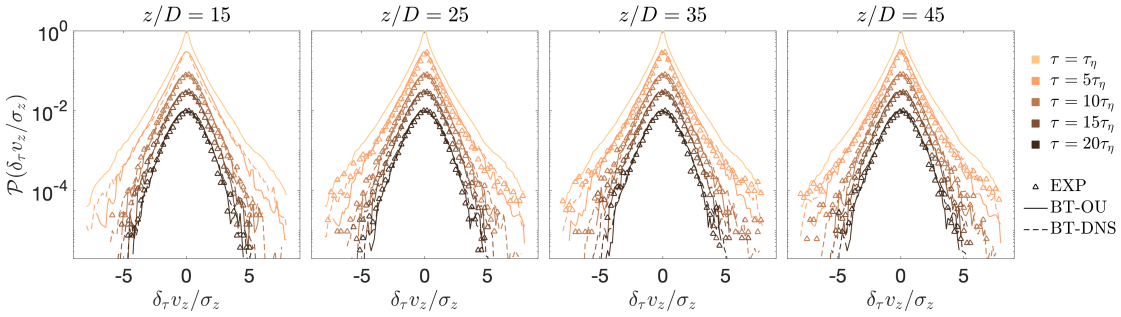

Figure 4.7: PDF of the axial velocity increment of the model and experiment for τ values provided in the legend at 4 locations downstream.

The normalized radial velocity difference at varying time scales is presented in figure 4.8. Here, noticeable differences are observed in comparison to the axial velocity increment PDFs (figure 4.7), most prominent is the observed positive skewness for all considered locations and time separations. The positive skewness is most amplified at the nearest jet exit location of $z/D = 15$ but persists within the range of downstream locations. This skewness is extremely well described by the model for both the OU and the DNS signals, providing indications of the acute ability of the model to accurately capture the multifractal behavior of the trajectories, over a range of scales, as they develop in the jet. It is of note that again, a minimal difference is observed for the tails of the PDFs for the BT-OU modeling (most easily observed in the negative velocity increments at the farthest downstream locations).

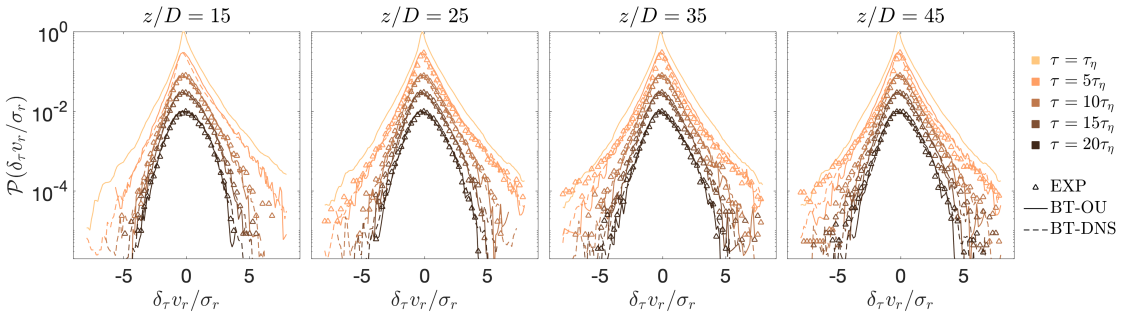

Figure 4.8: PDF of the radial velocity increment of the model and the experiment for τ values at 4 locations downstream.

Higher-order incremental analysis

The tails of the PDFs give indications of the accuracy of the model to capture true intermittency of the jet, but higher-order moment analysis will more distinctly highlight the behaviors present at the tails of the PDFs and the ability or inability of the modeling technique to replicate. This is important as differences in the BT-OU and BT-DNS models have already been noted, in a subtle way, from the tails of the velocity increment PDFs.

The flatness, $S_{4-z}/S_{2-z}^2/3$, shown in figure 4.9(a), provides these multifractal jet dynamics effects and those achievable from the models. There are clear differences between the far-dissipative (small timestep) tendencies. Here it is important to note that known deficits in the Ornstein–Uhlenbeck embedded modeling are observed in these scales as discussed in Section 2.3. In comparisons to DNS, it cannot capture this steep increase and this is again observed here by the differences in the BT-OU and BT-DNS curves.

For both the velocity components (axial in figure 4.9(a) and radial in figure 4.9(b)), for the near-field locations, the BT-DNS overestimates the EXP, but as

the jet develops, the model with the most accurate depiction of intermittency (BT-DNS) shows very good agreement. The BT-OU model shows fair comparisons to the EXP within the near-dissipative and inertial range, but the very small timescales are not well captured for the axial velocity kurtosis. The radial component of velocity shows better agreement for all curves, but no plateau is observed within the probed timescales for the model or the experiment. Overall, global trends are observed, it is a remarkable statistic that the model captures is the large rise in the flatness. Again the HIST-OU model is included and here, the extent of the highly non-Gaussian behavior of the radial velocity increments at small scales are observed in the experiment and reproduce with high accuracy by the modeled jet for both the BT-OU and BT-DNS.

The BT-OU and BT-DNS model provides information that cannot be achieved from the experimental data due to time resolution at small scales and interrogation volume limitations at large scales. This is observed in figure 4.9, where the modeled jet statistics present results that span larger and smaller $\tau D/V_J$ than EXP. Furthermore, the time scale and number of trajectories are inputs into the OU modeling and therefore, greater convergence of statistics is also attainable. The convergence can also be achieved with the DNS trajectories although, as previously noted, limitations exist on the observable time scales and the small scale resolution.

Evaluation of model

To characterize the abilities of the OU modeling to capture true statistics of the jet, an investigation into the effects of the finite number of layers is presented in figure 4.10, where only one location is considered ($z/D = 25$) for clarity. Here, an

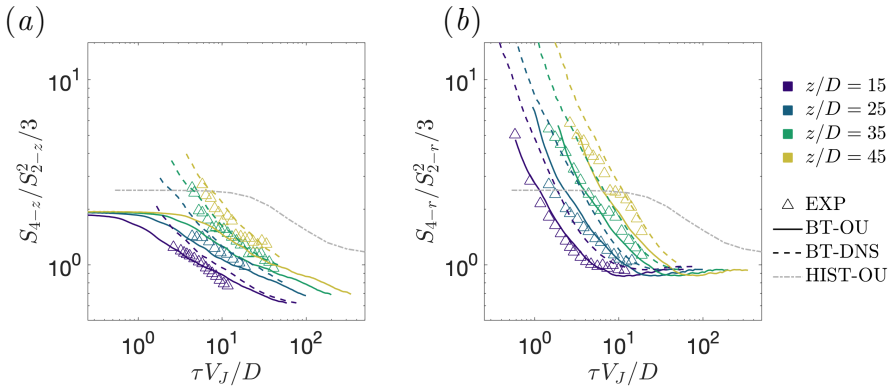

Figure 4.9: Kurtosis of the (a) axial velocity and (b) radial velocity as a function of $\tau D/V_J$ for the given locations.

Ornstein–Uhlenbeck model built with one-layer (BT-OU-1), two-layers (BT-OU-2) [Sawford, 1991], and nine-layers (BT-OU-9) (Section 2.3) are compared for previously presented statistics of the flow. Note that the single-layer model contains only a single time scale input and thus presents statistics for an infinite Re flow. The two-layer model by Sawford [1991] alleviates this by including a small scale into the second layer and thus creating a once-differentiable correlation of velocity.

Figure 4.10(a) provides the correlation function, which, due to the dominating large scale dynamics, shows good agreement between the three OU models and the experiment. The single layer model fails immediately once small scales become relevant, as seen in figure 4.10(b). Although there is not perfect agreement, the two-layer model shows more true dynamics with a τ^2 scaling in the dissipative range and τ scaling in inertial range. Even for these second-order statistics, there is the best agreement observed for the nine-layer model, at dissipate, inertial and even large scales, where the plateau can be observed. Considering higher-order moments, the flatness further emphasizes these differences between the models. Fair comparisons between all of the models and the experiment are seen in the inertial range, but the

known plateau at small scales for the flatness (observed in the nine-layer model) is not obtained in BT-OU-1 and BT-OU-2. The large scale should also converge (ideally to $S_{4-z}/S_{2-z}^2/3) = 1$, this turn to a constant flatness at large time scales is somewhat observed in BT-OU-9 while the single and double layer models continue to decay with a power-law.

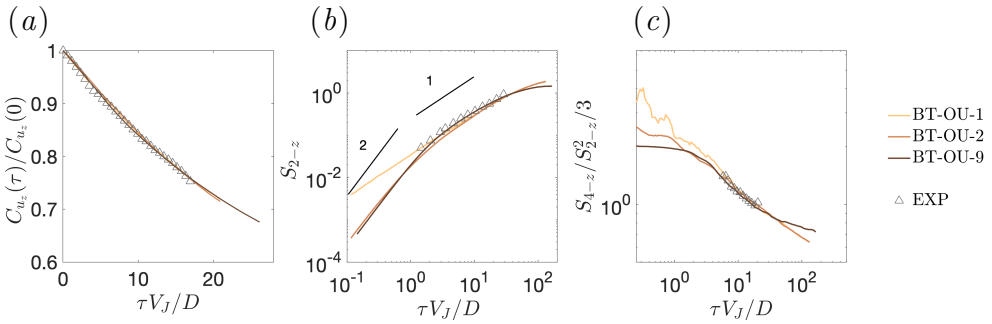

Figure 4.10: Comparison of output statistics for $z/D = 25$ for the OU model built with one, two or nine layers.

Another important factor of the modeling is the inclusion of intermittency to capture the true multifractal behavior of the velocity signals obtained via Ornstein–Uhlenbeck modeling. Similar to the investigations into the significance of the number of layers (i.e., the differentiability of the modeled trajectories), consequences of alteration to the intermittency coefficient γ are explored in figure 4.11 for the $z/D = 25$ location within the jet. Specifically, the nine-layer OU model is built with intermittency corrections of γ^2 =0, 0.085 and 0.17, where good agreement between modeling and true behaviors has been observed for $\gamma^2 = 0.085$ in Section 2.3. The correlation functions and the second-order structure functions are provided in figure 4.11(a) and 4.11(b). All curves collapse for the correlation function as intermittency does not play a crucial role in the large scale dynamics of the flow. Furthermore, the second-order structure function also collapse with

almost perfect agreement between the three models. True scaling behavior across all time scales are observed and again intermittency deficit or abundance is not causing discrepancy within this second-order statistic. Intermittency is crucial to the far-dissipative range dynamics and this is evident in the flatness representations presented in figure 4.11(c). Here, the performance of the model to accurately include multifractal behaviors is evident. The $\gamma = 0$ curve, severely under-represents the intermittent habits of the signal at small times but it should be noted that this curve shows no intermittency (i.e., $(S_{4-z}/S_{2-z}^2/3) = 1$ for the HIST output of the signal and therefore, the modeling of the trajectories instills some corrections to this Gaussian model, but is insufficient still. On the other end, if an over-estimation of intermittency is employed into the model, $\gamma^2 = 0.17$, the curve does not show the true inertial range and near-dissipative dynamics of the jet. Only when the well known $\gamma^2 = 0.085$ is applied does the most accurate depiction of the flatness, in comparison to the experimental data, occur. This only further acknowledges the intermittency coefficient to be $\gamma^2 = 0.085$.

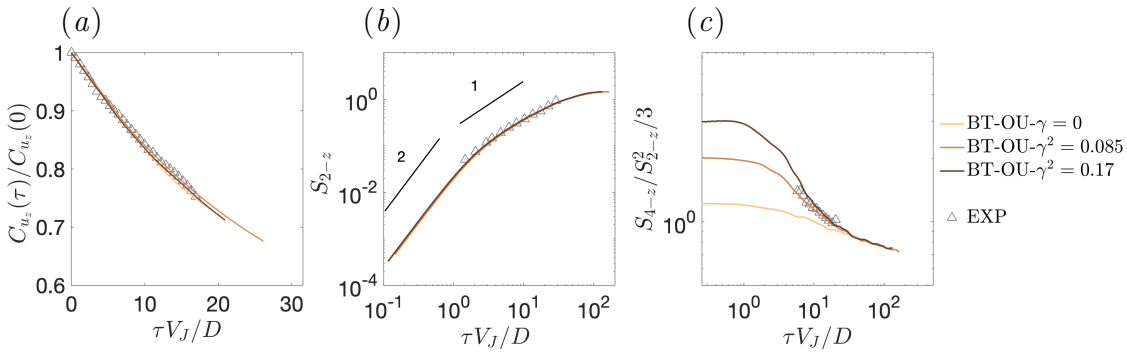

Figure 4.11: Comparison of output statistics for $z/D = 25$ for the OU model built with $\gamma^2 = 0$, 0.085 and 0.17.

4.4 Concluding remarks

A model is proposed which uses simple methods to transform a turbulent velocity signal which is homogeneous, isotropic and stationary to create Lagrangian trajectory velocities within a jet. The model is built using HIST velocity signals obtained from stochastic modeling and direct numerical simulations. Comparisons are made between the model and experimental data obtained from a water jet seeded with tracers. A number of statistics are analyzed, all show good agreement.

Notably, spatial first and second-order statistics are presented in their self-similar form and very good agreement is observed for all available statistics obtained from the experiment. Using techniques to compare Lagrangian statistics of non-stationary signals, both modeled jets and the experiment show similar velocity correlations. Velocity increment analysis is applied as well to study the second-order structure functions and the flatness. As expected, based on the velocity correlations, the second moment statistics again show nice trends, with minor differences observed within the nearer field of the jet, $z/D = 15$, for the radial component of velocity. The flatness presents a fair collapse of the profiles within the inertial range (i.e., where the higher-order statistics are more reliable from the experiment).

Most remarkable though, is the ability of the model to pick up the intermittent behaviors at varying time scales and locations, as it observed in the PDFs of the velocity increments for the axial and radial components. Specifically, the skewness of the radial velocity increments, which is non-trivial behavior observed in the radial velocity, is very accurately described by the model for both the OU and the DNS.

Finally, notes are made on the accuracy of less robust modeling techniques. Comparisons between the nine-layer embedded OU model and processes built with

a single or double-layer provide the reader with knowledge of what statistical advantages are present due to the higher level of differentiability of the inputted HIST velocity signal. Results show that large scales are unaffected (i.e., the correlations of velocity collapse) but the single-layer model, which suggest an infinite Re, fails for small scale representations. The two-layer model, although more accurate, presents discrepancies when compared to the nine-layer model in the far-dissipative range (as $\tau \to 0$) and also at very large scales. Intermittency corrections based on the input parameter γ are also compared to provide an idea of the necessity of an accurate coefficient to describe the sharp build up of the flatness as the time scale decreases. These effects are noted and convergence to the well known $\gamma^2 = 0.085$ is found to most accurately describe the inertial range and near-dissipative scales of the experimental data. The second-order structure function and the correlation of velocity show negligible dependence on the coefficient.

Chapter 5

Conclusions and Perspectives

5.1 Review of findings

The goal of this work was to improve the state of Lagrangian based modeling and analytics in order to enhance our understanding of flow mechanisms from this perspective and in turn possibly impact broader communities in turbulence. This was first accomplished by improving stochastic processes through the inclusion of more realistic behaviors at small scales. Specifically, this was achieved through increased differentiability of the velocity and acceleration processes and multifractal corrections, defined in the model in a causal way. Additionally, a simple filtering scheme was suggested to include non-tracer particle dynamics, which shows accurate results for inertial particle statistics based on Gaussian modeling efforts.

To investigate multi-scale phenomena in non-homogeneous flow, an experimental campaign was then performed where a jet of water was vertically injected into a tank and particle tracking velocimentry was invoked. Many relevant quantities were extracted from the experimental data, increasing our knowledge of large and small scale quantities and their dependence on location within the jet. This was possible due to the large interrogation volume of the experiment as well as the

ability to obtain adequate spatial and temporal resolution for both Eulerian and Lagrangian analysis of the particles. Most notable from the experimental findings was the stationarization technique (*á la* Batchelor) applied to the particle velocities and time steps. This not only enables the jet to be more easily characterized, but these techniques provide methods for any inhomogeneous flow to be analyzed with more ease. The successes found with this stationarization application led us to consider the modeling of inhomogeneous turbulence based on the transformation of the relations of Batchelor.

Specifically, this manifests itself as a set of simple equations which take a homogeneous, isotropic and stationary signal (obtained from stochastic modeling or simulations) to build up a jet with inputs of well known jet characteristics, such as spreading rate and centerline decay. This model was tested against trajectory statistics from the experimental jet and results show remarkable agreement in almost all statistical quantities. Most striking is the ability of the model to include the intermittency of the inputted signal, observed at varying time scales and locations by the PDFs of the velocity increment for both axial and radial components.

5.2 Outlook

Many open perspectives are left for ongoing studies from this project. First, the modeling of inertial particles is still in its infancy as far as the abilities of the processes to create realistic dynamics of the signals when dampened by the particle weight or size. Simple additions to the proposed model could entail updating the current filtering technique to include intermittency corrections, from which high-order moments could be captured and compared to simulations. The multifractal

formalism could also be used to model statistics with intermittency and could in turn be used in a similar fashion to the Batchelor parametrization presented for inertial particles.

The capability of the proposed Batchelor transformation of a set of homogeneous signals into an inhomogeneous flow leads to possible advancements in numerous fields. Within jets alone, the ability to track particle velocities is important to the entrainment and fallout during of volcanic episodes. Inputs can be tailored to accurately depict various real world circumstances, allowing the long dispersal of the fluid to be analyzed with greater accuracy.

In addition, this transformation will be extended to wind turbine wake dynamics to better model the underlying fluid mechanical processes. Current models for turbine wakes have difficulty including intermittency, which leads us to believe the Batchelor transformation we have proposed can benefit the wind power community. More specifically, this model, which can provide Lagrangian trajectories and Eulerian fields, is based on simple equations and contains the true multifractal behaviors of turbulence. Including intermittent behavior in the flow field is highly relevant to wind power as it is directly associated with causes of turbine component fatigue and needs to be taken into consideration in an accurate way.

Bibliography

R. Anderson and C. Meneveau. Effects of the similarity model in finite-difference les of isotropic turbulence using a lagrangian dynamic mixed model. *Flow, turbulence and combustion*, 62(3):201–225, 1999.

A. Arneodo, R. Benzi, J. Berg, L. Biferale, E. Bodenschatz, A. Busse, E. Calzavarini, B. Castaing, M. Cencini, L. Chevillard, R. T. Fisher, R. Grauer, H. Homann, D. Lamb, A. S. Lanotte, E. Lévèque, B. Lüthi, J. Mann, N. Mordant, W.-C. Müller, S. Ott, N. T. Ouellette, J.-F. Pinton, S. B. Pope, S. G. Roux, F. Toschi, H. Xu, and P. K. Yeung. Universal intermittent properties of particle trajectories in highly turbulent flows. *Physical Review Letters*, 100(25):254504, 2008.

E. Arneodo, A. Bacry and J.-F. Muzy. Random cascades on wavelet dyadic trees. *Journal of Mathematical Physics*, 39(8):4142–4164, 1998.

A. Arratia, A. Cabana, and E. Cabana. Modeling stationary data by a class of generalized ornstein-uhlenbeck processes: The gaussian case. In *International Symposium on Intelligent Data Analysis*, pages 13–24. Springer, 2014.

D. E. Aylor and T. K. Flesch. Estimating spore release rates using a lagrangian stochastic simulation model. *Journal of Applied Meteorology and Climatology*, 40 (7):1196–1208, 2001.

E. Bacry, J. Delour, and J.-F. Muzy. Multifractal random walk. *Physical Review E*, 64(2):026103, 2001.

T. Basset, B. Viggiano, T. Barois, M. Gibert, N.Mordant, R. B. Cal, R. Volk, and M. Bourgoin. Entrainment, diffusion and effective compressibility in a self-similar turbulent jet, 2022.

G. K. Batchelor. Kolmogoroff's theory of locally isotropic turbulence. In *Mathematical proceedings of the cambridge philosophical society*, volume 43, pages 533–559. Cambridge University Press, 1947.

G. K. Batchelor. The application of the similarity theory of turbulence to atmospheric diffusion. *Quarterly Journal of the Royal Meteorological Society*, 76(328): 133–146, 1950.

G. K. Batchelor. Pressure fluctuations in isotropic turbulence. In *Math. Proc. Cambridge Philos. Soc.*, volume 47, pages 359–374. Cambridge University Press, 1951.

G. K. Batchelor. Diffusion in free turbulent shear flows. *J. Fluid Mech.*, 3(1):67–80, 1957.

J. Bec, L. Biferale, G. Boffetta, A. Celani, M. Cencini, A. Lanotte, S. Musacchio, and F. Toschi. Acceleration statistics of heavy particles in turbulence. *J. Fluid Mech.*, 550:349–358, 2006.

J. Bec, L. Biferale, A. S. Lanotte, A. Scagliarini, and F. Toschi. Turbulent pair dispersion of inertial particles. *Journal of Fluid Mechanics*, 645:497–528, 2010.

J. Bec, L. Biferale, M. Cencini, A. S. Lanotte, and F. Toschi. Spatial and velocity statistics of inertial particles in turbulent flows. In *Journal of Physics-Conference Series*, volume 333, page 012003, 2011.

C. Beck. Lagrangian acceleration statistics in turbulent flows. *EPL (Europhysics Letters)*, 64(2):151, 2003.

L. Bentkamp, C. Lalescu, and M. Wilczek. Persistent accelerations disentangle lagrangian turbulence. *Nature communications*, 10(1):1–8, 2019.

R. Benzi, L. Biferale, A. Crisanti, G. Paladin, M. Vergassola, and A. Vulpiani. A random process for the construction of multiaffine fields. *Physica D: Nonlinear Phenomena*, 65(4):352–358, 1993.

R. Benzi, L. Biferale, R. Fisher, D. Lamb, and F. Toschi. Inertial range eulerian and lagrangian statistics from numerical simulations of isotropic turbulence. 2010.

T. Berk and F. Coletti. Transport of inertial particles in high-reynolds-number turbulent boundary layers. *Journal of Fluid Mechanics*, 903, 2020.

T. Berk and F. Coletti. Dynamics of small heavy particles in homogeneous turbulence: a lagrangian experimental study. *Journal of Fluid Mechanics*, 917, 2021.

G. Biferale, L. Boffetta, A. Celani, B. Devenish, A. Lanotte, and F. Toschi. Multifractal statistics of lagrangian velocity and acceleration in turbulence. *Physical review letters*, 93(6):064502, 2004.

L. Biferale, G. Boffetta, A. Celani, B. J. Devenish, A. Lanotte, and F. Toschi. La-

grangian statistics of particle pairs in homogeneous isotropic turbulence. *Physics of Fluids*, 17(11):115101, 2005.

M. S. Borgas. The multifractal lagrangian nature of turbulence. *Philosophical Transactions of the Royal Society of London. Series A: Physical and Engineering Sciences*, 342(1665):379–411, 1993.

M. S. Borgas and B. L. Sawford. Stochastic equations with multifractal random increments for modeling turbulent dispersion. *Physics of Fluids*, 6(2):618–633, 1994a.

M. S. Borgas and B. L. Sawford. A family of stochastic models for two-particle dispersion in isotropic homogeneous stationary turbulence. *Journal of fluid mechanics*, 279:69–99, 1994b.

W. Bos, L. Chevillard, J. Scott, and R. Rubinstein. Reynolds number effect on the velocity increment skewness in isotropic turbulence. *Physics of Fluids*, 24(1): 015108, 2012.

M. Bourgoin and S. G. Huisman. Using ray-traversal for 3D particle matching in the context of particle tracking velocimetry. Preprint arXiv:2003.12135 [physics.flu-dyn], 2020.

M. Bourgoin, N. T. Ouellette, H. Xu, J. Berg, and E. Bodenschatz. The role of pair dispersion in turbulent flow. *Science*, 311(5762):835–838, 2006.

R. D. Brown, Z. Warhaft, and G. A. Voth. Acceleration statistics of neutrally buoyant spherical particles in intense turbulence. *Physical review letters*, 103(19): 194501, 2009.

P. Burattini, R. A. Antonia, and L. Danaila. Similarity in the far field of a turbulent round jet. *Phys. Fluids*, 17(2):025101, 2005.

S. Byggstøyl and W. Kollmann. Closure model for intermittent turbulent flows. *International Journal of Heat and Mass Transfer*, 24(11):1811–1822, 1981.

E. Calzavarini, R. Volk, M. Bourgoin, E. Lévêque, J.-F. Pinton, and F. Toschi. Acceleration statistics of finite-sized particles in turbulent flow: the role of Faxén forces. *J. Fluid Mech.*, 630:179–189, 2009.

M. Cencini, J. Bec, L. Biferale, G. Boffetta, A. Celani, A. S. Lanotte, S. Musacchio, and F. Toschi. Dynamics and statistics of heavy particles in turbulent flows. *J. Turbul.*, (7):N36, 2006.

J. E. Cermak. Lagrangian similarity hypothesis applied to diffusion in turbulent shear flow. *J. Fluid Mech.*, 15(1):49–64, 1963.

L. Chevillard. Regularized fractional ornstein-uhlenbeck processes and their relevance to the modeling of fluid turbulence. *Physical review E*, 96(3):033111, 2017.

L. Chevillard, S. Roux, E. Lévêque, N. Mordant, J.-F. Pinton, and A. Arnéodo. Lagrangian velocity statistics in turbulent flows: Effects of dissipation. *Phys. Rev. Lett.*, 91(21):214502, 2003.

L. Chevillard, B. Castaing, and E. Lévêque. On the rapid increase of intermittency in the near-dissipation range of fully developed turbulence. *The European Physical Journal B-Condensed Matter and Complex Systems*, 45(4):561–567, 2005.

L. Chevillard, B. Castaing, E. Lévêque, and A. Arnéodo. Unified multifractal description of velocity increments statistics in turbulence: Intermittency and skewness. *Physica D*, 218(1):77–82, 2006.

L. Chevillard, B. Castaing, A. Arneodo, E. Lévêque, J.-F. Pinton, and S. G. Roux. A phenomenological theory of eulerian and lagrangian velocity fluctuations in turbulent flows. *Comptes Rendus Physique*, 13(9-10):899–928, 2012.

L. Chevillard, C. Garban, R. Rhodes, and V. Vargas. On a skewed and multifractal unidimensional random field, as a probabilistic representation of kolmogorov's views on turbulence. In *Annales Henri Poincaré*, volume 20, pages 3693–3741. Springer, 2019.

J. P. Chollet. Two-point closure used for a sub-grid scale model in large eddy simulations. In *Turbulent shear flows 4*, pages 62–72. Springer, 1985.

G. Comte-Bellot and S. Corrsin. Simple eulerian time correlation of full-and narrow-band velocity signals in grid-generated,'isotropic'turbulence. *Journal of Fluid Mechanics*, 48(2):273–337, 1971.

S. Corrsin. Investigation of flow in an axially symmetrical heated jet of air. Nat. Adv. Comm. f. Aeron., Adv. Conf. Rep. 3L23, Wartime Report W-94, 1943.

S. Du, B. L. Sawford, J. D. Wilson, and D. J. Wilson. Estimation of the Kolmogorov constant (C_0) for the Lagrangian structure function, using a second-order Lagrangian model of grid turbulence. *Phys. Fluids*, 7(12):3083–3090, 1995.

J. K. Eaton and J. R. Fessler. Preferential concentration of particles by turbulence. *International Journal of Multiphase Flow*, 20:169–209, 1994.

S. Edouard, B. Legras, F. Lefevre, and R. Eymard. The effect of small-scale inhomogeneities on ozone depletion in the arctic. *Nature*, 384(6608):444–447, 1996.

G. Falkovich, H. Xu, A. Pumir, E. Bodenschatz, L. Biferale, G. Boffetta, A. S. Lanotte, F. Toschi, and I. C. for Turbulence Research). On lagrangian single-particle statistics. *Physics of Fluids*, 24(5):055102, 2012.

P. Franzese. Lagrangian stochastic modeling of a fluctuating plume in the convective boundary layer. *Atmospheric Environment*, 37(12):1691–1701, 2003.

J. Friedrich, B. Viggiano, M. Bourgoin, R. B. Cal, and L. Chevillard. Single inertial particle statistics in turbulent flows from lagrangian velocity models. *Physical Review Fluids*, 7(1):014303, 2022.

R. Friedrich. Statistics of lagrangian velocities in turbulent flows. *Physical review letters*, 90(8):084501, 2003.

U. Frisch. *Turbulence: The Legacy of A.N. Kolmogorov*. Cambridge University Press, 1995.

C. Fureby, G. Tabor, H. G. Weller, and A. D. Gosman. A comparative study of subgrid scale models in homogeneous isotropic turbulence. *Physics of fluids*, 9(5): 1416–1429, 1997.

M. Gad-el Hak and S. Corrsin. Measurements of the nearly isotropic turbulence behind a uniform jet grid. *Journal of Fluid Mechanics*, 62(1):115–143, 1974.

R. Gatignol. The faxen formulas for a rigid particle in an unsteady non-uniform Stokes flow. *J. Mec. Theor. Appl,*, 1:143, 1983.

P. Gervais, C. Baudet, and Y. Gagne. Acoustic Lagrangian velocity measurement in a turbulent air jet. *Exp. Fluids*, 42(3):371–384, 2007.

T. Gotoh and D. Fukayama. Pressure spectrum in homogeneous turbulence. *Physical Review Letters*, 86(17):3775, 2001.

Y. G. Guezennec, R. S. Brodkey, N. Trigui, and J. C. Kent. Algorithms for fully automated three-dimensional particle tracking velocimetry. *Exp. Fluids*, 17(4): 209–219, 1994.

J. O. Hinze and B. G. V. D. H. Zijnen. Transfer of heat and matter in the turbulent mixing zone of an axially symmetrical jet. *Flow Turb. Combust.*, 1:435–461, 1949.

M. Holzner, A. Liberzon, N. Nikitin, B. Lüthi, W. Kinzelbach, and A. Tsinober. A Lagrangian investigation of the small-scale features of turbulent entrainment through particle tracking and direct numerical simulation. *J. Fluid Mech.*, 598: 465–475, 2008.

P. D. Huck. *Particle dynamics in turbulence : from the role of inhomogeneity and anisotropy to collective effects*. PhD thesis, Université de Lyon, 2017.

P. D. Huck, N. Machicoane, and R. Volk. Lagrangian acceleration timescales in anisotropic turbulence. *Phys. Rev. Fluids*, 4(6):064606, 2019.

T. J. R. Hughes, L. Mazzei, A. A. Oberai, and A. A. Wray. The multiscale formulation of large eddy simulation: Decay of homogeneous isotropic turbulence. *Physics of fluids*, 13(2):505–512, 2001.

H. J. Hussein, S. P. Capp, and W. K. George. Velocity measurements in a high-Reynolds-number, momentum-conserving, axisymmetric, turbulent jet. *J. Fluid Mech.*, 258:31–75, 1994.

T. Ishihara and Y. Kaneda. Relative diffusion of a pair of fluid particles in the inertial subrange of turbulence. *Physics of Fluids*, 14(11):L69–L72, 2002.

T. Ishihara, Y. Kaneda, M. Yokokawa, K. Itakura, and A. Uno. Small-scale statistics in high-resolution direct numerical simulation of turbulence: Reynolds number dependence of one-point velocity gradient statistics. *Journal of Fluid Mechanics*, 592:335–366, 2007.

T. Ishihara, T. Gotoh, and Y. Kaneda. Study of high–reynolds number isotropic turbulence by direct numerical simulation. *Annual Review of Fluid Mechanics*, 41:165–180, 2009.

J. Jiménez, A. A. Wray, P. G. Saffman, and R. S. Rogallo. The structure of intense vorticity in isotropic turbulence. *Journal of Fluid Mechanics*, 255:65–90, 1993.

H. S. Kang, S. Chester, and C. Meneveau. Decaying turbulence in an active-grid-generated flow and comparisons with large-eddy simulation. *Journal of Fluid Mechanics*, 480:129–160, 2003.

I. M. Kennedy and M. H. Moody. Particle dispersion in a turbulent round jet. *Exp. Therm. Fluid Sci.*, 18(1):11–26, 1998.

J.-T. Kim, A. Liberzon, and L. P. Chamorro. Characterisation of the eulerian and lagrangian accelerations in the intermediate field of turbulent circular jets. *Journal of Turbulence*, 18(1):87–102, 2017.

Y. Kimura and J. R. Herring. Diffusion in stably stratified turbulence. *Journal of Fluid Mechanics*, 328:253–269, 1996.

A. N. Kolmogorov. The local structure of turbulence in incompressible viscous fluid for very large Reynolds numbers. *Dokl. Akad. Nauk SSSR*, 30(4):301–305, 1941.

A. N. Kolmogorov. A refinement of previous hypotheses concerning the local structure of turbulence in a viscous incompressible fluid at high reynolds number. *Journal of Fluid Mechanics*, 13(1):82–85, 1962.

R. H. Kraichnan. Relation between Lagrangian and Eulerian correlation times of a turbulent velocity field. *Phys. Fluids*, 7(1):142–143, 1964.

P.-Å. Krogstad and P. A. Davidson. Is grid turbulence saffman turbulence? *Journal of Fluid Mechanics*, 642:373–394, 2010.

A. La Porta, G. A. Voth, A. M. Crawford, J. Alexander, and E. Bodenschatz. Fluid particle accelerations in fully developed turbulence. *Nature*, 409(6823):1017–1019, 2001.

A. G. Lamorgese, S. B. Pope, P. K. Yeung, and B. L. Sawford. A conditionally cubic-gaussian stochastic lagrangian model for acceleration in isotropic turbulence. *arXiv preprint cond-mat/0512212*, 2005.

M. Lesieur and O. Metais. New trends in large-eddy simulations of turbulence. *Annual review of fluid mechanics*, 28(1):45–82, 1996.

Y. Li, E. Perlman, M. Wan, Y. Yang, C. Meneveau, R. Burns, S. Chen, A. Szalay, and G. Eyink. A public turbulence database cluster and applications to study

lagrangian evolution of velocity increments in turbulence. *Journal of Turbulence*, (9):N31, 2008.

R.-C. Lien and E. A. D'Asaro. The Kolmogorov constant for the Lagrangian velocity spectrum and structure function. *Phys. Fluids*, 14(12):4456–4459, 2002.

R.-C. Lien, E. A. D'Asaro, and G. T. Dairiki. Lagrangian frequency spectra of vertical velocity and vorticity in high-Reynolds-number oceanic turbulence. *J. Fluid Mech.*, 362:177–198, 1998.

G. Lipari and P. K. Stansby. Review of experimental data on incompressible turbulent round jets. *Flow, turbulence and combustion*, 87(1):79–114, 2011.

G. Lipari, D. D. Apsley, and P. K. Stansby. Numerical particle tracking studies in a turbulent round jet. In *Particle-Laden Flow*, pages 207–219. Springer, 2007.

D. Lohse and A. Müller-Groeling. Bottleneck effects in turbulence: scaling phenomena in r versus p space. *Phys. Rev. Lett.*, 74(10):1747–1750, 1995.

N. Machicoane, P. D. Huck, and R. Volk. Estimating two-point statistics from derivatives of a signal containing noise: Application to auto-correlation functions of turbulent Lagrangian tracks. *Rev. Sci. Instrum.*, 88(6):065113, 2017a.

N. Machicoane, M. López-Caballero, M. Bourgoin, A. Aliseda, and R. Volk. A multi-time-step noise reduction method for measuring velocity statistics from particle tracking velocimetry. *Meas. Sci. Technol.*, 28(10):107002, 2017b.

N. Machicoane, A. Aliseda, R. Volk, and M. Bourgoin. A simplified and versatile

calibration method for multi-camera optical systems in 3D particle imaging. *Rev. Sci. Instrum.*, 90(3):035112, 2019.

M. R. Maxey and J. J. Riley. Equation of motion for a small rigid sphere in a nonuniform flow. *Phys. Fluids*, 26(1983):883, 1983.

C. Meneveau. Transition between viscous and inertial-range scaling of turbulence structure functions. *Physical Review E*, 54(4):3657, 1996.

C. Meneveau and K. R. Sreenivasan. Simple multifractal cascade model for fully developed turbulence. *Physical review letters*, 59(13):1424, 1987.

J.-P. Minier, S. Chibbaro, and S. B. Pope. Guidelines for the formulation of lagrangian stochastic models for particle simulations of single-phase and dispersed two-phase turbulent flows. *Physics of Fluids*, 26(11):113303, 2014a.

J.-P. Minier, S. Chibbaro, and S. B. Pope. Guidelines for the formulation of lagrangian stochastic models for particle simulations of single-phase and dispersed two-phase turbulent flows. *Physics of Fluids*, 26(11):113303, 2014b.

A. S. Monin and A. M. Yaglom. *Statistical Fluid Mechanics: Mechanics of Turbulence, Volume 2*. MIT Press, 1975.

M. Mordant, E. Lévêque, and J.-F. Pinton. Experimental and numerical study of the Lagrangian dynamics of high Reynolds turbulence. *New J. Phys*, 6(1):116, 2004a.

N. Mordant, P. Metz, O. Michel, and J.-F. Pinton. Measurement of Lagrangian velocity in fully developed turbulence. *Phys. Rev. Lett.*, 87(21):214501, 2001a.

N. Mordant, O. Michel, J.-F. Pinton, and P. Metz. Scaling and intermittency of lagrangian velocity in fully developed turbulence. Technical report, 2001b.

N. Mordant, J. Delour, E. Léveque, A. Arnéodo, and J.-F. Pinton. Long time correlations in lagrangian dynamics: a key to intermittency in turbulence. *Physical review letters*, 89(25):254502, 2002.

N. Mordant, J. Delour, E. Léveque, O. Michel, A. Arnéodo, and J.-F. Pinton. Lagrangian velocity fluctuations in fully developed turbulence: scaling, intermittency, and dynamics. *Journal of Statistical Physics*, 113(5):701–717, 2003.

N. Mordant, A. M. Crawford, and E. Bodenschatz. Experimental Lagrangian acceleration probability density function measurement. *Physica D*, 193(1-4):245–251, 2004b.

M. Nelkin. Multifractal scaling of velocity derivatives in turbulence. *Physical Review A*, 42(12):7226, 1990.

D. Nualart. *The Malliavin calculus and related topics*, volume 1995. Springer, 2006.

A. Obukhov. Spectral energy distribution in a turbulent flow. *Izv. Akad. Nauk. SSSR. Ser. Geogr. i. Geofiz*, 5:453–466, 1941.

S. A. Orszag. Numerical methods for the simulation of turbulence. *The Physics of Fluids*, 12(12):II–250, 1969.

N. T. Ouellette. Extending the reach of lagrangian analysis in turbulence. *Journal of Fluid Mechanics*, 924, 2021.

N. T. Ouellette, H. Xu, and E. Bodenschatz. A quantitative study of three-dimensional Lagrangian particle tracking algorithms. *Exp. Fluids*, 40(2):301–313, 2006a.

N. T. Ouellette, H. Xu, M. Bourgoin, and E. Bodenschatz. An experimental study of turbulent relative dispersion models. *New Journal of Physics*, 8(6):109, 2006b.

N. T. Ouellette, H. Xu, M. Bourgoin, and E. Bodenschatz. Small-scale anisotropy in Lagrangian turbulence. *New J. Phys*, 8(6):102, 2006c.

G. Paladin and A. Vulpiani. Degrees of freedom of turbulence. *Physical Review A*, 35(4):1971, 1987.

R. M. Pereira, C. Garban, and L. Chevillard. A dissipative random velocity field for fully developed fluid turbulence. *Journal of Fluid Mechanics*, 794:369–408, 2016.

R. M. Pereira, L. Moriconi, and L. Chevillard. A multifractal model for the velocity gradients dynamics in turbulent flows. *Journal of Fluid Mechanics*, 839:430–467, 2018.

J. F. Pinton and B. L. Sawford. A lagrangian view of turbulent dispersion and mixing. *Ten Chapters in Turbulence*, pages 132–175, 2012.

E. Pitton, C. Marchioli, V. Lavezzo, A. Soldati, and F. Toschi. Anisotropy in pair dispersion of inertial particles in turbulent channel flow. *Physics of Fluids*, 24(7): 073305, 2012.

S. B. Pope. Lagrangian microscales in turbulence. *Philosophical Transactions of*

the Royal Society of London. Series A: Physical and Engineering Sciences, 333 (1631):309–319, 1990.

S. B. Pope. *Turbulent Flows*. Cambridge University Press, 2000.

S. B. Pope. A stochastic lagrangian model for acceleration in turbulent flows. *Physics of Fluids*, 14(7):2360–2375, 2002.

S. B. Pope and Y. L. Chen. The velocity-dissipation probability density function model for turbulent flows. *Physics of Fluids A: Fluid Dynamics*, 2(8):1437–1449, 1990.

A. Popoulis and S. U. Pillai. Probability, random variables, and stochastic processes. *International Edition*, 1991.

A. Pumir and M. Wilkinson. Collisional Aggregation Due to Turbulence. *Annu. Rev. Condens. Matter Phys.*, 7(1):141–170, mar 2016. ISSN 1947-5462.

N. M. Qureshi, M. Bourgoin, C. Baudet, A. Cartellier, and Y. Gagne. Turbulent transport of material particles: An experimental study of finite size effects. *Phys. Rev. Lett.*, 99(18), 2007.

A. M. Reynolds. Superstatistical mechanics of tracer-particle motions in turbulence. *Physical review letters*, 91(8):084503, 2003.

A. M. Reynolds, N. Mordant, A. M. Crawford, and E. Bodenschatz. On the distribution of lagrangian accelerations in turbulent flows. *New Journal of Physics*, 7 (1):58, 2005.

R. Rhodes and V. Vargas. Gaussian multiplicative chaos and applications: a review. *Probability Surveys*, 11:315–392, 2009.

L. F. Richardson. *Weather prediction by numerical process.* Cambridge university press, 1922.

L. F. Richardson. Atmospheric diffusion shown on a distance-neighbour graph. *Proceedings of the Royal Society of London. Series A, Containing Papers of a Mathematical and Physical Character*, 110(756):709–737, 1926.

R. S. Rogallo and P. Moin. Numerical simulation of turbulent flows. *Annual review of fluid mechanics*, 16(1):99–137, 1984.

G. P. Romano and R. A. Antonia. Longitudinal and transverse structure functions in a turbulent round jet: effect of initial conditions and Reynolds number. *J. Fluid Mech.*, 436:231–248, 2001.

Y. Sato and K. Yamamoto. Lagrangian measurement of fluid-particle motion in an isotropic turbulent field. *J. Fluid Mech.*, 175:183–199, 1987.

B. L. Sawford. Reynolds number effects in Lagrangian stochastic models of turbulent dispersion. *Phys. Fluids A*, 3(6):1577–1586, 1991.

B. L. Sawford and P. K. Yeung. Lagrangian statistics in uniform shear flow: Direct numerical simulation and Lagrangian stochastic models. *Phys. Fluids*, 13(9):2627–2634, 2001.

B. L. Sawford, P. K. Yeung, M. S. Borgas, P. Vedula, A. La Porta, A. M. Crawford,

and E. Bodenschatz. Conditional and unconditional acceleration statistics in turbulence. *Physics of Fluids*, 15(11):3478–3489, 2003.

Z.-S. She and E. Leveque. Universal scaling laws in fully developed turbulence. *Physical review letters*, 72(3):336, 1994.

R. Shnapp, Y. Bohbot-Raviv, A. Liberzon, and E. Fattal. Turbulence-obstacle interactions in the lagrangian framework: applications for stochastic modeling in canopy flows. *Physical Review Fluids*, 5(9):094601, 2020.

E. D. Siggia. Numerical study of small-scale intermittency in three-dimensional turbulence. *Journal of Fluid Mechanics*, 107:375–406, 1981.

W. H. Snyder and J. L. Lumley. Some measurements of particle velocity autocorrelation functions in a turbulent flow. *Journal of Fluid Mechanics*, 48(1):41–71, 1971.

R. M. C. So and B. C. Hwang. On similarity solutions for turbulent and heated round jets. *Zeitschrift für angewandte Mathematik und Physik ZAMP*, 37(4): 624–631, 1986.

R. R. Taveira, J. S. Diogo, D. C. Lopes, and C. B. da Silva. Lagrangian statistics across the turbulent-nonturbulent interface in a turbulent plane jet. *Physical Review E*, 88(4):043001, 2013.

G. I. Taylor. Diffusion by continuous movements. *Proc. Lond. Math. Soc.*, 20(1): 196–212, 1922.

C.-M. Tchen. *Mean value and correlation problems connected with the motion of small particles suspended in a turbulent fluid*. Springer, 2013.

H. Tennekes and J. L. Lumley. *A first course in turbulence*. MIT press, 1972.

D. J. Thomson. Criteria for the selection of stochastic models of particle trajectories in turbulent flows. *Journal of fluid mechanics*, 180:529–556, 1987.

I. Torrano, M. Tutar, M. Martinez-Agirre, A. Rouquier, N. Mordant, and M. Bourgoin. Comparison of experimental and rans-based numerical studies of the decay of grid-generated turbulence. *Journal of Fluids Engineering*, 137(6), 2015.

F. Toschi and E. Bodenschatz. Lagrangian properties of particles in turbulence. *Ann. Rev. Fluid Mech.*, 41:375–404, 2009.

J. C. Vassilicos et al. *Intermittency in turbulent flows*. Cambridge University Press, 2001.

P. Vedula and P. K. Yeung. Similarity scaling of acceleration and pressure statistics in numerical simulations of isotropic turbulence. *Phys. Fluids*, 11(5):1208–1220, 1999.

B. Viggiano, J. Friedrich, R. Volk, M. Bourgoin, R. B. Cal, and L. Chevillard. Modelling Lagrangian velocity and acceleration in turbulent flows as infinitely differentiable stochastic processes. *J. Fluid Mech.*, 900:A27, 2020.

B. Viggiano, T. Basset, S. Solovitz, T. Barois, M. Gibert, N. Mordant, L. Chevillard, R. Volk, M. Bourgoin, and R. B. Cal. Lagrangian diffusion properties of a free shear turbulent jet. *J. Fluid Mech.*, 918:A25, 2021.

R. Volk, E. Calzavarini, G. Verhille, D. Lohse, N. Mordant, J.-F. Pinton, and F. Toschi. Acceleration of heavy and light particles in turbulence: Comparison between experiments and direct numerical simulations. *Physica D*, 237(14-17): 2084–2089, 2008.

R. Volk, E. Calzavarini, E. Lévêque, and J.-F. Pinton. Dynamics of inertial particles in a turbulent von Kármán flow. *J. Fluid Mech.*, 668:223–235, 2011.

G. A. Voth, K. Satyanarayan, and E. Bodenschatz. Lagrangian acceleration measurements at large reynolds numbers. *Physics of Fluids*, 10(9):2268–2280, 1998.

G. A. Voth, A. la Porta, A. M. Crawford, J. Alexander, and E. Bodenschatz. Measurement of particle accelerations in fully developed turbulence. *J. Fluid Mech.*, 469:121–160, 2002.

Z. Warhaft and J. L. Lumley. An experimental study of the decay of temperature fluctuations in grid-generated turbulence. *Journal of Fluid Mechanics*, 88(4):659–684, 1978.

T. Watanabe, C. B. da Silva, and K. Nagata. Multi-particle dispersion during entrainment in turbulent free-shear flows. *Journal of Fluid Mechanics*, 805, 2016.

J. C. Weil. A hybrid lagrangian dispersion model for elevated sources in the convective boundary layer. *Atmospheric Environment*, 28(21):3433–3448, 1994.

T. H. Weisgraber and D. Liepmann. Turbulent structure during transition to self-similarity in a round jet. *Exp. Fluids*, 24(3):210–224, 1998.

J. D. Wilson and B. L. Sawford. Review of Lagrangian stochastic models for trajectories in the turbulent atmosphere. *Boundary-Layer Meteorol.*, 78(1-2):191–210, 1996.

J. D. Wilson, G. W. Thurtell, and G. E. Kidd. Numerical simulation of particle trajectories in inhomogeneous turbulence, i: Systems with constant turbulent velocity scale. *Boundary-Layer Meteorology*, 21(3):295–313, 1981a.

J. D. Wilson, G. W. Thurtell, and G. E. Kidd. Numerical simulation of particle trajectories in inhomogeneous turbulence, ii: Systems with variable turbulent velocity scale. *Boundary-layer meteorology*, 21(4):423–441, 1981b.

J. D. Wilson, G. W. Thurtell, and G. E. Kidd. Numerical simulation of particle trajectories in inhomogeneous turbulence, iii: Comparison of predictions with experimental data for the atmospheric surface layer. *Boundary-Layer Meteorology*, 21(4):443–463, 1981c.

M. Wolf, B. Lüthi, M. Holzner, D. Krug, W. Kinzelbach, and A. Tsinober. Investigations on the local entrainment velocity in a turbulent jet. *Phys. Fluids*, 24(10): 105110, 2012.

P. K. Yeung. Lagrangian investigations of turbulence. *Ann. Rev. Fluid Mech.*, 34: 115–142, 2002.

P. K. Yeung and S. B. Pope. Lagrangian statistics from direct numerical simulations of isotropic turbulence. *J. Fluid Mech.*, 207:531–586, 1989.

P. K. Yeung, S. B. Pope, E. A. Kurth, and A. G. Lamorgese. Lagrangian conditional

statistics, acceleration and local relative motion in numerically simulated isotropic turbulence. *Journal of Fluid Mechanics*, 582:399–422, 2007.

H. Yu, K. Kanov, E. Perlman, J. Graham, E. Frederix, R. Burns, A. Szalay, G. Eyink, and C. Meneveau. Studying Lagrangian dynamics of turbulence using on-demand fluid particle tracking in a public turbulence database. *J. Turbul.*, (13):N12, 2012.

R. Zimmermann, H. Xu, Y. Gasteuil, M. Bourgoin, R. Volk, J.-F. Pinton, E. Bodenschatz, and International Collaboration for Turbulence Research. The Lagrangian exploration module: An apparatus for the study of statistically homogeneous and isotropic turbulence. *Rev. Sci. Instrum.*, 81(5):055112, 2010.

Appendix A

Propositions, properties and derivations concerning the Ornstein-Uhlenbeck and mutifractal formalism

A.1 Propositions concerning infinitely differentiable causal stochastic processes

Proposition A.1.1 *Assume $n \geq 2$. Then the correlation functions of velocity and acceleration are given by*

$$\mathcal{C}_{v_n}(\tau) = q_{(n)} \left(G_T \star G_{\tau_\eta}^{\star(n-1)} \right)(\tau), \tag{A.1}$$

and

$$\mathcal{C}_{a_n}(\tau) = -\frac{d^2 \mathcal{C}_{v_n}(\tau)}{d\tau^2}, \tag{A.2}$$

where the correlation product $\star$ is introduced, which is defined as, for any two functions g_1 and g_2,

$$(g_1 \star g_2)(\tau) = \int_{\mathbb{R}} g_1(t) g_2(t+\tau) dt,$$

with the corresponding short-hand notation,

$$g^{\star n} = \underbrace{g \star g \star \cdots \star g}_{n},$$

and the response function of the OU process at a given time scale τ (here $\tau = T$ or $\tau = \tau_\eta$)

$$t \in \mathbb{R} \mapsto G_\tau(t) = \frac{\tau}{2} e^{-|t|/\tau}. \tag{A.3}$$

For the sake of completeness, the spectral view of the correlation functions of velocity and acceleration (Eqs. A.1 and A.2) are included, which is especially useful when seeking their explicit expression for a given layer n, once injected into a symbolic calculation software. Resulting in

$$\mathcal{C}_{v_n}(\tau) = q_{(n)} \int_{\mathbb{R}} e^{2i\pi\omega\tau} \frac{T^2}{1 + 4\pi^2 T^2 \omega^2} \left[\frac{\tau_\eta^2}{1 + 4\pi^2 \tau_\eta^2 \omega^2} \right]^{n-1} d\omega, \tag{A.4}$$

and

$$\mathcal{C}_{a_n}(\tau) = q_{(n)} \int_{\mathbb{R}} 4\pi^2 \omega^2 e^{2i\pi\omega\tau} \frac{T^2}{1 + 4\pi^2 T^2 \omega^2} \left[\frac{\tau_\eta^2}{1 + 4\pi^2 \tau_\eta^2 \omega^2} \right]^{n-1} d\omega. \tag{A.5}$$

To finish with this proposition, the implied expression for the constant $q_{(n)}$ is stated to ensure the physical constraint on velocity variance (Eq. 2.17) by Parseval's identity,

$$\frac{\sigma^2}{q_{(n)}} = \int_{\mathbb{R}} \frac{T^2}{1 + 4\pi^2 T^2 \omega^2} \left[\frac{\tau_\eta^2}{1 + 4\pi^2 \tau_\eta^2 \omega^2} \right]^{n-1} d\omega. \tag{A.6}$$

Proof. Rephrased in the language of linear systems theory (see for instance Popoulis and Pillai [1991]), the system of equations Eqs. 2.12 to 2.16 defines a series of linear filters with a stochastic input. This explains the expression given for the velocity correlation of v_n (Eq. A.1).

The correlation function of v_n is computed, as it was done in Eq. 2.9 in a more straightforward manner, and drawing a connection with the approach adopted to

present the model of Sawford (Section 2.2.1), obtaining

$$\mathcal{C}_{v_n}(\tau) = \int_{-\infty}^{0}\int_{-\infty}^{\tau} e^{-(\tau-t_1-t_2)/T}\mathcal{C}_{f_{n-1}}(t_1-t_2)dt_1dt_2,$$

which can be formally rewritten as

$$\begin{aligned}
\mathcal{C}_{v_n}(\tau) &= \int_{\mathbb{R}^2} g_T(\tau+t_2)g_T(t_1)\mathcal{C}_{f_{n-1}}(t_1-t_2)dt_1dt_2 \\
&= \int_{\mathbb{R}^2} g_T(\tau+t_1+t_2)g_T(t_1)\mathcal{C}_{f_{n-1}}(t_2)dt_1dt_2 \\
&= \int_{\mathbb{R}} \left(g_T \star g_T\right)(\tau+t_2)\mathcal{C}_{f_{n-1}}(t_2)dt_2 \\
&= \left(g_T \star g_T \star \mathcal{C}_{f_{n-1}}\right)(\tau),
\end{aligned}$$

where $g_T(t) = e^{-t/T}1_{t\geq 0}$. Noticing that $G_T(t) = \left(g_T \star g_T\right)(t)$, one can arrive at the proposition made in Eq. A.1 after iterating the procedure for the $n-1$ remaining layers. The equivalent form of the velocity correlation in the spectral space (Eq. A.4) is a consequence of the convolution theorem, and that the Fourier transform of G_T is a Lorentzian function. *End of proof.*

Proposition A.1.2 *Take $n \geq 2$. Using the results of Proposition A.1.1,*

$$\mathcal{C}_{v_n}(\tau) = \frac{2\sigma^2 e^{-\tau_\eta^2/T^2}}{T\,\mathrm{erfc}\left(\tau_\eta/T\right)}\int_{\mathbb{R}} e^{2i\pi\omega\tau}\frac{T^2}{1+4\pi^2T^2\omega^2}\left[\frac{1}{1+\frac{4\pi^2\tau_\eta^2\omega^2}{n-1}}\right]^{n-1}d\omega, \tag{A.7}$$

such that

$$\mathcal{C}_v(\tau) \equiv \lim_{n\to\infty}\mathcal{C}_{v_n}(\tau) = \frac{2\sigma^2 e^{-\tau_\eta^2/T^2}}{T\,\mathrm{erfc}\left(\tau_\eta/T\right)}\int_{\mathbb{R}} e^{2i\pi\omega\tau}\frac{T^2}{1+4\pi^2T^2\omega^2}e^{-4\pi^2\tau_\eta^2\omega^2}d\omega. \tag{A.8}$$

This results in

$$\mathcal{C}_v(\tau) = \sigma^2 \frac{e^{-|\tau|/T}}{2\,\mathrm{erfc}(\tau_\eta/T)} \left[1 + \mathrm{erf}\left(\frac{|\tau|}{2\tau_\eta} - \frac{\tau_\eta}{T} \right) + e^{2|\tau|/T}\,\mathrm{erfc}\left(\frac{|\tau|}{2\tau_\eta} + \frac{\tau_\eta}{T} \right) \right], \quad \text{(A.9)}$$

with the particular value $\mathcal{C}_v(0) = \langle v^2 \rangle = \sigma^2$. *Concerning the acceleration correlation function, take (minus) the second derivative of* $\mathcal{C}_v$ *(Eq. A.9) and obtain*

$$\mathcal{C}_a(\tau) = \frac{\sigma^2}{2T^2\,\mathrm{erfc}(\tau_\eta/T)} \left[\frac{2T}{\tau_\eta\sqrt{\pi}} e^{-\left(\frac{\tau^2}{4\tau_\eta^2} + \frac{\tau_\eta^2}{T^2}\right)} - e^{-|\tau|/T} \left(1 + \mathrm{erf}\left(\frac{|\tau|}{2\tau_\eta} - \frac{\tau_\eta}{T} \right) \right) \right.$$
$$\left. - e^{|\tau|/T}\,\mathrm{erfc}\left(\frac{|\tau|}{2\tau_\eta} + \frac{\tau_\eta}{T} \right) \right]. \quad \text{(A.10)}$$

Proof. By Lebesgue's dominated convergence, one can safely commute $\lim_{n\to\infty}$ and the indefinite integral that enter in the expression given in Eq. A.7. Recall that $(1 + x/n)^n$ tends to e^x as $n \to \infty$, and get to Eq. A.8. Express then Eq. A.8 in the physical space as a convolution, and perform the remaining integral to arrive at Eq. A.9. The expression in Eq. A.10, the acceleration correlation function, also follows. *End of proof.*

Proposition A.1.3 *(On the statistical properties of the fields* $X_{1,\epsilon}$ *and its asymptotical log-correlated version* $X_1 \equiv \lim_{\epsilon\to 0} X_{1,\epsilon}$*)*

Recall first the definition of the OU-kernel $g_\tau(t) = e^{-t/\tau} 1_{t\geq 0}$, *where* $1_{t\geq 0}$ *stands for the indicator function of positive reals, and the associated response function* $G_\tau(t) = (g_\tau \star g_\tau)(t) = \frac{\tau}{2} e^{-|t|/\tau}$ *(Eq. A.3). Its derivative is also required, which reads as* $G'_\tau(t) = -\frac{t}{2|t|} e^{-|t|/\tau}$.

The unique solution $X_{1,\epsilon}$ *of the dynamics given in Eq. 2.30 is a zero-average Gaussian process, that reaches a statistically stationary regime at large time* t, *inde-*

pendently of the initial condition. In this statistically steady state, $X_{1,\epsilon}$ is thus fully characterized by its correlation function that reads

$$\mathcal{C}_{X_{1,\epsilon}}(\tau) = -\int_0^\infty \left[G'_T(\tau+h) - G'_T(\tau-h)\right] \frac{dh}{h+\epsilon+\sqrt{\epsilon(h+\epsilon)}} \tag{A.11}$$

$$= -e^{-|\tau|/T} \int_0^{|\tau|} \frac{\sinh\left(h/T\right) dh}{h+\epsilon+\sqrt{\epsilon(h+\epsilon)}} + \cosh(|\tau|/T) \int_{|\tau|}^\infty \frac{e^{-h/T} dh}{h+\epsilon+\sqrt{\epsilon(h+\epsilon)}}. \tag{A.12}$$

In particular,

$$\mathcal{C}_{X_{1,\epsilon}}(0) = \langle X_{1,\epsilon}^2 \rangle = \int_0^\infty \frac{e^{-h/T} dh}{h+\epsilon+\sqrt{\epsilon(h+\epsilon)}} \tag{A.13}$$

$$\underset{\epsilon\to 0}{=} \log\left(\frac{1}{\epsilon}\right) + O(1). \tag{A.14}$$

In the asymptotic regime $\epsilon \to 0$, whereas the variance of $X_{1,\epsilon}$ diverges, its correlation function at a given time lag $|\tau| > 0$ remains a bounded function of ϵ. This defines an asymptotic zero-average Gaussian process X_1 of infinite variance, but with a bounded covariance for $|\tau| > 0$, obtaining

$$\mathcal{C}_{X_1}(\tau) = \lim_{\epsilon\to 0} \mathcal{C}_{X_{1,\epsilon}}(\tau) = -\int_0^\infty \left[G'_T(\tau+h) - G'_T(\tau-h)\right] \frac{dh}{h} \tag{A.15}$$

$$= -e^{-|\tau|/T} \int_0^{|\tau|} \sinh\left(h/T\right) \frac{dh}{h} + \cosh(|\tau|/T) \int_{|\tau|}^\infty e^{-h/T} \frac{dh}{h} \tag{A.16}$$

$$= \log^+\left(\frac{T}{|\tau|}\right) + c(|\tau|), \tag{A.17}$$

where $\log^+(x) = \log\left(\max(x,1)\right)$ and $c(|\tau|)$ is a bounded function of its argument

such that it goes to 0 as $|\tau| \to \infty$*. Of special interest is the value of* c *at the origin,*

$$c(0) = \int_0^\infty e^{-y} \log(y) dy \approx -0.577216, \tag{A.18}$$

and is known as (minus) the Euler-Mascheroni constant.

The corresponding spectral representation of the correlation function of the limiting process X_1 *is given by*

$$\mathcal{C}_{X_1}(\tau) = \int_{\mathbb{R}} e^{2i\pi\omega\tau} 2\pi^2 |\omega| \frac{T^2}{1 + 4\pi^2 T^2 \omega^2} d\omega. \tag{A.19}$$

Proof.

Arguments developed in Chevillard [2017] can be easily adapted to show the expression of the correlation function of $X_{1,\epsilon}$ at a given finite ϵ (Eqs. A.11 and A.12) (see Pereira et al. [2018] for full derivation). The expression of its variance (Eq. A.13) is a consequence of Eq. A.12. To see the logarithmic divergence with respect to ϵ (Eq. A.14), split the integral entering in Eq. A.13 in two over $[0, \epsilon]$ and $[\epsilon, \infty]$ and observe that the first term tends to a bounded constant as $\epsilon \to 0$. Subtract then from the second term the quantity $\int_\epsilon^\infty e^{-h/T} dh/h$ and observe that the overall quantity remains bounded as $\epsilon \to 0$. This shows the logarithmic divergence since this is the case for this subtracted quantity (performing an integration by parts over the dummy variable h).

Similarly, expressions for the correlation function of the limiting process X_1 (Eqs. A.15 and A.16) are shown in Chevillard [2017] and Pereira et al. [2018]. Remark that the first integral on the RHS of Eq. A.16 vanishes as $\tau \to 0$, and observe (again by integration by parts) that the second integral diverges logarithmically with τ,

showing the small scale diverging behavior depicted in Eq. A.17. To prove the overall shape of $\mathcal{C}_{X_1}$ as it is given in Eq. A.17, the function c has to be shown to indeed be bounded and go to 0 at large arguments. It is easy to see that once the logarithmic diverging behavior is subtracted to the full expression, only bounded terms remain, which makes c bounded too. At large arguments, re-organize the terms in a proper way to see the convergence towards 0.

To show the spectral representation of the correlation function (Eq. A.19), use $G'_T(t) = \int e^{2i\pi\omega t} 2i\pi\omega T^2/(1+4\pi^2\omega^2T^2)d\omega$ and inject into Eq. A.15. Perform then the remaining integral over the dummy variable h using the known result $\int_0^\infty \sin(u)/u\, du = \pi/2$, and get Eq. A.19. As a final remark, whereas the regularization procedure over ϵ used in Eq. 2.30 may appear somehow arbitrary, and has some impact on the functional form of the correlation function $\mathcal{C}_{X_{1,\epsilon}}(\tau)$ (Eqs. A.11 and A.12), this dependence disappears in the limit $\epsilon \to 0$. In other words, the same correlation function $\mathcal{C}_{X_1}(\tau)$ (Eqs. A.15 and A.16) would have been obtained using another regularization procedure as long as the divergent behaviors of variance (Eq. A.14) and covariance (Eq. A.17) are ensured. This canonical behavior of the limiting process X_1 is consistent with the conclusions of Rhodes and Vargas [2009].

End of proof.

Proposition A.1.4 *(On the statistical properties of the fields $X_{n,\epsilon}$ and its asymptotical behavior)*

The unique solution $X_{n,\epsilon}$ of the dynamics given in Eq. 2.41 is a zero-average Gaussian process, and reaches a statistically stationary regime at large time T, independent of the initial condition. In this statistically steady state, $X_{n,\epsilon}$ is thus fully

characterized by its correlation function, conveniently expressed in spectral space as

$$\mathcal{C}_{X_{n,\epsilon}}(\tau) = \int_{\mathbb{R}} e^{2i\pi\omega\tau} 4\pi\omega \frac{T^2}{1+4\pi^2T^2\omega^2} \left[\frac{1}{1+\frac{4\pi^2\tau_\eta^2\omega^2}{n-1}}\right]^{n-1} \left(\int_0^\infty \frac{\sin(2\pi\omega h)dh}{h+\epsilon+\sqrt{\epsilon(h+\epsilon)}}\right) d\omega, \tag{A.20}$$

such that

$$\mathcal{C}_X(\tau) \equiv \lim_{n\to\infty}\lim_{\epsilon\to 0}\mathcal{C}_{X_{n,\epsilon}}(\tau) = \lim_{\epsilon\to 0}\lim_{n\to\infty}\mathcal{C}_{X_{n,\epsilon}}(\tau) \tag{A.21}$$

$$= \int_{\mathbb{R}} e^{2i\pi\omega\tau} 2\pi^2|\omega| \frac{T^2}{1+4\pi^2T^2\omega^2} e^{-4\pi^2\tau_\eta^2\omega^2} d\omega. \tag{A.22}$$

In particular,

$$\mathcal{C}_X(0) = \langle X^2\rangle = \int_{\mathbb{R}} 2\pi^2|\omega| \frac{T^2}{1+4\pi^2T^2\omega^2} e^{-4\pi^2\tau_\eta^2\omega^2} d\omega \tag{A.23}$$

$$\underset{\tau_\eta\to 0}{=} \log\left(\frac{T}{\tau_\eta}\right) + O(1),, \tag{A.24}$$

where the $O(1)$ constant is equal to minus one-half the Euler-Mascheroni constant (≈ -0.288), and

$$\lim_{\tau_\eta\to 0}\mathcal{C}_X(\tau) = \mathcal{C}_{X_1}(\tau), \tag{A.25}$$

where X_1 is the single-layer fractional Ornstein-Uhlenbeck process depicted in Proposition A.1.3.

Concerning the expression of this correlation function in the physical space, it

can be written for numerical purposes as

$$\mathcal{C}_X(\tau) = \frac{T}{4\tau_\eta^3} \int_{\mathbb{R}} e^{-\frac{|\tau - t|}{T}} \left[\tau_\eta - t\mathcal{F}\left(\frac{t}{2\tau_\eta}\right) \right] dt, \tag{A.26}$$

where the so-called Dawson integral $\mathcal{F}(x) = e^{-x^2} \int_0^x e^{y^2} dy$ *enters.*

Proof.

The correlation function $\mathcal{C}_{X_{n,\epsilon}}$ (Eq. A.20) corresponds to the successive linear operations made on a white noise $\widetilde{W}(dt)$: an OU process for a large time scale T, $n-2$ OU processes at the small time scale $\tau_\eta/\sqrt{n-1}$, and a fractional OU process of vanishing Hurst exponent at $\tau_\eta/\sqrt{n-1}$ (and defined in Proposition A.1.3). Expressions A.21 to A.25 follow from this spectral representation. The physical form of $\mathcal{C}_X$ (Eq. A.26) is obtained through inverse Fourier transformation of Eq. A.22.

End of proof.

Proposition A.1.5 *(Concerning the covariance structure of the infinitely differentiable causal MRW u and the corresponding acceleration process)*

Assume $\gamma^2 < 1$. *The unique statistically stationary solution* $u_{n,\epsilon}$ *of the set of equations Eqs. 2.35 to 2.39 converges, as far as the average and variance are concerned, when both* $\epsilon \to 0$ *and* $n \to \infty$ *(the limiting procedure commutes) to a zero-average process that is noted as u.*

Its correlation function reads

$$\mathcal{C}_u(\tau) = \int_{\mathbb{R}} G_T(h+\tau)\mathcal{C}_f(h)e^{\gamma^2\mathcal{C}_X(h)}dh \tag{A.27}$$

$$= Te^{-\frac{|\tau|}{T}}\int_0^{|\tau|}\cosh\left(\frac{h}{T}\right)\mathcal{C}_f(h)e^{\gamma^2\mathcal{C}_X(h)}dh + T\cosh\left(\frac{\tau}{T}\right)\int_{|\tau|}^{\infty}e^{-\frac{h}{T}}\mathcal{C}_f(h)e^{\gamma^2\mathcal{C}_X(h)}dh, \tag{A.28}$$

where $\mathcal{C}_X$ corresponds to the correlation function of the infinitely differentiable Gaussian process X depicted in Proposition A.1.4, and C_f the correlation function of the Gaussian force f entering in the dynamics of u_n (Eq. 2.35) once the limit $n \to \infty$ has been taken, and given by

$$\mathcal{C}_f(\tau) = \frac{\sigma^2}{T\int_0^{\infty}e^{-\frac{h}{T}}e^{-h^2/(4\tau_\eta^2)}e^{\gamma^2\mathcal{C}_X(h)}dh}e^{-\frac{\tau^2}{4\tau_\eta^2}}. \tag{A.29}$$

In the limit of infinite Reynolds numbers, i.e. as $\tau_\eta/T \to 0$, the correlation function $\mathcal{C}_u$ of u coincides with the one of the single-layered MRW u_1, which was shown in Section 2.2.2 to coincide itself with the one of the single-layered OU process v_1 (Eq. 2.2) of variance σ^2, and,

$$\lim_{\tau_\eta\to 0}\mathcal{C}_u(\tau) = \mathcal{C}_{u_1}(\tau) = \mathcal{C}_{v_1}(\tau) = \sigma^2 e^{-\frac{|\tau|}{T}}. \tag{A.30}$$

Rephrased in terms inherited from the phenomenology of turbulence, the asymptotic behavior of the correlation function (Eq. A.30) says that intermittent corrections observed at finite Reynolds numbers (Eq. A.27), and governed by the coefficient γ, disappear at infinite Reynolds numbers. In a similar spirit, these intermittent corrections only affect the dissipative range (i.e. τ of the order and smaller than

τ_η), and disappear in the inertial range $\tau_\eta \ll \tau \ll T$.

Going back to finite Reynolds number predictions, i.e. keeping τ_η finite and smaller than T, the expression of the Lagrangian integral time scale T_L is of special interest and is expressed as

$$T_L = \int_0^\infty \frac{\mathcal{C}_u(\tau)}{\mathcal{C}_u(0)} d\tau = \frac{T^2}{\sigma^2} \int_0^\infty \mathcal{C}_f(h) e^{\gamma^2 \mathcal{C}_X(h)} dh \underset{\tau_\eta \to 0}{\to} T. \tag{A.31}$$

The corresponding expression for the acceleration correlation function $\mathcal{C}_a$ is then obtained while taking (minus) the second derivatives of $\mathcal{C}_u$ (Eq. A.28), and reads

$$\mathcal{C}_a(\tau) = \mathcal{C}_f(\tau) e^{\gamma^2 \mathcal{C}_X(\tau)} - \frac{1}{T^2} \mathcal{C}_u(\tau). \tag{A.32}$$

Incidentally, the acceleration variance, and its behavior in the infinite Reynolds limit (i.e. while looking at the limit $\tau_\eta / T \to 0$), reads

$$\mathcal{C}_a(0) = \langle a^2 \rangle = \mathcal{C}_f(0) e^{\gamma^2 \mathcal{C}_X(0)} - \frac{\sigma^2}{T^2} \tag{A.33}$$

$$\underset{\tau_\eta / T \to 0}{\sim} \frac{\sigma^2}{\sqrt{\pi} T \tau_\eta}, \tag{A.34}$$

consistent with standard dimensional predictions, with no further intermittent corrections.

Proof.

Start with showing the form of the asymptotic correlation function $\mathcal{C}_f$ (Eq. A.29) of the force term f, when the number of layers n goes to infinity. Consider first this correlation at a finite n. One has, seeking for the stationary solution of Eq. 2.36

and computing its correlation function in the statistically steady regime,

$$\mathcal{C}_{f_{n-1}}(\tau) = \beta_n \int_{\mathbb{R}} e^{2i\pi\omega\tau} \left[\frac{\frac{\tau_\eta^2}{n-1}}{1 + \frac{4\pi^2\tau_\eta^2\omega^2}{n-1}} \right]^{n-1} d\omega.$$

Remark that for all positive x and integers n, by the binomial formula, $(1+x/n)^n$ is bounded from below by $1+x$, such that $(1+4\pi^2\tau_\eta^2\omega^2/(n-1))^{1-n}$ is bounded from above by $(1+4\pi^2\tau_\eta^2\omega^2)^{-1}$, which is an integrable function. This allows the use of dominated convergence to conclude on the convergence of $\mathcal{C}_{f_{n-1}}$ as $n \to \infty$, once β_n is taken as the expression in Eq. 2.40. Taking then the limit $n \to \infty$, the inverse Fourier transform of the obtained Gaussian function is computed to arrive at Eq. A.29.

Looking for the stationary solution of u (Eq. 2.35), once the limit $n \to \infty$ has been taken and keeping in mind that the log-correlated field X is independent of the forcing term f, the velocity correlation function reads $\mathcal{C}_u(\tau) = (g_T \star g_T \star \mathcal{C}_f e^{\gamma^2 \mathcal{C}_X})(\tau)$. This corresponds to the expression provided in Eq. A.27.

Whereas it is straightforward to show the convergence of the correlation function of the process as $\tau_\eta \to 0$ and then $\epsilon \to 0$, the convergence as $\epsilon \to 0$ and only then $\tau_\eta \to 0$, as it is stated in Eq. A.30, deserves attention. In any case, both ordering of limits give the same convergence towards the one of the OU process (Eq. A.30). The full demonstration of this is developed in Appendix A.3, where the respective convergence of the second order structure function is studied.

Other assertions of Proposition A.1.5 follow from the expression of $\mathcal{C}_u$.

End of proof.

Proposition A.1.6 *(Concerning the scaling of the higher-order structure functions*

of the infinitely differentiable causal MRW u)

Without loss of generality, consider an infinite number of layers $n \to \infty$, and call u_ϵ the respective process. Define the velocity increment of the process u_ϵ as

$$\delta_\tau u_\epsilon(t) = u_\epsilon(t+\tau) - u_\epsilon(t). \tag{A.35}$$

Accordingly, define the respective asymptotic structure functions as

$$\mathcal{S}_{u,m}(\tau) = \lim_{\epsilon \to 0} \langle (u_\epsilon(t+\tau) - u_\epsilon(t))^m \rangle \,. \tag{A.36}$$

As seen when presenting the correlation structure of u in proposition A.1.5, for $\gamma^2 < 1$,

$$\mathcal{S}_{u,2}(\tau) = \lim_{\epsilon \to 0} \mathcal{S}_{u_\epsilon,2}(\tau) = 2\left[\sigma^2 - \mathcal{C}_u(\tau)\right] \underset{\tau_\eta \to 0}{\longrightarrow} 2\sigma^2 \left[1 - e^{-\frac{|\tau|}{T}}\right]. \tag{A.37}$$

With respect to the convergence of the fourth-order structure function $\mathcal{S}_{u_\epsilon,4}$, a more subtle behavior related to the ordering of the limits is observed. It can be shown that, taking first the limit $\tau_\eta \to 0$ and keeping ϵ finite, $\mathcal{S}_{u_\epsilon,4}$ coincides with the fourth-order structure function of the single-layered MRW u_1 for which scaling properties are listed in Section 2.2.2. More precisely, for $4\gamma^2 < 1$

$$\lim_{\epsilon \to 0} \lim_{\tau_\eta \to 0} \mathcal{S}_{u_\epsilon,4}(\tau) = \mathcal{S}_{u_1,4}(\tau), \tag{A.38}$$

which exhibits an intermittent behavior (see Eq. 2.33, with $q = 2\sigma^2/T$ such that u and u_1 have same variance). In the reverse order of the limits, calculations get

intricate, but under an approximation procedure, the following scaling behavior is obtained

$$\lim_{\tau_\eta \to 0} \lim_{\epsilon \to 0} \mathcal{S}_{u_\epsilon,4}(\tau) = c_{\gamma,4} \mathcal{S}_{u_1,4}(\tau), \tag{A.39}$$

where $c_{\gamma,4}$ is a constant that depends only on the intermittency coefficient γ which can be computed. It can be observed that, in this approximation, the ordering of the limits has a consequence only on the value of the multiplicative constant entering in the power-laws (Eqs. A.38 and A.39), whereas the power-law exponent is the same in both cases, and exhibits an intermittent correction.

In a similar way, whereas taking the limit $\tau_\eta \to 0$ and then $\epsilon \to 0$ has no difficulties, it can be asserted that

$$\lim_{\tau_\eta \to 0} \lim_{\epsilon \to 0} \mathcal{S}_{u_\epsilon,2m}(\tau) = c_{\gamma,2m} \mathcal{S}_{u_1,2m}(\tau), \tag{A.40}$$

showing that u exhibits a lognormal spectrum (take a look at 2.34 with again $q = 2\sigma^2/T$) when the Reynolds number becomes infinite.

All proofs are gathered in Appendix A.3.

A.2 Scaling properties of the causal multifractal random walk structure functions

To set notations, various quantities that will enter in following calculations are first defined. The velocity increments read

$$\delta_\tau u_{1,\epsilon}(t) = u_{1,\epsilon}(t+\tau) - u_{1,\epsilon}(t) \tag{A.41}$$

$$= \int_{\mathbb{R}} g_{\tau,T}(t-s) e^{\gamma X_{1,\epsilon}(s) - \gamma^2 \langle X_{1,\epsilon}^2 \rangle} W(ds), \tag{A.42}$$

where $g_{\tau,T}$ corresponds to the OU-kernel associated to velocity increments, that is

$$g_{\tau,T}(t) = \sqrt{q} \left[e^{-\frac{t+\tau}{T}} 1_{t+\tau \geq 0} - e^{-\frac{t}{T}} 1_{t \geq 0} \right]. \tag{A.43}$$

Therefore,

$$\left\langle (\delta_\tau u_{1,\epsilon})^2 \right\rangle = \int_{\mathbb{R}^2} g_{\tau,T}(t-s_1) g_{\tau,T}(t-s_2) \left\langle e^{\gamma(X_{1,\epsilon}(s_1) + X_{1,\epsilon}(s_2)) - 2\gamma^2 \langle X_{1,\epsilon}^2 \rangle} W(ds_1) W(ds_2) \right\rangle \tag{A.44}$$

$$= \int_{\mathbb{R}^2} g_{\tau,T}(t-s_1) g_{\tau,T}(t-s_2) \left\langle e^{\gamma(X_{1,\epsilon}(s_1) + X_{1,\epsilon}(s_2)) - 2\gamma^2 \langle X_{1,\epsilon}^2 \rangle} \right\rangle \langle W(ds_1) W(ds_2) \rangle \tag{A.45}$$

$$= \int_{\mathbb{R}} g_{\tau,T}^2(t-s) \left\langle e^{2\gamma X_{1,\epsilon}(s) - 2\gamma^2 \langle X_{1,\epsilon}^2 \rangle} \right\rangle ds \tag{A.46}$$

$$= \int_{\mathbb{R}} g_{\tau,T}^2(s) ds, \tag{A.47}$$

where the independence of the fields $X_{1,\epsilon}$ and W is used, as well as the fact that $\langle e^x \rangle = e^{\frac{1}{2}\langle x^2 \rangle}$ for any zero-average Gaussian random variable x. It is then observed

that the result (Eq. A.47) would have been the same with the standard Ornstein-Uhlenbeck process v_1 (Eq. 2.2), which shows that the asymptotic process u_1 has no intermittent corrections up to second order. Performing the remaining integral that enters in Eq. A.47 leads to the result obtained in Eq. 2.32.

Similarly concerning the fourth-order structure function,

$$\left\langle (\delta_\tau u_{1,\epsilon})^4 \right\rangle = 3 \int_{\mathbb{R}^2} g^2_{\tau,T}(t-s_1) g^2_{\tau,T}(t-s_2) \left\langle e^{2\gamma(X_{1,\epsilon}(s_1)+X_{1,\epsilon}(s_2))-4\gamma^2\langle X^2_{1,\epsilon}\rangle} \right\rangle ds_1 ds_2 \tag{A.48}$$

$$= 3 \int_{\mathbb{R}^2} g^2_{\tau,T}(t-s_1) g^2_{\tau,T}(t-s_2) e^{4\gamma^2 \mathcal{C}_{X_{1,\epsilon}}(s_1-s_2)} ds_1 ds_2 \tag{A.49}$$

$$= 6 \int_0^\infty \left(g^2_{\tau,T} \star g^2_{\tau,T} \right)(s) e^{4\gamma^2 \mathcal{C}_{X_{1,\epsilon}}(s)} ds, \tag{A.50}$$

where Isserlis' theorem is implemented to factorize the four-time correlator of W in terms of products of its correlations, which gives rise to 3 symmetrical terms of equal contribution, an appropriate change of variables, and finally exploits the parity of the functions $\left(g^2_{\tau,T} \star g^2_{\tau,T} \right)$ and $\mathcal{C}_{X_{1,\epsilon}}$. Dominated convergence ensures that

$$\mathcal{S}_{u_1,4}(\tau) = \lim_{\epsilon \to 0} \left\langle (\delta_\tau u_{1,\epsilon})^4 \right\rangle \tag{A.51}$$

$$= 6 \int_0^\infty \left(g^2_{\tau,T} \star g^2_{\tau,T} \right)(s) e^{4\gamma^2 \mathcal{C}_{X_1}(s)} ds. \tag{A.52}$$

At this stage, remark that the integral provided in Eq. A.52 makes sense only if the singularity $\sim s^{-4\gamma^2}$ implied by $e^{4\gamma^2 \mathcal{C}_{X_1}(s)}$ (as easily seen in Eq. A.17) is integrable in the vicinity of the origin. This explains the bound on γ required by the existence

on the fourth order structure function, that is

$$4\gamma^2 < 1. \tag{A.53}$$

Compute then the function $\left(g^2_{\tau,T} \star g^2_{\tau,T}\right)(s)$, namely, for $s \geq 0$ and $\tau \geq 0$,

$$\left(g^2_{\tau,T} \star g^2_{\tau,T}\right)(s) = q^2 e^{-\frac{2s}{T}} \int_{\mathbb{R}} e^{-\frac{4x}{T}} \left[e^{-\frac{\tau}{T}} 1_{x+\tau\geq 0} - 1_{x\geq 0}\right]^2 \left[e^{-\frac{\tau}{T}} 1_{x+\tau+s\geq 0} - 1_{x+s\geq 0}\right]^2 dx, \tag{A.54}$$

which integrand is made up of simple exponentials over intricated domains, and get in an exact fashion (with the help of a symbolic calculation software),

$$\left(g^2_{\tau,T} \star g^2_{\tau,T}\right)(s) = \frac{q^2 T}{4} \left[\left(1 - e^{-\frac{\tau}{T}}\right)^3 \left(2 + e^{\frac{\tau}{T}} + e^{2\frac{\tau}{T}}\right) e^{-2\frac{s}{T}} \right. \tag{A.55}$$

$$\left. + 2\left(2e^{-\frac{\tau}{T}} - 1\right) \sinh\left(2\frac{\tau - s}{T}\right) 1_{\tau - s\geq 0}\right], \tag{A.56}$$

and inject it into the expression of $\mathcal{S}_{u_1,4}$ (Eq. A.52). Observe that the decrease of $\mathcal{S}_{u_1,4}$ as $\tau \to 0$ is governed by the second term $\left(g^2_{\tau,T} \star g^2_{\tau,T}\right)$ (Eq. A.56), since the first term (Eq. A.55) implies a decrease towards 0 as τ^3. Thus, only considering the leading contribution entering in Eq. A.56), using $\left(2e^{-\frac{\tau}{T}} - 1\right) \approx 1$, in good

approximation as $\tau \to 0$,

$$\mathcal{S}_{u_1,4}(\tau) \approx 3Tq^2 \int_0^\tau \sinh\left(\frac{2(\tau-s)}{T}\right) e^{4\gamma^2 \mathcal{C}_{X_1}(s)} ds \tag{A.57}$$

$$= 3Tq^2 \int_0^1 \sinh\left(\frac{2\tau(1-s)}{T}\right) e^{4\gamma^2 \mathcal{C}_{X_1}(\tau s)} \tau ds \tag{A.58}$$

$$\underset{\tau\to 0}{\sim} 6q^2\tau^2 \left(\frac{\tau}{T}\right)^{-4\gamma^2} e^{4\gamma^2 c(0)} \int_0^1 (1-s)\, s^{-4\gamma^2} ds \tag{A.59}$$

$$= \frac{3}{1-6\gamma^2+8\gamma^4} q^2\tau^2 \left(\frac{\tau}{T}\right)^{-4\gamma^2} e^{4\gamma^2 c(0)}, \tag{A.60}$$

where the constant $c(0)$ is explicitly known, and given in Eq. A.18. This entails Eq. 2.33.

Finally, to generalize former calculations up to any order:

$$\left\langle (\delta_\tau u_{1,\epsilon})^{2m} \right\rangle = \frac{(2m)!}{2^m m!} \int_{\mathbb{R}^m} \prod_{k=1}^m g_{\tau,T}^2(t-s_k) \left\langle e^{2\gamma \sum_{k=1}^m X_{1,\epsilon}(s_k) - 2m\gamma^2 \langle X_{1,\epsilon}^2 \rangle} \right\rangle \prod_{k=1}^m ds_k \tag{A.61}$$

$$= \frac{(2m)!}{2^m m!} \int_{\mathbb{R}^m} \prod_{k=1}^m g_{\tau,T}^2(t-s_k) e^{4\gamma^2 \sum_{k<p=1}^m \mathcal{C}_{X_{1,\epsilon}}(s_k-s_p)} \prod_{k=1}^m ds_k \tag{A.62}$$

$$\underset{\epsilon\to 0}{=} \frac{(2m)!}{2^m m!} \int_{\mathbb{R}^m} \prod_{k=1}^m g_{\tau,T}^2(t-s_k) e^{4\gamma^2 \sum_{k<p=1}^m \mathcal{C}_{X_1}(s_k-s_p)} \prod_{k=1}^m ds_k. \tag{A.63}$$

Once again, the exponential entering in Eq. A.63 gives both the condition of existence on γ, and intermittent corrections. The strongest singularity is encountered along the diagonal, that is when all dummy variables s_k coincide. It is equivalent to say that it is necessary to take

$$2m(m-1)\gamma^2 < 1, \tag{A.64}$$

to guarantee the existence of the integral given in Eq. A.63. Similarly, it implies an intermittent correction of order $(\tau/T)^{-2m(m-1)\gamma^2}$, as stated in Eq. 2.34, which concludes the proofs of Section 2.2.2.

A.3 Scaling properties of the infinitely differentiable causal multifractal random walk structure functions

Again, to set notations, definitions of various quantities that will enter in following calculations are provided. The velocity increments read

$$\delta_\tau u(t) = u(t+\tau) - u(t) \tag{A.65}$$

$$= \int_{\mathbb{R}} g_{\tau,T}(t-s) e^{\gamma X(s) - \frac{\gamma^2}{2}\langle X^2\rangle} f(s) ds, \tag{A.66}$$

where $g_{\tau,T}$ corresponds to the OU-kernel associated to velocity increments, that is

$$g_{\tau,T}(t) = e^{-\frac{t+\tau}{T}} 1_{t+\tau\geq 0} - e^{-\frac{t}{T}} 1_{t\geq 0}. \tag{A.67}$$

The following expressions is obtained

$$\left\langle (\delta_\tau u)^2 \right\rangle = \int_{\mathbb{R}^2} g_{\tau,T}(t-s_1) g_{\tau,T}(t-s_2) \mathcal{C}_f(s_1-s_2) \left\langle e^{\gamma(X(s_1)+X(s_2)) - \gamma^2\langle X^2\rangle} \right\rangle ds_1 ds_2 \tag{A.68}$$

$$= \int_{\mathbb{R}^2} g_{\tau,T}(t-s_1) g_{\tau,T}(t-s_2) \mathcal{C}_f(s_1-s_2) e^{\gamma^2 C_X(s_1-s_2)} ds_1 ds_2 \tag{A.69}$$

$$= \int_{\mathbb{R}} \left(g_{\tau,T} \star g_{\tau,T}\right)(s) \mathcal{C}_f(s) e^{\gamma^2 C_X(s)} ds \tag{A.70}$$

$$= 2\int_{\mathbb{R}^+} \left(g_{\tau,T} \star g_{\tau,T}\right)(s) \mathcal{C}_f(s) e^{\gamma^2 C_X(s)} ds, \tag{A.71}$$

where the independence of the fields X and f is used, and the fact that $\langle e^x \rangle = e^{\frac{1}{2}\langle x^2\rangle}$ for any zero-average Gaussian random variable x. This shows that, contrary to the MRW case u_1 (Eq. 2.32), the asymptotic process u (once the limit $\epsilon \to 0$ has been taken) has an intermittent correction up to second order when τ_η/T is finite. For

$\tau \geq 0$ and $s \geq 0$,

$$\left(g_{\tau,T} \star g_{\tau,T}\right)(s) = T\left(e^{-s/T} - e^{-\tau/T}\cosh(s/T) + \sinh\left(\frac{s-\tau}{T}\right)1_{s-\tau\geq 0}\right), \quad \text{(A.72)}$$

which shows that once injected in Eq. A.71, one can recover, in a consistent manner

$$\left\langle (\delta_\tau u)^2 \right\rangle = 2\left(\sigma^2 - C_u(\tau)\right). \quad \text{(A.73)}$$

To see the behavior of the second-order structure function in the (non-commuting) limit $\tau_\eta \to 0$ (i.e. the infinite Reynolds number limit) and then $\tau \to 0$ (i.e. the limit at small scales), regroup terms in Eq. A.72 and obtain, using the definition of $\mathcal{C}_f$ (Eq. A.29),

$$\left\langle (\delta_\tau u)^2 \right\rangle = 2\sigma^2\left[1 - \cosh\left(\frac{\tau}{T}\right)\right] + 2\sigma^2 \frac{\int_0^\tau \sinh\left(\frac{\tau-s}{T}\right) e^{-\frac{s^2}{4\tau_\eta^2}} e^{\gamma^2 \mathcal{C}_X(s)} ds}{\int_0^\infty e^{-\frac{s}{T}} e^{-\frac{s^2}{4\tau_\eta^2}} e^{\gamma^2 \mathcal{C}_X(s)} ds}. \quad \text{(A.74)}$$

Rescale then the dummy variable entering the second term by τ_η and obtain

$$\left\langle (\delta_\tau u)^2 \right\rangle = 2\sigma^2\left[1 - \cosh\left(\frac{\tau}{T}\right)\right] + 2\sigma^2 \frac{\int_0^{\tau/\tau_\eta} \sinh\left(\frac{\tau-s\tau_\eta}{T}\right) e^{-\frac{s^2}{4}} e^{\gamma^2 \mathcal{C}_X(s\tau_\eta)} ds}{\int_0^\infty e^{-\frac{s\tau_\eta}{T}} e^{-\frac{s^2}{4}} e^{\gamma^2 \mathcal{C}_X(s\tau_\eta)} ds}, \quad \text{(A.75)}$$

such that the simple result is obtained

$$\lim_{\tau_\eta \to 0} \left\langle (\delta_\tau u)^2 \right\rangle = 2\sigma^2\left[1 - e^{-\frac{\tau}{T}}\right], \quad \text{(A.76)}$$

showing that, up to second-order statistics, the infinitely differentiable causal multifractal walk u coincides with the underlying OU process (Eq. 2.2) in the infinite

Reynolds number limit $\tau_\eta \to 0$.

Concerning the fourth-order structure function, in a similar manner

$$\left\langle (\delta_\tau u)^4 \right\rangle = 3 \int_{\mathbb{R}^4} \prod_{k=1}^{4} g_{\tau,T}(t - s_k) \left\langle e^{\gamma \sum_{k=1}^{4} X(s_k) - 2\gamma^2 \langle X^2 \rangle} \right\rangle \mathcal{C}_f(s_1 - s_2) \mathcal{C}_f(s_3 - s_4) \prod_{k=1}^{4} ds_k \tag{A.77}$$

$$= 3 \int_{\mathbb{R}^4} \prod_{k=1}^{4} g_{\tau,T}(s_k) e^{\gamma^2 \sum_{k<p=1}^{4} \mathcal{C}_X(s_k - s_p)} \mathcal{C}_f(s_1 - s_2) \mathcal{C}_f(s_3 - s_4) \prod_{k=1}^{4} ds_k \tag{A.78}$$

$$= 3 \int_{\mathbb{R}^4} g_{\tau,T}(s) g_{\tau,T}(s - h_1) g_{\tau,T}(s - h_2) g_{\tau,T}(s - h_3) \tag{A.79}$$

$$\times e^{\gamma^2 (\mathcal{C}_X(h_1) + \mathcal{C}_X(h_2) + \mathcal{C}_X(h_3) + \mathcal{C}_X(h_1 - h_2) + \mathcal{C}_X(h_1 - h_3) + \mathcal{C}_X(h_2 - h_3))} \tag{A.80}$$

$$\times \mathcal{C}_f(h_1) \mathcal{C}_f(h_3 - h_2) ds \prod_{k=1}^{3} dh_k \tag{A.81}$$

$$= 3 \int_{\mathbb{R}^3} G_{\tau,T}(h_1, h_2, h_3) \mathcal{C}_f(h_1) \mathcal{C}_f(h_2 - h_3) e^{\gamma^2 \left(\sum_{k=1}^{3} \mathcal{C}_X(h_k) + \sum_{k<l,1}^{3} \mathcal{C}_X(h_k - h_l) \right)} \prod_{k=1}^{3} dh_k, \tag{A.82}$$

where it is noted

$$G_{\tau,T}(h_1, h_2, h_3) = \int_{\mathbb{R}} g_{\tau,T}(s) g_{\tau,T}(s + h_1) g_{\tau,T}(s + h_2) g_{\tau,T}(s + h_3) ds. \tag{A.83}$$

The exact expression of the function $G_{\tau,T}$ (Eq. A.83) could be obtained using a symbolic calculation software, although it is intricate. Instead, an approximative calculation is used, based on an ansatz for the correlation function $\mathcal{C}_X$ entering in the expression of the moment of velocity increments (Eq. A.82), get then an equivalent at infinite Reynolds number (i.e. $\tau_\eta \to 0$), from which the scaling behavior as τ goes to zero is deduced.

As has been observed, the correlation function $\mathcal{C}_X(\tau)$ of X (Eq. A.22) has several obvious limiting behaviors. First, it goes to zero at large arguments $\tau \gg T$. Secondly, as $\tau_\eta \to 0$, its value at the origin blows up logarithmically with τ_η (Eq. A.24), and in the same limit, point-wise, for strictly positive arguments $\tau > 0$, it behaves logarithmically with τ as $\tau \to 0$. A simple ansatz for $\mathcal{C}_X(\tau)$ consistent with these limiting behaviors could be written in an approximative and simple way as

$$\mathcal{C}_X(\tau) \approx \frac{1}{2} \log \frac{T^2}{\tau_\eta^2 + \tau^2} 1_{|\tau| \leq T} + d_{\tau_\eta}(\tau), \tag{A.84}$$

where $d_{\tau_\eta}(\tau)$ is a bounded function of τ and τ_η, that goes to zero at large arguments. Furthermore, it is known that $d_{\tau_\eta}(0) \to d(0)$ coincides with minus one-half the Euler-Mascheroni constant (i.e. ≈ -0.288) as $\tau_\eta \to 0$ (Eq. A.24). Henceforth, calculations will not be performed in a rigorous way since the ansatz (Eq. A.84) in only an approximative, although realistic, form of $\mathcal{C}_X$.

Find now the point-wise behavior of the correlation function C_f of f (Eq. A.29). Looking for an equivalent of the multiplicative factor entering in Eq. A.29 and using the ansatz proposed in Eq. A.84, the following is obtained

$$\frac{T(T/\tau_\eta)^{\gamma^2} e^{\gamma^2 d(0)} g(\gamma)}{\sigma^2} \mathcal{C}_f(\tau) \underset{\tau_\eta \to 0}{\sim} \frac{1}{\sqrt{4\pi\tau_\eta^2}} e^{-\frac{\tau^2}{4\tau_\eta^2}}, \tag{A.85}$$

where

$$g(\gamma) = \frac{1}{\sqrt{4\pi}} \int_0^\infty e^{-h^2/4} \frac{1}{(1+h^2)^{\gamma^2}} dh. \tag{A.86}$$

From the equivalent derived in Eq. A.85, one can see that $\mathcal{C}_f$, properly weighted, will participate to the fourth-order moment of increments (Eq. A.82) similar to a

distributional Dirac function, and will greatly simplify its expression. Check the realism of the ansatz (Eq. A.85) on the second-order structure function (Eq. A.70) and obtain $\left\langle (\delta_\tau u)^2 \right\rangle \sim \frac{\sigma^2}{Tg(\gamma)} \left(g_{\tau,T} \star g_{\tau,T}\right)(0) = \frac{\sigma^2}{g(\gamma)}(1 - e^{-\tau/T})$ as $\tau_\eta \to 0$. The approach based on the ansatz (Eq. A.84) introduces an error compared to the exact result given in Eq. A.76: instead of the exact factor 2 entering in Eq. A.76, the factor $1/g(\gamma) \approx 2.1388$ is used as the empirical intermittency coefficient given in Eq. 2.82, corresponding thus to an overestimation of order $1/(2g(\gamma)) \approx 7\%$ of the multiplicative constant, the remaining power-law dependence on τ being correct.

Having justified the good performance of this approximative procedure, inject then Eq. A.85 into Eq. A.82, use the limiting behavior of $\mathcal{C}_X$ as $\tau_\eta \to 0$ (Eq. A.25), and obtain, in a heuristic fashion, the following expression

$$\left\langle (\delta_\tau u)^4 \right\rangle \underset{\tau_\eta \to 0}{\sim} 6 \frac{\sigma^4}{g^2(\gamma) T^2} \int_0^\infty G_{\tau,T}(0,h,h) e^{4\gamma^2 \mathcal{C}_{X_1}(h)} dh. \tag{A.87}$$

Noticing that $G_{\tau,T}(0,h,h) = \left(g_{\tau,T}^2 \star g_{\tau,T}^2\right)(h)$, the fourth-order structure function of the MRW process (Eq. A.52) is recovered using $q = 2\sigma^2/T$ in Eq. A.43 (to make sure that two processes of same variance σ^2 are compared) up to a multiplicative factor such that

$$\left\langle (\delta_\tau u)^4 \right\rangle \underset{\tau_\eta \to 0}{\sim} \frac{1}{4g^2(\gamma)} \left\langle (\delta_\tau u_1)^4 \right\rangle. \tag{A.88}$$

The numerical value of this factor is $\frac{1}{4g^2(\gamma)} \approx 1.1436$ working with the empirical value for γ (Eq. 2.82), saying that $\left\langle (\delta_\tau u)^4 \right\rangle$ is very similar to $\left\langle (\delta_\tau u_1)^4 \right\rangle$ at large Reynolds number, in particular its (intermittent) scaling behavior with τ (see Eq. A.60).

This appendix is finished by computing, under the same approximation based

on Eq. A.84, higher-order structure functions. This results in

$$\left\langle (\delta_\tau u)^{2m} \right\rangle \tag{A.89}$$

$$= \frac{(2m)!}{2^m m!} \int_{\mathbb{R}^{2m}} \prod_{k=1}^{2m} g_{\tau,T}(t-s_k) \left\langle e^{\gamma \sum_{k=1}^{2m} X(s_k) - m\gamma^2 \langle X^2 \rangle} \right\rangle \prod_{k=1}^{m} \mathcal{C}_f(s_{2k-1} - s_{2k}) \prod_{k=1}^{2m} ds_k \tag{A.90}$$

$$= \frac{(2m)!}{2^m m!} \int_{\mathbb{R}^{2m}} \prod_{k=1}^{2m} g_{\tau,T}(t-s_k) e^{\gamma^2 \sum_{k<l,1}^{2m} \mathcal{C}_X(s_k - s_l)} \prod_{k=1}^{m} \mathcal{C}_f(s_{2k-1} - s_{2k}) \prod_{k=1}^{2m} ds_k \tag{A.91}$$

$$\underset{\tau_\eta \to 0}{\sim} \frac{(2m)!}{2^m m!} \left(\frac{\sigma^2}{g(\gamma) T} \right)^m \int_{\mathbb{R}^m} \prod_{k=1}^{m} g_{\tau,T}^2(t-s_k) e^{\gamma^2 \sum_{k<l,1}^{m} \mathcal{C}_{X_1}(s_k - s_l)} \prod_{k=1}^{m} ds_k, \tag{A.92}$$

showing that

$$\left\langle (\delta_\tau u)^{2m} \right\rangle \underset{\tau_\eta \to 0}{\sim} \frac{1}{2^m g^m(\gamma)} \left\langle (\delta_\tau u_1)^{2m} \right\rangle, \tag{A.93}$$

which entails Eq. A.40.

A.4 Derivation of the Reynolds number dependence of the acceleration variance

The Reynolds number dependence, or equivalently the dependence on the free parameters τ_η and T, of the acceleration variance, and the scaling behavior of $\mathcal{S}_{2m}(\tau)$ with τ at infinite Reynolds number (i.e. for $\tau_\eta \to 0$) is herein provided. As it is detailed in Chevillard et al. [2012], or simply deduced from Eq. 2.57 using $\mathcal{S}_2(\tau) = \langle a^2 \rangle \tau^2 + o(\tau^2)$, one obtains

$$\langle a^2 \rangle = \frac{2\sigma^2}{T^2} \frac{1}{\mathcal{Z}(0)} \int_{h_{\min}}^{h_{\max}} \left(\frac{\tau_\eta}{T}\right)^{2\frac{2(h-1)+1-\mathcal{D}^L(h)}{2h+1}} dh, \tag{A.94}$$

with

$$\mathcal{Z}(0) = \int_{h_{\min}}^{h_{\max}} \left(\frac{\tau_\eta}{T}\right)^{2\frac{1-\mathcal{D}^L(h)}{2h+1}} dh. \tag{A.95}$$

Follow then a steepest-descent procedure. Compute first the minimum and the minimizer of the exponents entering in Eqs. A.94 and A.95, using for $\mathcal{D}^L$ the expression provided in Eq. 2.54. Notice that $\min_h \frac{1-\mathcal{D}^L(h)}{2h+1} = 0$ and assume $\gamma^2 < 2 - \sqrt{3}$ to guarantee the positivity of these real-valued minimizers, a condition which is fulfilled by the empirical value of the intermittency coefficient (Eq. 2.82). To get an estimation of the remaining multiplicative constant following this steepest-descent calculation, perform a Taylor series of the exponents entering in Eqs. A.94 and A.95 around their respective minimizer up to second order, and finally approximate the remaining Gaussian integrals extending the integration range over $h \in \mathbb{R}$. Eventually, the following exact equivalent is obtained as the Reynolds number goes to

infinity:

$$\langle a^2 \rangle \underset{\tau_\eta \to 0}{\sim} \frac{2\sigma^2}{T^2} \frac{\left[1 - 4\gamma^2 + \gamma^4\right]^{\frac{1}{4}}}{\sqrt{1+\gamma^2}} \left(\frac{\tau_\eta}{T}\right)^{\frac{\gamma^2 - 1 + \sqrt{1-4\gamma^2+\gamma^4}}{\gamma^2}} . \tag{A.96}$$

The multifractal prediction of acceleration variance (Eq. A.96) does exhibit an intermittent correction, as it was already derived in a very similar way by Borgas [1993], Sawford et al. [2003].

Appendix B

Batchelor modeling algorithms

B.1 Tabulation of constants used for the Batchelor transformation based on fits of the experimental data

$$\frac{\overline{u}_z(r,z)}{U_0(z)} = e^{-A_1\eta^2}$$

$$\frac{\overline{u}_r(r,z)}{U_0(z)} = \left(\eta e^{-A_1\eta^2} - \frac{1-e^{-A_1\eta^2}}{2A_1\eta}\right)$$

$$\frac{\sigma^2_{u_z}(r,z)}{U_0^2(z)} = C_2 e^{-A_2(\eta-B_2)^2}$$

$$\frac{\sigma^2_{u_r}(r,z)}{U_0^2(z)} = C_3 e^{-A_3\eta^2}$$

$$\frac{\sigma^2_{u_\theta}(r,z)}{U_0^2(z)} = C_4 e^{-A_4(\eta-B_4)^2}$$

$$T_{E_z}(z) = C_5 z^2$$

A_1	A_2	A_3	A_4	B_2	B_4	C_2	C_3	C_4	C_5
79.0	57.4	32.3	72.9	0.027	0.039	0.073	0.044	0.039	0.84

Parameters inputted into the model based on fits of the experimental self-similarity profiles.

B.2 Mathematical algorithm of the Batchelor transformation

Data obtained from the HIST-OU or HIST-DNS, denoted with a tilde, is created in Cartesian grid and converted to cylindrical coordinates to build up the jet. First, the first-order ordinary differential equation for the Lagrangian path of a tracer fluid element is presented as:

$$\frac{d\boldsymbol{X}(t)}{dt} \equiv \boldsymbol{v}(\boldsymbol{X}(t)),$$

where $\boldsymbol{v}(\boldsymbol{X}(t))$ is the Lagrangian velocity. The homogeneous, isotropic and stationary turbulent velocity signal in Cartesian coordinates (x, y and z) is herein denoted as:

$$\tilde{\boldsymbol{v}}(t) = \begin{cases} \tilde{v}_x(t) \\ \tilde{v}_y(t) \\ \tilde{v}_z(t). \end{cases}$$

Therefore, initial condition must be converted for $\tilde{v}_r$ and $\tilde{v}_\theta$ such that:

$$\tilde{v}_{r,0} = \tilde{v}_{x,0}\cos(\theta_0) + \tilde{v}_{y,0}\sin(\theta_0)$$

$$\tilde{v}_{\theta,0} = -\tilde{v}_{x,0}\sin(\theta_0) + \tilde{v}_{y,0}\cos(\theta_0).$$

Next initial velocities are obtained for the jet based on a given initial cylindrical

location (r_0, θ_0, z_0),

$$
\begin{aligned}
v_{r,0} &= \tilde{v}_{r,0}\sigma_{u_r}(r_0, z_0) + \overline{u}_r(r_0, z_0) \\
v_{\theta,0} &= \tilde{v}_{\theta,0}\sigma_{u_\theta}(r_0, z_0) \\
v_{z,0} &= f_{rz}(r_0, z_0)\frac{\tilde{v}_{r,0}}{\sigma_{v_r}(r_0, z_0)} \\
&\quad + \sqrt{\sigma_{v_r}(r_0, z_0)^2\sigma_{v_{z,0}}(r_0, z_0)^2 - f_{rz}^2(r_0, z_0)}\frac{\tilde{v}_{z,0}}{\sigma_{v_r}(r_0, z_0)} + \overline{u}_z(r_0, z_0),
\end{aligned}
$$

recalling that the v_z component requires special attention to produce the true stress behaviors of the jet.

Finally, the domain must return to Cartesian coordinates to obtain the following position of the jet. This is found by

$$
\begin{aligned}
v_{x,0} &= v_{r,0}\cos(\theta_0) - v_{\theta,0}\sin(\theta_0) \\
v_{y,0} &= v_{r,0}\sin(\theta_0) + \tilde{v}_{\theta,0}\cos(\theta_0).
\end{aligned}
$$

Given all previously defined initial conditions as well as the initial time $\tau_0 = 0$, the jet can be built such that

$$
\begin{aligned}
\tau_n &= \tau_{n-1} + \mathrm{d}\tilde{\tau}T_{E_z}(r(\tau_{n-1}), z(\tau_{n-1})) \\
x_n &= x_{n-1} + v_{x,n-1}d\tau_n \\
y_n &= y_{n-1} + v_{y,n-1}d\tau_n \\
z_n &= z_{n-1} + v_{z,n-1}d\tau_n,
\end{aligned}
$$

where, $\mathrm{d}\tau_n = \tau_n - \tau_{n-1}$.

At each time step, a corresponding location in cylindrical coordinates is found to continually convert the HIST signal from Cartesian to cylindrical coordinates to utilize the known self-similarity properties of the jet. Therefore,

$$r_n = \sqrt{x_n^2 + y_n^2}$$
$$\theta_n = \arctan\left(y_n / x_n\right)$$

and

$$\tilde{v}_{r,n} = \tilde{v}_{x,n}\cos\left(\theta_n\right) + \tilde{v}_{y,n}\sin\left(\theta_n\right)$$
$$\tilde{v}_{\theta,n} = -\tilde{v}_{x,n}\sin\left(\theta_n\right) + \tilde{v}_{y,n}\cos\left(\theta_n\right).$$

and the velocity at the given location of the jet for a given trajectory is obtained by,

$$\begin{aligned} v_{r,n} &= \tilde{v}_{r,n}\sigma_{u_r}(r_n, z_n) + \overline{u}_r(r_n, z_n) \\ v_{\theta,n} &= \tilde{v}_{\theta,n}\sigma_{u_\theta}(r_n, z_n) \\ v_{z,n} &= f_{rz}(r_n, z_n)\frac{\tilde{v}_{r,n}}{\sigma_{v_r}(r_n, z_n)} \\ &\quad + \sqrt{\sigma_{v_r}^2(r_n, z_n)\sigma_{v_{z,n}}^2(r_n, z_n) - f_{rz}^2(r_n, z_n)}\frac{\tilde{v}_{z,n}}{\sigma_{v_r}(r_n, z_n)} + \overline{u}_z(r_n, z_n). \end{aligned}$$

Last, the velocities are converted to Cartesian coordinates to acquire the follow-

ing position of the jet,

$$v_{x,n} = v_{r,n}\cos(\theta_n) - v_{\theta,n}\sin(\theta_n)$$
$$v_{y,n} = v_{r,n}\sin(\theta_n) + \tilde{v}_{\theta,n}\cos(\theta_n).$$

B.3 Diagonalization of the covariance - inclusion of the $v_r'v_z'$ correlation

Recall that a first-order ordinary differential equation is solved,

$$\frac{d\boldsymbol{X}(t)}{dt} \equiv \boldsymbol{v}(\boldsymbol{X}(t)),$$

where $\boldsymbol{v}(\boldsymbol{X}(t))$ is the Lagrangian velocity and the HIST velocity signal is in Cartesian coordinates (x, y and z). Restrictions on the model cause unit variance and zero-average velocities, mathematically:

$$\langle\tilde{v}_x(t)\rangle = \langle\tilde{v}_y(t)\rangle = \langle\tilde{v}_z(t)\rangle = 0$$

and

$$\langle\tilde{v}_x^2(t)\rangle = \langle\tilde{v}_y^2(t)\rangle = \langle\tilde{v}_z^2(t)\rangle = \sigma^2,$$

where for simplicity, $\sigma^2 = 1$. Next obtain the HIST velocity signals in cylindrical coordinates, where θ is known *a priori* by $\boldsymbol{X}(t)$. Explicitly

$$\tilde{\boldsymbol{v}}_{cyl} = \begin{cases} \tilde{v}_r &= \tilde{v}_x\cos(\theta) + \tilde{v}_y\sin(\theta) \\ \tilde{v}_\theta &= -\tilde{v}_x\sin(\theta) + \tilde{v}_y\cos(\theta) \\ \tilde{v}_z &= \tilde{v}_z \end{cases}$$

The transformed velocity field continues to be zero-average with unit variance.

The jet is then built up based on this cylindrical HIST signal, $\tilde{\boldsymbol{v}}_{cyl}$. First, denoted $\boldsymbol{v}_{cyl}$ as the jet velocity, the outcome of the model predicts that:

$$\langle \boldsymbol{v}_{cyl} \rangle = \begin{bmatrix} v_r(r,z) \\ v_\theta(r,z) \\ v_z(r,z) \end{bmatrix},$$

and

$$\langle (\boldsymbol{v}_{cyl} - \langle \boldsymbol{v}_{cyl} \rangle)(\boldsymbol{v}_{cyl} - \langle \boldsymbol{v}_{cyl} \rangle)^T \rangle = \begin{bmatrix} \sigma^2_{v_r}(r,z) & f_{r\theta}(r,z) & f_{rz}(r,z) \\ f_{r\theta}(r,z) & \sigma^2_{v_\theta}(r,z) & f_{\theta z}(r,z) \\ f_{rz}(r,z) & f_{\theta z}(r,z) & \sigma^2_{v_z}(r,z) \end{bmatrix} = \boldsymbol{\mathcal{C}}(r,z),$$

where $\boldsymbol{\mathcal{C}}$ is a symmetric positive-definite matrix by calculation. The elements of the diagonal, i.e., the variance, should be known *a prior* by the self-similarity relations.

Then, consider a matrix $\boldsymbol{\mathcal{L}}$ such that $\boldsymbol{\mathcal{L}}\boldsymbol{\mathcal{L}}^T = \boldsymbol{\mathcal{C}}$ and take

$$\boldsymbol{v}_{cyl} = \boldsymbol{\mathcal{L}}\tilde{\boldsymbol{v}}_{cyl}.$$

Experimental results dictate that $f_{r\theta}(r,z) = f_{\theta z}(r,z) = 0$ and therefore

$$\boldsymbol{\mathcal{C}}(r,z) = \begin{bmatrix} \sigma^2_{v_r}(r,z) & 0 & f_{rz}(r,z) \\ 0 & \sigma^2_{v_\theta}(r,z) & 0 \\ f_{rz}(r,z) & 0 & \sigma^2_{v_z}(r,z). \end{bmatrix},$$

The solution for $\boldsymbol{\mathcal{L}}$ is given as

$$\boldsymbol{\mathcal{L}} = \begin{bmatrix} \sigma_{v_r}(r,z) & 0 & 0 \\ 0 & \sigma_{v_\theta}(r,z) & 0 \\ \frac{f_{rz}(r,z)}{\sigma_{v_r}(r,z)} & 0 & \sqrt{\sigma^2_{v_z}(r,z) - \frac{f^2_{rz}(r,z)}{\sigma^2_{v_r}(r,z)}} \end{bmatrix}.$$